

A Measurement of the Relative Branching Ratio
 $BR(B^- \rightarrow D^0 K^-)/BR(B^- \rightarrow D^0 \pi^-)$ in Three D^0 Decay Modes

by

Hung-Chung Fang

A dissertation submitted in partial satisfaction of the

requirements for the degree of

Doctor of Philosophy

in

Physics

in the

Graduate Division

of the

University of California, Berkeley

Committee in charge:

Professor Marjorie D. Shapiro, Chair

Professor Robert G. Jacobsen

Professor Stephen E. Derenzo

Fall 2011

A Measurement of the Relative Branching Ratio
 $BR(B^- \rightarrow D^0 K^-)/BR(B^- \rightarrow D^0 \pi^-)$ in Three D^0 Decay Modes

Copyright 2011

by

Hung-Chung Fang

Abstract

A Measurement of the Relative Branching Ratio
 $BR(B^- \rightarrow D^0 K^-)/BR(B^- \rightarrow D^0 \pi^-)$ in Three D^0 Decay Modes

by

Hung-Chung Fang

Doctor of Philosophy in Physics

University of California, Berkeley

Professor Marjorie D. Shapiro, Chair

Using 1.3 fb^{-1} of data from $p\bar{p}$ collisions at $\sqrt{s} = 1.96 \text{ TeV}$ collected with the CDF II detector at the Fermilab Tevatron, we have measured the relative branching ratio $BR(B^- \rightarrow D^0 K^-)/BR(B^- \rightarrow D^0 \pi^-)$ and its charge conjugate in the D^0 flavor decay mode $D_f^0 \rightarrow K^- \pi^+$ and the CP-even decay modes $D^0 \rightarrow K^- K^+$ and $D^0 \rightarrow \pi^- \pi^+$. From these measurements, we derive:

$$\begin{aligned} R &= \frac{BR(B^- \rightarrow D_f^0 K^-) + BR(B^+ \rightarrow \bar{D}_f^0 K^+)}{BR(B^- \rightarrow D_f^0 \pi^-) + BR(B^+ \rightarrow \bar{D}_f^0 \pi^+)} \\ &= (7.99 \pm 0.33 \text{ (stat.)} \pm 0.38 \text{ (sys.)})\%, \end{aligned}$$

$$\begin{aligned} R_{\text{CP}^+} &= \frac{BR(B^- \rightarrow D_{\text{CP}^+}^0 K^-) + BR(B^+ \rightarrow D_{\text{CP}^+}^0 K^+)}{[BR(B^- \rightarrow D_f^0 K^-) + BR(B^+ \rightarrow \bar{D}_f^0 K^+)]/2} \\ &= 1.15 \pm 0.17 \text{ (stat.)} \pm 0.02 \text{ (sys.)}, \end{aligned}$$

$$\begin{aligned} A_{\text{CP}^+} &= \frac{BR(B^- \rightarrow D_{\text{CP}^+}^0 K^-) - BR(B^+ \rightarrow D_{\text{CP}^+}^0 K^+)}{BR(B^- \rightarrow D_{\text{CP}^+}^0 K^-) + BR(B^+ \rightarrow D_{\text{CP}^+}^0 K^+)} \\ &= 0.10 \pm 0.15 \text{ (stat.)} \pm 0.02 \text{ (sys.)}. \end{aligned}$$

These values are consistent with Standard Model expectations.

To my parents

Contents

List of Figures	v
List of Tables	viii
1 Introduction	1
2 Theoretical Preliminaries	2
2.1 The Standard Model	2
2.2 Fermion mass terms, the CKM matrix, and CP violation	4
2.3 The Unitarity triangle and the measurement of its angle γ	8
3 The Tevatron and the CDF II Experiment	14
3.1 The Fermilab accelerator complex	14
3.1.1 The proton source	14
3.1.2 The antiproton source	15
3.1.3 The Main Injector	15
3.1.4 The Recycler	15
3.1.5 The Tevatron	15
3.2 The CDF II detector	16
3.2.1 Inner trackers	16
3.2.2 Trigger system	20
4 Analysis Fundamentals	22
4.1 Synopsis	22
4.2 Data samples and B candidate reconstruction	24
4.3 Monte Carlo datasets	26
4.4 Analysis cuts	28
4.4.1 Comments on cut variables	29
4.4.2 Analysis cuts for the $D^0 X^-$ signal samples and the $D^{*+} X^-$ control sample	29
4.4.3 Analysis cuts for the $D^+ X^-$ control sample	30
4.5 The maximum likelihood fitter	33

4.6	Fit components and their templates	34
4.6.1	Single- B modes	34
4.6.2	Fake- D background	35
4.6.3	Real- D combinatorial background	36
4.7	Z templates for pions and kaons	37
4.8	Efficiency corrections on the fit output	39
4.9	Toy Monte Carlo validation of the fitter	40
5	Control Samples	48
5.1	D^+X^- fits	48
5.1.1	Fit configuration	48
5.1.2	Results	51
5.1.3	Toy Monte Carlo validation of the fitter	51
5.1.4	Discussion of the fit residuals in Z	51
5.1.5	Systematic uncertainties	52
5.1.6	Comparison with world averages	54
5.2	$D^{*+}X^-$ fits	54
5.2.1	Fit configuration	55
5.2.2	Results	56
5.2.3	Toy Monte Carlo validation of the fitter	56
5.2.4	Comparison with world averages	56
6	Signal Samples	77
6.1	Mass constraints on the D^0 candidates	77
6.2	$D^0[K^-\pi^+]X^-$ fits	78
6.2.1	Fit configuration	78
6.2.2	Results	80
6.2.3	Toy Monte Carlo validation of the fitter	81
6.3	$D_{\text{CP}^+}^0X^-$ fits	81
6.3.1	Fit configuration	81
6.3.2	Results	84
6.3.3	Toy Monte Carlo validation of the fitter	85
6.4	Systematic uncertainties	85
6.4.1	Systematic uncertainties on the relative branching ratios	86
6.4.2	Systematic uncertainties on R , R_{CP^+} and A_{CP^+}	88
7	Results and Conclusions	126
	Bibliography	128

A	<i>dE/dx</i> templates	133
A.1	Introduction	133
A.2	The Z variable	133
A.3	Data samples and candidate selection	134
A.4	Sideband subtraction	134
A.5	Z dependences and reweighting	136
A.6	Run-dependent corrections	136
A.7	Z profiles	136
A.8	Hit merging and proxies	138
A.9	Reweighting in two dimensions	138
A.10	Summary of procedure	139

List of Figures

2.1	The unitarity triangle.	9
2.2	Tree level Feynman diagrams for $B^- \rightarrow D^0 K^-$ and $B^- \rightarrow \bar{D}^0 K^-$. . .	11
3.1	Side view of half of the CDF II detector in cross section	17
3.2	An r - z view of a quarter of the CDF II detector	18
3.3	An r - z view showing the placement of layers in half of the CDF II silicon tracking system	19
4.1	Decay mode content of the $\bar{B}^0 \rightarrow D^+ \pi^- (n\gamma)$ Monte Carlo sample reconstructed as $D^+ \pi^-$	42
4.2	Decay mode content of the semi-inclusive $\bar{B}^0/B^0 \rightarrow D^+ X$ Monte Carlo sample reconstructed as $D^+ \pi^-$	43
4.3	Decay mode content of the semi-inclusive $B^\pm \rightarrow D^+ X$ Monte Carlo sample reconstructed as $D^+ \pi^-$	43
4.4	Decay mode content of the semi-inclusive $B_s \rightarrow D_s[\phi\pi]X$ Monte Carlo sample reconstructed as $D^+ \pi^-$	44
4.5	Decay mode content of the $\bar{B}^0 \rightarrow D^{*+} \pi^- (n\gamma)$ Monte Carlo sample reconstructed as $D^{*+} \pi^-$	44
4.6	Decay mode content of the semi-inclusive $B^\pm \rightarrow D^0 X$ Monte Carlo sample reconstructed as $D^{*+} \pi^-$	45
4.7	Decay mode content of the $\bar{B}^0/B^0 \rightarrow D^0 X$ Monte Carlo sample reconstructed as $\bar{B}^0 \rightarrow D^{*+} \pi^-$	45
4.8	Decay mode content of the $B^- \rightarrow D^0 [K^- \pi^+] \pi^- (n\gamma)$ Monte Carlo sample reconstructed as $D^0 [K^- \pi^+] \pi^-$	46
4.9	Decay mode content of the $B^- \rightarrow D^0 [K^- \pi^+] K^- (n\gamma)$ Monte Carlo sample reconstructed as $D^0 [K^- \pi^+] \pi^-$	46
4.10	Decay mode content of the semi-inclusive $B^\pm \rightarrow D^0 [K^- \pi^+] X$ Monte Carlo sample reconstructed as $D^0 [K^- \pi^+] \pi^-$	47
4.11	Decay mode content of the semi-inclusive $B^0/\bar{B}^0 \rightarrow D^0 [K^- \pi^+] X$ Monte Carlo sample reconstructed as $D^0 [K^- \pi^+] \pi^-$	47
5.1	Mass templates used for the $D^+ X^-$ fit components	63
5.2	Pion and kaon Z template histograms for the $D^+ X^-$ fit (full sample)	64

5.3	Auxiliary D^+ -sideband fit for the full D^+X^- sample	65
5.4	D^+ mass fit for fake- D background normalization study	66
5.5	Real- D^+ background template fit in wrong sign D^+X^+	66
5.6	Mass projection of the fit on the full D^+X^- sample	67
5.7	Z projections of the fit on the full D^+X^- sample.	68
5.8	Likelihood scans for the D^+X^- fit components.	69
5.9	Pull distributions for the D^+X^- fit components.	70
5.10	Mass templates used for the $D^{*+}X^-$ fit components	71
5.11	Pion and kaon Z template histograms for the $D^{*+}X^-$ fit (full sample)	72
5.12	Mass projection of the fit on the full $D^{*+}X^-$ sample	73
5.13	Z projections of the fit on the full $D^{*+}X^-$ sample.	74
5.14	Likelihood scans for the $D^{*+}X^-$ fit components.	75
5.15	Pull distributions for the $D^{*+}X^-$ fit components.	76
6.1	Pion and kaon Z template histograms for the $D^0[K^-\pi^+]X^-$ fit (both charges)	103
6.2	Likelihood scan of the Monte Carlo mass scale factor	104
6.3	Likelihood scan of the Monte Carlo smearing width	104
6.4	Auxiliary D^0 -sideband fit for the $D^0[K^-\pi^+]X^-$ sample (both charges).	105
6.5	Auxiliary D^0 -sideband fit for the $D^0[K^-\pi^+]X^-$ sample (X^- only). . .	106
6.6	Auxiliary D^0 -sideband fit for the $\overline{D}^0[K^+\pi^-]X^+$ sample (X^+ only). . .	107
6.7	Mass projection of the fit on the $D^0[K^-\pi^+]X^-$ sample (both charges). (Fit not used in measuring R .)	108
6.8	Mass projection of the fit on the $D^0[K^-\pi^+]X^-$ sample (X^- only). . .	109
6.9	Mass projection of the fit on the $\overline{D}^0[K^+\pi^-]X^+$ sample (X^+ only). . .	110
6.10	Z projections of the fit on the $D^0[K^-\pi^+]X^-$ sample (both charges) .	111
6.11	Z projections of the fit on the $D^0[K^-\pi^+]X^-$ sample (X^- only)	112
6.12	Z projections of the fit on the $\overline{D}^0[K^+\pi^-]X^+$ sample (X^+ only)	113
6.13	Auxiliary D^0 -sideband fit for the $D^0[\pi^-\pi^+]X^-$ sample (X^- only) . .	114
6.14	Auxiliary D^0 -sideband fit for the $\overline{D}^0[\pi^+\pi^-]X^+$ sample (X^+ only) . .	115
6.15	Mass projection of the fit on the $D^0[\pi^-\pi^+]X^-$ sample (X^- only) . . .	116
6.16	Mass projection of the fit on the $\overline{D}^0[\pi^+\pi^-]X^+$ sample (X^+ only) . . .	117
6.17	Z projections of the fit on the $D^0[\pi^-\pi^+]X^-$ sample (X^- only)	118
6.18	Z projections of the fit on the $\overline{D}^0[\pi^+\pi^-]X^+$ sample (X^+ only)	119
6.19	Auxiliary D^0 -sideband fit for the $D^0[K^-K^+]X^-$ sample (both charges)	120
6.20	Stack histograms of K^-K^+ backgrounds from generic B Monte Carlo	121
6.21	Mass projection of the fit on the $D^0[K^-K^+]X^-$ sample (X^- only) . .	122
6.22	Mass projection of the fit on the $\overline{D}^0[K^+K^-]X^+$ sample (X^+ only) . .	123
6.23	Z projections of the fit on the $D^0[K^-K^+]X^-$ sample (X^- only) . . .	124
6.24	Z projections of the fit on the $\overline{D}^0[K^+K^-]X^+$ sample (X^+ only) . . .	125
A.1	$\langle Z \rangle$ versus run number in the prompt D^* sample	143

A.2	Pion Z profiles for a prompt- D^* sample after sideband subtraction . .	144
A.3	Kaon Z profiles for a prompt- D^* sample after sideband subtraction . .	145
A.4	Pion Z profiles for a $B \rightarrow D^* X$ sample after sideband subtraction . .	146
A.5	Kaon Z profiles for a $B \rightarrow D^* X$ sample after sideband subtraction . .	147
A.6	Kinematic variable distributions of tracks from four different populations	148
A.7	Z templates before and after various reweighting schemes	149

List of Tables

2.1	Standard Model matter fields and their gauge group representations	4
4.1	Data samples skimmed from the two-track-trigger dataset.	26
4.2	Monte Carlo samples used in our fitter	27
4.3	Analysis cuts for the three $D^0 X^-$ signal samples and the $D^{*+} X^-$ control sample	32
4.4	Analysis cuts for the $D^+ X^-$ control sample	32
5.1	Fit components of the $D^+ X^-$ and $D^{*+} X^-$ fits	57
5.2	Fit parameters returned in the $D^+ X^-$ and $D^{*+} X^-$ fits.	58
5.3	Correlation coefficients for the $D^+ X^-$ fit on the full sample.	59
5.4	Comparison of $D^+ X^-$ and $D^{*+} X^-$ fit results with ratios derived from world averages	60
5.5	Pull means and widths for the $D^+ X^-$ fit components.	61
5.6	Systematic uncertainties on the ratio $BR(\bar{B}^0 \rightarrow D^+ K^-)/BR(\bar{B}^0 \rightarrow D^+ \pi^-)$	61
5.7	Correlation coefficients for the $D^{*+} X^-$ fit on the full sample.	61
5.8	Pull means and widths for the $D^{*+} X^-$ fit components.	62
6.1	Fit components of the $D^0 [K^- \pi^+] X^-$ fits	90
6.2	Fit parameters returned in the $D^0 [K^- \pi^+] X^-$ fits	91
6.3	Correlation coefficients for the $D^0 [K^- \pi^+] X^-$ fit components	92
6.4	Three measures of fitter bias on the relative branching ratio $BR(B^- \rightarrow D^0 K^-)/BR(B^- \rightarrow D^0 \pi^-)$ for all three D^0 decay modes	93
6.5	Fit components of the $D^0 [\pi^- \pi^+] X^-$ fits	94
6.6	Fit parameters returned in the $D^0 [\pi^- \pi^+] X^-$ fits	95
6.7	Correlation coefficients for the $D^0 [\pi^- \pi^+] X^-$ fit components	96
6.8	Fit components of the $D^0 [K^- K^+] X^-$ fits	97
6.9	Fit parameters returned in the $D^0 [K^- K^+] X^-$ fits	98
6.10	Correlation coefficients for the $D^0 [K^- K^+] X^-$ fit components	99
6.11	Central values and statistical errors of the relative branching ratios $BR(B^- \rightarrow D^0 K^-)/BR(B^- \rightarrow D^0 \pi^-)$ before XFT corrections	100

6.12	Summary of statistical uncertainties on R , $R_{\text{CP}+}$, and $A_{\text{CP}+}$ for all three D^0 modes	100
6.13	Systematic uncertainties on the relative branching ratio $BR(B^- \rightarrow D^0 K^-)/BR(B^- \rightarrow D^0 \pi^-)$ for all three D^0 decay modes	101
6.14	Systematic uncertainties on R , $R_{\text{CP}+}$, and $A_{\text{CP}+}$	102
7.1	Comparison of our measured values for $R_{\text{CP}+}$ and $A_{\text{CP}+}$ with those from other analyses.	127
A.1	B and $D^{(*)}$ selection cuts and Z template track cuts	135
A.2	Effect of two reweighting schemes on $\langle Z \rangle$ (reweighted to $D^{*+} X^-$ distributions)	141
A.3	Effect of two reweighting schemes on $\langle Z \rangle$ (reweighted to $D^+ X^-$ distributions)	142

Acknowledgments

I owe much gratitude to my advisor, Marjorie Shapiro, for her guidance and support throughout the research process and for her kindness and patience.

I thank Alessandro Cerri for his extensive advice and assistance, especially the indispensable help he provided during the initial development of the fitter described in this dissertation.

I have worked very closely with Johannes Mülmenstädt and Amanda Deisher. They have performed B physics analyses related to the one described here. Their collaborative efforts are greatly appreciated. In particular, I thank Johannes for his work in expanding the fitter code into a highly configurable framework and for his contribution to the study of the control samples.

In addition to the LBL group members already mentioned, I owe particular thanks to Juerg Beringer, Lina Galtieri, Maurice Garcia-Sciveres, Young-Kee Kim, Jeremy Lys, Ramon Miquel, Laurent Vacavant, and Weiming Yao.

I have greatly enjoyed the company of my fellow LBL–CDF graduate students Adam, Amanda, Amy, Erik, Greg, Henri, Johannes, John, Paul, and Tony. They have been a vital source of support.

Thanks are due to the many CDF collaborators who have provided assistance, especially Satyajit Behari, Stefano Giagu, Petar Maksimovic, Matthew Martin, Aseet Mukherjee, Reid Mumford, Donatella Lucchesi, Simone Pagan Griso, and Giuseppe Salamanna.

Thanks are also due to the members of my dissertation committee.

I am grateful to Alex, Amanda, Dylan, and Huilin for their untiring moral support. I have also benefited very much from the encouragement of Charles and Norie, Devin, Gersende and João, Greg, Joe and Maria, Johannes, Laurent, Leah, Max, Paul and Juliana, Ramon, Steven, Tommy, and many, many others.

Finally, I would like to thank my parents for their unwavering support and for their faith in me.

Chapter 1

Introduction

The advent of the BaBar and Belle experiments in the waning days of the last century heralded a period of great vigor in the study of heavy flavor physics. In the past decade or so, the two experiments, situated respectively at the two asymmetric e^+e^- colliders PEP-II and KEKB, have collected B meson samples of high purity and unprecedented size. These samples have allowed these “ B factories” to develop physics programs of remarkable scope and depth.

This decade of activity at the B factories largely coincides with Run II of the Tevatron at Fermilab. The two multi-purpose experiments at the Tevatron, CDF and DØ, have devised strategies to extract large charm and bottom hadron samples from a high-background $p\bar{p}$ collision environment. These collaborations have thus created bottom physics programs that are complementary to and often directly competitive with the physics programs at the B factories.

In this dissertation, we present a measurement at CDF of certain CP asymmetries in the decays of charged B mesons with the aim of contributing to the understanding of quark flavor. In Chapter 2, we review the theory of quark flavor and CP violation in the Standard Model and place our measurement in a theoretical context. The Tevatron and its supporting accelerators systems are the subject of Chapter 3; we also describe the CDF experiment with an emphasis on the detector and trigger subsystems most relevant to our analysis. In Chapter 4, the basic components of our analysis are introduced. This includes a description of our data samples, event selection, and maximum likelihood fitter. To validate our analysis technique, we apply our fitter to two control samples in Chapter 5. In Chapter 6, our analysis tools are applied to the three signal samples. The relevant quantities are extracted and systematic uncertainties studied. Our conclusions are presented in Chapter 7.

Chapter 2

Theoretical Preliminaries

In the first section of this chapter, we give an account of the most salient features of the Standard Model of particle physics: its gauge structure, its field content, and the mechanism for electroweak symmetry breaking. We then describe in greater detail those aspects of the Standard Model that relate most closely to our analysis, *viz.*, charged weak currents, the quark sector, quark mixing and the CP violation that arises as a result. In the final section, we summarize the formalism behind measuring the angle γ of the unitarity triangle through charged B meson decays, with an emphasis on the method that forms the basis of our measurement. It is an understatement to say that there exists an enormous literature on the Standard Model and on CP violation—here we closely follow Refs. [1], [2], [3], [4], and the Particle Data Group [5] reviews Refs. [6] and [7] in our general exposition of these two topics.¹ For our discussion of the specific methods for measuring γ , we follow the papers cited in the text.

2.1 The Standard Model

The Standard Model is a renormalizable quantum field theory encompassing the strong, weak, and electromagnetic (but not gravitational) interactions of the known elementary matter fields,² the leptons and the quarks. The strong interactions are described by the $SU(3)$ gauge theory called quantum chromodynamics (QCD); the weak and electromagnetic interactions are unified in a spontaneously broken $SU(2) \times U(1)$ gauge theory known as the Glashow-Salam-Weinberg theory of electroweak interactions.³ The Standard Model has been verified extensively by experiment.⁴ For our

¹Other general references include Refs. [8], [9], and [10].

²See Table 2.1.

³See, for instance, Refs. [1] and [9] for a detailed discussion.

⁴See Refs. [11] and [12] for reviews of experimental tests of QCD and electroweak theory, respectively.

purposes, we can afford to ignore the relatively recent but already persuasive evidence of neutrino mixing that would require an extension to the Standard Model.⁵

For a given gauge group, each of the matter fields transform under a particular finite-dimensional representation of the group in question.⁶ Gauge invariance then determines the possible interactions of each matter field according to its particular gauge group representation. We will refrain from attempting to reproduce all the terms in the Lagrangian field density of the Standard Model. Instead, we simply list in Table 2.1 (adapted from [14]) the Standard Model matter fields (all spin-1/2) along with their gauge group representations.

In Table 2.1, the subscripts L and R on the fermion fields denote left and right-handed fields, respectively. The $SU(3)_C$ acts on the degree of freedom usually termed “color”; thus the subscript C . The $SU(2)_L$ group acts on the space of weak isospin; the subscript L here is a reminder that only the left-handed matter fields transform (and therefore couple) non-trivially under this $SU(2)$. The hypercharge Y , associated with a $U(1)$ gauge symmetry, is related to the electric charge Q and the third component of the weak isospin I_3 by $Y \equiv Q - I_3$. The symbols $\mathbf{3}$ and $\mathbf{2}$ stand for the three and two-dimensional fundamental representations⁷ of the $SU(3)$ and $SU(2)$ groups, respectively; the $\mathbf{1}$ indicates a singlet. Additionally, the superscript $i = 1, 2, 3$ labels the three generations of quarks and leptons,⁸ shown as three sub-columns in the table.

For a particular gauge group, each group generator is associated with a spin-1 field⁹—these are the gauge bosons. Therefore, $SU(3)_C$ gives us 8 gluons (g); $SU(2)_L$ the three bosons W_i , where $i = 1, 2, 3$; and $U(1)_Y$ the B boson. Gauge symmetry by itself would require all of these gauge bosons to be massless.¹⁰ However, one may postulate the existence of a weak isodoublet of complex spin-0 fields (the Higgs field) $\phi \equiv (\phi^+, \phi^0)$ and allow it to acquire a vacuum expectation value of $\langle \phi \rangle = (0, v/\sqrt{2})$.¹¹ This spontaneously breaks the $SU(2)_L \times U(1)_Y$ symmetry of the vacuum. The unbroken subgroup of $SU(2)_L \times U(1)_Y$ now has one generator only. As a result, one vector boson remain massless while the other three acquire mass. The four mass eigenstates of the electroweak gauge bosons are now the massive $W^\pm = (W_1 \mp iW_2)/\sqrt{2}$ and Z^0 , and the massless photon γ , where Z^0 and γ are orthogonal linear combinations of W_3 and B .¹²

⁵A review can be found in Ref. [13].

⁶See, for instance, Ref. [1], pp. 497–500.

⁷See Ref. [1], p. 499.

⁸The quarks comprise the up (u), down (d), charm (c), strange (s), top (t), and bottom (b) quarks. The charged leptons are the electron (e), muon (μ), and tau (τ). The three neutrinos ν_e , ν_μ , and ν_τ are named after their charged counterparts as indicated in their subscripts.

⁹See §15.2 of Ref. [1].

¹⁰Explicit mass terms would violate gauge symmetry and sacrifice renormalizability. For a discussion of the latter, see for instance §2.3 of Ref. [2].

¹¹Much more complicated scenarios for electroweak symmetry breaking are possible; see pp. 717–9 (§20.2) of Ref. [1] for a discussion.

¹²See §§20.1–20.2 of Ref. [1] for a detailed discussion of electroweak symmetry breaking.

		Matter fields			$SU(3)_C$	$SU(2)_L$	$U(1)_Y$
quarks	Q_L^i	$\begin{pmatrix} u \\ d \end{pmatrix}_L$	$\begin{pmatrix} c \\ s \end{pmatrix}_L$	$\begin{pmatrix} t \\ b \end{pmatrix}_L$	3	2	+1/6
	u_R^i	u_R	c_R	t_R	3	1	+2/3
	d_R^i	d_R	s_R	b_R	3	1	-1/3
leptons	L_L^i	$\begin{pmatrix} \nu_e \\ e \end{pmatrix}_L$	$\begin{pmatrix} \nu_\mu \\ \mu \end{pmatrix}_L$	$\begin{pmatrix} \nu_\tau \\ \tau \end{pmatrix}_L$	1	2	-1/2
	e_R^i	e_R	μ_R	τ_R	1	1	-1

Table 2.1: Standard Model matter fields and their gauge group representations. See text for discussion. Table adapted from Table 1.1 of [14].

2.2 Fermion mass terms, the CKM matrix, and CP violation

Below we continue to hew closely to the exposition in Sections 20.2–20.3 of Ref. [1], Chapter 2 of Ref. [2], and later on in the section, Refs. [6] and [7].¹³ Explicit fermion mass terms such as those for the up quark mass

$$-m_u \bar{u}_L u_R - m_u \bar{u}_R u_L \quad (2.1)$$

are forbidden by gauge symmetry, since u_L and u_R belong to different types of $SU(2)$ multiplets and have different values of the weak hypercharge Y . Since the universe is replete with massive fermions, the situation is clearly unsatisfactory. This is remedied by the introduction of the Higgs field — terms of the following type are invariant under $SU(2) \times U(1)$ and therefore allowed:¹⁴

$$\mathcal{L}_m = -\lambda_d^{ij} \bar{Q}_L^i \phi d_R^j - \lambda_u^{ij} \epsilon^{ab} \bar{Q}_{La}^i \phi_b^\dagger u_R^j + \text{h. c.}, \quad (2.2)$$

where the λ 's are matrices of complex coefficients with the i and j indices running over the three quark generations, ϵ_{ab} is the anti-symmetric tensor of rank 2, and “h. c.” denotes the Hermitian conjugate of the previous terms. The vacuum expectation value of the Higgs field $\langle \phi \rangle = (0, v/\sqrt{2})$ then effectively converts Eq. (2.2) into mass terms for down and up-type quarks (thus the subscripts on the λ matrices), with cross terms that mix the generations. In the Standard Model, lepton mass terms are generated in an analogous manner.

Having generated mass terms for the quarks, one may now find the mass eigenstates by diagonalizing the two λ matrices. This can be accomplished by first diago-

¹³The first half of this section summarizes the relevant parts of §§20.2–20.3 in Ref. [1].

¹⁴Ref. [1], Eq. (20.133), p. 722.

nalizing the Hermitian matrices $\lambda^\dagger\lambda$ and $\lambda\lambda^\dagger$ in the following manner¹⁵

$$\lambda_u\lambda_u^\dagger = V_u D_u^2 V_u^\dagger, \quad \lambda_u^\dagger\lambda_u = W_u D_u^2 W_u^\dagger, \quad (2.3)$$

$$\lambda_d\lambda_d^\dagger = V_d D_d^2 V_d^\dagger, \quad \lambda_d^\dagger\lambda_d = W_d D_d^2 W_d^\dagger, \quad (2.4)$$

where the V and W matrices are 3×3 unitary matrices in the space of quark generations, and the D 's non-negative diagonal matrices. This gives us $\lambda_u = V_u D_u W_u^\dagger$ and $\lambda_d = V_d D_d W_d^\dagger$.¹⁶ This naturally suggests the following rotations of the quark fields into the mass basis:¹⁷

$$u'_L = V_u^\dagger u_L, \quad u'_R = W_u^\dagger u_R, \quad (2.5)$$

$$d'_L = V_d^\dagger d_L, \quad d'_R = W_d^\dagger d_R, \quad (2.6)$$

where the primed fields are in the mass basis and the unprimed fields in the weak basis.¹⁸ If one defines¹⁹ the diagonal mass matrix $m^{ij} \equiv D^{ij} \cdot v/\sqrt{2}$, Eq. (2.2) takes the form of Eq. (2.1)

$$\mathcal{L}_m = -m_d^i \bar{d}'_L d'^i_R - m_u^i \bar{u}'_L u'^i_R + \text{h. c.}, \quad (2.7)$$

in the new basis, just as we desired.²⁰

We now proceed to examine the form of the quark currents that couple to the various gauge bosons. These currents have terms of two types. The first type contains terms of the form $\bar{q}_L \gamma^\mu q_L$ or $\bar{q}_R \gamma^\mu q_R$, where q is any quark field. These terms appear in the currents that couple to the neutral gauge bosons, *i.e.*, the gluons, the Z , and the photon. Rotations of the type in Eqs. (2.5) and (2.6) leave these terms invariant.²¹

Terms of the second type appear in the quark currents that couple to the W^\pm . Specifically, the fermion kinetic energy terms $\bar{\psi} i \not{D} \psi$ give the following W^\pm -quark-quark interaction terms²²

$$\mathcal{L}_{Wqq} = g(W_\mu^+ J_W^{\mu+} + W_\mu^- J_W^{\mu-}), \quad (2.8)$$

where g is the coupling constant and the currents J_W are defined by²³

$$J_W^{\mu+} = \frac{1}{\sqrt{2}} \bar{u}_L^i \gamma^\mu d_L^i \quad \text{and} \quad J_W^{\mu-} = \frac{1}{\sqrt{2}} \bar{d}_L^i \gamma^\mu u_L^i. \quad (2.9)$$

¹⁵Ref. [1], Eq. (20.135), p. 722.

¹⁶Ibid., Eqs. (20.136) and (20.137).

¹⁷See Eqs. (20.138) and (20.140), *ibid.*

¹⁸See discussion below of the quark currents that couple to the W^\pm .

¹⁹Ref. [1], Eq. (20.141).

²⁰See Eq. (20.142), *ibid.*

²¹See p. 723., *ibid.*

²²From Ref. [1], Eq. (20.79).

²³From Ref. [1], Eq. (20.80).

In terms of the mass eigenstates, this becomes²⁴

$$J_W^{\mu+} = \frac{1}{\sqrt{2}} \bar{u}_L^i \gamma^\mu V_{CKM}^{ij} d_L^j \quad \text{and} \quad J_W^{\mu-} = \frac{1}{\sqrt{2}} \bar{d}_L^j \gamma^\mu V_{CKM}^{*ji} u_L^i, \quad (2.10)$$

where

$$V_{CKM} \equiv V_u^\dagger V_d \equiv \begin{pmatrix} V_{ud} & V_{us} & V_{ub} \\ V_{cd} & V_{cs} & V_{cb} \\ V_{td} & V_{ts} & V_{tb} \end{pmatrix} \quad (2.11)$$

is called the Cabibbo-Kobayashi-Maskawa (CKM) matrix (Ref. [15]), which connects the physical quark states, *i.e.*, the mass eigenstates, with the basis of states that directly participate in the weak interactions.

At this point, the 3×3 unitary matrix V_{CKM} has nine real parameters, including six phases and three rotation angles. By redefining the phases of the six left-handed quark states, five of these phases may be eliminated.²⁵ Thus the parameterization of Kobayashi and Maskawa [15], which includes the three rotation angles and one phase δ that cannot be removed. In current standard notation [6], this is given as

$$V_{CKM} = \begin{pmatrix} c_{12}c_{13} & s_{12}c_{13} & s_{13}e^{-i\delta} \\ -s_{12}c_{23} - c_{12}s_{23}s_{13}e^{i\delta} & c_{12}c_{23} - s_{12}s_{23}s_{13}e^{i\delta} & s_{23}c_{13} \\ s_{12}s_{23} - c_{12}c_{23}s_{13}e^{i\delta} & -c_{12}s_{23} - s_{12}c_{23}s_{13}e^{i\delta} & c_{23}c_{13} \end{pmatrix}, \quad (2.12)$$

where the c_{ij} and s_{ij} are shorthands for $\cos \theta_{ij}$ and $\sin \theta_{ij}$, respectively.

Empirically, the CKM matrix is known to have small off-diagonal elements.²⁶ This leads to the following parameterization [6] due originally to Wolfenstein [16]

$$V_{CKM} = \begin{pmatrix} 1 - \lambda^2/2 & \lambda & A\lambda^3(\rho - i\eta) \\ -\lambda & 1 - \lambda^2/2 & A\lambda^2 \\ A\lambda^3(1 - \rho - i\eta) & -A\lambda^2 & 1 \end{pmatrix} + \mathcal{O}(\lambda^4), \quad (2.13)$$

where $\lambda \sim 0.23$ (Ref. [5]) and A , ρ , and η are all real parameters.

In the Glashow-Iliopoulos-Maiani model²⁷, where there are only two quark generations, the matrix equivalent to the CKM matrix is given by

$$V = \begin{pmatrix} \cos \theta_C & \sin \theta_C \\ -\sin \theta_C & \cos \theta_C \end{pmatrix}, \quad (2.14)$$

²⁴Ref. [1], Eqs. (20.106) and (20.107).

²⁵See Ref. [1], §20.3, pp. 723–4. See Ref. [2], pp. 59–60 for an explicit construction. See also Ref. [10], pp. 150–2 for another method of counting degrees of freedom.

²⁶See Ref. [6] for a review of measurements determining the magnitudes of elements of the CKM matrix.

²⁷See, for instance, Ref. [10], pp. 19–21

which is characterized by one parameter, the Cabibbo angle θ_C [17]. In contrast, the CKM matrix, in addition to having two extra rotation angles, also possesses a non-trivial phase δ . This latter fact is crucial to an understanding of CP violation in the Standard Model.

Since $W_\mu^+ \bar{u}_L^i \gamma^\mu d_L^j \leftrightarrow W_\mu^- \bar{d}_L^j \gamma^\mu u_L^i$ under a CP transformation (with reflection of spatial axes in the field arguments),²⁸ the action will be CP-invariant if $V_{CKM} = V_{CKM}^*$ in some basis. As we have seen in the discussion above, this is not generally the case for three generations of quarks, due to the existence of the phase δ . This phase is then the source of CP violation in the Standard Model, as theorized by Kobayashi and Maskawa [15].²⁹ If we shift the quark fields from the mass basis back to the weak basis, the Yukawa couplings λ_d^{ij} and λ_u^{ij} will be found to be complex.³⁰

We have seen how the phase in the CKM matrix results in non-trivial CP-violating Lagrangian terms. In terms of quantities observable in meson decays, there are several ways in which these terms manifest themselves: CP violation (1) in decay, (2) in mixing, and (3) in interference between mixed and unmixed decays.³¹ The last two kinds of CP violation involve mixing and are only relevant for neutral mesons; since our measurement is concerned with charged meson decays, we will focus on the first kind.

If a decay is dominated by a single Feynman diagram, the presence of a CP violating phase ϕ in the diagram is insufficient to cause CP violation in the decay width, since it is the squared modulus of the amplitude that is proportional to the decay width Γ . However, if multiple diagrams, each with a different CP-violating phase, contribute to a decay amplitude, it may be possible to observe CP violation in the width of the decay. Following, for instance, Ref. [3], pp. 54–5; Ref. [7]; Ref. [4], pp. 58–9, let us consider the decay $i \rightarrow f$ of some particle from an initial state i to a final state f . Let us assume that the decay is dominated by two amplitudes A_1 and A_2 . Each amplitude may contain CP-*even* phases due, for instance, to intermediate on-shell states that scatter to the final state f ; complex coefficients (for instance the CKM matrix elements) in the Lagrangian, however, may result in CP-*odd* phases in the amplitudes. The CP-even and CP-odd phases are often referred to by their synonyms *strong* and *weak* phases, which often (but not necessarily) coincide with the type of interaction from which they arise.³² If we denote the CP-even and CP-odd phases by the symbols δ and ϕ respectively, we may express the amplitudes for the

²⁸Ref. [4], pp. 48–49; Ref. [2], p. 61.

²⁹We will ignore the strong CP problem here. See, for instance, §16 of Ref. [4] or §27 of Ref. [3].

³⁰Ref. [7]; Ref. [1], p. 722; Ref. [3], pp. 162–3. For a rigorous discussion of the conditions for CP violation in the Standard Model, see, for instance, Ref. [3], §14.

³¹Ref. [7]; Ref. [3], pp. 78–9.

³²Ref. [3], p. 52; Ref. [7].

decay $i \rightarrow f$ and its CP conjugate $\bar{i} \rightarrow \bar{f}$ as³³

$$A_{i \rightarrow f} = |A_1|e^{i(\delta_1 + \phi_1)} + |A_2|e^{i(\delta_2 + \phi_2)} \quad (2.15)$$

$$A_{\bar{i} \rightarrow \bar{f}} = |A_1|e^{i(\delta_1 - \phi_1)} + |A_2|e^{i(\delta_2 - \phi_2)} \quad (2.16)$$

The CP asymmetry in the decay width is then immediately found to be³⁴

$$\mathcal{A} \equiv \frac{\Gamma(i \rightarrow f) - \Gamma(\bar{i} \rightarrow \bar{f})}{\Gamma(i \rightarrow f) + \Gamma(\bar{i} \rightarrow \bar{f})} = -\frac{2|A_1||A_2|\sin(\Delta\delta)\sin(\Delta\phi)}{|A_1|^2|A_2|^2 + 2|A_1||A_2|\cos(\Delta\delta)\cos(\Delta\phi)}, \quad (2.17)$$

where the Γ 's are the decay widths, $\Delta\delta \equiv \delta_1 - \delta_2$ and $\Delta\phi \equiv \phi_1 - \phi_2$. Note that both $\delta_1 \neq \delta_2$ and $\phi_1 \neq \phi_2$ need to hold for the asymmetry to be non-zero.³⁵

2.3 The Unitarity triangle and the measurement of its angle γ

Since the CKM matrix is unitary, *i.e.*,

$$V_{CKM}V_{CKM}^\dagger = V_{CKM}^\dagger V_{CKM} = \mathbf{1}, \quad (2.18)$$

the following conditions are satisfied by its components

$$\sum_{k=1}^3 V_{ik}V_{jk}^* = \sum_{k=1}^3 V_{ki}^*V_{kj} = \delta_{ij}. \quad (2.19)$$

The cases in which $i \neq j$ in Eq. (2.19) give six distinct triangles in the complex plane with sides of the form $V_{ki}^*V_{kj}$, of which the one corresponding to

$$V_{ud}V_{ub}^* + V_{cd}V_{cb}^* + V_{td}V_{tb}^* = 0 \quad (2.20)$$

is most often displayed.³⁶ All three terms in Eq. (2.20) are $O(A\lambda^3)$ in the Wolfenstein parameterization; as a consequence, none of the three interior angles are significantly smaller than the others [7].³⁷ Conventionally, the sides are scaled down by a factor

³³See Ref. [3], p. 54; Ref. [7]; Ref. [4], p. 58.

³⁴Ref. [3], p. 55; Ref. [7]; Ref. [4], p. 59.

³⁵Ref. [3], pp. 54–5; Ref. [7]; Ref. [4], pp. 58–9.

³⁶Ref. [4], pp. 127–8, 159–61; Ref. [3], pp. 166–8; Refs. [6] and [7].

³⁷There is another triangle with sides all of order λ^3 ($V_{td}V_{ud}^*$, $V_{ts}V_{us}^*$ and $V_{tb}V_{ub}^*$); however, its angles are similar (up to $O(\lambda)$) to those of our default triangle. See, for instance, Ref. [4], p. 161 and Ref. [7].

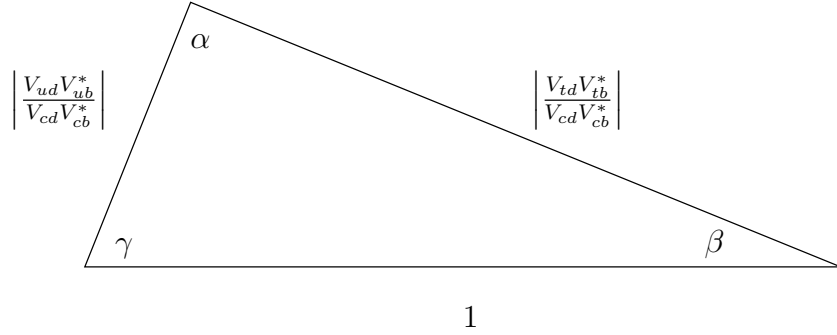


Figure 2.1: The unitarity triangle.

of $V_{cd}V_{cb}^*$.³⁸, as shown in Fig. 2.1. The interior angles are named³⁹

$$\alpha \equiv \phi_2 \equiv \arg \left(-\frac{V_{td}V_{tb}^*}{V_{ud}V_{ub}^*} \right), \quad (2.21)$$

$$\beta \equiv \phi_1 \equiv \arg \left(-\frac{V_{cd}V_{cb}^*}{V_{td}V_{tb}^*} \right), \quad (2.22)$$

$$\gamma \equiv \phi_3 \equiv \arg \left(-\frac{V_{ud}V_{ub}^*}{V_{cd}V_{cb}^*} \right). \quad (2.23)$$

A useful parameterization⁴⁰ of the CKM matrix is in terms of the two angles β and γ above, the two sides $R_t \equiv |V_{td}V_{tb}|/|V_{cd}V_{cb}|$ and $R_b \equiv |V_{ud}V_{ub}|/|V_{cd}V_{cb}|$, and the parameters λ and A . To third order in λ , it is given by⁴¹

$$\begin{pmatrix} 1 - \lambda^2/2 & \lambda & AR_b\lambda^3 \exp(-i\gamma) \\ -\lambda & 1 - \lambda^2/2 & A\lambda^2 \\ AR_t\lambda^3 \exp(-i\beta) & -A\lambda^2 & 1 \end{pmatrix}. \quad (2.24)$$

The unitarity triangle geometrically encapsulates the quark flavor structure in the Standard Model. One of the grand projects of the high-energy physics community in the past two decades has been to experimentally test the CKM picture of quark flavor. A central part of this project is the extensive effort to overdetermine the shape of the unitarity triangle by redundant measurement of its sides and angles. A summary of our current knowledge is provided by the CKM fits from both the CKMfitter Group [18] and the UTfit Collaboration [19] and also from the Particle Data Group [20] and Heavy Flavor Averaging Group [21].

³⁸Ref. [6]; Ref. [7]; Ref. [3], p. 166.

³⁹Ref. [6], Ref. [7].

⁴⁰Attributed to Buras and Fleischer in Ref. [3], p. 196.

⁴¹Ref. [3], Eq. (16.38).

In the following, we shall focus exclusively on the determination of the angle γ . (See Eq. (2.23) for the definition of γ .) An important family of methods (see below) determines γ from the interference⁴² of two decay modes of the charged- B meson⁴³ (and their CP conjugates): $B^- \rightarrow D^0 K^-$ and $B^- \rightarrow \bar{D}^0 K^-$.⁴⁴ From the tree-level Feynman diagrams as represented in Fig. (2.2), we see that the two decays take advantage of the weak transitions $b \rightarrow c\bar{u}s$ and $b \rightarrow u\bar{c}s$, respectively, and therefore have amplitudes proportional to the following CKM factors [24]:

$$A(B^- \rightarrow D^0 K^-) \propto V_{cb}V_{us}^* \sim A\lambda^3, \quad (2.25)$$

$$A(B^- \rightarrow \bar{D}^0 K^-) \propto V_{ub}V_{cs}^* \sim AR_b\lambda^3 \exp(-i\gamma), \quad (2.26)$$

where the last relation in each line is from the parameterization in Eq. (2.24) and is correct to $O(\lambda^4)$.⁴⁵

Since $B^- \rightarrow D^0 K^-$ and $B^- \rightarrow \bar{D}^0 K^-$ have different nominal final states, common decay modes of the D^0 and \bar{D}^0 must be selected for the two decay processes to interfere. ($D^0 - \bar{D}^0$ oscillation is generally taken to be negligible.⁴⁶) There are at least three experimentally important methods [21], which differ in what neutral D mesons final states interfere:⁴⁷ (1) **The Gronau-London-Wyler (GLW) method.**⁴⁸ Even and odd CP eigenstates of the D^0 are selected by reconstructing the decays $D_{\text{CP}^+} \rightarrow K^- K^+$, $\pi^- \pi^+$ and $D_{\text{CP}^-} \rightarrow K_S \pi^0$, $K_S \rho^0$, $K_S \phi$, $K_S \omega$, etc. (2) **The Atwood-Dunietz-Soni (ADS) method.**⁴⁹ Since $B^- \rightarrow \bar{D}^0 K^-$ is color suppressed relative to $B^- \rightarrow D^0 K^-$, the Cabibbo-allowed $\bar{D}^0 \rightarrow K^+ \pi^-$ in the former decay is made to interfere with the doubly Cabibbo-suppressed $D^0 \rightarrow K^+ \pi^-$ in the latter to compensate. (3) **The Dalitz plot method.**⁵⁰ The three-body decay of $D^0/\bar{D}^0 \rightarrow K_S \pi^- \pi^+$ is reconstructed and the resulting interference in its Dalitz plot is studied.

Since it is quantities required by the GLW method that we measure in this dissertation, we will restrict our attention to this method and summarize it below.⁵¹

⁴²Refs. [22] and [23]. See also Refs. [24], [6], and [7].

⁴³Quark content for mesons relevant to our discussion here: $B^0(\bar{b}d)$, $B^+(\bar{b}d)$, $D^+/D^{*+}(c\bar{u})$, $D^0/D^{*0}(c\bar{d})$ and $K^-/K^{*-}(s\bar{u})$. The ones with an asterisk are vector mesons ($J^P = 1^-$); all others are pseudo-scalar mesons ($J^P = 0^-$).

⁴⁴To be sufficiently general, these decays should be represented as $B^- \rightarrow D^{(*)0}K^{(*)-}$ and $B^- \rightarrow \bar{D}^{(*)0}K^{(*)-}$, respectively. For the sake of simplicity, and since we do not measure the modes containing the D^* or the K^* in this dissertation, we will not refer to the vector mesons unless absolutely necessary.

⁴⁵See Ref. [3], p. 196 for higher order terms.

⁴⁶See Ref. [25] for a review.

⁴⁷Refs. [6] and [7].

⁴⁸Refs. [26] and [27].

⁴⁹Refs. [28] and [29].

⁵⁰Refs. [30] and [31].

⁵¹Our summary of the GLW method follows Refs. [26], [27], [32], and [33]. The notation is mainly that of [33].

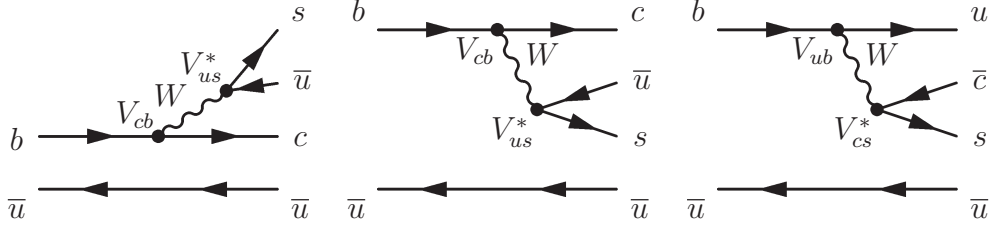


Figure 2.2: Tree level Feynman diagrams for (1) $B^- \rightarrow D^0 K^-$ through external W^- emission, (2) $B^- \rightarrow D^0 K^-$ through internal W^- emission, and (3) color-suppressed $B^- \rightarrow \bar{D}^0 K^-$.

In their original proposal [27], Gronau and Wyler apply to time-independent decays of the type $B^- \rightarrow DK^-$ the triangle relations (see below) between amplitudes developed by Gronau and London [26] for time-*dependent* studies of *neutral* B meson decays. Given the CP-even and CP-odd eigenstates of the neutral D meson

$$|D_{\text{CP}\pm}^0\rangle = \frac{1}{\sqrt{2}}(|D^0\rangle \pm |\bar{D}^0\rangle), \quad (2.27)$$

the following relations⁵² between decay amplitudes hold [27]:

$$A(B^- \rightarrow D_{\text{CP}+} K^-) = \frac{1}{\sqrt{2}}(A(B^- \rightarrow D^0 K^-) + A(B^- \rightarrow \bar{D}^0 K^-)), \quad (2.28)$$

$$A(B^+ \rightarrow D_{\text{CP}+} K^+) = \frac{1}{\sqrt{2}}(A(B^+ \rightarrow \bar{D}^0 K^+) + A(B^+ \rightarrow D^0 K^+)). \quad (2.29)$$

Each equality in Eqs. (2.28) and (2.29) can be expressed as a triangle in the complex plane [27]. Since $B^- \rightarrow D^0 K^-$ and $B^- \rightarrow \bar{D}^0 K^-$ are separately dominated by one weak phase (0 and γ , respectively, in our convention), neither of these two decays is expected to violate CP on its own. One may then define $|A_f| \equiv |A(B^- \rightarrow D^0 K^-)| = |A(B^+ \rightarrow \bar{D}^0 K^+)|$ and $|\bar{A}_f| \equiv |A(B^- \rightarrow \bar{D}^0 K^-)| = |A(B^+ \rightarrow D^0 K^+)|$. The ratio r , defined as

$$r \equiv \frac{|\bar{A}_f|}{|A_f|} \equiv \frac{|A(B^- \rightarrow \bar{D}^0 K^-)|}{|A(B^- \rightarrow D^0 K^-)|}, \quad (2.30)$$

which includes both the effect of CKM matrix elements and that of color suppression, is expected to be in the 0.1–0.2 range.⁵³ Without loss of generality, the strong

⁵²Lest the notation becomes laden with \pm -signs, we restrict the equations to those for the CP-even states, as in Ref. [27]. The equations for the CP-odd D mesons may be recovered by substituting in the appropriate minus signs. In any case, in this dissertation we do not measure (relative) branching ratios for final states containing the CP-odd D meson.

⁵³See, for instance, Refs. [7], [28], [29], [32], [33] or [31].

phases for $B^- \rightarrow D^0 K^-$ and $B^- \rightarrow \bar{D}^0 K^-$ can be taken to be 0 and δ , respectively. Eqs. (2.28) and (2.29) then become [27]

$$A(B^- \rightarrow D_{\text{CP}^+} K^-) = \frac{1}{\sqrt{2}}(|A_f| + |\bar{A}_f| e^{i\delta} e^{-i\gamma}), \quad (2.31)$$

$$A(B^+ \rightarrow D_{\text{CP}^+} K^+) = \frac{1}{\sqrt{2}}(|A_f| + |\bar{A}_f| e^{i\delta} e^{+i\gamma}). \quad (2.32)$$

The strong phase difference δ is expected to be different from zero, since the final states $D^0 K^-$ and $\bar{D}^0 K^-$ have different isospin compositions.⁵⁴ A CP asymmetry is then expected for the decay $B^- \rightarrow D_{\text{CP}^+} K^-$. The original proposal [27], however, does not depend on this fact to extract γ ; exploiting the fact that 2γ is the angle between $A(B^+ \rightarrow D^0 K^+)$ and $A(B^- \rightarrow \bar{D}^0 K^-)$ in the complex plane, $\sin \gamma$ can be determined up to a four-fold degeneracy⁵⁵ by measuring the four independent amplitudes, $|A_f|$, $|\bar{A}_f|$, $|A(B^- \rightarrow D_{\text{CP}^+} K^-)|$, and $|A(B^+ \rightarrow D_{\text{CP}^+} K^+)|$ in Eqs. (2.28) and (2.29).⁵⁶ In Ref. [28], however, it is noted that a measurement of the amplitude $A(B^- \rightarrow \bar{D}^0 K^-)$ in the usual $\bar{D}^0 \rightarrow K^+ \pi^-$ mode is rendered impracticable by interference from the decay chain $B^- \rightarrow D^0 K^-$, $D^0 \rightarrow K^+ \pi^-$.⁵⁷

A modified proposal by Gronau (Refs. [32] and [33]), involves measuring the two ratios

$$R_{\text{CP}\pm} \equiv \frac{2(\Gamma(B^- \rightarrow D_{\text{CP}\pm}^0 K^-) + \Gamma(B^+ \rightarrow D_{\text{CP}\pm}^0 K^+))}{\Gamma(B^- \rightarrow D^0 K^-) + \Gamma(B^+ \rightarrow \bar{D}^0 K^+)} \quad (2.33)$$

along with the two CP asymmetries

$$A_{\text{CP}\pm} \equiv \frac{\Gamma(B^- \rightarrow D_{\text{CP}\pm}^0 K^-) - \Gamma(B^+ \rightarrow D_{\text{CP}\pm}^0 K^+)}{\Gamma(B^- \rightarrow D_{\text{CP}\pm}^0 K^-) + \Gamma(B^+ \rightarrow D_{\text{CP}\pm}^0 K^+)} \quad (2.34)$$

defined in the usual manner, where the Γ 's are the partial decay widths. Once the four quantities $R_{\text{CP}\pm}$ and $A_{\text{CP}\pm}$ are measured, the quantities r , γ , and δ can be extracted using the following expressions⁵⁸

$$R_{\text{CP}\pm} = 1 + r^2 \pm 2r \cos \delta \cos \gamma, \quad (2.35)$$

$$A_{\text{CP}\pm} = \pm 2r \sin \delta \sin \gamma / R_{\text{CP}\pm}, \quad (2.36)$$

both of which follow directly from Eqs. (2.28) and (2.29) and the fact that the partial width $\Gamma(i \rightarrow f)$ of a decay process is directly proportional to the squared modulus of

⁵⁴Refs. [24] and [27].

⁵⁵See Ref. [27] for the expression.

⁵⁶Similarly, $|A_f|$, $|\bar{A}_f|$, $|A(B^- \rightarrow D_{\text{CP}^-} K^-)|$ and $|A(B^+ \rightarrow D_{\text{CP}^-} K^+)|$ can also be used to determine γ . [27]

⁵⁷The two interfering amplitudes are predicted to be of similar size in Refs. [28] and [29]. This is, in fact, the basis for the ADS method above.

⁵⁸Refs. [32] and [33].

its amplitude $|A(i \rightarrow f)|^2$. To obviate the need for precisely determined D branching ratios, we follow Gronau [33] in using the following approximation⁵⁹

$$R_{\text{CP}\pm} \simeq \frac{R_{\pm}}{R}, \quad (2.37)$$

where

$$R_{\pm} \equiv \frac{BR(B^- \rightarrow D_{\text{CP}\pm}^0 K^-) + BR(B^+ \rightarrow D_{\text{CP}\pm}^0 K^+)}{BR(B^- \rightarrow D_{\text{CP}\pm}^0 \pi^-) + BR(B^+ \rightarrow D_{\text{CP}\pm}^0 \pi^+)}, \quad (2.38)$$

and

$$R \equiv \frac{BR(B^- \rightarrow D^0 K^-) + BR(B^+ \rightarrow \bar{D}^0 K^+)}{BR(B^- \rightarrow D^0 \pi^-) + BR(B^+ \rightarrow \bar{D}^0 \pi^+)}. \quad (2.39)$$

In the present analysis, we measure R_+ , defined in Eq. (2.38), for the CP-*even* modes $D_{\text{CP}+} \rightarrow K^- K^+$ and $D_{\text{CP}+} \rightarrow \pi^- \pi^+$, along with R defined in Eq. (2.39) to calculate the approximation to $R_{\text{CP}+}$ defined in Eq. (2.37). Similarly, we measure

$$A_{\text{CP}+} \simeq \frac{\frac{BR(B^- \rightarrow D_{\text{CP}+} K^-)}{BR(B^- \rightarrow D_{\text{CP}+} \pi^-)} - \frac{BR(B^+ \rightarrow D_{\text{CP}+} K^+)}{BR(B^+ \rightarrow D_{\text{CP}+} \pi^+)}}{\frac{BR(B^- \rightarrow D_{\text{CP}+} K^-)}{BR(B^- \rightarrow D_{\text{CP}+} \pi^-)} + \frac{BR(B^+ \rightarrow D_{\text{CP}+} K^+)}{BR(B^+ \rightarrow D_{\text{CP}+} \pi^+)}} \quad (2.40)$$

in the $K^- K^+$ and $\pi^- \pi^+$ modes.

The challenges presented by the GLW method to the experimentalist are rather formidable. Due to the smallness of the ratio r (defined in Eq. (2.30)), we expect the deviation of $R_{\text{CP}\pm}$ and $A_{\text{CP}\pm}$ from one and zero, respectively, to be modest at best. (See Eqs. (2.35) and (2.36).) As a result, high precision measurements of $R_{\text{CP}\pm}$ and $A_{\text{CP}\pm}$ are necessary to meaningfully constrain the value of γ . Another difficulty stems from the fact that decays such as $B^- \rightarrow D_{\text{CP}+}[\pi^- \pi^+]K^-$ or $D_{\text{CP}+}[K^- K^+]K^-$ are suppressed by two orders of magnitude or more compared to the relatively abundant $B^- \rightarrow D^0[K^- \pi^+] \pi^-$ decays. This severely limits the CP-mode sample sizes accessible to the experiments. There are many other experimental difficulties; in the following chapters, we will address those relevant to our analysis. The measurement of $R_{\text{CP}\pm}$ and $A_{\text{CP}\pm}$ ($R_{\text{CP}+}$ and $A_{\text{CP}+}$ in our case) by as many experiments as possible then serves two purposes: the combination of independent measurements enhances the statistical power of the constraints on γ ; the comparison of measurements from different experiments and different collision environments ($e^+ e^-$ versus $p\bar{p}$) increases our confidence that experimental effects are properly understood.

An updated list of the various measurements based on the GLW method is maintained by [21]. In the $B \rightarrow DK$ mode, the latest published measurements are from the BaBar (Ref. [34]) and Belle (Ref. [35]) collaborations. The CDF collaboration has published a measurement [36] using a different method of analysis.

⁵⁹This is achieved in Ref. [33] by neglecting a doubly Cabibbo-suppressed, color-suppressed contribution to $A(B^- \rightarrow D^0 \pi^-)$ of relative size $\sim r|V_{us}V_{cd}/V_{ud}V_{cs}| \sim 0.01$.

⁶⁰This is originally defined in Ref. [33] as $BR(B^- \rightarrow D^0 K^-)/BR(B^- \rightarrow D^0 \pi^-)$.

Chapter 3

The Tevatron and the CDF II Experiment

3.1 The Fermilab accelerator complex

The four-mile long Tevatron collider, the centerpiece of the Fermilab accelerator complex, supplies the proton-antiproton collisions that form the raw material for any physics analysis at the CDF experiment. The Tevatron itself, however, is only the last in a long chain of beam production, storage, and accelerating systems at the Fermilab site. In this section, we provide a brief summary of the architecture of the Tevatron and its ancillary systems, drawn foremost from the descriptions in Chapter 1 of Ref. [37] but also from the references cited in each paragraph. To avoid unnecessarily complicating the discussion, we only highlight the functions that are directly involved in providing the Tevatron with colliding beams, and ignore those related exclusively to the fixed-target and neutrino experiments.

3.1.1 The proton source

1. **Preaccelerator**

Here hydrogen gas (H_2) is ionized by a charged dome into H^- ions and accelerated to 750 keV. The resulting beam is transferred to the Linac. [37]

2. **Linac**

The 750 keV H^- beam passes through the Linear Accelerator, a series of drift tubes connected by a transition section to more energetic side-coupled cavity modules. The result is a 400 MeV H^- beam. [37]

3. **Booster**

The H^- beam from the Linac enters the Booster, a synchrotron 75 meters in radius, and leaves, deprived of its electrons, an 8 GeV proton beam. At

this point, the protons are ready for transfer to the Main Injector, described below. [37][38]

3.1.2 The antiproton source

At the antiproton **target station**, a 120 GeV proton beam generated by the Main Injector (see Section 3.1.3 below) is aimed at a nickel-alloy target, producing a variety of particles, from which antiprotons at roughly 8 GeV are extracted. These antiprotons first arrive at the **Debuncher**, a triangular synchrotron with rounded vertices, to be stochastically cooled at 8 GeV, and are then transferred to the **Accumulator**, a similarly shaped but slightly smaller synchrotron sharing the same tunnel, to be further cooled and stored. Transfer lines connect the Accumulator with the Main Injector. [39][37]

3.1.3 The Main Injector

The Main Injector is a synchrotron located in an oblong tunnel very close to the Tevatron. For the purpose of antiproton production mentioned above, protons are accelerated by the Main Injector from 8 GeV to 120 GeV and directed towards the antiproton target station. To supply beam to the Tevatron, protons from the Booster and antiprotons from the antiproton source or the Recycler are accelerated by the Main Injector to 150 GeV. The protons may then be injected into the Tevatron one bunch at a time; the antiprotons are injected four bunches at a time. [40][37]

3.1.4 The Recycler

The Recycler, which operates at 8 GeV, is situated some 47 inches above the Main Injector in the very same tunnel. Besides serving as a storage ring for antiprotons from the antiproton source, the Recycler was also intended to store antiprotons salvaged from the Tevatron — hence its name. Currently, only the former function is operational. The Recycler has cooling capabilities superior to that of the Accumulator, since electron cooling, necessary for loads above 2×10^{12} antiprotons, is employed in addition to stochastic cooling. For antiprotons from the Accumulator to reach the Recycler, they must briefly pass through the Main Injector first. A separate transfer line is used to extract antiprotons from the Recycler to the Main Injector. [41][37]

3.1.5 The Tevatron

The Tevatron is a nearly circular synchrotron one kilometer in radius. Cryogenic systems supply liquid helium to cool the niobium-titanium superconducting magnets of the Tevatron to an operating temperature of 4.6 K, permitting magnetic field

strengths of up to 4.4 T.¹ Protons and antiprotons arriving from the Main Injector at 150 GeV are accelerated to 980 GeV and then allowed to collide, providing collisions at a center-of-mass energy $\sqrt{s}=1.96$ TeV. The two collision points of the Tevatron are located inside the service buildings labeled B0 and D0, both of which are situated along straight sections of the ring. These buildings serve as the collision halls for Fermilab’s two large, multi-purpose high-energy physics experiments, **CDF** (the Collider Detector at Fermilab) and the **DØ** experiment, respectively. [37][42]

3.2 The CDF II detector

The CDF II detector, situated at the B0 interaction point of the Tevatron, is a multi-purpose particle detector consisting of a variety of detector systems, which include tracking systems inside a solenoidal magnetic field, electromagnetic and hadronic calorimeters, and muon chambers.² (See Fig. 3.1).

We will not attempt to provide a comprehensive overview of the CDF II detector here; numerous descriptions exist elsewhere.³ Since our analysis relies most directly on the tracking capabilities of the detector, we will content ourselves with highlighting the inner tracking systems of CDF II and their associated trigger systems. Our description closely follows that of the general references Refs. [44], [45], [46], and [47] and the detector and trigger-specific references cited in the following sections.

3.2.1 Inner trackers

General charged particle tracking at CDF II is provided by the silicon trackers and the drift chamber. Both systems are located within the 1.5 meter radius of the superconducting solenoid and immersed in its 1.4 T magnetic field.⁴ The magnetic field is along the z -direction, allowing the measurement of the transverse momentum of tracks.⁵

The CDF II **silicon tracking system**⁶ relies on silicon microstrip sensor ladders

¹Refs. [37], [42], and [43].

²Ref. [44], §1.4.

³Standard references used here include the Technical Design Report, Ref. [44] and the CDF papers Refs. [45], [46], and [47].

⁴Ref. [44], §1.4.

⁵The (right-handed) CDF coordinate system has its origin at the center of the detector. The z -coordinate increases in the nominal direction of the proton beam (which circulates clockwise along the Tevatron ring when viewed from above) and the x -axis points away from the center of the ring. The spherical coordinates ϕ (the azimuthal angle) and θ (the polar angle) are also used. The variable r typically refers to the radial cylindrical coordinate. The **pseudorapidity** $\eta \equiv -\ln \tan(\theta/2)$ is often quoted in place of θ . A particle with momentum p and polar angle θ is said to have a **transverse momentum** of $p_T \equiv p \sin \theta$. (Ref. [44], §1.4; Ref. [45]; Ref. [46]; Ref. [37], p.3.)

⁶References for this silicon tracker section include Ref. [44], §§5–6; Refs. [45], [46], [49], [48], [50], [51], and [47].

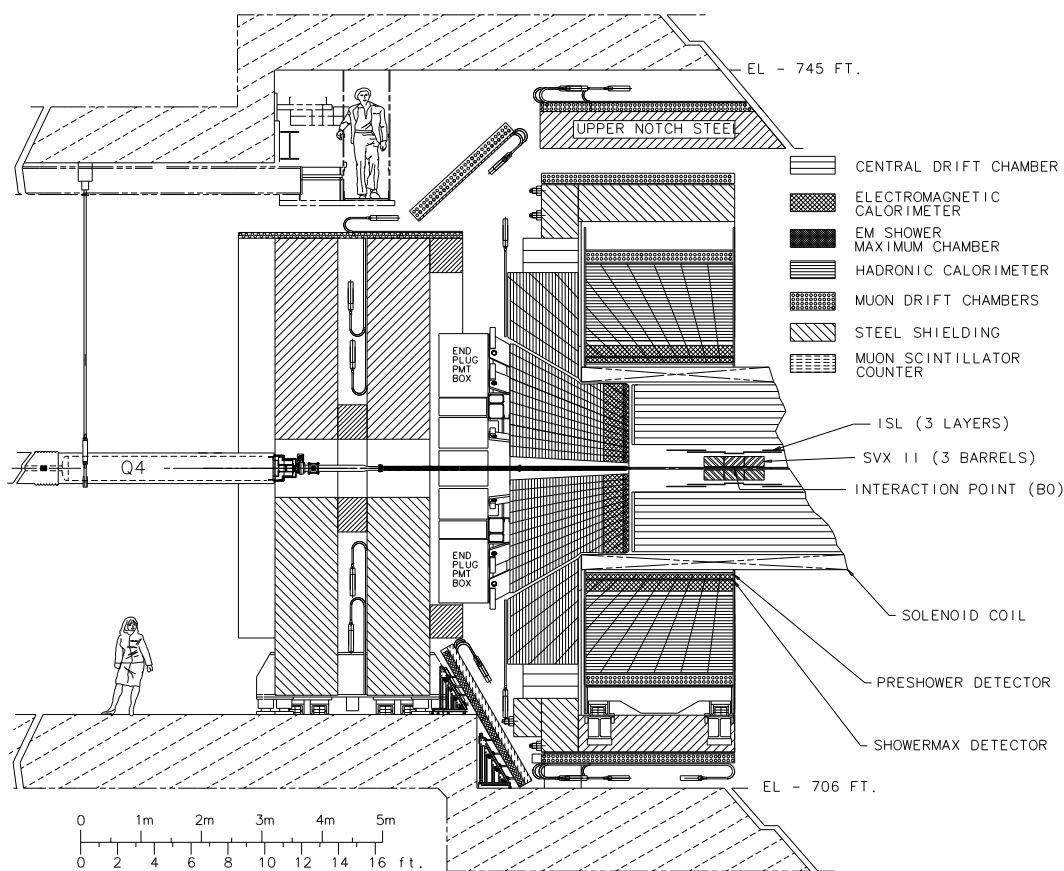


Figure 3.1: Side view of half of the CDF II detector in cross section. From Ref. [44], §1.

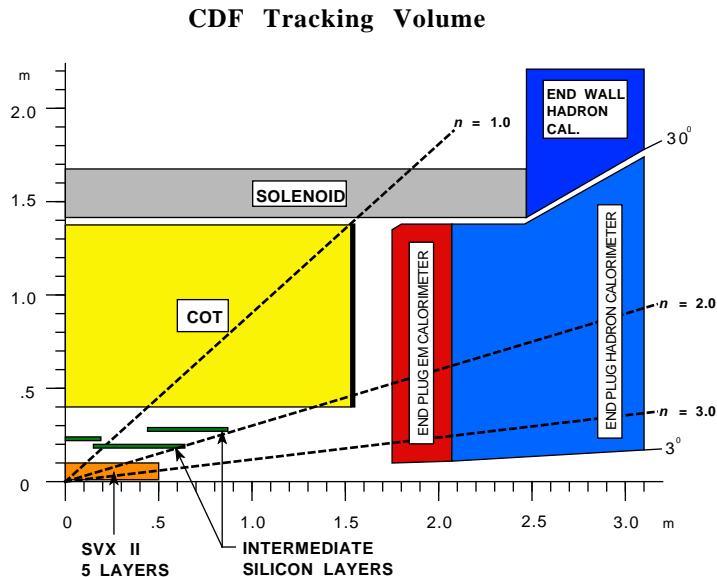


Figure 3.2: An r - z view of a quarter of the CDF II detector. The muon chambers and Layer 00 are not shown. From Ref. [44], §1.

organized into cylindrical layers centered on the beam pipe. (See Figs. 3.2 and 3.3.) In order of increasing distance r from the beampipe, there are three subsystems:

- The innermost is **Layer 00 (L00)**, named after the layer of single-sided sensors attached to the beampipe at $r=1.35$ and 1.62 cm. These sensors provide information on the ϕ position of hits. The length in z is 95 cm. [50]
- Outside L00, roughly between $r=2.5$ cm and $r=11$ cm and containing double-sided sensors, are the five layers belonging to the upgraded **Silicon Vertex Detector (SVX II)**. The axial side of each sensor provides azimuthal hit information as in the L00 case. The other side, however, may provide either 90° stereo (layers 1, 2, and 4) or small-angle ($\pm 1.2^\circ$) stereo information (layers 3 and 5).⁷
- Located between the SVX and the COT (see below), the sensors of the **Intermediate Silicon Layers (ISL)** are also double sided, with the stereo side being of the small-angle type. The geometry of the ISL is more complicated than the other two subsystems: the higher- η regions ($1 < |\eta| < 2$) have two layers at $r \sim 20$ and 28 cm, whereas the central region ($|\eta| < 1$) has one layer at ~ 23 cm. The additional layer at high η compensates for the poor drift chamber (see below) coverage in this η range (see Fig. 3.2).⁸

⁷Ref. [44], §5; Refs. [46], [48], [49], and [44].

⁸Ref. [51]; Ref. [44], §6.1; Ref. [48].

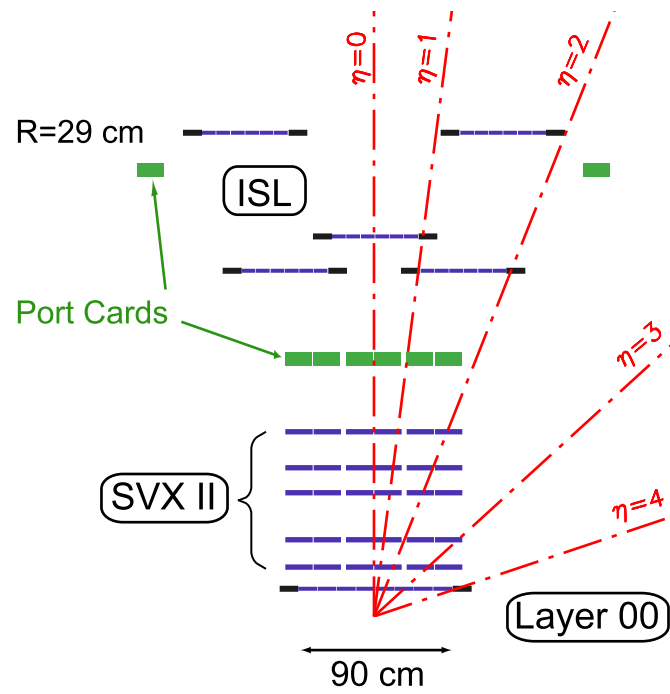


Figure 3.3: An r - z view showing the placement of layers in half of the CDF II silicon tracking system. Note the compression of the horizontal scale relative to the vertical. From Ref. [48].

For a sample of muons with $p_T \sim 1.5$ GeV,⁹ the average impact parameter resolution of “outside-in” tracking, the type of tracking that starts with a COT track (see below) and adds SVX (but not L00) information, is $\sigma(d_0) = 34 \mu\text{m}$. [45]

The **Central Outer Tracker (COT)**, located outside the silicon tracking system, is the multiwire drift chamber at CDF II with an active volume 310 cm long in the z direction and spanning $r = 43.4$ to 132.3 cm in the radial direction, giving effective coverage of tracks up to $\eta = 1$. (See Fig. 3.2.) The drift gas is equal amounts argon and ethane. The COT has 96 layers of gold-coated tungsten sense wires, divided into 8 superlayers. Each superlayer contains drift cells that extend at a 35° angle from the radial and are separated in the azimuthal direction from their neighbors by mylar field sheets coated with gold. Each of the 12 sense wires in a cell is separated from its closest neighbor by a potential wire. The superlayers, numbered 1 to 8 in order of increasing radius, contain wires that are strung either in the axial (z) direction (even-numbered superlayers) or at a 2° stereo angle from the axial (odd-numbered superlayers). In addition to providing timing information for hits, the COT readout relates the time width of the signal before digitization to the logarithm of the amount of charge collected by a given wire. This allows the dE/dx (charge deposition per unit length) of a track to be calculated later on without significantly compromising the ability to resolve hits in time. The p_T and impact parameter resolutions measured in high momentum COT-only tracks (no silicon information) are given by $\sigma(p_T)/p_T^2 \sim 0.1\%$ and $\sigma(d_0) \sim 350 \mu\text{m}$, respectively.¹⁰

3.2.2 Trigger system

Since interesting events in particle collisions are rare, colliders are designed to provide collisions at a sufficiently high rate. The Tevatron collision rate is 1.7 MHz;¹¹ the rate at which events may be stored at CDF II is roughly 100 Hz or less. The chasm between these two rates is bridged by a three-level trigger system designed to efficiently identify interesting events while avoiding significant data acquisition dead time. [53][54]

At **Level 1**, the trigger has access to coarse information from the calorimeters, the XFT (this is the COT track trigger; see below), and the muon chambers to decide whether detector data stored in a pipeline 42 buffers long should be accepted and sent to one of four buffers for Level 2 processing. At **Level 2**, shower maximum

⁹We will follow the high-energy physics convention in which the speed of light c is set to 1. Units for momentum and mass are then identical to those for energy. For instance, GeV/c and GeV/c^2 both become GeV .

¹⁰COT references: Refs. [52], [45], and [46]; Ref. [44], §§1.4 and 4.6.

¹¹The interval between beam crossings is 396 ns, corresponding to a rate of ~ 2.5 MHz. The actual collision rate is only ~ 1.7 MHz, however, due to the existence of gaps that accommodate the time needed for ramping up magnets used to abort the beam. See Ref. [42] for more information on proton and antiproton bunch spacing in the Tevatron.

information from the electromagnetic calorimeter and silicon tracks from the SVT (see below) become available. The Level 2 CPU allows more sophisticated quantities to be calculated and decides whether the event is to be read out and sent to the event builder and Level 3. At **Level 3**, all the data in an event is available for processing by one of several hundred computing nodes running reconstruction software similar to that run offline. Events accepted at Level 3 are written to tape. [53][54][47][45]

Analyses such as the one described in this thesis depend on obtaining large samples of B mesons in non-leptonic (*i.e.*, hadronic) decay modes. In order to accomplish this without allowing background events to saturate the trigger bandwidth, CDF track triggers exploit the fact that B mesons, given their relatively long lifetimes,¹² tend to decay into tracks with relatively large impact parameters.¹³ Below we describe two important track trigger components, the XFT and the SVT.

For a given event, the **Extremely Fast Tracker (XFT)** uses a pattern-matching algorithm to find track segments that correspond to the observed hit configuration on the sense wires in each of the four COT axial (even-numbered) superlayers. Another algorithm then searches for combinations of the identified track segments that are consistent with being from tracks of $p_T \geq 1.5$ GeV, typically with the requirement that each of the four superlayers contribute exactly one segment per track. The list of XFT tracks thus found, along with their ϕ and p_T values, is then sent to the **extrapolation unit (XTRP)**, which allows matching to calorimeter and muon trigger information. XFT tracks are also sent to the SVT (see below). [56][47][46][45]

The **Silicon Vertex Tracker (SVT)** finds clusters of hits in the five axial sensor layers of the SVX and calculates their centroid positions. These hits are placed in bins four to six strips wide. Extrapolated XFT track positions are similarly placed in bins. A track pattern is a set comprising a binned XFT track position and four binned SVT hits (from different SVX layers) that is consistent with being from an SVX track. The list of occupied bins is sent in parallel to an array of associative memory chips loaded with up to 512k pre-identified track patterns for each 30° wedge of the SVX. Once the matched patterns are found, the underlying hit positions are then used to perform linearized fits to obtain the curvature c , impact parameter d_0 , and azimuthal angle ϕ of the corresponding tracks. These SVT tracks are then made available to the Level 2 trigger as mentioned above.¹⁴

¹² B^\pm and B^0 mesons have lifetimes times the speed of light of $c\tau = 492 \pm 2$ and 455 ± 2 μm , respectively. (2011 update to Ref. [55].)

¹³See, for instance, Ref. [44], §12.4.3.

¹⁴SVT references: Ref. [44], §12.4.3; Refs. [53], [54], and [57].

Chapter 4

Analysis Fundamentals

In this chapter, we provide a synopsis of our analysis goals. We then introduce the basic components of our analysis: our data and Monte Carlo samples, our B candidate selection cuts, our maximum likelihood fitter and its inputs, the corrections we perform on the fitter output, and the method we use to validate our fitter.

The text is adapted from three of our CDF Notes, CDF 8705 [58], CDF 8777 [59], and CDF 8716 [60]. The figures and tables in this chapter are also from Refs. [58] and [59].

4.1 Synopsis

Analysis objectives

As stated in Section 2.3, the purpose of the analysis described in this dissertation is to measure (a) the double ratio

$$R_{\text{CP}^+} \simeq \frac{R_+}{R}, \quad (2.37')$$

where

$$R_+ \equiv \frac{BR(B^- \rightarrow D_{\text{CP}^+}K^-) + BR(B^+ \rightarrow D_{\text{CP}^+}K^+)}{BR(B^- \rightarrow D_{\text{CP}^+}\pi^-) + BR(B^+ \rightarrow D_{\text{CP}^+}\pi^+)}, \quad (2.38')$$

and

$$R \equiv \frac{BR(B^- \rightarrow D^0K^-) + BR(B^+ \rightarrow \bar{D}^0K^+)}{BR(B^- \rightarrow D^0\pi^-) + BR(B^+ \rightarrow \bar{D}^0\pi^+)}, \quad (2.39)$$

and (b) the asymmetry

$$A_{\text{CP}^+} \simeq \frac{\frac{BR(B^- \rightarrow D_{\text{CP}^+}K^-)}{BR(B^- \rightarrow D_{\text{CP}^+}\pi^-)} - \frac{BR(B^+ \rightarrow D_{\text{CP}^+}K^+)}{BR(B^+ \rightarrow D_{\text{CP}^+}\pi^+)}}{\frac{BR(B^- \rightarrow D_{\text{CP}^+}K^-)}{BR(B^- \rightarrow D_{\text{CP}^+}\pi^-)} + \frac{BR(B^+ \rightarrow D_{\text{CP}^+}K^+)}{BR(B^+ \rightarrow D_{\text{CP}^+}\pi^+)}}. \quad (2.40)$$

Intermediate measurements

Our measurement of $R_{\text{CP}+}$ and $A_{\text{CP}+}$ then entails measuring six ratios of B^\pm branching ratios. The first pair involves reconstructing the D^0 (\bar{D}^0) in the flavor eigenstate of $K^-\pi^+$ ($K^+\pi^-$):

$$R_{K\pi}^- \equiv BR(B^- \rightarrow D^0[K^-\pi^+]K^-)/BR(B^- \rightarrow D^0[K^-\pi^+]\pi^-), \quad (4.1)$$

$$R_{K\pi}^+ \equiv BR(B^+ \rightarrow \bar{D}^0[K^+\pi^-]K^+)/BR(B^+ \rightarrow \bar{D}^0[K^+\pi^-]\pi^+). \quad (4.2)$$

For the next two pairs of ratios, the D^0 is reconstructed in the CP+ eigenstates of $\pi^-\pi^+$ and K^-K^+ , respectively:

$$R_{\pi\pi}^- \equiv BR(B^- \rightarrow D_{\text{CP}+}[\pi^-\pi^+]K^-)/BR(B^- \rightarrow D_{\text{CP}+}[\pi^-\pi^+]\pi^-), \quad (4.3)$$

$$R_{\pi\pi}^+ \equiv BR(B^+ \rightarrow D_{\text{CP}+}[\pi^-\pi^+]K^+)/BR(B^+ \rightarrow D_{\text{CP}+}[\pi^-\pi^+]\pi^+); \quad (4.4)$$

$$R_{KK}^- \equiv BR(B^- \rightarrow D_{\text{CP}+}[K^-K^+]K^-)/BR(B^- \rightarrow D_{\text{CP}+}[K^-K^+]\pi^-), \quad (4.5)$$

$$R_{KK}^+ \equiv BR(B^+ \rightarrow D_{\text{CP}+}[K^-K^+]K^+)/BR(B^+ \rightarrow D_{\text{CP}+}[K^-K^+]\pi^+). \quad (4.6)$$

In other words, the quantities we directly measure are six relative branching ratios $BR(B \rightarrow D^0 K)/BR(B \rightarrow D^0 \pi)$, one for each combination of D^0 decay mode ($K^-\pi^+$, $\pi^-\pi^+$, or K^-K^+) and B meson charge (B^- or B^+). These quantities, along with their errors, are combined to calculate $A_{\text{CP}+}$ and $R_{\text{CP}+}$.

In Eqs. (4.1) to (4.6), we see that the decay channels we wish to measure are of the form $B \rightarrow D\pi$ and $B \rightarrow DK$, where the D meson is a D^0 decaying to $K^-\pi^+$, $\pi^-\pi^+$, or K^-K^+ . We will call the samples in which we reconstruct these decays the **$D^0 X^-$ signal samples**. The X^- here refers to the charged track of unknown species attached to the D^0 to form a B^- candidate. This track will be referred to as the “ B daughter track”.

To extract the six required relative branching fractions, we will in due course perform maximum likelihood fits on the three $D^0 X^-$ signal samples. These fits are in two dimensions, the mass of the B candidate and the COT specific ionization (dE/dx) of the B daughter track. Before these $D^0 X^-$ fits are performed, however, we choose to extensively validate our fitting apparatus on two **control samples** where the D meson is a D^+ or a D^{*+} instead of a D^0 as in the signal samples. In Chapters 5 and 6, we apply our fitter on the control samples and the signal samples, respectively.

In the remainder of this chapter, we will describe our data and Monte Carlo samples, the reconstruction of B candidates, and the selection cuts for the analyses. We will also discuss the structure of our maximum likelihood fitter and how we arrive at the mass and dE/dx distributions employed in the fitter.

4.2 Data samples and B candidate reconstruction

The control samples and the signal samples contain data acquired during the period February 2002 to September 2006. The signal sample, however, benefits from extra data taken until November 2006.¹ The integrated luminosities of the two sets of samples are ~ 1.2 and $\sim 1.3 \text{ fb}^{-1}$, respectively.

In Section 3.2.2, we have described the ability of the SVT to detect and flag charged tracks that are displaced from the primary $p\bar{p}$ primary interaction vertex. These displaced SVT tracks often signal long-lived particles such as charm and bottom hadrons and are therefore of great interest to students of B physics. Common strategies to prevent the SVT triggers from saturating the available bandwidth include: (a) demanding the existence of a lepton (an electron or a muon) in addition to the presence of a single displaced track, or (b) simply requiring the existence of two displaced tracks. This latter trigger strategy gives us the so-called **two-track triggers**, a class of trigger paths that require at the very minimum two displaced tracks each with $p_T > 2 \text{ GeV}$.

It is from the two-track trigger dataset that we reconstruct the B candidates for our control and signal samples. If an event contains a B candidate passing the loose cuts we describe below, we place the event into one of the skimmed samples (see Table 4.1) according to the reconstructed candidate type.

We start with the CDF two-track trigger datasets after standard CDF offline event reconstruction. Several adjustments are made: The track fits are redone according to the standard B group adjustments regarding passive detector material, the COT covariance matrix, and the resolution of hits in the silicon tracker. To ensure good track quality, tracks must satisfy $|\eta| < 2.0$ and have a minimum of 5 hits in each of 2 axial and 2 stereo COT superlayers. All tracks, except for soft pions in D^* reconstruction, are required to have at least 3 silicon hits.

The B candidate reconstruction procedure is as follows:

- In each event, we attempt to reconstruct a D^0 , D^+ , D^{*+} , or D_s meson candidate in the following decay modes:

1. $D^+ \rightarrow K^- \pi^+ \pi^+$;
2. $D^{*+} \rightarrow D^0 [K^- \pi^+] \pi^+$;
3. $D^0 \rightarrow K^- \pi^+$, $\pi^- \pi^+$, or $K^- K^+$;
4. $D_s^+ \rightarrow \phi [K^- K^+] \pi^+$.

The mass window for the D^0 and D^+ candidates is $[1.81, 1.92] \text{ GeV}$; for the D_s we require $m(D) \in [1.91, 2.03] \text{ GeV}$. The D candidate must contain one track

¹The end date for the signal sample was determined by the disabling of the COT dE/dx readout for superlayers 1 and 2.

matched to a displaced SVT track. The candidate must also satisfy $L_{xy}(D) > 200 \mu\text{m}$.²

- Once a D candidate is found, an extra track is attached to it by means of a vertex fit.³ This fit constrains the D daughter tracks to come from a common vertex; the D candidate momentum is in turn extrapolated and constrained to form another vertex with the extra track. The result of this vertex fit is our B candidate. The fit may optionally require a mass constraint on the D or the constraint that the B candidate point toward the primary vertex. Since our particle identification capabilities only allow statistical separation of pions and kaons from each other and from other species of particles, we uniformly assign the pion mass to this extra track and delay the use of particle identification information (the dE/dx mentioned above) to the likelihood fit performed later on. Such a B candidate can therefore be a genuine $D\pi$ or DK event, a partial reconstruction of a B decaying into a D and two or more particles, or simply random tracks masquerading as a B (*i.e.*, combinatorial background).

We take the four momentum of the B candidate (whether we believe it to be fully reconstructed or otherwise, signal or background) to be the sum of the four-momenta of the D candidate and the track assumed to be a pion. (This track, the “ B daughter track” mentioned before, will be designated, when necessary, by the symbol π_B without any prejudice regarding its actual species.) The invariant mass calculated from the B four-momentum is then called the B candidate mass, denoted as $m_{D\pi}$, or simply $m(B)$, and is required to be in the interval of $[4.65, 6.5]$ GeV.

B candidates are required to contain two tracks matched to displaced SVT tracks and satisfy minimal two-track trigger requirements. Stricter trigger confirmation is postponed to the analysis stage described below.

Additionally, the transverse momentum of the candidate must satisfy $p_T(B) > 5.5$ GeV. An impact parameter cut $|d_0(B)| < 100 \mu\text{m}$ is made on the B with respect to the beamline. Candidates are required to have $L_{xy} > 300 \mu\text{m}$ and fit $\chi_{xy}^2 < 30$. Although a D mass constraint may optionally be imposed for future use in the analysis, we base our present selection only on quantities calculated in the absence of such a constraint.

- The $p\bar{p}$ primary interaction vertex is calculated for each event. This information is also reserved for future use in the analysis; at the present stage, the selection does not involve quantities based on this calculation.

In Table 4.1, the control samples are **skbh24** ($\bar{B}^0 \rightarrow D^{*+}\pi^-$) and **skbh29** ($\bar{B}^0 \rightarrow D^+\pi^-$). The “wrong-sign” **skbh30** (“ B ” $\rightarrow D^+\pi^+$) is used for background modeling.

²The L_{xy} is the length of the decay distance projected onto the transverse plane.

³Our vertex fits are performed with CTVMFT (Ref. [61]).

Dataset name	Decay mode
skbh13	$\overline{B}_s^0 \rightarrow D_s^+ \pi^-$ ($D_s \rightarrow K^* K$)
skbh14	$\overline{B}_s^0 \rightarrow D_s^+ \pi^+$ ($D_s \rightarrow K^* K$)
skbh16	$\overline{B}_s^0 \rightarrow D_s^+ \pi^-$ ($D_s \rightarrow 3\pi$)
skbh17	$\overline{B}_s^0 \rightarrow D_s^+ \pi^+$ ($D_s \rightarrow 3\pi$)
skbh21	$B^- \rightarrow D^0 \pi^-$, ($D^0 \rightarrow K\pi$)
skbh22	$B^- \rightarrow D^0 \pi^-$, ($D^0 \rightarrow \pi\pi$)
skbh23	$B^- \rightarrow D^0 \pi^-$, ($D^0 \rightarrow KK$)
skbh24	$\overline{B}^0 \rightarrow D^{*+} \pi^-$ ($D^{*+} \rightarrow D^0 \pi$, $D^0 \rightarrow K\pi$)
skbh26	$\overline{B}_s^0 \rightarrow D_s^+ \pi^-$ ($D_s \rightarrow \phi\pi$, $\phi \rightarrow KK$)
skbh27	$\overline{B}_s^0 \rightarrow D_s^+ \pi^+$ ($D_s \rightarrow \phi\pi$, $\phi \rightarrow KK$)
skbh29	$\overline{B}^0 \rightarrow D^+ \pi^-$ ($D^+ \rightarrow K^- \pi^+ \pi^+$)
skbh30	“ B ” $\rightarrow D^+ \pi^+$ ($D^+ \rightarrow K^- \pi^+ \pi^+$)

Table 4.1: Data samples skimmed from the two-track-trigger dataset.

The signal samples are **skbh21** ($B^- \rightarrow D^0[K^- \pi^+] \pi^-$), **skbh22** ($B^- \rightarrow D^0[\pi^- \pi^+] \pi^-$), and **skbh23** ($B^- \rightarrow D^0[K^- K^+] \pi^-$). The B_s samples are not used in this analysis. Ntuples are created from the skimmed data samples to facilitate our analysis.

4.3 Monte Carlo datasets

Since one of the dimensions of our likelihood fit⁴ is the mass $m(B)$ of the B candidate in the $D\pi$ hypothesis, it is essential that we have a means of obtaining the mass probability distribution functions (PDFs) of our signal and background modes. For the signal $B \rightarrow DK$ and $B \rightarrow D\pi$ decays and partially reconstructed background modes of the type $B \rightarrow DX^-$, we rely on Monte Carlo simulation (with certain adjustments; see below) to provide the mass distributions.⁵

All of the Monte Carlo datasets we use are generated using **Bgenerator**⁶ and **EvtGen**⁷ as implemented in the CDF software framework. Standard detector and trigger simulations are performed on the generated data.

A list of Monte Carlo samples used in this analysis is given in Table 4.2. In Figures 4.1–4.4, 4.5–4.7, and 4.8–4.11 we show the decay mode content of various Monte Carlo samples used in the D^+X , $D^{*+}X$, and D^0X fits, respectively.

There are, broadly speaking, two categories of Monte Carlo samples used in our

⁴See Section 4.5.

⁵See Section 4.6 for the treatment of other types of background.

⁶Refs. [62] and [63].

⁷Ref. [64].

Sample content	Sample name
$D^+ X^-$ control sample fits	
$\overline{B}^0 \rightarrow D^+ \pi^- (n\gamma)$	b0dkpp
$\overline{B}^0/B^0 \rightarrow D^+ X$	z35ba0
$B^-/B^+ \rightarrow D^+ X$	bdpkpx
$B_s \rightarrow D_s^- [\phi\pi^-] X$	mcbh03
$D^{*+} X^-$ control sample fits	
$\overline{B}^0 \rightarrow D^{*+} \pi^- (n\gamma)$	b0dspp
$\overline{B}^0/B^0 \rightarrow D^0 X$	z35b90*
$B^-/B^+ \rightarrow D^0 X$	bd0kpx*
$D^0 X^-$ signal sample fits	
$B^- \rightarrow D^0 \pi^- (n\gamma)$	bd0kpp
$B^- \rightarrow D^0 K^- (n\gamma)$	—
$\overline{B}^0/B^0 \rightarrow D^0 X$	z35b90*
$B^-/B^+ \rightarrow D^0 X$	bd0kpx*
$B^- \rightarrow K^- K^+ K^-, K^- \pi^+ \pi^-, \text{ and } \pi^- \pi^+ \pi^-$	—

Table 4.2: Monte Carlo samples used in our fitter. The samples marked with an asterisk are shared between the $D^{*+} X^-$ control sample and $D^0 X^-$ signal sample fits.

fits. The first consists of semi-inclusive samples of B mesons decaying into final states of the form DX , where the X represents one or more particles. Among these are the $B \rightarrow D^+ X$ samples used in the $D^+ X^-$ fit and the $B \rightarrow D^0 X$ samples used for both the $D^{*+} X^-$ and $D^0 X^-$ fits. A sample of $B_s \rightarrow D_s^- [\phi\pi] X^+$ events is also used in the modeling of the $D^+ X^-$ control sample background.

Belonging to a second category of Monte Carlo samples are those we generate specifically to model the mass shape of the $D\pi$ (and in the case of the signal sample, also $D^0 K$). Since these $D\pi$ and DK final states are precisely those that appear in Eqs. (4.1) to (4.6), it is important that their shapes be modeled with sufficient accuracy. This requires that the Monte Carlo samples be large enough so that we are not limited by statistical uncertainties in the mass shape. Additionally, the mass region where the $D\pi$ and DK overlap must be treated with care. In particular, we are concerned with the low mass tail of the $D\pi$ peak, the shape of which is sculpted by the emission of soft photons we do not reconstruct. To model this “radiative tail”, we use the PHOTOS decay model [65] in EvtGen with the default photon energy cutoff of 10 MeV. Since we expect the simulation to describe the shape of the radiative tail more accurately than the normalization [66], the $D\pi$ radiative tail is left as a free component with a normalization to be determined as an output of the fit. This important subject is treated in greater detail in the description of the individual fits. In Table 4.2, the samples generated for this purpose are given the extra label $(n\gamma)$ in

the final state as a shorthand for the possible existence of one or (rather infrequently) more photons accompanying the B decay.

An additional Monte Carlo sample is that consisting of charged- B decays to all-hadronic three-charged-track final states (see last line of Table 4.2). A subset of the `EvtGen` decay table is used. This sample enables us to model the decays $B^- \rightarrow K^- K^+ K^-$, $K^- \pi^+ \pi^-$, and $\pi^- \pi^+ \pi^-$, the first two of which are significant peaking backgrounds underneath our $B^- \rightarrow D^0 K^-$ signal in the $D^0[KK]$ and $D^0[\pi\pi]$ modes, respectively.⁸

Another Monte Carlo sample, not listed in Table 4.2, since it is not used to obtain mass templates used in our fits, is an inclusive b decay sample, containing both b baryon and B meson decays, kindly provided by the Johns Hopkins group. We have used this sample to study b backgrounds other than those of the type DX .

In general, Monte Carlo samples are reconstructed with the same set of scripts used for actual data, save for changes necessary for technical reasons. However, residual discrepancies between the Monte Carlo and data have been observed. By studying the $\bar{B}^0 \rightarrow D^{*+} \pi^-$ mass peak, which has a very low background level, we find it prudent in the control sample analyses to apply a mass scale factor of 1.00025 ± 0.00012 to the Monte Carlo distributions. Similarly, we correct the Monte Carlo mass resolution by applying a Gaussian resolution function with $\sigma = 6.43 \pm 2.09$ MeV. The statistical uncertainties in these two corrections are taken as sources of systematic uncertainties in Section 5.1.5.

In the signal $D^0 X$ sample, we obtain analogous corrections using a different approach. As shown in Figures 6.2 and 6.3, we perform fitter likelihood scans on the $D^0[K^-\pi^+]X^-$ data sample (both charges combined). Based on the results of these scans, we account for residual discrepancies in the $B \rightarrow D^0 X$ fit by applying to Monte Carlo distributions a mass scale factor of 1.000236 ± 0.000020 and a Gaussian resolution function with $\sigma = 4.61 \pm 0.33$ MeV. Again, we assign systematic uncertainties on the measured branching ratios by varying the scaling and smearing according to the quoted errors. See Section 6.4.1 for more details.

4.4 Analysis cuts

In this section we describe the analysis cuts for the control and signal samples and the method by which the cuts were obtained. The analysis cuts for the $D^{*+} X$ control sample and the $D^0 X$ signal samples can be found in Table 4.3; those for the $D^+ X$ control sample are listed in Table 4.4.

⁸See Section 6.3.1 for a detailed discussion of these backgrounds.

4.4.1 Comments on cut variables

In our fits, we do not use the track dE/dx values directly. Instead we use the Z variable defined as

$$Z \equiv \ln(dE/dx)[\text{measured}] - \ln(dE/dx)[\text{predicted for pions}]. \quad (4.7)$$

(See Section 4.7 for a discussion.) The B daughter track of each B candidate is therefore required to possess a valid Z measurement. Furthermore, the use of Z constrains us to make the p_T and track quality cuts on the B daughter track at least as stringent as those made on the tracks used to obtain the Z templates. This imposes, at a minimum, a $p_T > 2$ GeV cut on the B daughter track.

In the context of cut variables described below, the *significance* of a variable X denotes the quantity X/σ_X , where σ_X is the uncertainty on X .

The variable $z_0(B)$ is defined to be the impact parameter of the B candidate with respect to the three-dimensional primary vertex position that is calculated for each event during the candidate reconstruction process (Section 4.2). The *isolation* of a B candidate $\text{iso}_{1.0}(B)$ is defined as

$$\text{iso}_{1.0}(B) = \frac{p_T(B)}{p_T(B) + \sum_{\text{tracks}} p_T(\text{track})}, \quad (4.8)$$

where the sum extends over all tracks within a cone of $\Delta R \equiv \sqrt{(\Delta\phi)^2 + (\Delta\eta)^2} = 1.0$ around the direction of the B .⁹ The SVT match distance is a χ^2 -like quantity calculated in two track parameters, ϕ_0 and c (the curvature).

4.4.2 Analysis cuts for the $D^0 X^-$ signal samples and the $D^{*+} X^-$ control sample

First we explain the optimization procedure we use to obtain the analysis cuts on the $D^0[K^-\pi^+]X$ sample. Since the statistical uncertainty on the branching ratio of $B \rightarrow DK$ relative to $B \rightarrow D\pi$ is dominated by the statistical uncertainty on the Cabibbo-suppressed $B^- \rightarrow D^0 K^-$ yield, we choose to maximize $S^2/(S+B)$ for the $B^- \rightarrow D^0 K^-$ in as unbiased a manner as possible.

We use $B^- \rightarrow D^0 X$ Monte Carlo to model $B^- \rightarrow D^0 K^-$, $B^- \rightarrow D^0 \pi^-$, and the rest of $B^- \rightarrow D^0 X$. The combinatorial background is taken from the high $m(B)$ sideband of the statistically independent $\bar{B}^0 \rightarrow D^+ X$ sample. After scaling the $B^- \rightarrow D^0 X$ Monte Carlo and $D^+ X$ data yields to that expected in $D^0 X$ data and taking into account the shape of the combinatorial background, the cuts are scanned and $S^2/(S+B)$ calculated for each combination of cuts. The signal S is

⁹Since our Monte Carlo generator `Bgenerator` produces the requested b hadron but not the rest of the event, the isolation cut has no effect on these simulated events.

the $B^- \rightarrow D^0 K^-$ yield, whereas the background B includes $B^- \rightarrow D^0 \pi^-$, the rest of $B^- \rightarrow D^0 X$, and the combinatorial background.

We have looked at 18 variables with varying degrees of correlations amongst themselves. We choose seven variables that are relatively uncorrelated and show reasonable potential for the purpose of separating signal from background. Three of these ($\text{iso}_{1.0}(B)$ and the $z_0(B)$ and $d_0(B)$ significances) are not modeled by `Bgenerator` Monte Carlo; we fix these cuts at values that keep most of the signal. The remaining four variables are then subject to a four-dimensional optimization using the method explained above. These four variables are simultaneously scanned in the following ranges:

- $L_{xy}(B)$ significance: 9 steps in the range 4 to 12,
- $p_T(\pi_B)$: 5 steps in the range 2 to 3 GeV,
- $L_{xy}(B \leftarrow D)$ significance: 9 steps in the range -6 to 2,
- B vertex probability:¹⁰ 4 steps in the range 10^{-6} to 10^{-3} .

$S^2/(S+B)$ and its error are calculated for each of the 1620 scan points. The results are sorted by $S^2/(S+B)$. Many of the $S^2/(S+B)$ points are statistically indistinguishable. Out of the top few dozen in $S^2/(S+B)$, as our optimal point, we pick a cut combination that does not have leave us in an anomalous corner of cut space. The resultant cuts are shown in Table 4.3.

To further enhance the signal-to-background ratio in the CP modes, the D^0 mass window has been narrowed from ± 20 to ± 12 MeV around the nominal D^0 mass. The B -to- D L_{xy} significance cut has also been tightened to 0 for the CP modes in order to suppress background from three-body B^- decays. (See Section 6.3.1.)

An additional veto is introduced for the $D^0[\pi\pi]$ mode. $B^- \rightarrow J/\psi[\mu^-\mu^+]K^-$ decays reconstructed as $B^- \rightarrow D^0[\pi\pi]\pi^-$ candidates peak in the $D^0[\pi\pi]K^-$ signal region and form a significant background. In order to eliminate these events, a veto in a ± 50 MeV window around the nominal J/ψ mass is performed (in the $\mu\mu$ mass hypothesis) on the track pair consisting of the B daughter track and the opposite-signed daughter of the $D^0[\pi\pi]$ candidate.

The $D^{*+}X$ cuts are identical to the $D^0[K^-\pi^+]X$ cuts, save for an extra cut on the mass difference $m(D^{*+}) - m(D^0)$.

4.4.3 Analysis cuts for the D^+X^- control sample

The optimization of our D^+X analysis cuts begins with those used in the CDF B_s oscillation measurement.¹¹

¹⁰Before we compute the χ_{xy}^2 probability, the χ_{xy}^2 is scaled down by a factor of 1.7 to ensure the flatness of the the resultant probability distribution.

¹¹Refs. [67] and [68].

As before, the use of dE/dx in our fit requires a cut of at least $p_T > 2$ GeV on the B daughter track. We perform one-dimensional optimizations of $S^2/(S + B)$ in the remaining cut variables. Both the signal S and background B are taken from the B peak region ($m(B) \in [5.26, 5.40]$ GeV). D sidebands events are used to model the background and sideband-subtracted D peak events are used to model the signal. This yields the following cuts:

- $|d_0(B)| > 60 \mu\text{m}$,
- $L_{xy}(B \leftarrow D) > 0$,
- $\chi_{xy}^2(B) < 10$.

The $L_{xy}(B)$ significance cut is also loosened to 8. Since the combinatorial background is a large source of systematic uncertainty, we apply the $z_0(B)$ significance cut and the isolation cut from the $D^0 X^-$ optimization to further reduce background.

Instead of increasing the number of components in our $D^+ X$ fit, we have chosen to veto $D^+ \rightarrow K^- \pi^+ \pi^+$ candidates consistent with being incorrectly reconstructed $D^{*+} \rightarrow D^0 [K^- \pi^+ \pi^0] \pi^+$ or $\Lambda_c \rightarrow p K^- \pi^+$ decays. To veto the $D^{*+} \rightarrow D^0 [K^- \pi^+ \pi^0] \pi^+$ decay, we first calculate $\Delta m \equiv m(K^- \pi^+ \pi^+) - m(K^- \pi^+)$. Since there are two possible choices for the charged pion in the quantity $m(K^- \pi^+)$, we calculate two values for Δm . If either Δm is less than 180 MeV, the candidate is vetoed. The $\Lambda_c \rightarrow p K^- \pi^+$ veto also admits two possibilities; a $D^+ \rightarrow K^- \pi^+ \pi^+$ candidate is eliminated when assigning the proton mass to either of the pion tracks brings the candidate mass to within 250 MeV of the Λ_c mass.

$\text{prob}(\chi_{xy}^2(B)/1.7, n(\text{dof}))$	> 0.001
$L_{xy}(B)/\sigma_{L_{xy}}(B)$	> 8
$L_{xy}(B \leftarrow D)/\sigma_{L_{xy}}(B \leftarrow D)$	> -2 (> 0 for D_{CP}^0 modes)
$ d_0(B)/\sigma_{d_0}(B) $	< 3
$p_T(\pi_B)$ (GeV)	> 2.0
$ z_0(B)/\sigma_{z_0}(B) $	< 3
$\text{iso}_{1.0}(B)$	> 0.5
$ m(D^0) - 1864.6 $ (MeV)	< 20 (< 12 for D_{CP}^0 modes)
π_B SVT match distance	< 25
π_B SVT χ^2	< 15
π_B SVT p_T (GeV)	> 2
$m(D^{*+}) - m(D^0)$ (MeV)	$144 < \Delta m < 147$ (D^* mode only)
valid Z (dE/dx) measurement	yes
good run	yes
J/ψ veto	($D^0[\pi\pi]$ mode only)

Table 4.3: Analysis cuts for the three $D^0 X^-$ signal samples and the $D^{*+} X^-$ control sample. Cuts are applied to the unconstrained candidates. See text for details.

$\chi_{xy}^2(B)$	< 10
$\chi_{xy}^2(D)$	< 15
$L_{xy}(B)/\sigma_{L_{xy}}(B)$	> 8
$L_{xy}(B \leftarrow D)$	> 0
$ d_0(B) $ (μm)	< 60
$p_T(\pi_B)$ (GeV)	> 2.0
$ z_0(B)/\sigma_{z_0}(B) $	< 3
$\text{iso}_{1.0}(B)$	> 0.5
π_B SVT match distance	< 25
π_B SVT χ^2	< 15
π_B SVT p_T (GeV)	> 2
$m(K, \pi \mapsto p, \pi)$ (MeV)	$ m - 2285 > 250$
$m(K\pi\pi) - m(K\pi)$ (MeV)	$\Delta m > 180$
valid Z (dE/dx) measurement	yes
good run	yes

Table 4.4: Analysis cuts for the $D^+ X^-$ control sample. See text for details.

4.5 The maximum likelihood fitter

To extract the branching ratios required for our measurement, we perform unbinned maximum likelihood fits on each of our samples. We fit in two variables: (1) the invariant mass $\mathbf{m}(\mathbf{B})$ of the candidate under the $D\pi$ mass hypothesis and (2) the particle identification variable \mathbf{Z} for the B daughter track, defined previously in Eq. (4.7). There are two possibilities for our likelihood function,¹² the extended likelihood

$$L(n_1, \dots, n_M) = \frac{\exp(-\sum_j n_j)}{N!} \prod_{i=1}^N \sum_{j=1}^M n_j p_j(m_i) q_j(Z_i) \quad (4.9)$$

and the non-extended likelihood

$$L(f_1, \dots, f_{M-1}) = \prod_{i=1}^N \sum_{j=1}^M f_j p_j(m_i) q_j(Z_i), \quad \text{where } f_M \equiv 1 - \sum_{j=1}^{M-1} f_j. \quad (4.10)$$

In either case, the index i runs over the N candidates passing our analysis cuts. The second index j runs over the components of the fit, where a component is defined as any decay mode, convenient grouping of decay modes, or type of background treated as a single unit in the fit. In the extended case, the fitter returns the set of M n_j 's, where n_j is the number of candidates in component j . In the non-extended case, the fraction of events f_j in each component is returned instead; only $M - 1$ of these fractions are independent, since the sum of the f_j 's is constrained to equal 1.

For a given component j , $p_j(m)$ and $q_j(Z)$ represent its mass and Z PDFs, respectively. A general explanation of how these PDFs are obtained is given below. Details specific to each sample are described in Chapters 5 and 6.

In practice, as is customary, we minimize the negative log-likelihood, $-\ln L$, instead of maximizing L itself. In the extended case, for instance, we minimize

$$-\ln L(n_1, \dots, n_M) = \sum_{j=1}^M n_j - \sum_{i=1}^N \ln \left(\sum_{j=1}^M n_j p_j(m_i) q_j(Z_i) \right), \quad (4.11)$$

in which a constant term $\ln N!$ is suppressed. The minimizations are performed using the MINUIT [70] package as implemented in ROOT [71].

Additional capabilities of the fitter include fixing the relative sizes of components, imposing Gaussian constraints on the relative sizes, and the use of extra parameters beyond fractions or normalizations (*e.g.*, shape parameters for background parameterization). A single mass PDF may also be coupled with several different Z templates for different mass subranges.

¹²See, for instance, §6 of Ref. [69].

4.6 Fit components and their templates

In this section, we describe in general terms the three categories of components that enter our likelihood fits. An overview of the mass and Z templates associated with these components is provided. For different fits, the specifics of template configuration may vary substantially. Detailed descriptions of control and signal sample fits are presented in Chapters 5 and 6, respectively.

4.6.1 Single- B modes

This category consists of B candidates that represent actual B mesons, either fully or partially reconstructed. The D candidates are properly reconstructed D mesons of the stated type. Both the D candidate and the track are decay products of the same B meson.

The $B \rightarrow DK$, $B \rightarrow D\pi$, and the $B \rightarrow D\pi(n\gamma)$ radiative tail¹³ are always included as separate components. Other modes (*e.g.*, partially reconstructed modes, reflections, etc.) may also be treated as separate components if justified by size, particle content, or proximity to the DK signal. A catch-all $B \rightarrow DX$ “remainder” component is also included.

Mass templates

Mass PDFs for single- B modes are obtained from the Monte Carlo samples described in Section 4.3. In a large number of cases, these components possess mass shapes that cannot be accurately described by simple parameterizations. We therefore represent the mass PDFs as histograms and rely on the fact that our Monte Carlo samples are larger than our data samples by at least a factor of three. The mass PDFs are histograms with bins 10 MeV wide.

As detailed in Section 4.3, an additional smearing of the histograms and adjustment of the mass scale is applied to improve the agreement between Monte Carlo and data. After this smearing, we avoid edge effects by narrowing the candidate mass range from [4.65, 6.50] GeV in the skim to [4.85, 6.45] GeV in the fit. The increase in the lower mass cutoff from 4.65 GeV to 4.85 GeV also limits our exposure to a region where knowledge of B branching ratios is poor.

Z templates

For a given single- B mode, the particle content of its Z template is well defined. (This is in contrast to the background modes described in the next sections.) What remains to be done is to obtain Z templates for the different possible species of B daughters, the most important of which are the kaons and the pions. The method by

¹³See Section 4.3 for a discussion of the radiative tail.

which these templates are obtained is summarized in Section 4.7. See Appendix A for a detailed description.

In all cases, the mass and Z PDFs for these modes are represented as histograms. There are some cases where the assumption of separable PDFs is relaxed (see the discussion of the $B \rightarrow D^0 X$ “remainder” template in Sec. 6.2.1, for instance), and a two-dimensional PDF of the form

$$PDF(m, Z) = p(m)q'(Z|m) \quad (4.12)$$

is used instead. In these cases, $q'(Z|m)$ is obtained from the Monte Carlo prediction for the particle species content in each mass bin.

4.6.2 Fake- D background

In this category, the D candidate does not represent a properly reconstructed D meson of the stated type. These events include both true combinatorial background (where tracks may come from both B 's or the underlying event) and also partially reconstructed or reflected single- B decays that are very broad in their D candidate mass distribution. In all samples apart from the $D^* X$, fake- D events constitute the larger of the two background components. In the $D^* X$ case, the very low background level allows us to treat the fake- D and real- D background (see below) as one unit; the $D^+ X$ fake- D background model is used as the sole background model in the $D^* X$ fit.

Both the mass and Z PDFs for this component are measured in the data using the D sidebands. Possible real- D “leakage” into the D sidebands and contamination from localized single- B modes are removed.

Mass templates

For the $D^+ X$ control sample and the $D^0[K^-\pi^+]X$ and $D^0[\pi^-\pi^+]X$ signal samples, the fake- D mass template is modeled using the sum of a falling exponential function and a constant term,

$$p_{\text{bg}}(m) = k_1 \exp(-\alpha m) + k_2 \beta, \quad (4.13)$$

where the normalization constants k_1 and k_2 are functions of the shape parameters α and β and the fit range limits m_{min} and m_{max} .

To properly determine the shape parameters α and β , an auxiliary mass fit is employed to remove real- D contamination from the D sidebands. To wit, an extra fit with the following components is performed in the $m(B)$ histogram obtained from events in the D sidebands: (1) a fake- D component of the form Eq. (4.13) and (2) a component representing poorly reconstructed real D 's, *i.e.*, genuine D candidates far in the tails of the mass distribution. The shape (but not the normalization) of this real- D part is a histogram taken from the D sidebands in Monte Carlo.

In the $D^0[K^-K^+]X$ signal sample, the shape given by Eq. (4.13) does not adequately describe the sideband data, and a contamination-subtracted histogram is used instead.

Z templates

The normalization of the real- D contamination in the D sidebands is already given by the auxiliary fit described above. Additionally, the Z distribution of this contamination can be constructed by using (a) the particle species fractions predicted for the D sidebands by semi-inclusive Monte Carlo, and (b) the templates for each of these particle species obtained using the method described in Section 4.7. We therefore have a model for both the size and shape of the Z distribution of the real- D contamination.

To obtain the Z template for the fake- D component, we begin with the Z histogram of B daughter tracks in the D sideband. From this histogram, we may then subtract out the real- D contamination (modeled above) to obtain our fake- D Z template.

It should be noted that we observe a non-negligible mass dependence of the fake- D background Z template thus acquired. We interpret this mass dependence to be due to the partially reconstructed B decays present in the region below the B mass. Therefore, we have elected to construct two Z templates for this component, one for the B mass region above 5.40 GeV, and one for the region below.

4.6.3 Real- D combinatorial background

In this case, the D candidate is a properly reconstructed D meson of the stated type. However, the D and the extra track attached to it do not have as their common source a single B meson. Instead of coming from the B meson that produces the D meson, the track may come from the other B meson or elsewhere in the event. Alternately, the D meson may simply not have a B meson as its antecedent.

This is the smaller of the two background components for the D^+X sample and all three of the D^0X samples. We assume that this background is universal for all the control and signal samples; we use a sample of “wrong-sign” D^+X^+ events (sideband-subtracted in the D mass) as a proxy sample to model this background. The wrong-sign candidates are selected with the same cuts as the right-sign candidates.

Mass template

We begin with the $D\pi$ mass histogram of wrong-sign D^+X^+ candidates and perform a sideband subtraction in the D^+ mass. A two-parameter curve is then fit to the sideband-subtracted histogram. The curve determined in this fit is used as the mass template of the real- D background in the main fit.

For the D^+X control sample, the two-parameter curve used in this wrong-sign D^+X^+ auxiliary fit is again a curve of the form found in Eq. (4.13).

For the D^0X signal samples, however, the wrong-sign D^+X^+ sample is given a somewhat more sophisticated treatment. Please see the real- D background section in Section 6.2.1 for more details.

Z template

The Z template is obtained by directly using the Z histogram of the wrong sign data in the D peak region. Due to the low statistics of the wrong-sign sample, no sideband subtraction is performed.

As with the fake- D background, we have elected to split this Z template into two, one for the B mass region above 5.40 GeV, and one for the region below.

4.7 Z templates for pions and kaons

Here we summarize the method by which we obtain our pion and kaon templates. A full exposition may be found in Appendix A.

The success of our analysis depends, in great part, on our ability to separate the Cabibbo-suppressed $B^- \rightarrow D^0K^-$ decay from processes that give pions as the B daughter track, the most important of which is the Cabibbo-allowed (and therefore much larger) $B^- \rightarrow D^0\pi^-$ decay. Since the D^0K and $D^0\pi$ modes partially overlap in their mass distributions, the use of a particle identification variable such as dE/dx (or equivalently, Z) is necessary. At CDF, the Z distributions for kaons and pions in the COT (under a fixed particle hypothesis) have significant overlap. (See Figure 6.1 for an example.) This means that the Z variable has limited power to separate kaons from pions. It is therefore of great import that we use Z templates of sufficient accuracy lest we incur large systematic uncertainties on our measurements.

At CDF, there are two levels of offline dE/dx corrections. The first level consists of hit-level corrections [72] performed in the standard reconstruction. A number of effects related to the geometry, electronics, and operating conditions of the COT are accounted for at this level.

A second level of corrections [73] is provided by the CDF B group in the form of a software macro. These track-level dE/dx corrections include those that depend on track ϕ and η , the number of hits on a track, and run number. A universal curve parameterized as a function of track $\beta\gamma = p/m$ is also made available. From this curve, the predicted dE/dx for a particle track can be calculated. Since the curve depends on $\beta\gamma$, the prediction depends on the mass of the particle, or in other words, its species. It is from this macro that we obtain our Z values, defined above in Eq. (4.7), where the dE/dx prediction is always made under the pion hypothesis, regardless of the actual species of the track. The Z distributions are approximately

Gaussian in shape. For pions, we expect the distribution to be centered very close to zero.

In $D^{*+} \rightarrow D^0[K^-\pi^+]\pi_*^+$ decays, the charge of the soft pion π_*^+ from the D^* decay coincides with the charge of the pion from the D^0 decay. Thus the kaon and the pion from the D^0 decay may be unambiguously identified by noting the charge of the soft pion π_* . By performing a cut on $\Delta m \equiv m(D^*) - m(D)$ (and sideband subtraction later on), D^{*+} samples of high purity may be obtained. These D^* samples then provide clean samples of kaons and pions from D^0 decays.

For this analysis, the pion and kaon Z templates come from a large sample (almost three million tracks per species after sideband subtraction) of “prompt” D^{*+} decays, *i.e.*, D^{*+} mesons reconstructed without a minimum L_{xy} cut. The pion and kaon tracks from the D^0 mesons in this sample are subject to the same p_T and SVT matching cuts as the B daughter track of our control and signal $B \rightarrow DX$ samples.

It should be stressed that the hit-level and track-level corrections from Refs. [72] and [73] are already very good. However, it is necessary that we verify the robustness of our templates, because even small inaccuracies in determining the Z templates can potentially undermine our measurement. To this end, we compare the Z templates made from the prompt- D^* sample to those made from a second D^* sample, a sample consisting of D^* 's reconstructed in $B \rightarrow D^*X$ events. This comparison reveals sample-dependent variations in the means of the pion and kaon Z templates. These variations are typically a few percent of the overall mean K - π separation in Z .

To understand the observed variation, we have studied the dependence of pion and kaon Z values against 17 variables. It is important to note that a correlation between Z and a given variable is not in itself a cause for concern. The correlation only becomes an issue when the distributions of this variable differ sufficiently between the prompt- D^* sample (the source of our templates) and our control and signal samples (the samples to which the templates are applied, the “target samples”).

With this in mind, we have found two effects of note. The first mainly concerns the kaons: since the Z measured for the kaons is, by our definition, in the wrong mass hypothesis, a momentum dependence on the predicted dE/dx value, and therefore also on the returned Z value, is naturally induced.

A second effect is evident in both the pions and kaons. On average, we observe a significant dependence of the Z of a track on variables correlated with COT activity in the vicinity of the track. This is qualitatively explained as a by-product of hit merging algorithms present in both the COT readout and the offline reconstruction. [74] We pay special attention to two of the variables that reflect COT activity: (1) the number of tracks in the event (N_{trks}), and (2) the *secance* (s), defined as the number of $r - \phi$ intersections of the track in question with other tracks.

An additional effect, which we note in passing, is a run number dependence due to the absence, at the time of the analysis, of corrections for certain late runs.

Thus for every fit we perform on a target sample to extract branching fractions, we apply, in advance, a correction procedure on our Z templates that is specifically

tailored to the target sample in question. A summary of the procedure follows: We start with the $D^0 \rightarrow K^- \pi^+$ daughter tracks in the prompt D^{*+} sample. These already contain the hit-level corrections of Ref. [72]. The track-level corrections of Ref. [73] are then applied. A run-dependent correction is made. A two-dimensional reweighting in secance (s) and momentum (p) is performed on the templates made from the prompt D^* sample so that the secance and momentum distributions of the template tracks match those of the B daughter tracks in the target sample. A similar reweighting is performed for events in the Δm sideband. Sideband subtraction is then performed on the reweighted templates. This yields the templates we use for a given target sample.

A separate set of templates reweighted in N_{trks} and p is used only in the study of systematic uncertainties, not in any default fit.

For reasons that are only of historical interest, our reweighting procedure is in practice performed separately for subsets of our full dataset. These subsets, labeled `xbhd0d`, `xbhd0h`, and `xbhd0i`, correspond to different data taking periods. For signal or control sample fits using the full range of data, a weighted combination of the separately derived templates is used.

Some types of background channels, such as the semileptonic decays $B \rightarrow De\bar{\nu}$ and $B \rightarrow D\mu\bar{\nu}$ give an electron or a muon as the B daughter track. In the electron case, Z templates are generated using the expected dE/dx values and resolutions predicted in Ref. [73]. In the muon case, the pion Z templates are used. Since leptonic contributions in the mass region containing DK and $D\pi$ are small, we do not expect our choice of lepton Z templates to contribute significantly to the systematic uncertainty.

4.8 Efficiency corrections on the fit output

In this analysis, we are interested in measuring relative branching ratios of the form b_1/b_2 , where b_1 and b_2 could represent, for instance, $BR(B \rightarrow DK)$ and $BR(B \rightarrow D\pi)$, respectively. Our fits, however, have as their output the normalizations n_i (or fractions f_i in the non-extended case) of each fit component. Before b_1/b_2 may be quoted, we must therefore take into account the relative efficiencies and acceptances that intervene to produce the observed normalizations, n_1 and n_2 .

The n_i satisfy the following equation

$$\frac{n_1}{n_2} = \frac{b_1 \epsilon_1 \kappa_1 \eta_1}{b_2 \epsilon_2 \kappa_2 \eta_2} \quad (4.14)$$

where η represents trigger efficiency factors not modeled in the simulation (see below); ϵ accounts for all other efficiencies and acceptances, including those associated with data acquisition, detector systems, event reconstruction, and selection and analysis cuts; κ is the fraction of events of the mode in question contained inside our fit range (for the DK and $D\pi$, this factor is essentially 1).

If we generate events of both channels 1 and 2 in a single simulation job, as we have done for our semi-inclusive $B \rightarrow DX$ samples, the Monte Carlo yields y_i of the two channels after all cuts (including the mass range cuts of the fitter) will satisfy

$$\frac{y_1}{y_2} = \frac{N' b'_1 \epsilon'_1 \kappa_1}{N' b'_2 \epsilon'_2 \kappa_2}, \quad (4.15)$$

where N' is the total number of B mesons generated and b'_i represents the branching ratio used in the generation of channel i .

By solving Eqs. (4.14) and (4.15), we find

$$\frac{b_1}{b_2} = \frac{n_1 b'_1 / (y_1 \eta_1)}{n_2 b'_2 / (y_2 \eta_2)}. \quad (4.16)$$

Therefore, the relative branching fraction b_1/b_2 may be calculated from n_1/n_2 with the help of our semi-inclusive $B \rightarrow DX$ Monte Carlo samples, as long as we account for the relative efficiency η_1/η_2 not properly modeled in the simulation.

For our analysis, the factor η_1/η_2 represents a particular effect in the XFT, the track trigger system of the COT.¹⁴ Since kaons and pions have different mass, the $\beta\gamma = p/m$ for a kaon and pion of the same momentum is different. In the momentum range of our B daughter tracks ($p_T > 2$ GeV), pions on average deposit more charge than kaons. Since a certain number of hits per axial layer is required in the XFT trigger, pions have a higher trigger efficiency relative to kaons. This effect is not well modeled in the simulation. A study of this effect has been performed in [75] and an XFT efficiency function has been provided to us by the authors. This function parameterizes the XFT efficiency according to run number, p_T , and particle species. A systematic uncertainty on the parameterization is also provided. For each fit, we use the XFT efficiency function and the appropriate $B \rightarrow DX$ Monte Carlo sample to determine the relative trigger efficiency η_π/η_K and its uncertainty.

4.9 Toy Monte Carlo validation of the fitter

We validate the fitter by generating toy Monte Carlo experiments and inspecting the bias and pull distributions¹⁵ of either the n_j returned by the fit or selected ratios of the n_j . For a well-behaved fitter, we expect to see pull distributions with means consistent with zero and widths consistent with one.

For the purpose of generating toy Monte Carlo experiments, we choose the “true” value of n_j , the size of the j th component, to be \hat{n}_j , the value returned for that component in the actual data fit. To generate a particular pseudo-experiment, we

¹⁴See Section 3.2.2 for a description of the XFT.

¹⁵The “pull” for a quantity x is defined as $(x_{\text{out}} - x_{\text{in}})/\sigma_x$, where x_{in} is the input, or “true”, value of x , x_{out} the value of x returned by the fitter, and σ_x the returned error on x .

then perform \tilde{n}_j extractions on the mass and Z PDFs for each fit component j , where \tilde{n}_j is a Poisson-distributed random variable with \hat{n}_j as its mean. After a pseudo-experiment is generated, a standard fit is performed. After a predetermined number of pseudo-experiments, we plot the pull distributions of the normalizations or ratios of normalizations returned by the fitter. We then perform Gaussian fits on these distributions to extract their means and widths.

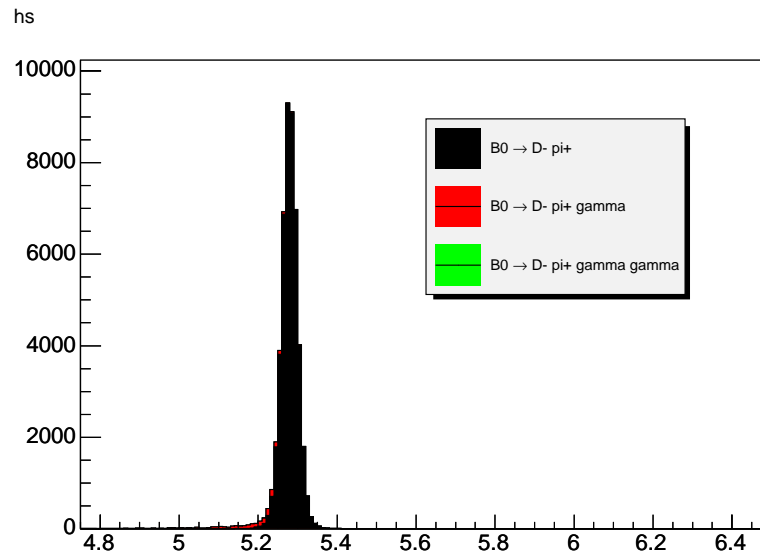


Figure 4.1: Decay mode content of the $\overline{B}^0 \rightarrow D^+ \pi^- (n\gamma)$ Monte Carlo sample reconstructed as $D^+ \pi^-$.

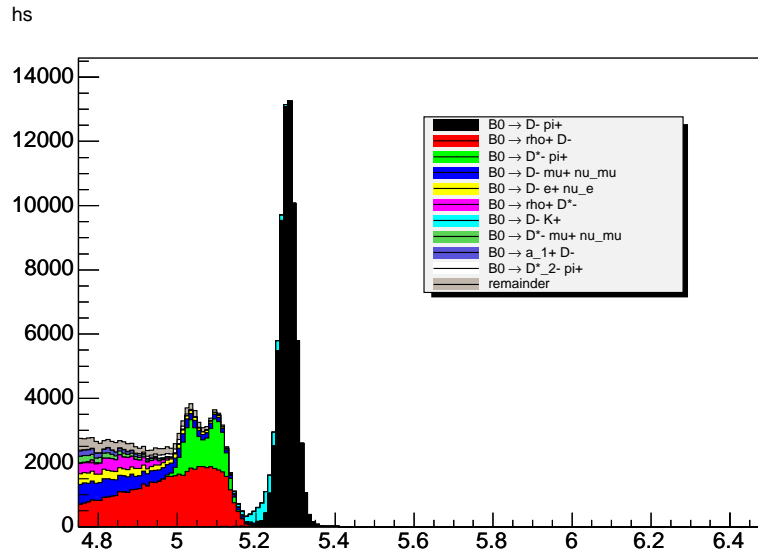


Figure 4.2: Decay mode content of the semi-inclusive $\bar{B}^0/B^0 \rightarrow D^+ X$ Monte Carlo sample reconstructed as $D^+ \pi^-$.

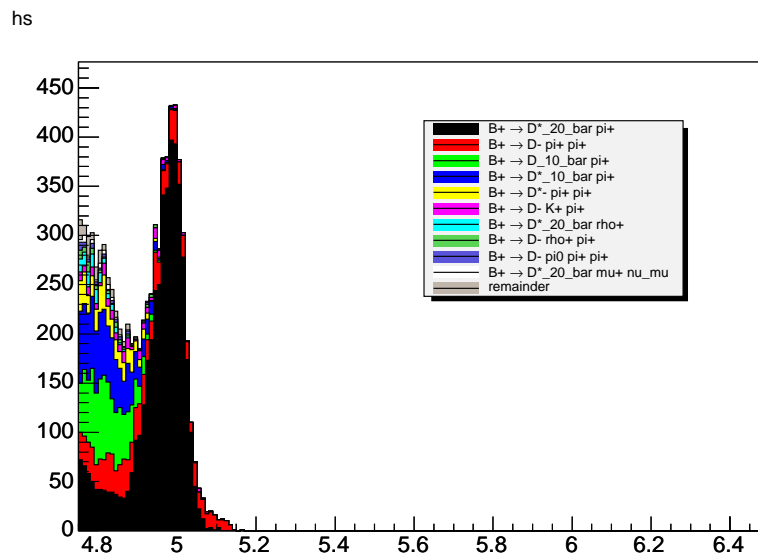


Figure 4.3: Decay mode content of the semi-inclusive $B^\pm \rightarrow D^+ X$ Monte Carlo sample reconstructed as $D^+ \pi^-$.

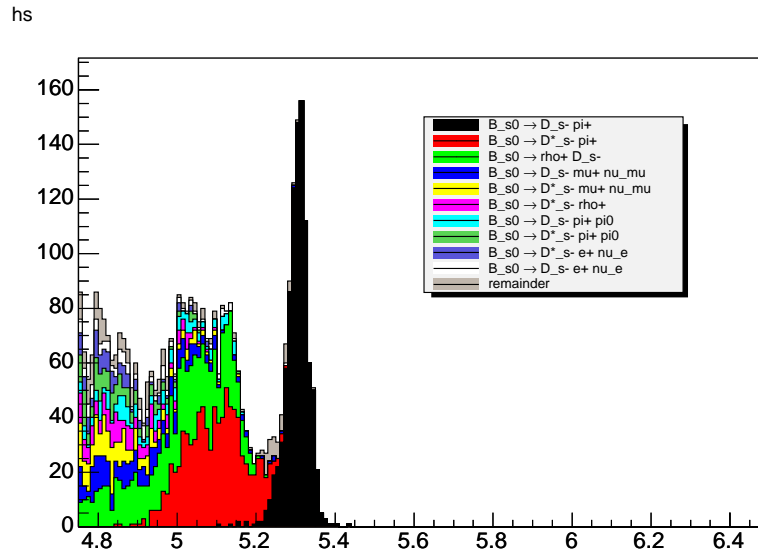


Figure 4.4: Decay mode content of the semi-inclusive $B_s \rightarrow D_s[\phi\pi]X$ Monte Carlo sample reconstructed as $D^+\pi^-$.

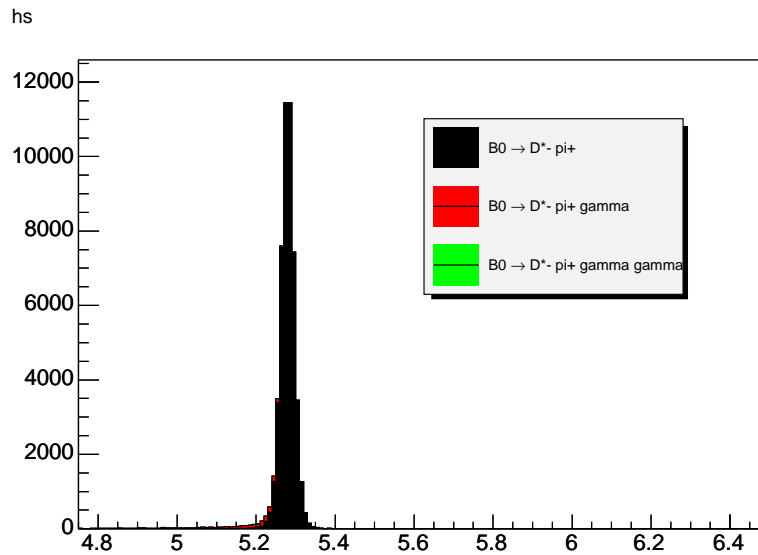


Figure 4.5: Decay mode content of the $\bar{B}^0 \rightarrow D^{*+}\pi^-(n\gamma)$ Monte Carlo sample reconstructed as $D^{*+}\pi^-$.

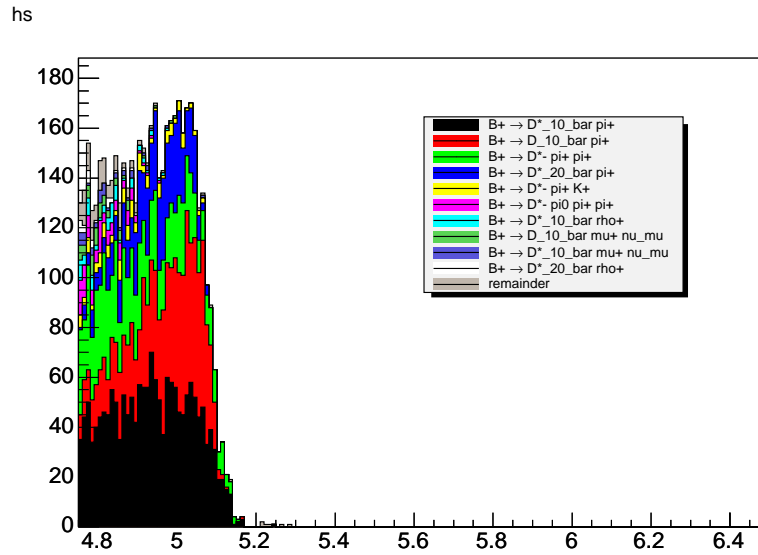


Figure 4.6: Decay mode content of the semi-inclusive $B^\pm \rightarrow D^0 X$ Monte Carlo sample reconstructed as $D^{*+}\pi^-$.

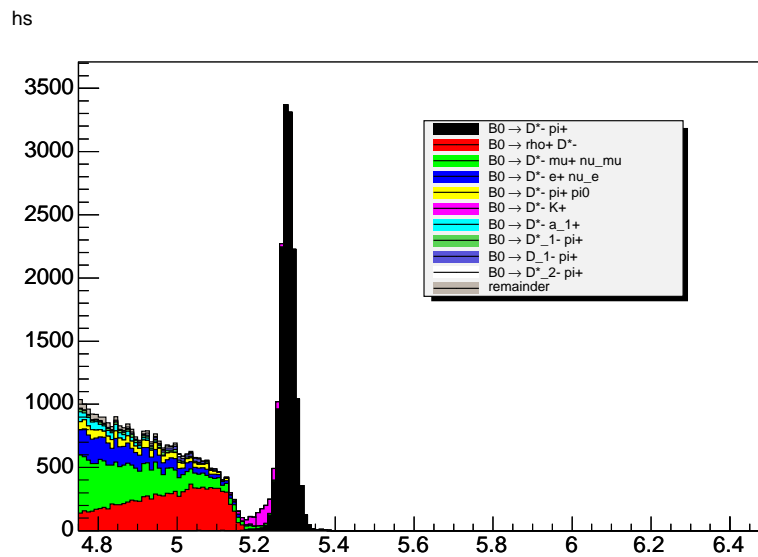


Figure 4.7: Decay mode content of the $\bar{B}^0/B^0 \rightarrow D^0 X$ Monte Carlo sample reconstructed as $\bar{B}^0 \rightarrow D^{*+}\pi^-$.

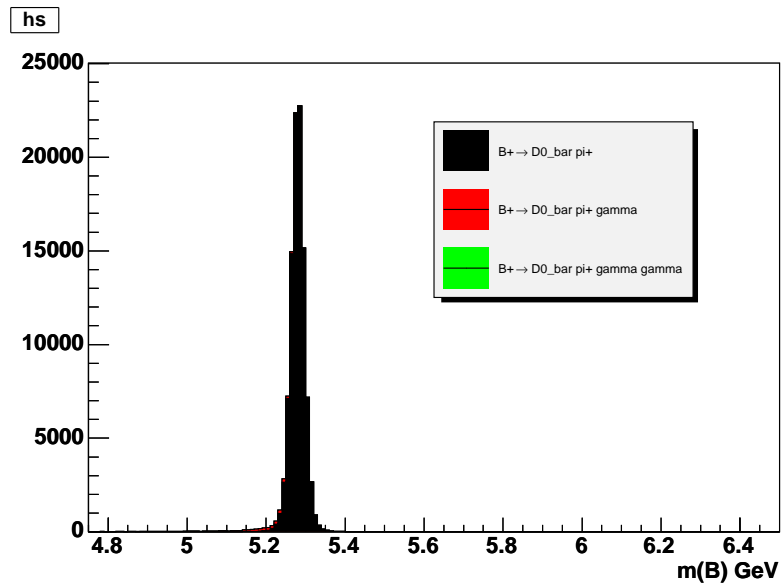


Figure 4.8: Decay mode content of the $B^- \rightarrow D^0[K^-\pi^+]\pi^- (n\gamma)$ Monte Carlo sample reconstructed as $D^0[K^-\pi^+]\pi^-$.

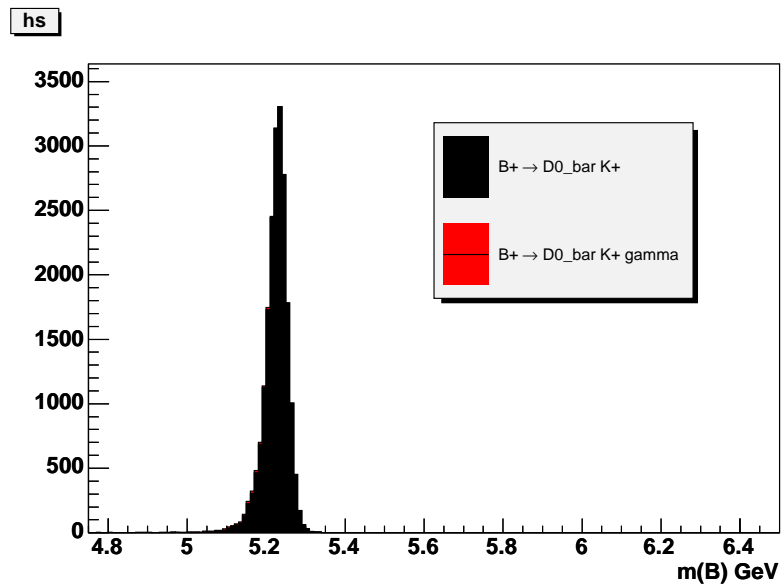


Figure 4.9: Decay mode content of the $B^- \rightarrow D^0[K^-\pi^+]K^- (n\gamma)$ Monte Carlo sample reconstructed as $D^0[K^-\pi^+]\pi^-$.

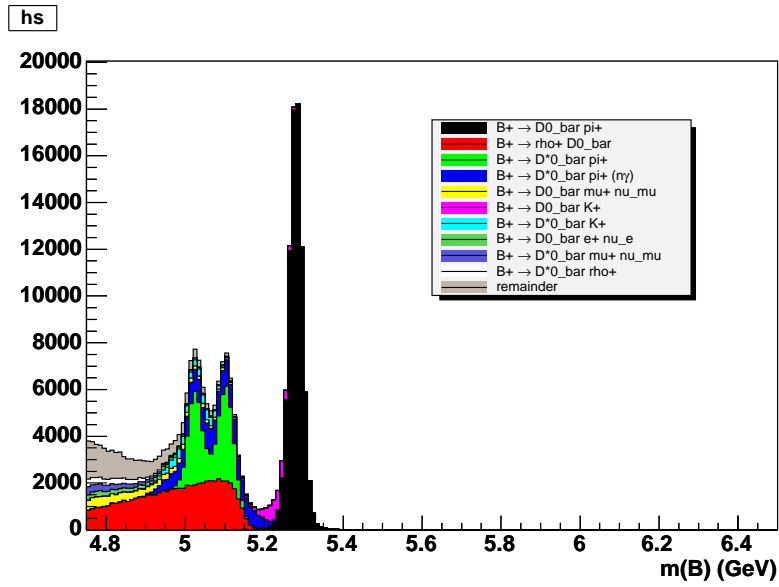


Figure 4.10: Decay mode content of the semi-inclusive $B^\pm \rightarrow D^0[K^-\pi^+]X$ Monte Carlo sample reconstructed as $D^0[K^-\pi^+]\pi^-$.

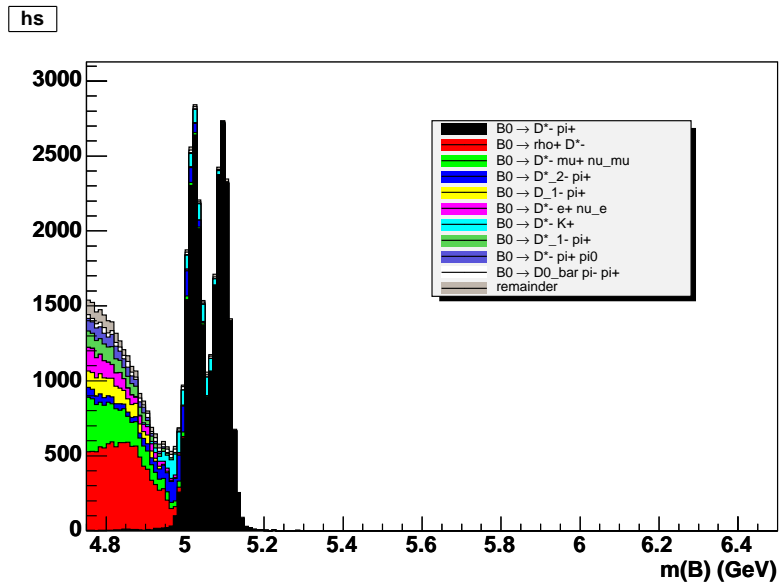


Figure 4.11: Decay mode content of the semi-inclusive $B^0/\bar{B}^0 \rightarrow D^0[K^-\pi^+]X$ Monte Carlo sample reconstructed as $D^0[K^-\pi^+]\pi^-$.

Chapter 5

Control Samples

In this chapter, we seek to demonstrate the validity of our fit technique by applying our fitter to two control samples, the D^+X^- sample and the $D^{*+}X^-$ sample. The specifics of each fit, the fit results, and comparisons with published measurements are given.

The text is adapted mainly from our CDF Note, CDF 8705 [58], and to a lesser extent from two of our other CDF Notes, CDF 8777 [59] and CDF 8716 [60]. The figures and tables in this chapter are also from Ref. [58].

5.1 D^+X^- fits

The first and more complicated of the two control samples is the D^+X^- sample. We present the specifics of the fit configuration and the fit results. Systematic uncertainties are also assessed. Finally, we compare the results to world averages.

5.1.1 Fit configuration

The main D^+X^- fit is an extended maximum likelihood fit in two dimensions. No D mass constraint is used during the B vertex fit. (See discussion of fake- D templates below.) The fit range in mass is $m(B) \in [4.85, 6.45]$ GeV. The fit configuration is summarized in the top portion of Table 5.1. See Figure 5.1 for the mass template histograms used in the D^+X^- fits. An example of the Z template histograms used can be found in Figure 5.2.

Single- B templates

Please refer to Section 4.6.1 for a general discussion.

- **Mass component.** The mass templates for the single- B modes are histograms obtained either from dedicated $\overline{B}^0 \rightarrow D^+\pi^-(n\gamma)$ and $\overline{B}^0 \rightarrow D^+K^-$ Monte Carlo

samples or the semi-inclusive $B \rightarrow D^+ X$ Monte Carlo samples. As described in Section 4.3, a mass scale factor of 1.00025 and a Gaussian resolution smearing of 6.43 MeV are applied to the histograms. These are determined from studies performed on the $D^* X$ data sample.

In Table 5.1, the mass templates for the single- B modes are marked as “MC” in the Mass PDF column. The catch-all “remainder” template encompasses most of the partially reconstructed $B \rightarrow D^+ X$ modes. The $D^+ \rho^-$ and $D^{*+} \pi^-$ are separated out, since their high mass tails extend into the $D^+ K$ mass region; their normalizations are allowed to float.

The treatment of the remainder template here is less elegant than in the signal samples. As a result, modes of significant size that would contribute non-pion B daughters to the remainder template are explicitly separated out. There are two such groups of modes: the $D^{(*)} K^{(*)}$ modes contribute kaons and the semileptonic $D^{(*)} e X$ modes contribute electrons; their normalizations are fixed to the remainder $\overline{B}^0/B^- \rightarrow D^+ X$ template according to Monte Carlo predictions. The $BR(B^- \rightarrow D_2^* \pi^-)$ mode is also isolated and fixed relative to the remainder template to take advantage of a measurement of its branching ratio Ref. [76] not used in our original decay table.

To account for the reflection of $D_s^+ X^-$ events into to our $D^+ X^-$ sample, we also include a $B_s \rightarrow D_s^- [\phi \pi^-] X$ template in the fit.

For a summary of how the various fit components are normalized, please see the column labeled “normalization” in Table 5.1.

- **Z component.** The Z template sources for the single- B modes are summarized in the Z PDF column of Table 5.1.

The largest group of templates consists of those marked “prompt D^* ”. These are the K and π templates obtained from a large prompt D^* sample using the procedure described in Section 4.7 and Appendix A. To summarize, the hit-level (Ref. [72]) and track-level (Ref. [73]) corrections have already been applied. Two-dimensional reweighting in secance (s) and momentum (p) is performed. The reweighted templates are sideband-subtracted in the $D^* \Delta m$ variable.

The electron template required by the semileptonic $D^{(*)} e X$ modes is generated from the parametric simulation described at the end of Section 4.7.

The $B_s \rightarrow D_s^- X$ Z template uses the pion, kaon, electron, and muon fractions predicted in the $B_s \rightarrow D_s^- X$ Monte Carlo sample. The templates for the individual species are again as described in Section 4.7. There are, in fact, four Z templates for this fit component, one for each of the following B mass regions: the region of partially reconstructed B 's ($m(B) \in [4.85, 5.17]$ GeV); the $D^+ K^-$ region ($m(B) \in [5.17, 5.26]$ GeV); the $D^+ \pi^-$ region ($m(B) \in [5.26, 5.4]$ GeV); and the high mass region ($m(B) \in [5.4, 6.45]$ GeV).

The fake- D template

Please refer to Section 4.6.2 for a general discussion.

- **Mass component.** To obtain the shape parameters for the fake- D mass template, the auxiliary mass fit described in Section 4.6.2 is performed on events taken from the sidebands of the D^+ mass peak. The fit determines the shape parameters of the fake- D mass template while taking into account real- D contamination in the sidebands. The D^+ sidebands are given by $m(D^+) \in [1.825, 1.84] \cup [1.9, 1.915]$ GeV. Figure 5.3 shows the result of this fit. The shape parameters obtained in this auxiliary fit are then used to fix the parameters for the fake- D template in the main fit. In the main fit, the normalization of the fake- D component is allowed to float.

Since we expect Monte Carlo simulation to model D^+X events in the D^+ mass peak region better than in the tails of the D^+ distribution, the auxiliary fit described here is performed on B candidates that are not fit with a D^+ mass constraint.

The relative normalization of fake and real D determined in the auxiliary fit mentioned above can also be determined independently in a binned fit performed directly on the D^+ mass histogram, as shown in Figure 5.4. The D^+ mass histogram is modeled as two Gaussian distributions, representing the D^+ mass peak, on top of a linear background. The relative normalization obtained in this fit is used only for the purpose of assessing systematic uncertainties in Section 5.1.5.

- **Z component.** We obtain the Z templates for the fake- D^+ component by performing the subtraction of real- D^+ contamination described in Section 4.6.2. As mentioned before, there are two templates, one for the mass region above 5.40 GeV, and one for the region below.

The real- D background template

Please refer to Section 4.6.3 for a general discussion.

- **Mass component.** As described in Section 4.6.3, the real- D background mass template is obtained from a fit on sideband-subtracted wrong-sign D^+X^+ candidates. The fit is shown in Figure 5.5.

The fit function is of the form described in Eq. (4.13). The shape parameters obtained from this auxiliary fit are used in the main D^+X^- fit. The normalization of the template is allowed to float in the main fit. As described in Section 6.2.1, a different fit strategy is used for the signal D^0X^- samples.

- **Z component.** As described in Section 4.6.3, the Z templates for the real- D^+ component are taken directly from the wrong-sign D^+X^+ data sample. There are two templates, one for the mass region above 5.40 GeV, and one for the region below.

5.1.2 Results

We have performed the D^+X^- fit separately for the three subsamples `xbhd0d`, `xbhd0h`, and `xbhd0i`. A fourth D^+X^- fit is performed on the full 1.2 fb^{-1} sample. For each subsample, separate fake- D and real- D auxiliary fits are performed. Z templates are also produced separately for each subsample. To avoid repetition, we will only show the histograms for the fit on the full 1.2 fb^{-1} data sample. A summary of the values of $BR(\bar{B}^0 \rightarrow D^+\pi^-)/BR(\bar{B}^0 \rightarrow D^+\pi^-)$ measured in the three subsamples and in the full sample is given in Table 5.4. Correlations between the fit parameters have been taken into account. For the D^+X^- sample, the XFT relative efficiency η_π/η_K is found to be 1.0499 ± 0.0281 .

The output of the D^+X^- likelihood fits is given in the top section of Table 5.2. The correlation coefficients are given in Table 5.3. The mass projection is shown in Figure 5.6. The Z projections are shown in Figure 5.7.

5.1.3 Toy Monte Carlo validation of the fitter

The procedure for validating the fitter using toy Monte Carlo is described in Section 4.9. An average of 46498 events are generated for each of 10000 pseudo-experiments. Gaussian fits of the pull distributions of the parameters are shown in Figure 5.9. A summary of the pull means and widths extracted from the Gaussian fits can be found in Table 5.5. Likelihood scans for the D^+X^- fit components can be found in Figure 5.8.

5.1.4 Discussion of the fit residuals in Z

The Z projection of our fit results (see Figure 5.7) is presented in four separate mass regions. Of the four, the DK region ($m(B) \in [5.17, 5.26]$ GeV; upper-right plot) and the $D\pi$ region ($m(B) \in [5.26, 5.40]$ GeV; lower-left plot) GeV are of special importance to us, since the DK and $D\pi$ are the objects of our analysis. In the residual histograms under each projection, one particular feature in the $D\pi$ region (lower-left plot) stands out: the excess in the Z residuals between $Z = -0.2$ and -0.1 .

To study the Z -residual excess, we have examined the average Z of the B daughter track as a function of $m(B)$, and have found lower-than-expected values (for pure pions the average Z should be zero) in the $D\pi$ region. This suggested an excess of kaons or protons centered at 5.28 GeV underneath the large $D\pi$ peak.

Using our Monte Carlo samples, we have studied and ruled out a number of possible sources: the two processes $\Lambda_b \rightarrow D^- p$ and non-resonant $\Lambda_b \rightarrow [pK^- \pi^+] K^-$ do not appear to be large enough; the $D_s^+ K^-$ and $\Lambda_c K^-$ reflections do not lie in the right $m(B) \equiv m_{D^+ \pi}$ range; an insufficient amount of $\Lambda_b \rightarrow \Lambda_c [p\pi^+ \pi^-] K^-$ survives the $m(D^+)$ mass cut; neither does the auto-reflection of the $\bar{B}^0 \rightarrow D^+ \pi^-$, in which the K^- from the D^+ and the B pion are confused, pass the D^+ mass cut at high enough a rate.

The track parameters of the tracks that contribute to the excess in the Z residuals are not meaningfully different from the other tracks in the same mass region. A dependence of the track secance on $m(B)$ has also been ruled out as an explanation.

No firm conclusions can be drawn from the comparison of the $D^+ X^-$ fit to the $D^{*+} X^-$ fit, due to the smaller sample size of the this latter sample. We have extracted the excess in Z itself (rather than the excess in the Z residuals, which is measured in units of σ) and added it to the pion template in the $D^{*+} X^-$ fit. The fit quality in Z for the region of concern ($m(B) \in [5.26, 5.40]$) is subsequently degraded, but not to a disastrous extent: the χ^2 changes from 12.6 to 24.0 for 21 degrees of freedom. In Section 5.1.5, we use this excess in Z to assess a systematic uncertainty.

For the $D^0 X$ signal fits (see Chapter 6), we consider the possibility that the excess reflects a shift in the pion Z template.

5.1.5 Systematic uncertainties

Here we present the studies used in determining the systematic uncertainties on the ratio $BR(\bar{B}^0 \rightarrow D^+ K^-)/BR(\bar{B}^0 \rightarrow D^+ \pi^-)$. A summary of the results can be found in Table 5.6.

Background mass shape

As described in Section 5.1.1, the default background model consists of two parts, a fake- D and a real- D component. The shapes of the two components are determined separately in two auxiliary fits. In the main fit, their normalizations float.

There are many possible alternative background models. We will restrict ourselves to physically well-motivated models that do not destabilize the fit by introducing an excessive number of parameters. One such model has already been suggested. In our discussion of the fake- D mass template configuration (see Section 5.1.1), we described a method of independently determining the fake- D background normalization. The method involved performing a binned auxiliary fit in the D^+ mass histogram. (See Figure 5.3.) In an alternate version of our main fit, we fix the fake- D normalization to the value determined in such a manner. The two shape parameters of the real- D background, in addition to its normalization, are then allowed to float in the main fit.

To obtain the systematic uncertainty associated with our choice of background mass shape, we first fit the data with our alternate model. With all the fit parameters in the alternate fit thus fixed, we generate pseudo-experiments according to the alternate model and fit them with the default model. Averaged over all the fits on the pseudo-experiments, the difference in the $DK/D\pi$ relative branching ratio between the output and input values is -0.17% . We quote this value as the systematic uncertainty.

Monte Carlo mass scale and resolution

As mentioned in Section 4.3, studies on the $D^*\pi$ mass peak suggest a mass scale factor of 1.000236 ± 0.000020 and a Gaussian resolution smearing of $\sigma = 4.61 \pm 0.33$ MeV for our Monte Carlo mass templates.

The systematic uncertainty associated with the quoted error on the scale factor is obtained by generating two sets of pseudo-experiments; the scale factor is varied by $+1\sigma$ in one set and -1σ in the other. The difference between the output and input $DK/D\pi$ relative branching ratios is recorded for each pseudo-experiment and the average difference is calculated for each of the two sets. This average difference is not symmetric with respect to the $\pm 1\sigma$ variations of the scale factor. We take the greater of the two differences to be the systematic uncertainty.

The systematic uncertainty due to the quoted errors on the resolution smearing is determined in an analogous manner.

dE/dx (Z) templates

We consider four sources of systematic uncertainties related to the determination of Z templates:

1. **Reweighting method for prompt D^* templates.** As described in Section 4.7, we perform a two-dimensional reweighting in secance and momentum on the Z templates obtained from the prompt D^* sample.

The secance variable is chosen over the N_{trks} variable, because the former is expected to be more sensitive to the hit density in the vicinity of the track. We nevertheless consider N_{trks} to be a reasonable variable to reweight in, even though it describes activity in the entire COT.

Therefore, as an alternate model to the default Z templates reweighted in secance- p , we consider templates reweighted in $N_{\text{trks}}-p$. The pseudo-experiments are generated with the latter and fit with the former. The difference between the output and input $DK/D\pi$ values, averaged over all pseudo-experiments, is -0.31% . This value is used as the systematic uncertainty associated with the reweighting method.

2. **Excess in Z residuals.** In Section 5.1.4, we noted an excess in the Z residual histogram for the $D^+\pi^-$ -dominated mass region, $m(B) \in [5.26, 5.4]$ GeV. An alternate model is developed by taking the difference between the Z data and the fit projection in the $D^+\pi^-$ mass region and adding it to our standard prompt- D^* pion template. These modified templates are used for the $D^+\pi^-$ and $D^+\pi^-(n\gamma)$ modes in an alternate fit model. We generate pseudo-experiments using the alternate model and fit them with the default model. The average difference between the output and the input values for the $DK/D\pi$ ratio is -0.45% . This value is taken to be the systematic uncertainty associated with the observed excess in the Z residuals.
3. **Species composition of the $D_s X$ template.** Since many of the decay modes in the $B_s \rightarrow D_s X$ Monte Carlo sample have branching ratios that are either unknown or poorly measured in data, the species composition of the $B_s \rightarrow D_s X$ Z template is a source of systematic uncertainties. We determine the size of this uncertainty by halving the kaon content of the $B_s \rightarrow D_s X$ Z templates in an alternate fit model; this change is large enough to cover the uncertainty in the $B_s \rightarrow D_s^\pm K^\mp$ branching ratio. The systematic uncertainty is again obtained by generating and fitting pseudo-experiments with different fit models.
4. **Z template for fake- D background.** As discussed in Sections 4.6.2 and 5.1.1, the fake- D Z templates are obtained by removing real- D contamination from the D -sideband Z histograms. In an alternate fit model, this subtraction is not performed. The systematic uncertainty is obtained by generating pseudo-experiments with the alternate fit model and fitting with the default.

5.1.6 Comparison with world averages

A comparison of our results with world averages is shown in Table 5.4. The PDG value for $BR(\bar{B}^0 \rightarrow D^+ K^-)$ is from a single Belle measurement [77]. In the table, we compare our results to the value of $BR(\bar{B}^0 \rightarrow D^+ K^-)/BR(\bar{B}^0 \rightarrow D^+ \pi^-)$ measured directly in Ref. [77]. In this reference, the $D^+ K^-$ yield is found to be 33.7 ± 7.3 events. Without taking into account our systematic uncertainties, the discrepancy between our result and the Belle measurement is $\sim 1.4\sigma$. The discrepancy is reduced to $\sim 1.3\sigma$ when our systematic uncertainties are included.

5.2 $D^{*+} X^-$ fits

The second of our control samples is the $D^{*+} X^-$ sample. In this section, we describe the $D^{*+} X^-$ fit configuration. The fit results are presented and compared to world averages. Compared to the $D^+ X^-$ sample, the $D^{*+} X^-$ sample is smaller and has significantly less background. Consequently, we expect the statistical uncertainty

to be the dominant uncertainty in the $D^{*+}X^-$ sample. The exercise of assessing systematic uncertainties is therefore omitted.

5.2.1 Fit configuration

The main $D^{*+}X^-$ fit is a non-extended maximum likelihood fit in two dimensions. The $D^*\pi$ mass is obtained from a vertex fit with a D^0 mass constraint applied. As in the D^+X^- fit, the fit range in mass is $m(B) \in [4.85, 6.45]$ GeV. The fit configuration is summarized in the bottom portion of Table 5.1.

A general discussion of the fit components and their templates can be found in Section 4.6. See Figure 5.10 for the mass template histograms used in the $D^{*+}X^-$ fits. An example of the Z template histograms used can be found in Figure 5.11.

Single- B templates

The mass templates for the single- B modes are histograms obtained either from dedicated $\bar{B}^0 \rightarrow D^{*+}\pi^-(n\gamma)$ and $\bar{B}^0 \rightarrow D^{*+}K^-$ Monte Carlo samples or the semi-inclusive $B \rightarrow D^0X$ Monte Carlo samples. We use the same mass scale factor and resolution smearing as in the D^+X^- fits.

The $D^{*+}\rho^-$ is the only partially reconstructed mode separated out from the “remainder” $D^{*+}X$ template.

As before, all corrections (see Section 4.7), including those at the hit and track levels, along with reweighting and sideband subtraction, have been applied to the templates marked “prompt D^* ” in Table 5.1. These prompt- D^* templates supply the Z templates for all single- B modes except in the case of the “remainder” $D^{*+}X$ component. The Z template for the $D^{*+}X$ remainder is obtained from the parametric simulation described in Section 4.7.

Combinatorial background templates

In contrast with our other samples, the $D^{*+}X^-$ sample contains a very low level of combinatorial background. This prevents us from effectively separating the background into fake and real- D components. Even when we treat the background as a single component, it is very difficult to extract the background shape from the $D^{*+}X^-$ sample in a meaningful way. Instead we use the fake- D background shape in the D^+X^- as the background shape for the $D^{*+}X^-$ sample. The Z template for the background is taken from the Z histogram of the D^+ sidebands. As would be expected for a sample of high purity, the fit results are insensitive to the details of the background templates.

In a non-extended maximum likelihood fit such as our $D^{*+}X^-$ fit, the fit fractions must sum to one. This means that there must be one fit fraction that is not an independent parameter in the fit, even though it corresponds to a fit component

with a floating normalization. In the $D^{*+}X^-$ fit, this component is chosen to be the combinatorial background.

5.2.2 Results

As in the case of the D^+X^- fit, we have performed the $D^{*+}X^-$ fit separately for the three subsamples `xbhd0d`, `xbhd0h`, and `xbhd0i`. A fourth $D^{*+}X^-$ fit is performed on the full 1.2 fb^{-1} sample. The Z templates are produced separately for each subsample. As before, we show only the histograms for the fit on the full 1.2 fb^{-1} data sample. A summary of the values of $BR(\overline{B}^0 \rightarrow D^{*+}\pi^-)/BR(\overline{B}^0 \rightarrow D^{*+}\pi^-)$ measured in the three subsamples and in the full sample is given in the bottom portion of Table 5.4. Correlations between the fit parameters have been taken into account. The XFT relative efficiency has also been included.

The output of the $D^{*+}X^-$ likelihood fit for the full 1.2 fb^{-1} is given in the bottom section of Table 5.2. The correlation coefficients are shown in Table 5.7. The mass projection is shown in Figure 5.12. The Z projections are shown in Figure 5.13.

5.2.3 Toy Monte Carlo validation of the fitter

The procedure for validating the fitter is as described in Section 4.9, with a few necessary concessions to the non-extended nature of the $D^{*+}X^-$ maximum likelihood fit. The number of events generated for component j in a given pseudo-experiment is a Poisson-distributed variable \tilde{n}_j with a mean value of $\hat{N}\hat{f}_j$, where \hat{N} is the total number of candidates in data and \hat{f}_j the fit fraction returned in the fit on the actual data. As mentioned in Section 5.2.1, the background fraction is given by $f_b = 1 - \sum_{j=1}^{M-1} f_j$, where M is the number of components with a floating normalization. Its uncertainty is calculated by straightforward error propagation: $\sigma_b^2 = \sum_{j,k}^{M-1} \sigma_{jk}$.

An average of 9664 events are generated for each of 10000 pseudo-experiments. Gaussian fits to the pull distributions are shown in Figure 5.15. A summary of the pull means and widths extracted from Gaussian fits can be found in Table 5.8. Likelihood scans for the $D^{*+}X^-$ fit components can be found in Figure 5.14.

5.2.4 Comparison with world averages

A comparison of our results with world averages is shown in Table 5.4. The PDG value for $BR(\overline{B}^0 \rightarrow D^{*+}K^-)$ is from a single BaBar measurement [78]. In the table, we quote the value of $BR(\overline{B}^0 \rightarrow D^{*+}K^-)/BR(\overline{B}^0 \rightarrow D^{*+}\pi^-)$ measured directly in Ref. [78]. Our measurement is in good agreement with this value.

Fit component	Mass PDF	Z PDF	normalization
D^+X^- fits			
$\overline{B}^0 \rightarrow D^+\pi^-$	MC	prompt $D^* \rightarrow \pi, s : p$ reweight	floating
$\overline{B}^0 \rightarrow D^+\pi^-(n\gamma)$	MC	prompt $D^* \rightarrow \pi, s : p$ reweight	floating
$\overline{B}^0 \rightarrow D^+K^-$	MC	prompt $D^* \rightarrow K, s : p$ reweight	floating
$\overline{B}^0 \rightarrow D^+\rho^-$	MC	prompt $D^* \rightarrow \pi, s : p$ reweight	floating
$\overline{B}^0 \rightarrow D^{*+}\pi^-$	MC	prompt $D^* \rightarrow \pi, s : p$ reweight	floating
$D_2^*\pi^-$	MC	prompt $D^* \rightarrow \pi, s : p$ reweight	fixed to $\overline{B}^0/B^- \rightarrow D^+X$
$D^{(*)}K^{(*)}$	MC	prompt $D^* \rightarrow K, s : p$ reweight	fixed to $\overline{B}^0/B^- \rightarrow D^+X$
$D^{(*)}eX$	MC	parametric e simulation	fixed to $\overline{B}^0/B^- \rightarrow D^+X$
$\overline{B}^0/B^- \rightarrow D^+X$	MC	prompt $D^* \rightarrow \pi, s : p$ reweight	floating
$\overline{B}_s^0 \rightarrow D_s^+X$	MC	species fractions from MC	floating
$D^+(\text{sb})$ (fake- D bg)	D SB	D SB, signal-subtracted	floating; shape fixed
D^+X^+ (real- D bg)	WS (SBS)	WS (D signal region)	floating; shape fixed
$D^{*+}X^-$ fits			
$D^{*+}\pi^-$	MC	prompt $D^* \rightarrow \pi, s : p$ reweight	floating
$D^{*+}K^-$	MC	prompt $D^* \rightarrow K, s : p$ reweight	floating
$D^{*+}\rho^-$	MC	prompt $D^* \rightarrow \pi, s : p$ reweight	floating
$D^{*+}\pi^-(n\gamma)$	MC	prompt $D^* \rightarrow \pi, s : p$ reweight	floating
remainder ($D^{*+}X$)	MC	parametric simulation	floating
combinatorial bg	D^+ SB	D^+ SB	floating; shape fixed

Table 5.1: Fit components of the D^+X^- and $D^{*+}X^-$ fits. See text for an explanation of the “Mass PDF” and “Z PDF” columns.

Fit component	par no	Fit result			
		xbhd0d	xbhd0h	xbhd0i	full sample
D^+X^- fits					
$\bar{B}^0 \rightarrow D^+\pi^-$	2	4130.0 \pm 81.2	5085.5 \pm 89.6	4128.2 \pm 80.8	13336.0 \pm 145.4
$\bar{B}^0 \rightarrow D^+\pi^-(n\gamma)$	3	256.5 \pm 67.0	231.5 \pm 72.7	287.7 \pm 68.3	734.5 \pm 119.8
$\bar{B}^0 \rightarrow D^+K^-$	4	334.5 \pm 31.0	526.4 \pm 36.5	361.6 \pm 31.8	1230.0 \pm 57.6
$\bar{B}^0 \rightarrow D^+\rho^-$	5	2314.4 \pm 290.2	4083.6 \pm 321.6	2680.7 \pm 286.9	8799.9 \pm 519.2
$\bar{B}^0 \rightarrow D^{*+}\pi^-$	6	1406.3 \pm 137.9	1302.4 \pm 153.8	1331.0 \pm 138.0	4118.4 \pm 248.5
$D_2^*\pi^-$	7		fixed to $\bar{B}^0/B^- \rightarrow D^+X$		
$D^{(*)}K^{(*)}$	8		fixed to $\bar{B}^0/B^- \rightarrow D^+X$		
$D^{(*)}eX$	9		fixed to $\bar{B}^0/B^- \rightarrow D^+X$		
$\bar{B}^0/B^- \rightarrow D^+X$	10	2471.1 \pm 165.6	2434.4 \pm 183.1	2300.9 \pm 165.3	7262.7 \pm 296.6
$\bar{B}_s^0 \rightarrow D_s^+X$	11	715.9 \pm 179.7	808.4 \pm 194.5	644.8 \pm 176.8	2156.9 \pm 318.6
D^+ (sb) (fake- D bg)	12	2376.1 \pm 168.5	2855.9 \pm 176.1	2105.2 \pm 236.6	7361.2 \pm 321.4
D^+X^+ (real- D bg)	13	333.3 \pm 70.4	497.1 \pm 79.4	494.9 \pm 150.8	1498.5 \pm 180.1
$D^{*+}X^-$ fits					
$D^{*+}\pi^-$	2	0.342 \pm 0.009	0.367 \pm 0.008	0.367 \pm 0.009	0.359 \pm 0.005
$D^{*+}K^-$	3	0.035 \pm 0.005	0.028 \pm 0.004	0.032 \pm 0.004	0.032 \pm 0.003
$D^{*+}\rho^-$	4	0.299 \pm 0.021	0.287 \pm 0.018	0.283 \pm 0.020	0.287 \pm 0.011
$D^{*+}\pi^-(n\gamma)$	5	0.030 \pm 0.009	0.024 \pm 0.008	0.025 \pm 0.009	0.026 \pm 0.005
remainder ($D^{*+}X$)	6	0.250 \pm 0.020	0.255 \pm 0.017	0.260 \pm 0.019	0.257 \pm 0.011
combinatorial bg			fixed to $1 - \sum_i f_i$		

Table 5.2: Fit parameters returned in the D^+X^- and $D^{*+}X^-$ fits.

Parameter	Correlation coefficients											
	global	2	3	4	5	6	10	11	12	13		
2	0.52875	1.000	0.008	-0.014	0.157	0.015	0.025	-0.491	0.045	-0.024		
3	0.59392	0.008	1.000	-0.341	-0.012	0.013	0.095	-0.254	-0.180	0.101		
4	0.41565	-0.014	-0.341	1.000	0.051	-0.003	0.005	-0.016	-0.071	0.039		
5	0.95049	0.157	-0.012	0.051	1.000	-0.823	-0.768	-0.253	-0.054	0.022		
6	0.88356	0.015	0.013	-0.003	-0.823	1.000	0.659	-0.046	0.039	-0.009		
10	0.87800	0.025	0.095	0.005	-0.768	0.659	1.000	-0.037	-0.152	0.046		
11	0.83216	-0.491	-0.254	-0.016	-0.253	-0.046	-0.037	1.000	-0.244	0.129		
12	0.87826	0.045	-0.180	-0.071	-0.054	0.039	-0.152	-0.244	1.000	-0.767		
13	0.80764	-0.024	0.101	0.039	0.022	-0.009	0.046	0.129	-0.767	1.000		

Table 5.3: Correlation coefficients for the $D^+ X^-$ fit on the full sample.

	$D^+K^-/D^+\pi^-$ (%)	$D^+\rho^-/D^+\pi^-$	$D^{*+}\pi^-/D^+\pi^-$
world avg.	6.80 ± 1.66	2.21 ± 0.68	0.81 ± 0.22
xbhd0d	$8.03 \pm 0.81 \pm 0.22$ (0.66 σ)	2.10 ± 0.26 (-0.15 σ)	1.21 ± 0.13 (1.56 σ)
xbhd0h	$10.43 \pm 0.81 \pm 0.28$ (1.95 σ)	3.05 ± 0.25 (1.17 σ)	0.93 ± 0.11 (0.46 σ)
xbhd0i	$8.62 \pm 0.82 \pm 0.23$ (0.98 σ)	2.41 ± 0.26 (0.29 σ)	1.14 ± 0.12 (1.29 σ)
comb	$9.21 \pm 0.47 \pm 0.25$ (1.38 σ)	2.49 ± 0.15 (0.40 σ)	1.11 ± 0.07 (1.26 σ)
	$D^{*+}K^-/D^{*+}\pi^-$ (%)	$D^{*+}\rho^-/D^{*+}\pi^-$	
world avg.	7.76 ± 0.45	2.46 ± 0.38	
xbhd0d	$9.59 \pm 1.49 \pm 0.26$ (1.16 σ)	3.37 ± 0.31 (1.86 σ)	
xbhd0h	$7.39 \pm 1.11 \pm 0.20$ (-0.31 σ)	3.08 ± 0.25 (1.37 σ)	
xbhd0i	$8.39 \pm 1.27 \pm 0.22$ (0.46 σ)	3.02 ± 0.27 (1.21 σ)	
comb	$8.39 \pm 0.73 \pm 0.22$ (0.71 σ)	3.13 ± 0.16 (1.62 σ)	

Table 5.4: Comparison of D^+X^- and $D^{*+}X^-$ fit results with ratios derived from world averages. The results are corrected for relative kinematic and XFT efficiencies. For the $DK/D\pi$ ratio, the first uncertainty is statistical and the second is from the XFT relative efficiency correction. The numbers in parentheses indicate the deviation from the world average value.

Channels	Pull mean (%)	Pull width ($\% \sigma$)
$B^0 \rightarrow D^- \pi^+$	-2.194 ± 1.006	99.631 ± 0.729
$B^0 \rightarrow D^- \pi^+(n\gamma)$	-0.726 ± 1.001	99.500 ± 0.716
$B^0 \rightarrow D^- K^+$	-1.450 ± 1.004	99.887 ± 0.713
$B^0 \rightarrow D^- \rho^+$	-1.406 ± 1.027	102.151 ± 0.730
$B^0 \rightarrow D^{*-} \pi^+$	1.101 ± 1.026	101.983 ± 0.734
$B^0/B^+ \rightarrow D^- X$	0.825 ± 1.024	101.908 ± 0.724
$B_s \rightarrow D_s X$	0.753 ± 1.012	100.605 ± 0.721
$D^-(sb)$	-0.847 ± 1.022	101.772 ± 0.725
$D^- X^-$	-1.340 ± 1.025	101.809 ± 0.734

Table 5.5: Pull means and widths for the $D^+ X^-$ fit components.

Effect	$D^+ K^- / D^+ \pi^-$ (fit - generated) (%)
Background mass shape	-0.17
Monte Carlo mass scale (mean- 1σ)	0.15
Monte Carlo mass resolution(mean+ 1σ)	0.16
Z template reweighting method	-0.31
Excess in Z residuals	-0.45
Composition of the $D_s X$ Z template	0.16
Fake- D Z template	-0.30
Sum in quadrature	0.70

Table 5.6: Systematic uncertainties on the ratio $BR(\bar{B}^0 \rightarrow D^+ K^-) / BR(\bar{B}^0 \rightarrow D^+ \pi^-)$

Parameter	Correlation coefficients					
	global	2	3	4	5	6
2	0.72894	1.000	-0.103	-0.134	0.204	-0.173
3	0.55815	-0.103	1.000	0.038	0.400	-0.035
4	0.92648	-0.134	0.038	1.000	0.199	-0.829
5	0.72548	-0.204	-0.400	-0.199	1.000	0.002
6	0.92304	-0.173	-0.035	-0.829	0.002	1.000

Table 5.7: Correlation coefficients for the $D^{*+} X^-$ fit on the full sample.

Channels	Pull mean (%)	Pull width (%)
$D^{*+}\pi^{-}$	0.121 ± 1.015	100.638 ± 0.742
$D^{*+}K^{-}$	-5.114 ± 1.003	100.187 ± 0.713
$D^{*+}\rho^{-}$	-0.704 ± 1.005	100.472 ± 0.712
$D^{*+}\pi^{-}(n\gamma)$	-0.880 ± 1.011	100.989 ± 0.718
remainder	0.011 ± 1.003	100.258 ± 0.710
combinatorial background	-4.995 ± 1.003	100.130 ± 0.715

Table 5.8: Pull means and widths for the $D^{*+}X^{-}$ fit components.

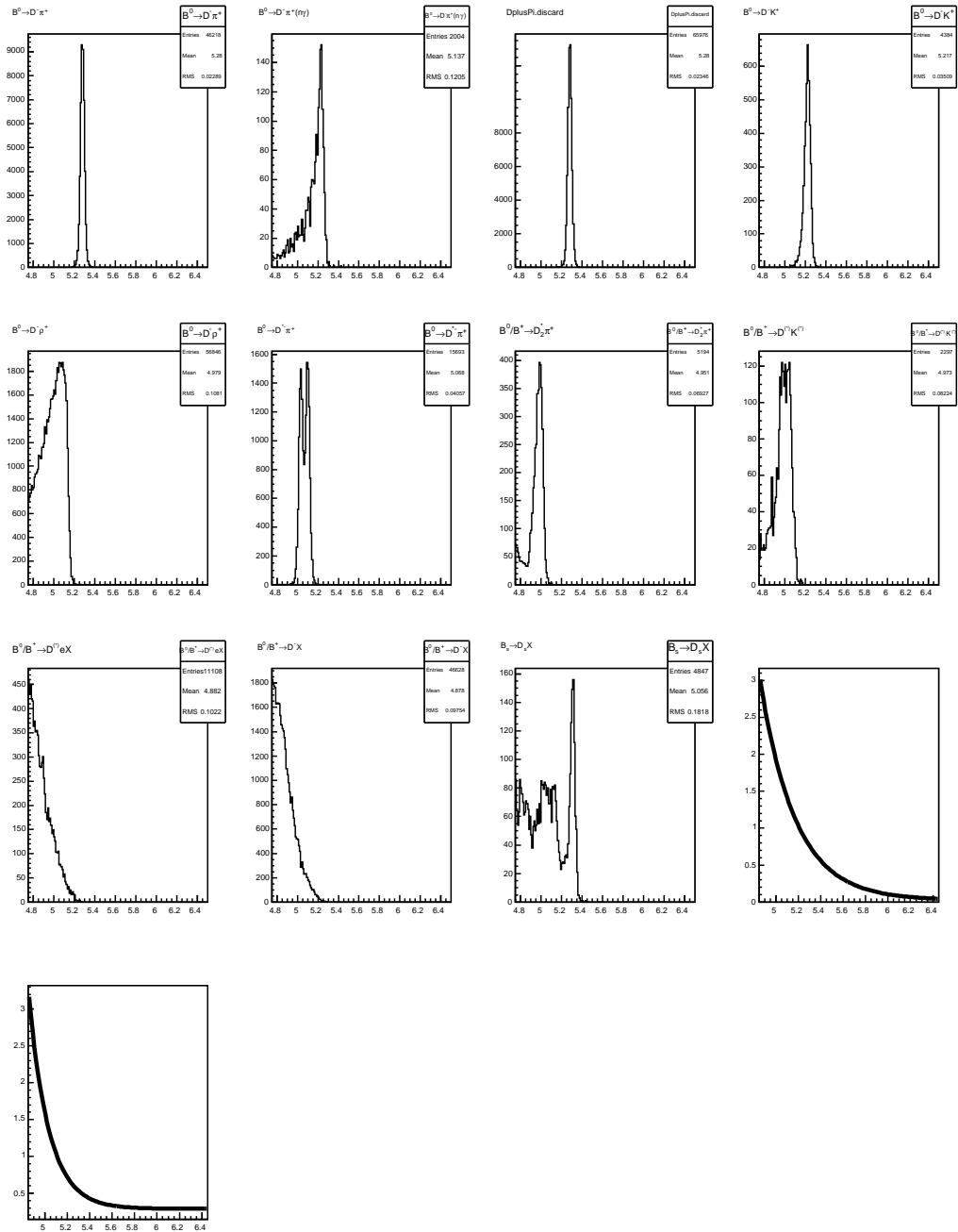


Figure 5.1: Mass templates used for the D^+X^- fit components. The histogram marked “DplusPi.discard” (third histogram, top row), which is from the semi-inclusive $B \rightarrow D^+X$ Monte Carlo sample, is used not as a fit template, but only for the purpose of determining the $D^+K^-/D^+\pi^-$ relative yield; in the actual fit, the template from the dedicated $\bar{B}^0 \rightarrow D^+\pi^-(n\gamma)$ Monte Carlo is used in its stead.

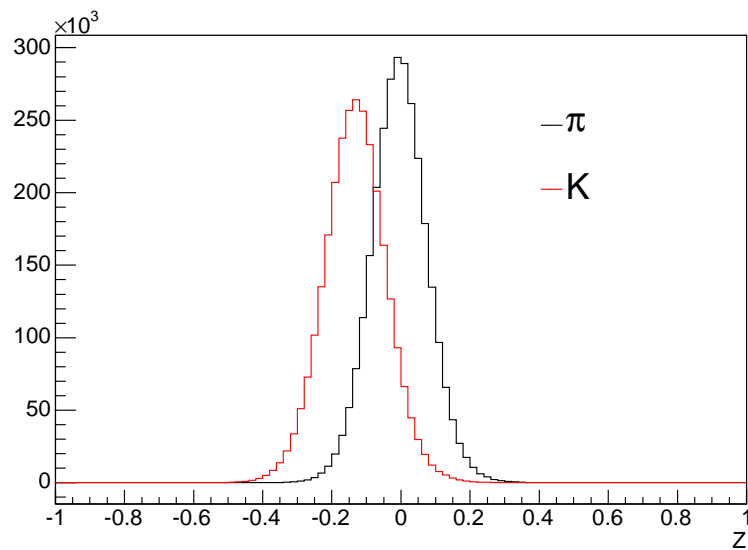


Figure 5.2: Pion and kaon Z template histograms for the D^+X^- fit (full sample). These are obtained from the prompt D^* sample and reweighted simultaneously in secance and p to the D^+X^- distributions.

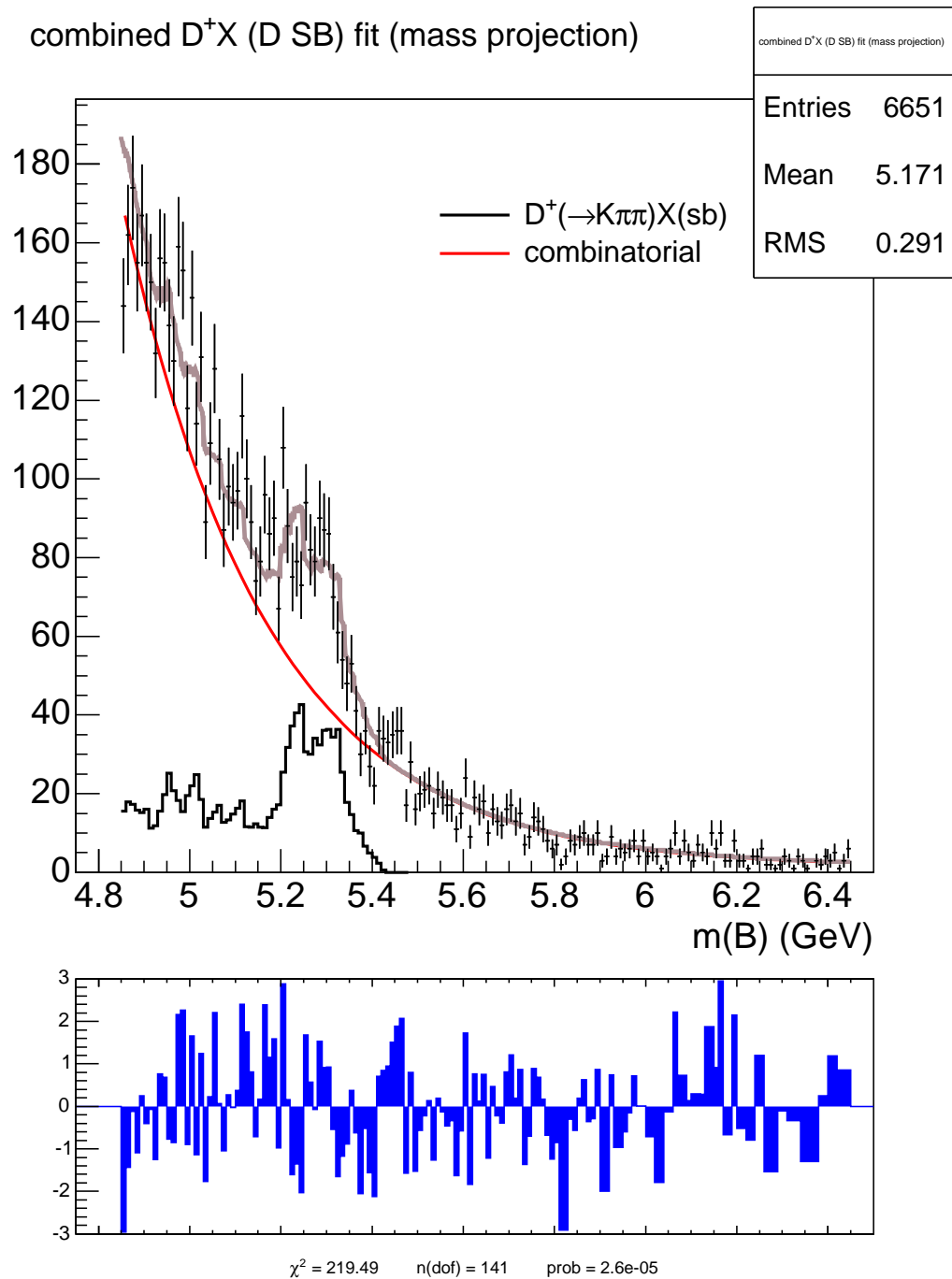


Figure 5.3: Auxiliary D^+ -sideband fit for the full D^+X^- sample. The smaller histogram shows the fit residuals, defined as the excess of the data points over the fit, expressed in units of σ . For the purpose of calculating residuals, neighboring bins are combined until at least 5 events are expected.

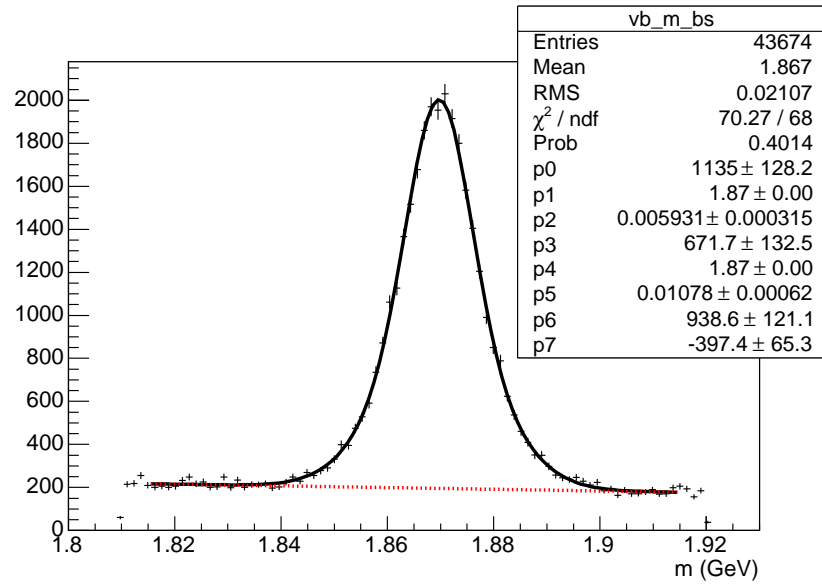


Figure 5.4: D^+ mass fit for fake- D background normalization study (full sample). This fit is used only for assessing systematic uncertainties.

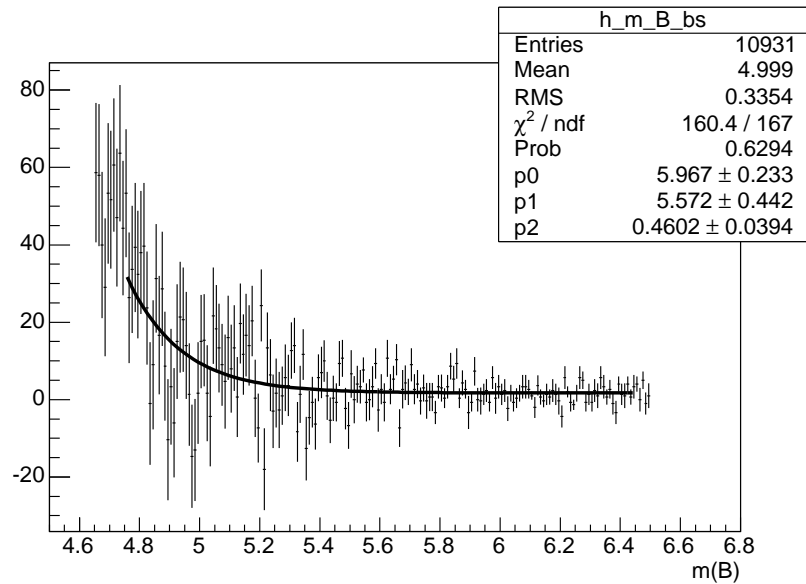


Figure 5.5: Real- D^+ background template fit in wrong sign $D^+ X^+$ (full sample).

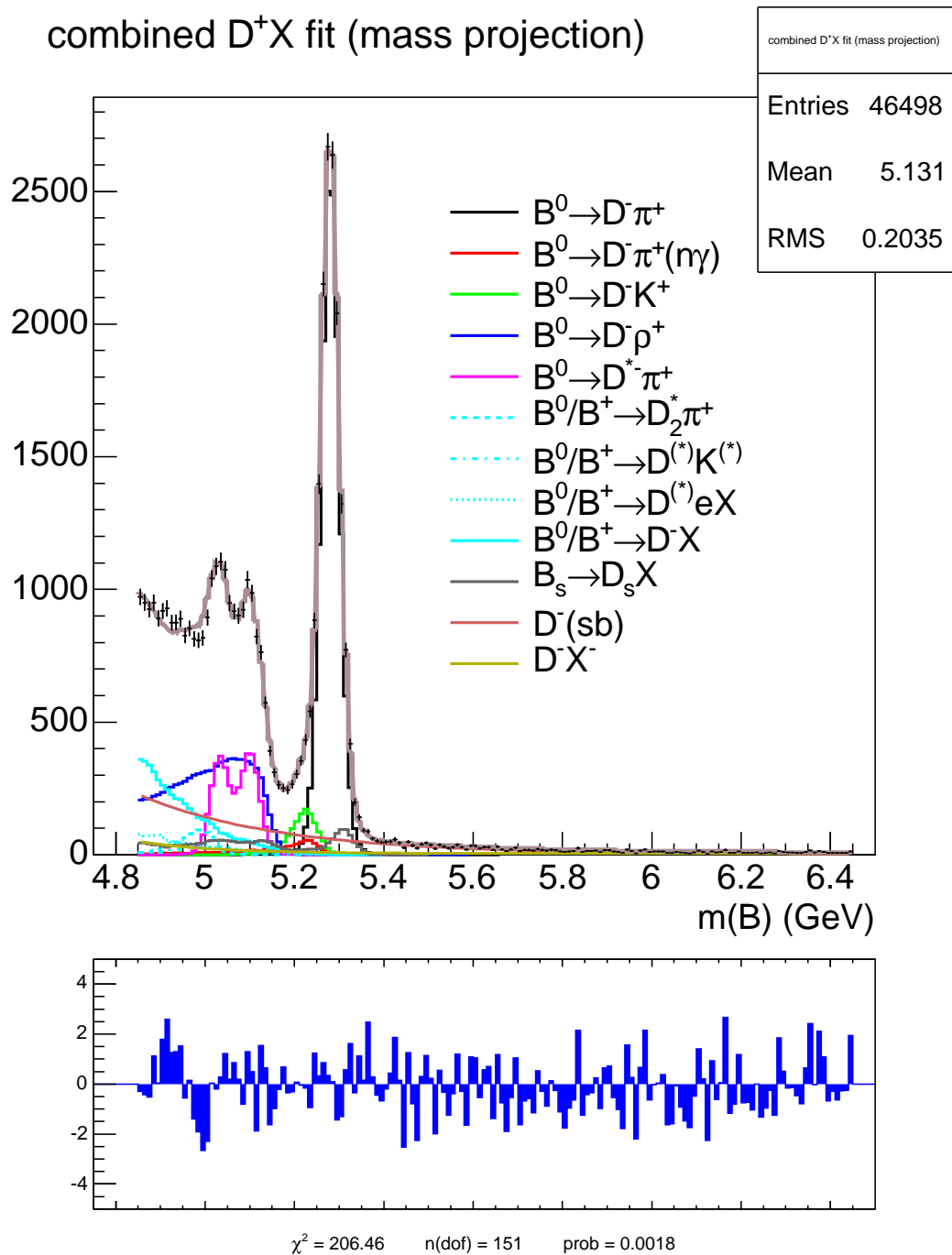


Figure 5.6: Mass projection of the fit on the full D^+X^- sample. The smaller histogram shows the fit residuals, defined as the excess of the data points over the fit, expressed in units of σ . For the purpose of calculating residuals, neighboring bins are combined until at least 5 events are expected.

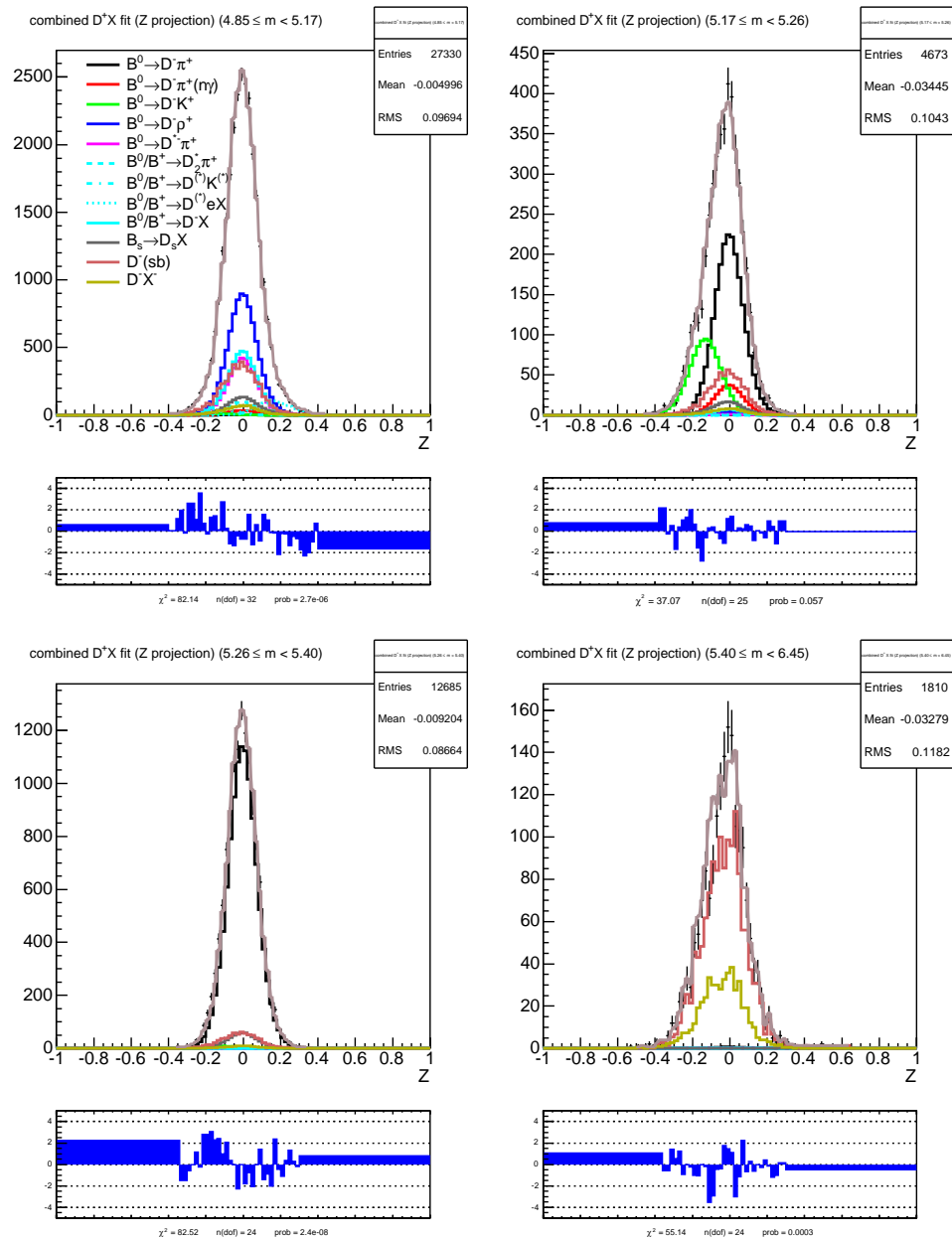
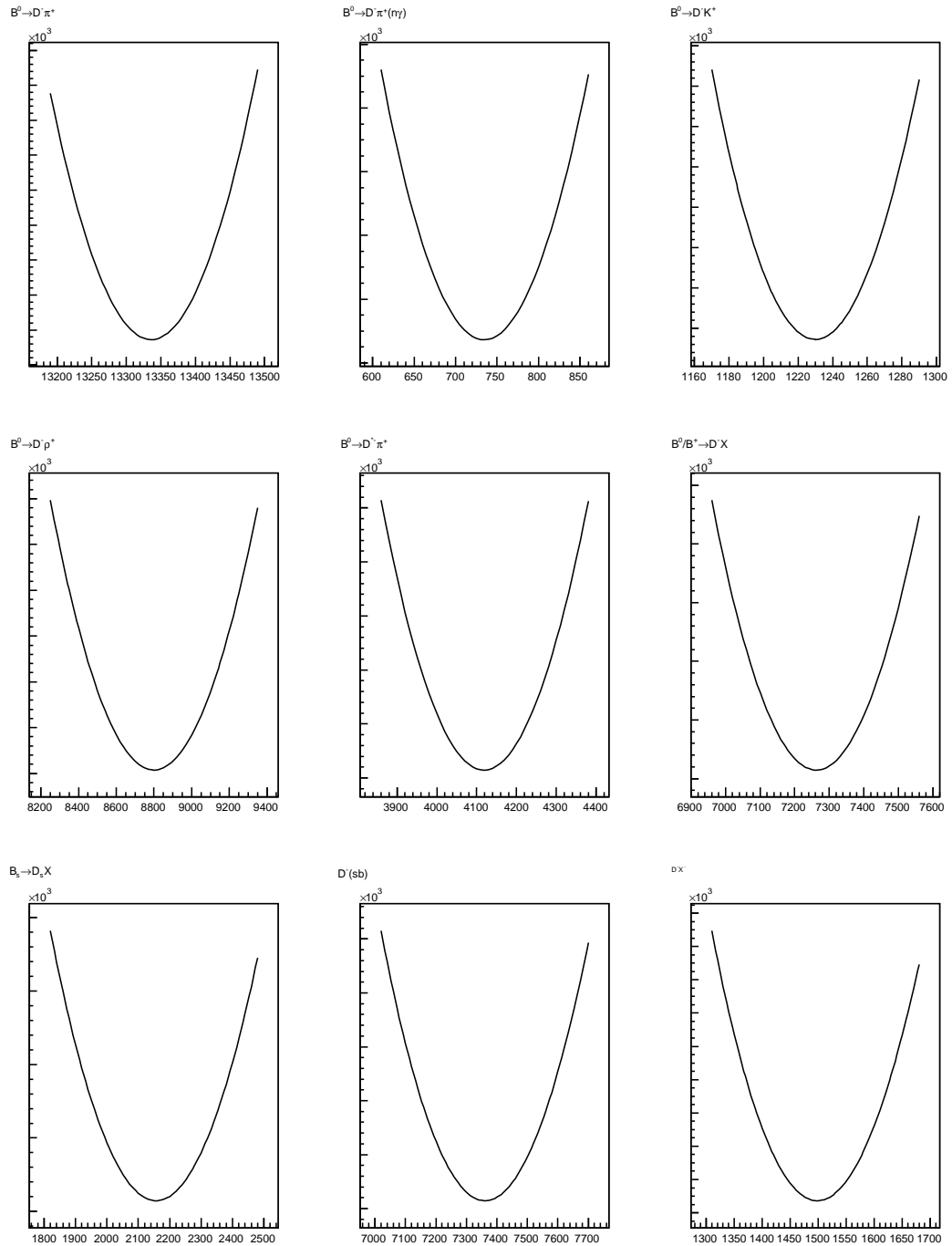
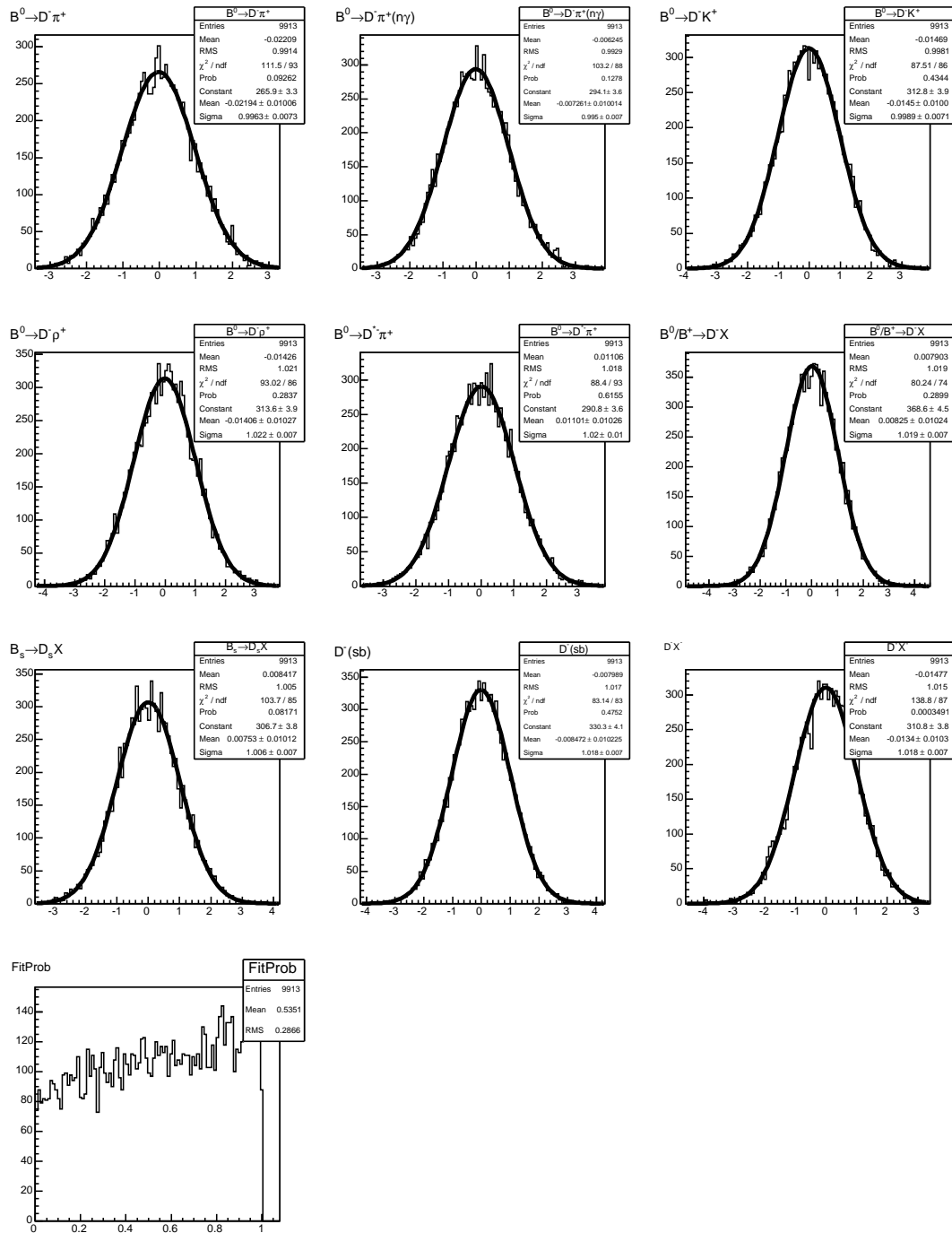


Figure 5.7: Z projections of the fit on the full D^+X^- sample. The Z projections are shown in four B mass regions:

upper-left [4.85, 5.17] GeV upper-right [5.17, 5.26] GeV
lower-left [5.26, 5.40] GeV lower-right [5.40, 6.45] GeV

The pion-dominated region is shown in the lower-left plot. The smaller histograms show the fit residuals.

Figure 5.8: Likelihood scans for the D^+X^- fit components.

Figure 5.9: Pull distributions for the $D^+ X^-$ fit components.

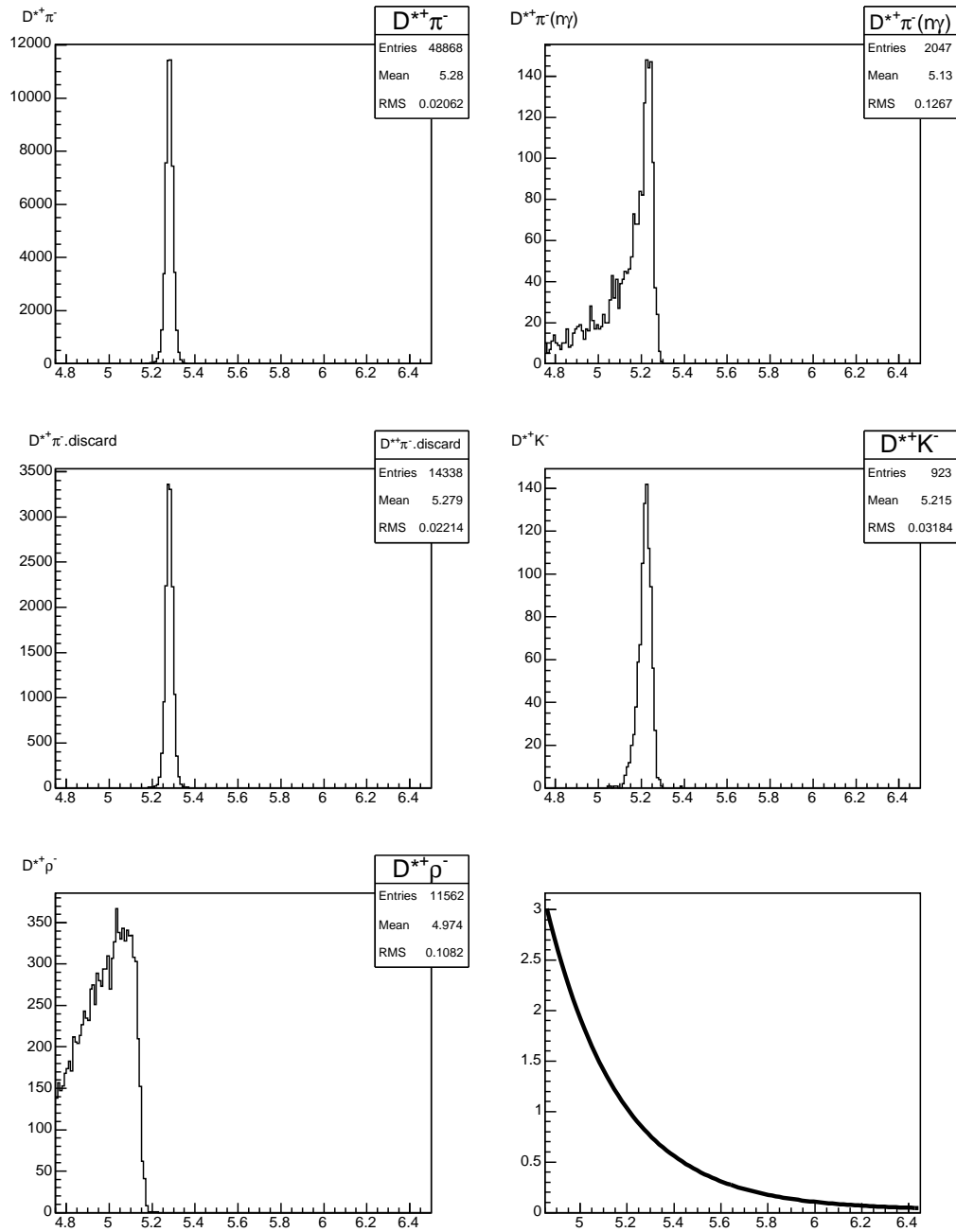


Figure 5.10: Mass templates used for the $D^{*+}X^-$ fit components. The histogram marked “ $D^{*+}\pi^-.discard$ ” (first histogram, middle row), which is from the semi-inclusive $B \rightarrow D^0X$ Monte Carlo sample, is used not as a fit template, but only for the purpose of determining the $D^{*+}K^-/D^{*+}\pi^-$ relative yield; in the actual fit, the template from the dedicated $\bar{B}^0 \rightarrow D^{*+}\pi^-(n\gamma)$ Monte Carlo is used in its stead.

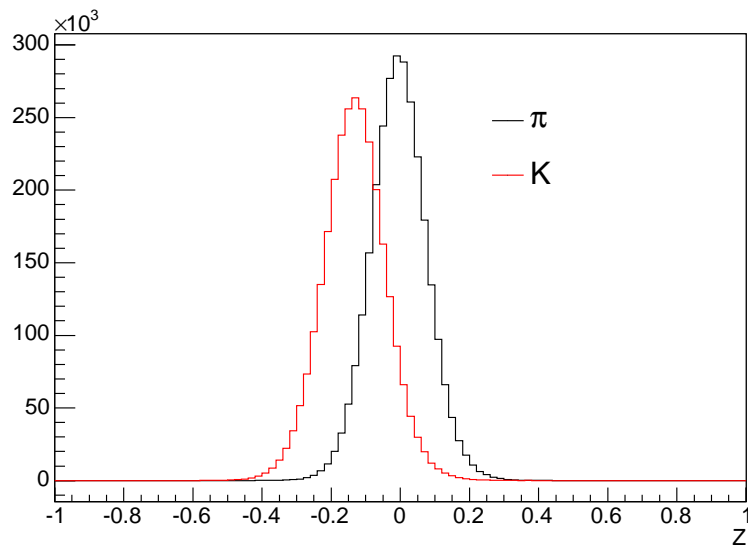


Figure 5.11: Pion and kaon Z template histograms for the $D^{*+}X^-$ fit (full sample). These are obtained from the prompt D^* sample and reweighted simultaneously in secance and p to the $D^{*+}X^-$ distributions.

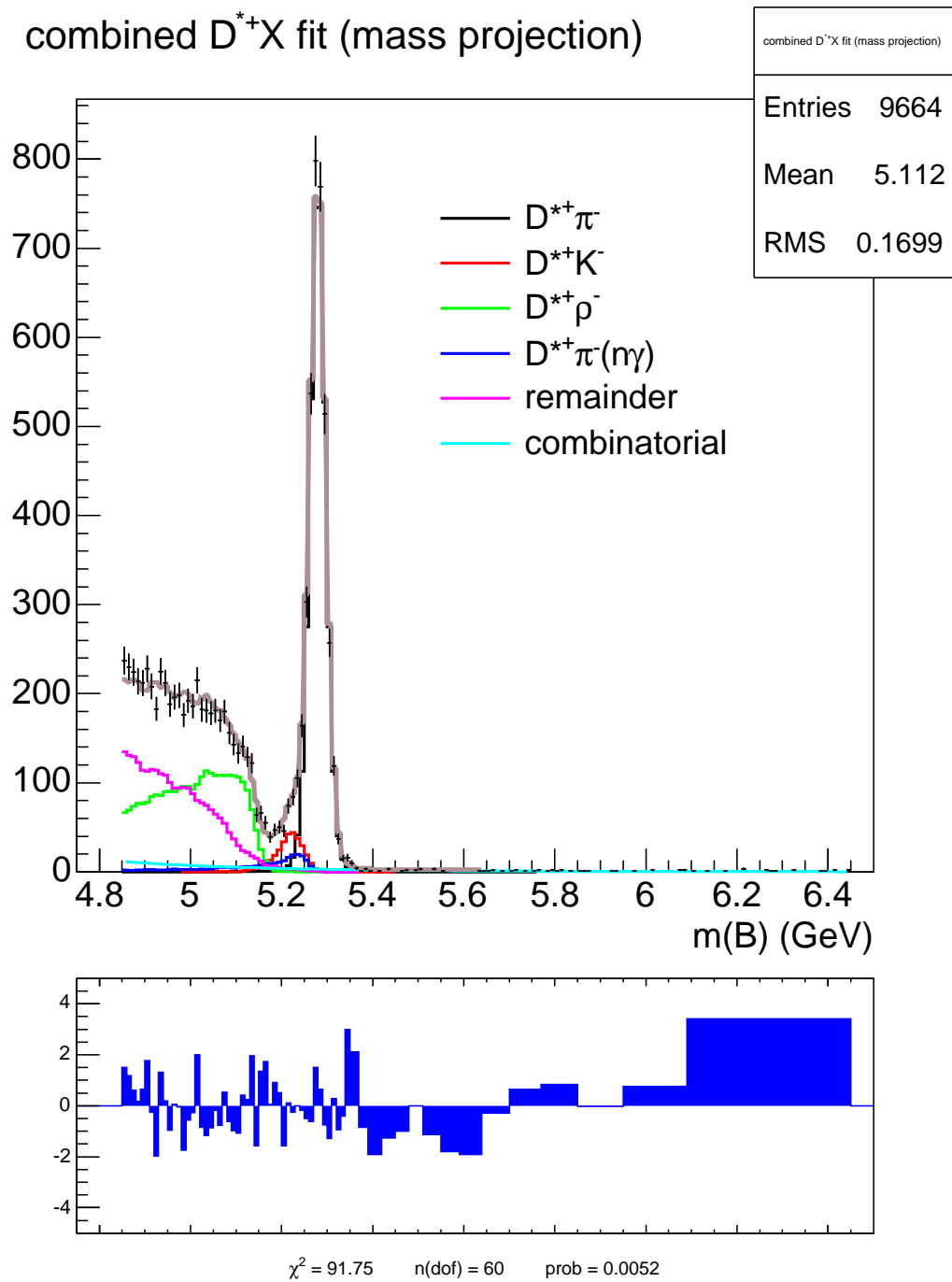
combined $D^{*+}X$ fit (mass projection)

Figure 5.12: Mass projection of the fit on the full $D^{*+}X^-$ sample. The smaller histogram shows the fit residuals, defined as the excess of the data points over the fit, expressed in units of σ . For the purpose of calculating residuals, neighboring bins are combined until at least 5 events are expected.

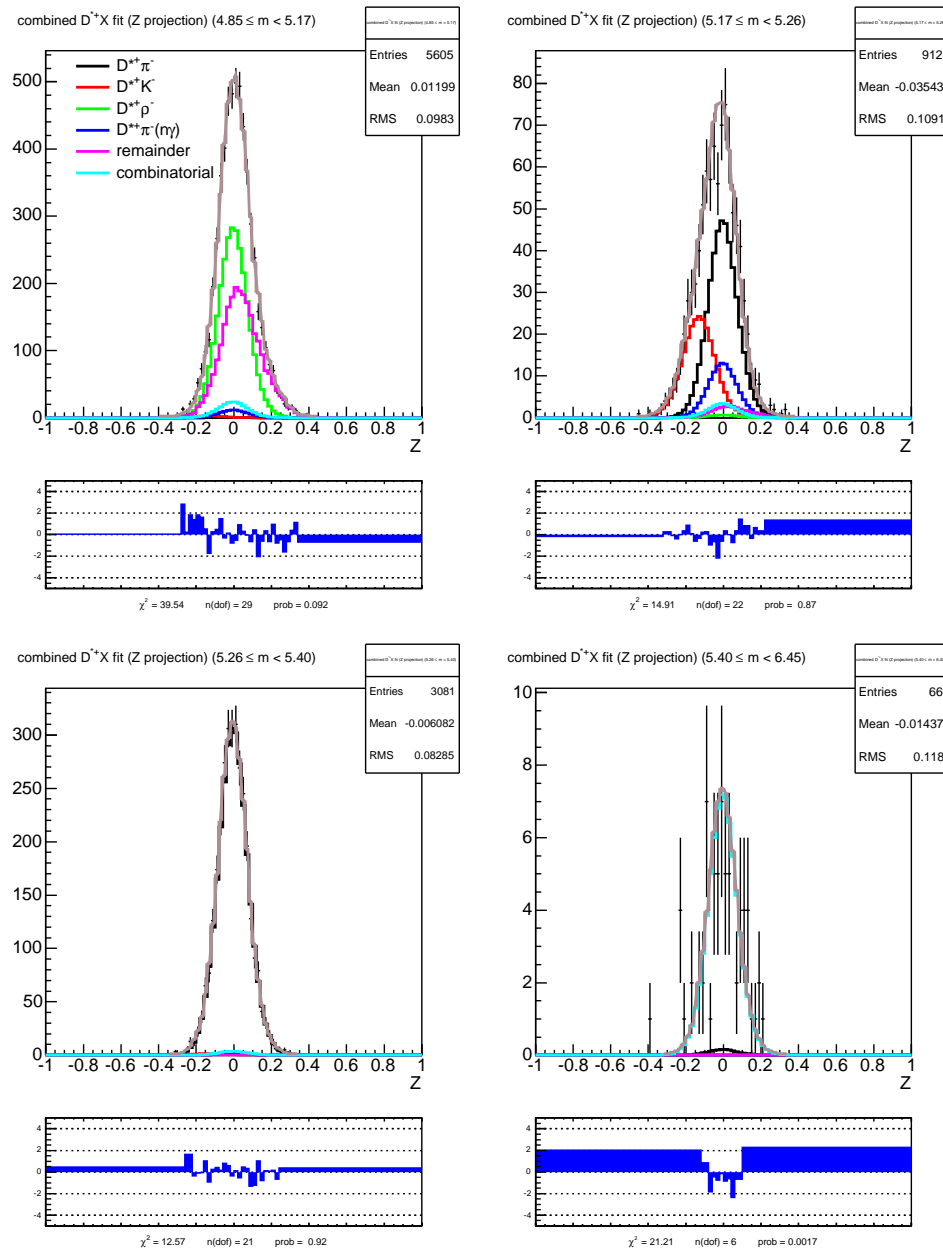


Figure 5.13: Z projections of the fit on the full $D^{*+}X^{-}$ sample. The Z projections are shown in four B mass regions:

$$\begin{array}{ll}
 \text{upper-left} & [4.85, 5.17] \text{ GeV} \\
 \text{lower-left} & [5.26, 5.40] \text{ GeV} \\
 \text{upper-right} & [5.17, 5.26] \text{ GeV} \\
 \text{lower-right} & [5.40, 6.45] \text{ GeV}
 \end{array}$$

The pion-dominated region is shown in the lower-left plot. The smaller histograms show the fit residuals.

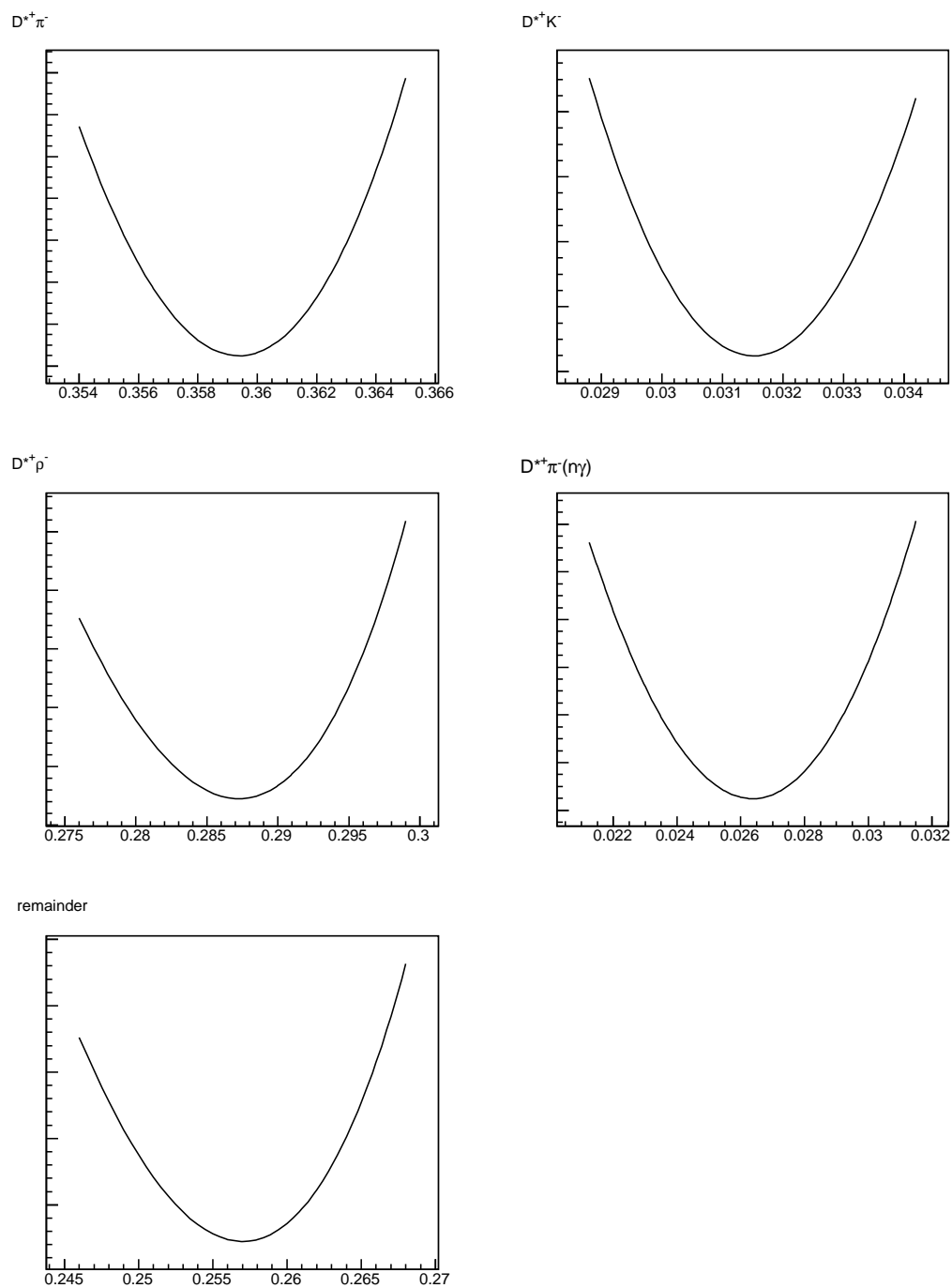
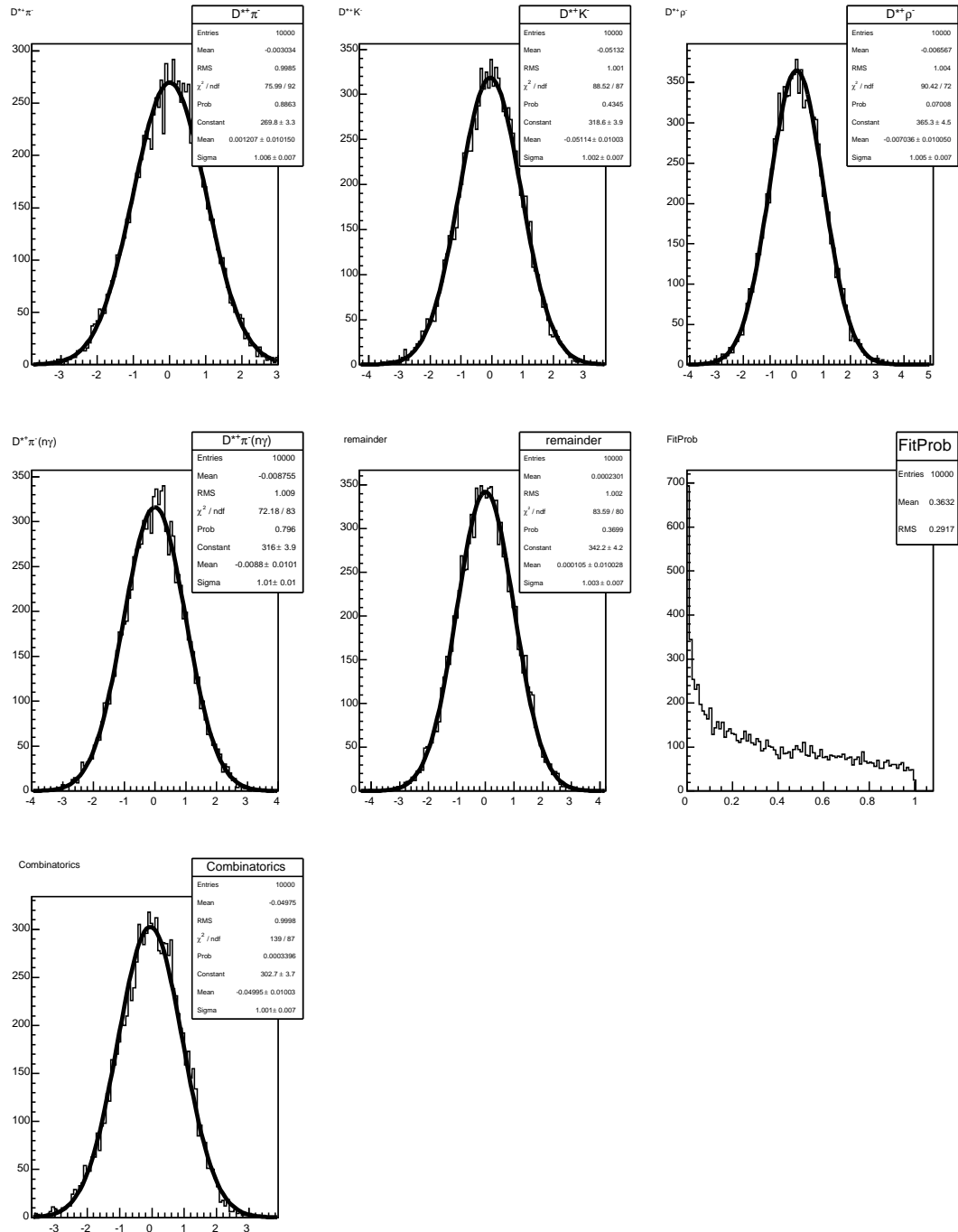


Figure 5.14: Likelihood scans for the $D^{*+}X^-$ fit components.

Figure 5.15: Pull distributions for the $D^{*+}X^{-}$ fit components.

Chapter 6

Signal Samples

In this chapter, we apply our fitter to the three D^0X signal samples. The fitter configuration for each fit is discussed in detail. The six ratios of the form $BR(B \rightarrow D^0K)/BR(B \rightarrow D^0\pi)$, defined in Eqs. (4.1) to (4.6), and their statistical uncertainties are extracted from the fits. The systematic uncertainties on these ratios are also ascertained. Finally, we combine the ratios to produce measurements of R , R_{CP+} , and A_{CP+} .

During the process of configuring and testing the code for the D^0X fits, an arbitrary offset (the value of which was unknown to the author) was added to the fitter output of $BR(B \rightarrow D^0K)/BR(B \rightarrow D^0\pi)$ to prevent unconscious biases in setting up the fitter.

The text of this chapter is adapted from our CDF Note, CDF 8777 (Ref. [59]). The figures and tables are also from Ref. [59].

6.1 Mass constraints on the D^0 candidates

Before a detailed explanation of the fit configurations is given, a discussion of the use of D mass constraints is due.

The B mass used for all D^0X fits is that obtained from a fit where the tracks from the D^0 are vertex constrained and the D^0 is mass constrained; this is desirable since the mass constraint reduces the width of both the Cabibbo-allowed $D^0\pi$ and the Cabibbo-suppressed D^0K mass distributions and thus increases the statistical separation of the two. However, as will be explained in greater detail in Sections 6.2.1 and 6.3.1, we use events in the D^0 sideband to model fake- D background. For this to be a good model, the selection cuts for D^0 sideband events ought to be identical to those for the D^0 -peak signal save for the necessary difference in the D mass requirement. One very soon realizes that a χ^2 cut on a D^0 -mass-constrained candidate tends to reject events in the sidebands of the unconstrained D^0 mass. This becomes a problem if one is to retain enough sideband events for the sidebands

to be a useful and unbiased background proxy. Therefore, we choose to apply our selection cuts on B candidates *without* a D mass constraint applied but use, for the actual measurement, the B mass obtained from the same candidates *with* the D mass constraint applied in a refit of the vertex.

6.2 $D^0[K^-\pi^+]X^-$ fits

In this section we apply the fitter to both the $D^0[K^-\pi^+]X^-$ sample and its charge conjugate to determine R and its statistical uncertainty. To this end, we can either fit the D^0X^- and \bar{D}^0X^+ samples simultaneously or fit the two samples separately and combine the results. We choose the latter to maintain a unified treatment with the CP+ modes, for which the two charges need to be separately measured in order to obtain $A_{\text{CP}+}$. This treatment has the added advantage of enabling us to configure the two fits separately (especially the fake- D background proxies and the dE/dx templates) so that we may better accommodate possible charge dependences in the samples.

Systematic uncertainties will be discussed along with those for the CP modes in Section 6.4.

6.2.1 Fit configuration

The fits are extended maximum likelihood fits in two dimensions. The $D^0\pi$ mass is obtained from a vertex fit with a D^0 mass constraint applied. The fit range in mass is $m(B) \in [4.85, 6.45]$ GeV. The fit configuration is summarized in Table 6.1.

Single- B templates

Please refer to Section 4.6.1 for a general discussion.

- **Mass component.** The mass templates for the single- B modes are histograms obtained either from dedicated $B^- \rightarrow D^0\pi^-(n\gamma)$ and $B^- \rightarrow D^0K^-(n\gamma)$ Monte Carlo samples or the semi-inclusive $B \rightarrow D^0X$ Monte Carlo samples. As described in Section 4.3, a mass scale factor of 1.000236 and a Gaussian resolution smearing of 4.61 MeV are applied to the histograms. These are determined from the D^0X likelihood scans shown in Figures 6.2 and 6.3.

In Table 6.1, the mass templates for the single- B modes are marked as “MC” in the Mass PDF column. As in the control samples, the normalization of the $B^- \rightarrow D^0\pi^-(n\gamma)$ template, the PHOTOS radiative tail of the Cabibbo-allowed peak, is allowed to float. Also as before, the catch-all “remainder” template encompasses the great majority of the partially reconstructed $B \rightarrow D^0X$ modes. Compared to the control sample, however, the treatment of the Z component of the remainder template is more sophisticated. (See below.) As a result, the only

modes that are separated out are the following: the $D^0\rho^-$ and $D^{*(0/+)}\pi^-$, since their high mass tails extend into the D^0K mass region; the $D^{*0}K^-$, to correct for its outdated branching ratio in our Monte Carlo sample. The normalizations of all modes float in the fit.

- **Z component.** With one exception mentioned below, the Z templates are marked as “prompt D^* ” in the Z PDF column of Table 6.1. These are the K and π templates obtained from a large prompt D^* sample using the procedure described in Section 4.7 and Appendix A. To summarize, the hit-level (Ref. [72]) and track-level (Ref. [73]) corrections have already been applied. Two-dimensional reweighting in secance (s) and momentum (p) is performed. The reweighted templates are sideband-subtracted in the D^* Δm variable.

However, we still observe a residual difference between the mean of the pion template and the mean Z of the data in the $D\pi$ -dominated region, even after the procedure described above. To correct for this difference, we shift the pion Z templates by -5.57×10^{-3} and -2.79×10^{-3} for negative and positive B daughter tracks, respectively. The size of the shifts are those required to bring the pion template means to agree with those in the $D\pi$ -dominated region ($m(D\pi) \in [5.26, 5.40]$ GeV) in their respective samples, after accounting for the contribution to the mean Z of the other fit components in that region.

The “remainder” template is in all but name a two-dimensional template. (See also Section 4.6.1.) For every mass bin, the fractions of pions, kaons, muons, and electrons inside the bin are calculated according to predictions obtained from the semi-inclusive $B \rightarrow D^0X$ Monte Carlo samples. A separate Z template is then constructed for each mass bin using the correct proportion of pion, kaon, muon, and electron Z templates. The π and K templates are the same as those described above. The electron template is from the parametric dE/dx simulation described in Section 4.7. The pion template is used in lieu of the muon template (a small component).

The fake- D template

Please refer to Section 4.6.2 for a general discussion.

- **Mass component.** To obtain the shape parameters for the fake- D mass template, the auxiliary mass fit described in Section 4.6.2 is performed on events taken from the sidebands of the D^0 mass peak. The fit determines the shape parameters of the fake- D mass template while taking into account real- D contamination in the sidebands. The D^0 sidebands are given by $m(D^0) \in [1.820, 1.835] \cup [1.895, 1.910]$ GeV. Figures 6.4–6.6 show the results of this fit. The shape parameters obtained in this auxiliary fit are then used to fix the parameters for the fake- D template in the main fit. In the main fit, the normalization of the fake- D component is allowed to float.

- **Z component.** We obtain the Z templates for the fake- D^0 component by performing the subtraction of real- D^0 contamination described in Section 4.6.2. As before, there are two templates, one for the mass region above 5.40 GeV, and one for the region below.

The real- D background template

Please refer to Section 4.6.3 for a general discussion.

- **Mass component.** As described in Section 4.6.3, the real- D background mass template is obtained from a fit on sideband-subtracted wrong-sign D^+X^+ candidates.

The fit strategy here differs from that used in the D^+X^- control sample. The fit function is a first-degree polynomial. To avoid contamination from partially reconstructed B decays, this fit excludes candidates below 5.1 GeV. This lower limit is determined by studying D^+X^+ events in the fully inclusive b Monte Carlo sample described in Section 4.3. The slope obtained from this auxiliary fit is used in the main D^0X^- fit. The normalization of the template is allowed to float in the main fit.

- **Z component.** As in the control sample case, the Z templates for the real- D^0 component are taken from the wrong-sign D^+X^+ control sample data. There are two templates, one for the mass region above 5.40 GeV, and one for the region below.

6.2.2 Results

The results of the likelihood fits are given in Table 6.2; the correlation coefficients of the fit components are given in Table 6.3. The mass projection is shown in Figure 6.7 (and Figures 6.8 and 6.9 for the charges separately); the Z projections are shown in Figures 6.10–6.12.

To calculate ratios of branching fractions from ratios of fit fractions, we proceed as described in Section 4.8. Taking into account the relative K - π efficiencies and acceptances, but not the XFT corrections, we obtain $BR(B^- \rightarrow D^0[K^-\pi^+]K^-)/BR(B^- \rightarrow D^0[K^-\pi^+]\pi^-) = (7.84 \pm 0.46)\%$; the value of the charge-conjugated ratio is $(7.41 \pm 0.43)\%$. The errors quoted are statistical and take into account the correlation between fit components. As mentioned at the beginning of this section, we average the measurements for the two charges with weights determined by their respective statistical errors to obtain the combined value of $(7.61 \pm 0.32 \text{ (stat.)})\%$ (still before the XFT corrections). We note in passing that fitting the negative and positive samples together and using an average background model gives a consistent result of $(7.57 \pm 0.32 \text{ (stat.)})\%$.

The relative XFT K - π efficiency is calculated in the same manner as before. (See Section 4.8 for a summary.) The relative efficiency is found to be 1.050 ± 0.028 for the $D^0 X^-$ sample. Applying this correction factor, we find that $R = (7.99 \pm 0.33(\text{stat.}) \pm 0.21(\text{XFT}))\%$.

6.2.3 Toy Monte Carlo validation of the fitter

The general procedure for fitter validation is described in Section 4.9. In particular, we look for a non-zero bias or a non-unit pull in the distributions for

$$\frac{n[D^0 K]}{n[D^0 \pi] + n[D^0 \pi(n\gamma)]},$$

the ratio from which $BR(B \rightarrow DK)/BR(B \rightarrow D\pi)$ is eventually derived. We generate ~ 1000 such pseudo-experiments for each data sample we fit on and graph the resulting bias and pull distributions. See Table 6.4 for a summary. The small deviations from zero bias are taken into account when we assess systematic uncertainties in Section 6.4. The $D^0 X^-$ and $\bar{D}^0 X^+$ pseudo-experiments have a mean total number of events of $\hat{N} = 43256$ and 43076, respectively; these are identical to the total number of events in the actual data samples.

6.3 $D_{\text{CP}^+}^0 X^-$ fits

Although fits to the $D_{\text{CP}^+}^0 [K^+ K^- / \pi^+ \pi^-] X^-$ samples use the same framework as described in previous sections, the fitter configurations differ in several important respects. There are additional background modes that are of significant size in the $B^- \rightarrow D_{\text{CP}^+}^0 K^-$ mass region. These include the reflection from the flavor mode and decays of the B^- to three-body final states. Several of these modes have high kaon content. The much smaller CP+ branching ratios further magnify the importance of these backgrounds. We also choose to constrain some fit parameters in the CP+ modes to the values determined in the flavor mode fit. The treatment of the fake- D background proxies, especially in the $K^- K^+$ mode, also differs from that in the flavor mode. Details of these differences from the flavor mode are given below, together with the fit return values and statistical uncertainties of $BR(B^- \rightarrow D_{\text{CP}^+}^0 K^-)/BR(B^- \rightarrow D_{\text{CP}^+}^0 \pi^-)$ in the $D^0 \rightarrow \pi^+ \pi^-$ and $D^0 \rightarrow K^+ K^-$ modes.

6.3.1 Fit configuration

The fit configurations for the $D^0 \rightarrow \pi^+ \pi^-$ and $K^+ K^-$ modes are summarized in Tables 6.5 and 6.8, respectively.

Single- B templates

For the flavor mode, we let the normalization of the PHOTOS radiative tail $B^- \rightarrow D^0\pi^-(n\gamma)$ be determined in the fit itself. Allowing the same in the CP+ mode fits would result in much larger uncertainties, since the CP+ sample sizes are significantly smaller. Instead, we add to the CP+ mode likelihood function a Gaussian constraint on the ratio of the radiative tail size relative to the size of the main $B^- \rightarrow D^0\pi^-(0\gamma)$ peak. The central value and width of this constraint are given by the central value and uncertainty measured in the flavor mode.

Additional modes that were either non-existent or negligible in the case of the flavor mode have been included here. There are four such modes, and they fall into two categories:

- **The flavor mode reflection.** When we reconstruct a two-body decay of the D^0 meson in a given mass hypothesis of the D^0 daughter tracks, we obtain three reasonably well separated peaks, which correspond to the K^-K^+ , $K^-\pi^+$, and $\pi^-\pi^+$ decay modes, in order of ascending reconstructed mass. Due to the large size of the flavor mode relative to the two CP+ modes, the number of flavor mode events that happen to fall in the two CP mode mass windows cannot be neglected. Therefore, we include these $B \rightarrow D^0[K^-\pi^+]X^-$ events as an extra component in the CP+ mode fits. The size of this reflected flavor mode component is Gaussian constrained to a value determined by scaling the MC prediction so that the size of the Cabibbo-allowed peak in the flavor mode MC matches that in the actual flavor mode data.
- **Three-body final states.** There are six possible three-body decays of the B^- that involve only charged kaons and pions. Among these, the three-body modes $B^- \rightarrow K^-\pi^+\pi^-$ and $B^- \rightarrow K^-K^+K^-$ form mass peaks in the same regions as our $B^- \rightarrow D^0[\pi^-\pi^+]K^-$ and $B^- \rightarrow D^0[K^-K^+]K^-$ signal channels, respectively, and must be taken into account. For the sake of completeness, we also include the three-body mode $B^- \rightarrow \pi^-\pi^+\pi^-$. This gives a total of three three-body modes included in each of our CP+ mode fits. (In [79], only limits have been given for the remaining charged three-body modes, $B^- \rightarrow K^-K^+\pi^-$, $K^-\pi^+K^-$, and $\pi^-K^+\pi^-$; we do not include these modes.) Since the three-body modes are fully reconstructed, they cannot be suppressed by requiring the B candidate momentum to point back to the primary vertex. Moreover, the poor B -to- D resolution and the short D^0 lifetime preclude the efficient rejection of these modes without significant loss of signal. Therefore, we only slightly tighten the B -to- D L_{xy} -significance cut from -2 to 0 in order to suppress three-body background.

The three-body modes are modeled with the aid of the Monte Carlo sample mentioned in Section 4.3. To summarize, the sample includes the subset of all EvtGen B^\pm decays to three-body final states that contain only charged kaons or

pions. The PDFs of the three-body modes are two-dimensional templates in the same sense as the “remainder” template described in Section 6.2.1. The number of events in each three-body mode is Gaussian-constrained in the negative log likelihood function with a term of the form

$$C_k = \frac{1}{2} \frac{(r_k - r_k^{\text{pred}})^2}{\sigma_k^2}, \quad (6.1)$$

where r_k is the acceptance-corrected yield of the mode in question relative to the reference $B \rightarrow D^0\pi$ mode (radiative tail included), r_k^{pred} the same ratio as derived from the PDG value, and σ_k the uncertainty on this ratio (mainly from the PDG error but also from the statistical uncertainty on the acceptance correction).

The fake- D template

As in the flavor mode, we obtain the fake- D templates for the CP+ modes by studying the B mass distributions of events that fall in the D sidebands. Despite the narrower signal mass window of the CP+ modes, the sidebands are still given by $m(D^0) \in [1.820, 1.835] \cup [1.895, 1.910]$ GeV. As before, we need to remove signal “leakage” events from the sidebands, if any. Additionally, flavor mode reflection and three-body mode events that fall in the sideband region are removed to avoid double counting in the main fit. The nature of the remaining sideband events differ for the $\pi\pi$ and KK cases. This results in a difference in how the fake- D templates are obtained for the two modes. We first describe how we arrive at the mass components of the PDFs:

- The $D^0 \rightarrow \pi^-\pi^+$ case. In a manner analogous to that for the flavor mode, auxiliary sideband fits are performed with a smooth component described by Eq. (4.13), a signal leakage component from $B \rightarrow D^0X$ sideband MC, a flavor mode reflection, and three components for the three three-body modes. The normalizations of the flavor mode reflection and the three-body modes are fixed to their predicted values. The only free parameters are the two shape parameters of the smooth component and the normalization of the signal leakage. This fit model describes the data well, as can be seen in Figures 6.13 through 6.14. As in the flavor mode, the smooth component is used as the fake- D mass PDF in the main fit; its parameters are fixed but its normalization is allowed to float.
- The $D^0 \rightarrow K^-K^+$ case. Figure 6.19 shows the fit model used in the $\pi\pi$ case to be inadequate in describing the KK data. This is a result of the more complicated composition of the KK sidebands. Studies using the fully inclusive b Monte Carlo sample indicate that a significant number of “fake- D ” events in the KK sidebands in fact contain a partially reconstructed D^0 or D^+ meson. Due to the larger background in the KK sidebands and the narrower width of

the KK mass peak relative to the $\pi\pi$ peak (such a difference is also seen in Monte Carlo), a signal leakage component is not visible in the sidebands and is excluded from consideration in this case. Moreover, the partially reconstructed D^0 and D^+ events have a characteristic wedge shape in the B mass distribution that tapers off at approximately the nominal B mass. (See Figures 6.20(a) and 6.20(b) for a demonstration of this in the Monte Carlo.) This is the reason the smooth function (4.13) fails to describe the shape of the remaining sideband events. Since we fix the normalizations of the flavor mode reflection and the three-body modes to their predicted values, as we do in the $\pi\pi$ mode, there are no components left with unknown normalizations. Therefore, as our fake- D proxy, we simply use a histogram of the B mass distribution with the three-body modes and the flavor mode reflection subtracted out.

After we obtain the mass component for a particular mode, we construct the corresponding fake- D Z template by subtracting the Z PDFs of the flavor mode reflection, the three-body modes, and the signal leakage (in the $D^0 \rightarrow \pi^- \pi^+$ case) from the Z histogram of the sideband data. The normalizations of the components are the same as those used in obtaining the mass PDFs. The Z PDFs for the various subtracted components are constructed from the particle species fractions predicted in Monte Carlo. As in the flavor mode case, we split the fake- D Z PDF into two components, one for the region above 5.40 GeV, and one for the region below.

The real- D background template

The real- D background templates are the same as those used in the flavor mode fits. See Section 6.2.1 for details.

6.3.2 Results

The results of the $D^0[\pi^- \pi^+]X$ likelihood fits are given in Table 6.6; the correlation coefficients of the fit components are given in Table 6.7. The mass projections are shown in Figures 6.15 and 6.16 for the charges separately; the Z projections are shown in Figures 6.17 and 6.18.

Similarly, results of the $D^0[K^- K^+]X$ likelihood fits are given in Table 6.9; the correlation coefficients of the fit components are given in Table 6.10. The mass projections are shown in Figures 6.21 and 6.22 for the charges separately; the Z projections are shown in Figures 6.23 and 6.24.

We perform four fits, one for each combination of D^0 mode ($\pi^- \pi^+$ or $K^- K^+$) and B charge (negative or positive). From these, we obtain measurements of the relative branching ratios $BR(B^- \rightarrow D^0 K^-)/BR(B^- \rightarrow D^0 \pi^-)$ before XFT corrections are applied. For the $\pi^- \pi^+$ mode, we find the relative branching ratios to be $(8.62 \pm 3.45)\%$ ($q < 0$) and $(8.05 \pm 4.05)\%$ ($q > 0$); for the $K^- K^+$, they are $(10.08 \pm 2.14)\%$ ($q < 0$) and $(7.81 \pm 1.97)\%$ ($q > 0$). See Table 6.11 for a summary.

We combine the K^-K^+ and $\pi^-\pi^+$ relative branching ratio measurements and calculate $A_{\text{CP}^+} = 0.103 \pm 0.145$ (stat.); using the value of R before XFT corrections, obtained in Section 6.2.2, we find $R_{\text{CP}^+} = 1.149 \pm 0.173$ (stat.). The equivalents of R_{CP^+} and A_{CP^+} , calculated separately for the $\pi\pi$ and KK modes, can be found in Table 6.12. See Section 6.4.2 For a discussion of the calculation of the central values and uncertainties of R , R_{CP^+} , and A_{CP^+} .

6.3.3 Toy Monte Carlo validation of the fitter

Fitter validation in the CP^+ modes is entirely analogous to that in the flavor mode. Please see Sections 4.9 and 6.2.3 for detailed explanations. See Table 6.4 for a summary of mean biases, pull means, and pull widths. As before, the small deviations from zero bias are used in the assessment of systematic uncertainties in Section 6.4.

6.4 Systematic uncertainties

In this section, we determine the systematic uncertainties on R , R_{CP^+} , and A_{CP^+} . At this point, we have measured six relative branching ratios of the form $BR(B \rightarrow D^0 K)/BR(B \rightarrow D^0 \pi)$, one for each combination of B charge (negative or positive) and D^0 decay mode ($K^-\pi^+$, $\pi^-\pi^+$, or K^-K^+). For each of these relative branching ratios, there are various sources of uncertainties. As a first step, we determine for each source the systematic uncertainties on each of the six relative branching ratios.

For each source of uncertainty, the six uncertainties on the relative branching ratios are then propagated into systematic uncertainties on R , R_{CP^+} , and A_{CP^+} . This error propagation involves assumptions on how the systematic uncertainties on the six relative branching ratios are correlated; the correlations may be different for different sources of uncertainties. The assumed correlations are of the following three types:

- Type (i). All uncertainties from this source are assumed to be uncorrelated.
- Type (ii). All uncertainties from this source are assumed to be 100% correlated.
- Type (iii). 100% correlation among like-charged fits. No correlation between any pair of positive and negative fits.

After the systematic uncertainties on R are determined for all the potential sources, we sum together all the uncertainties in quadrature to obtain the total systematic uncertainty for R . The same procedure is repeated separately for R_{CP^+} and A_{CP^+} .

In Section 6.4.1, we describe the sources of systematic uncertainties on the relative branching ratios, the models we use to estimate them, and the assumed correlations for each of them. The derived errors on R , R_{CP^+} , and A_{CP^+} will be summarized in Section 6.4.2.

6.4.1 Systematic uncertainties on the relative branching ratios

All systematic uncertainties on $BR(B \rightarrow D^0 K)/BR(B \rightarrow D^0 \pi)$ are determined as follows. An alternate model is developed to account for the effect in question. Toy Monte Carlo data is then generated by sampling the mass and Z templates in the alternate fit configuration. This toy Monte Carlo data is fit with the default fit configuration. The bias on $BR(B^- \rightarrow D^0 K^-)/BR(B^- \rightarrow D^0 \pi^-)$, averaged over ~ 1000 pseudo-experiments, is used as the systematic uncertainty associated with the effect being studied. Since we include the intrinsic fitter bias itself as a source of systematic error, we also subtract out any fitter bias at this point to avoid double counting. Table 6.13 summarizes the systematic uncertainties on the relative branching ratios before the XFT efficiency correction is taken into account. For the calculation of systematic errors on R , these values need to be scaled by the XFT K - π relative efficiency of $1.050(\pm 0.028)$ quoted in Section 6.2.2. For R_{CP+} and A_{CP+} , however, the same XFT correction factor appears in both the numerators and denominators of these expressions and therefore cancels out. We describe the individual systematic effects in the following paragraphs.

Monte Carlo mass scale and resolution

Here we study the systematic uncertainties associated with the small uncertainties in our knowledge of the mass scale factor and the width of the Gaussian resolution smearing as described in Section 4.3.

- The required mass scale factor of the Monte Carlo is determined by a scan of the likelihood on flavor mode data. (Since many of our mass templates are represented by histograms, the mass scale is a fixed parameter of the likelihood for any given fit.) The scan is shown in Figure 6.2. The $\pm 1\sigma$ values of the scale factor are those that give $\Delta \log L = 1/2$ above the minimum. Due to the roughness of the likelihood in this scan, we choose the central value to be the midpoint of the $\pm 1\sigma$ range. We determine the scale factor to be 1.000236 ± 0.000020 .
- The Monte Carlo mass templates are convoluted with (smeared by) a Gaussian resolution function of a given width (or standard deviation). The required width is determined by a scan of the likelihood on flavor mode data. (Since many of our mass templates are represented by histograms, this smearing width is also a fixed parameter of the likelihood for any given fit.) This scan is shown in Figure 6.3. The $\pm 1\sigma$ values of the width are those that give $\Delta \log L = 1/2$ above the minimum. The central value coincides with the midpoint of the $\pm 1\sigma$ range. We determine the smearing width to be 4.61 ± 0.33 MeV.

We assess the systematic uncertainty associated with the scale factor by generating pseudo-experiments with the scale factor varied by $\pm 1\sigma$ from the central value. The same method is employed to determine the systematic uncertainty associated with the smearing. For both the scale factor and the smearing, type (i) correlations are assumed, *i.e.*, all the uncertainties are assumed to be uncorrelated.

dE/dx (Z) templates

We have performed several studies to assess the systematic uncertainties associated with the dE/dx templates. The dominant effect is that reflected in the structure in the Z residual histogram of the $D\pi$ -dominated mass region [5.26, 5.40] GeV. The D^+X control sample shows an effect similar to that seen in the D^0X signal sample.

As described in Section 6.2.1, the default fit configurations use a pion template with ad hoc shifts of -5.57×10^{-3} and -2.79×10^{-3} (for negative and positive B daughter tracks, respectively) with respect to the secance: p -reweighted templates from the prompt D^* sample. These shift values are determined separately for the two charges from the $D^0\pi$ -dominated region of the high-statistics $D^0[K^-\pi^+]X$ sample. Below we describe three sources of systematic uncertainties associated with our choice of default Z templates.

1. **Statistical errors in determining the ad hoc shifts.** Since we determine the ad hoc shifts from data in the $D^0[K\pi]\pi$ -dominated region, there is a statistical uncertainty in determining the true mean values of the pion templates simply due to finite statistics. For the charges separately, the uncertainty is roughly 1.0×10^{-3} in Z . We assess the systematic uncertainties associated with this statistical uncertainty by generating pseudo-experiments with the ad hoc shifts varied by $\pm 1\sigma$ from the central value. Type (iii) correlations are assumed for this source of systematic uncertainty.
2. **Possible kaon template shifts.** This alternate model entails shifting the kaon templates by the same amount the pion templates are shifted. Since there is no kaon-dominated region in the data (control sample or otherwise), the merits of this configuration relative to the default cannot be directly evaluated. The resulting systematic uncertainty is assumed to be two sided and symmetric. Type (ii) correlations are assumed for this source of systematic uncertainty.
3. **Sample dependence.** This is relevant because we apply the shift values obtained from the high-statistics $D^0[K\pi]X$ sample to the two $D_{\text{CP}^+}^0X$ samples. It is possible to perform a similar exercise using the D^+X control sample instead. If we determine the ad hoc shift for tracks of both charges together, we obtain the shifts -4.14×10^{-3} and -4.42×10^{-3} for the $D^0[K\pi]X$ and $D^+[K\pi\pi]X$ cases, respectively. We use the difference between the two (-0.28×10^{-3}) as a 1σ estimate of the size of a possible sample dependence of the ad hoc shifts.

We assess the systematic uncertainties associated with this sample dependence by generating pseudo-experiments with the ad hoc shifts varied by $\pm 1\sigma$ from the central value. Type (i) correlations are assumed.

Combinatorial background mass shapes

1. **Real- D background shape.** The smaller of our two combinatorial backgrounds comes from combinations of real D mesons and random tracks. We model this background by performing a linear fit to the wrong-sign D^+X^+ sample. To avoid the partially-reconstructed single- B background present in this sample, the fit range is chosen to be [5.1, 6.45] GeV. As an alternate model, we use the fit parameters obtained from the same fit in the range [5.4, 6.45] GeV, starting above the main B mass peak. Type (i) correlations are assumed.
2. **Fake- D background shape.** As described in detail before, the fake- D background shapes in the $D^0[K\pi]$ and $D^0[\pi\pi]$ modes are obtained from auxiliary fits to data in the D sidebands. The background shapes are parameterized as the sum of a falling exponential component and a flat component. We vary the decay constant of the exponential component by $\pm 1\sigma$ (statistical) to obtain the alternate models. Type (i) correlations are assumed.

Fitter bias

The fitter biases obtained in Sections 6.2.3 and 6.3.3 are also included as systematic uncertainties on the relative branching ratios. Type (i) correlations are assumed.

6.4.2 Systematic uncertainties on R , R_{CP+} and A_{CP+}

In Table 6.13, the values of the systematic uncertainties described in the previous section are summarized; also summarized are the assumed correlation types. If $+1\sigma$ and -1σ values are both given for a particular source of systematic errors, we choose the value with the larger absolute value in each column.

At this point, we have all the ingredients needed to calculate the central values and statistical and systematic uncertainties of R , R_{CP+} and A_{CP+} . The input values to these calculations include (1) the six relative branching ratios $BR(B \rightarrow DK)/BR(B \rightarrow D\pi)$, one for each combination of D^0 decay mode ($K^-\pi^+$, $\pi^-\pi^+$, or K^-K^+) and B charge (negative or positive), (2) the statistical uncertainties on these relative branching ratios, and (3) the systematic uncertainties on each of the relative branching ratios, separately for each source of uncertainty, and the correlation structure for each source. (1) and (2) are summarized in Table 6.11; (3) is summarized in Table 6.13. Each of the relative branching ratios carries a weight proportional to $1/\sigma^2$, where σ is the statistical error. When propagating systematic uncertainties, the

statistical weights and the correlation structure of the particular source of systematic uncertainty are both taken into account. Systematic uncertainties from different sources are assumed to be uncorrelated. See Table 6.14 for a summary of the systematic uncertainties thus propagated, both separately for each source and combined in quadrature for all sources; the central values and statistical uncertainties are also shown for comparison.

See Chapter 7 for our conclusions and a summary of results.

Fit component	Mass PDF	Z PDF	normalization
$B^- \rightarrow D^0 \pi^-$	MC	$D^0 [K^- \pi^+] X^-$ fits	floating
$B^- \rightarrow D^0 \pi^- (n\gamma)$	MC	prompt $D^* \rightarrow \pi, s : p$ reweight, shifted	floating
$B^- \rightarrow D^0 K^-$	MC	prompt $D^* \rightarrow \pi, s : p$ reweight, shifted	floating
$B^- / \bar{B}^0 \rightarrow D^{*(0/+)} \pi^-$	MC	prompt $D^* \rightarrow K, s : p$ reweight	floating
$B^- \rightarrow D^{*0} K^-$	MC	prompt $D^* \rightarrow \pi, s : p$ reweight, shifted	floating
$B^- \rightarrow D^0 \rho^-$	MC	prompt $D^* \rightarrow K, s : p$ reweight	floating
$B^- / \bar{B}^0 \rightarrow D^0 X(\text{remainder})$	MC	prompt $D^* \rightarrow \pi, s : p$ reweight, shifted	floating
fake- D background	D^0 SB	see Section 6.2.1 for explanation	floating
real- D background	$D^+ X^+$ WS SBS	D^0 SB, signal-subtracted $D^+ X^+$ WS (D signal region)	floating; shape fixed floating; shape fixed

Table 6.1: Fit components of the $D^0 [K^- \pi^+] X^-$ fits. See text for an explanation of the “Mass PDF” and “Z PDF” columns. “SB” denotes the D sidebands; “SBS” indicates sideband subtraction in the D mass.

fit component	par no	fit result
$B^- \rightarrow D^0 \pi^-$	3	$1.05215\text{e}+04 \pm 1.08506\text{e}+02$
$B^- \rightarrow D^0 \pi^- (n\gamma)$	4	$5.25765\text{e}+02 \pm 1.02467\text{e}+02$
$B^- \rightarrow D^0 K^-$	5	$8.77150\text{e}+02 \pm 4.83100\text{e}+01$
$B^- / \bar{B}^0 \rightarrow D^{*(0/+)} \pi^-$	6	$1.30497\text{e}+04 \pm 3.10378\text{e}+02$
$B^- \rightarrow D^{*0} K^-$	7	$5.43027\text{e}+02 \pm 8.12401\text{e}+01$
$B^- \rightarrow D^0 \rho^-$	8	$7.09939\text{e}+03 \pm 4.77669\text{e}+02$
$B^- / \bar{B}^0 \rightarrow D^0 X(\text{remainder})$	15	$7.11861\text{e}+03 \pm 2.45760\text{e}+02$
fake- D background	16	$2.96028\text{e}+03 \pm 2.19718\text{e}+02$
real- D background	17	$5.60607\text{e}+02 \pm 9.08391\text{e}+01$
$B^+ \rightarrow \bar{D}^0 \pi^+$	3	$1.07868\text{e}+04 \pm 1.09624\text{e}+02$
$B^+ \rightarrow \bar{D}^0 \pi^+ (n\gamma)$	4	$5.74939\text{e}+02 \pm 1.02417\text{e}+02$
$B^+ \rightarrow \bar{D}^0 K^+$	5	$8.52528\text{e}+02 \pm 4.64687\text{e}+01$
$B^+ / B^0 \rightarrow \bar{D}^{*(0/-)} \pi^+$	6	$1.32773\text{e}+04 \pm 3.11208\text{e}+02$
$B^+ \rightarrow \bar{D}^{*0} K^+$	7	$7.90808\text{e}+02 \pm 8.16191\text{e}+01$
$B^+ \rightarrow \bar{D}^0 \rho^+$	8	$7.02588\text{e}+03 \pm 4.75243\text{e}+02$
$B^+ / B^0 \rightarrow \bar{D}^0 X(\text{remainder})$	15	$7.08799\text{e}+03 \pm 2.43949\text{e}+02$
fake- D background	16	$3.03201\text{e}+03 \pm 2.24633\text{e}+02$
real- D background	17	$6.46750\text{e}+02 \pm 8.79289\text{e}+01$

Table 6.2: Fit parameters returned in the $D^0[K^-\pi^+]X^-$ fits (negative and positive charges fit separately).

		Negative Charge Fit														
Parameter		Correlation coefficients														
global	3	4	5	6	7	8	15	16	17							
3	0.20549	1.000	-0.132	-0.031	0.031	0.012	-0.004	0.030	-0.075	0.042						
4	0.55701	-0.132	1.000	-0.385	-0.191	0.077	0.070	-0.048	-0.205	0.131						
5	0.43732	-0.031	-0.385	1.000	0.022	-0.009	0.030	0.019	-0.082	0.061						
6	0.88276	0.031	-0.191	0.022	1.000	-0.122	-0.855	0.679	-0.012	0.008						
7	0.42289	0.012	0.077	-0.009	-0.122	1.000	0.022	-0.109	-0.195	0.150						
8	0.93736	-0.004	0.070	0.030	-0.855	0.022	1.000	-0.808	-0.056	0.038						
15	0.86889	0.030	-0.048	0.019	0.679	-0.109	-0.808	1.000	-0.214	0.165						
16	0.86243	-0.075	-0.205	-0.082	-0.012	-0.195	-0.056	-0.214	1.000	-0.816						
17	0.81931	0.042	0.131	0.061	0.008	0.150	0.038	0.165	-0.816	1.000						

		Positive Charge Fit														
Parameter		Correlation coefficients														
global	3	4	5	6	7	8	15	16	17							
3	0.19838	1.000	-0.123	-0.033	0.030	0.010	-0.002	0.031	-0.077	0.042						
4	0.54978	-0.123	1.000	-0.355	-0.207	0.080	0.090	-0.050	-0.233	0.148						
5	0.40812	-0.033	-0.355	1.000	0.024	-0.011	0.026	0.020	-0.073	0.051						
6	0.88130	0.030	-0.207	0.024	1.000	-0.132	-0.853	0.671	0.005	-0.006						
7	0.40654	0.010	0.080	-0.011	-0.132	1.000	0.039	-0.124	-0.174	0.127						
8	0.93590	-0.002	0.090	0.026	-0.853	0.039	1.000	-0.797	-0.085	0.061						
15	0.86584	0.031	-0.050	0.020	0.671	-0.124	-0.797	1.000	-0.214	0.160						
16	0.85497	-0.077	-0.233	-0.073	0.005	-0.174	-0.085	-0.214	1.000	-0.797						
17	0.80104	0.042	0.148	0.051	-0.006	0.127	0.061	0.160	-0.797	1.000						

Table 6.3: Correlation coefficients for the $D^0[K^-\pi^+]X^-$ fit components (negative and positive charges fit separately).

		mean bias (%)	pull mean ($\% \sigma$)	pull width ($\% \sigma$)
$D^0[K^-\pi^+]X$	$q < 0$	0.030 ± 0.014	3.977 ± 3.095	97.581 ± 2.209
	$q > 0$	0.000 ± 0.014	-2.780 ± 3.221	101.838 ± 2.282
$D^0[\pi^-\pi^+]X$	$q < 0$	0.077 ± 0.102	-9.367 ± 3.087	97.189 ± 2.225
	$q > 0$	-0.005 ± 0.107	-11.359 ± 2.970	93.249 ± 2.165
$D^0[K^-K^+]X$	$q < 0$	0.130 ± 0.060	0.463 ± 2.889	91.280 ± 2.056
	$q > 0$	0.087 ± 0.056	-1.289 ± 2.971	93.689 ± 2.131

Table 6.4: Three measures of fitter bias on the relative branching ratio $BR(B^- \rightarrow D^0 K^-)/BR(B^- \rightarrow D^0 \pi^-)$ for all three D^0 decay modes. For an unbiased fitter, the mean bias and the pull mean are expected to be consistent with 0, the pull width consistent with 1. *N.B.:* All quantities are expressed in % or $\% \sigma$.

Fit component	Mass PDF	Z PDF	normalization
$D^0[\pi^-\pi^+]X^-$ fits			
$B^- \rightarrow D^0\pi^-$	MC	prompt $D^* \rightarrow \pi, s : p$ reweight, shifted	floating
$B^- \rightarrow D^0\pi^-(n\gamma)$	MC	prompt $D^* \rightarrow \pi, s : p$ reweight, shifted	floating
$B^- \rightarrow D^0K^-$	MC	prompt $D^* \rightarrow K, s : p$ reweight	floating
$B^-/\bar{B}^0 \rightarrow D^{*(0/+)}\pi^-$	MC	prompt $D^* \rightarrow \pi, s : p$ reweight, shifted	floating
$B^- \rightarrow D^{*0}K^-$	MC	prompt $D^* \rightarrow K, s : p$ reweight	floating
$B^- \rightarrow D^0\rho^-$	MC	prompt $D^* \rightarrow \pi, s : p$ reweight, shifted	floating
$B^-/\bar{B}^0 \rightarrow D^0[K\pi]X$	MC	see Section 6.3.1 for explanation	constrained
$B^- \rightarrow \pi^-\pi^+\pi^-$	MC	see Section 6.3.1 for explanation	constrained
$B^- \rightarrow K^-\pi^+\pi^-$	MC	see Section 6.3.1 for explanation	constrained
$B^- \rightarrow K^-K^+K^-$	MC	see Section 6.3.1 for explanation	constrained
$B^-/\bar{B}^0 \rightarrow D^0X$ (remainder)	MC	see Section 6.2.1 for explanation	floating
fake- D background	D^0 SB	D^0 SB, signal-/reflection-subtracted	floating, shape fixed
real- D background	D^+X^+ WS SBS	D^+X^+ WS (D signal region)	floating, shape fixed

Table 6.5: Fit components of the $D^0[\pi^-\pi^+]X^-$ fits. See text for an explanation of the “Mass PDF” and “Z PDF” columns. “SB” denotes the D sidebands; “SBS” indicates sideband subtraction in the D mass.

fit component	par no	fit result
$B^- \rightarrow D^0 \pi^-$	3	$2.99089\text{e}+02 \pm 1.86871\text{e}+01$
$B^- \rightarrow D^0 \pi^- (n\gamma)$	4	$1.53332\text{e}+01 \pm 2.24045\text{e}+00$
$B^- \rightarrow D^0 K^-$	5	$2.74413\text{e}+01 \pm 1.00421\text{e}+01$
$B^- / \bar{B}^0 \rightarrow D^{*(0/+)} \pi^-$	6	$2.64404\text{e}+02 \pm 5.39924\text{e}+01$
$B^- \rightarrow D^{*0} K^-$	7	$2.18942\text{e}+01 \pm 2.77621\text{e}+00$
$B^- \rightarrow D^0 \rho^-$	8	$2.79015\text{e}+02 \pm 8.61973\text{e}+01$
$B^- / \bar{B}^0 \rightarrow D^0 [K\pi] X$	9	$3.83564\text{e}+01 \pm 3.23819\text{e}+00$
$B^- \rightarrow \pi^- \pi^+ \pi^-$	10	$4.98130\text{e}+00 \pm 5.85604\text{e}-01$
$B^- \rightarrow K^- \pi^+ \pi^-$	11	$1.33105\text{e}+01 \pm 1.92897\text{e}+00$
$B^- \rightarrow K^- K^+ K^-$	12	$1.35197\text{e}+01 \pm 1.32421\text{e}+00$
$B^- / \bar{B}^0 \rightarrow D^0 X (\text{remainder})$	15	$1.98201\text{e}+02 \pm 4.59952\text{e}+01$
fake- D background	16	$2.50917\text{e}+02 \pm 6.54352\text{e}+01$
real- D background	17	$1.68282\text{e}+02 \pm 4.13220\text{e}+01$
$B^+ \rightarrow \bar{D}^0 \pi^+$	3	$2.63423\text{e}+02 \pm 1.80189\text{e}+01$
$B^+ \rightarrow \bar{D}^0 \pi^+ (n\gamma)$	4	$1.34030\text{e}+01 \pm 2.00962\text{e}+00$
$B^+ \rightarrow \bar{D}^0 K^+$	5	$2.25848\text{e}+01 \pm 1.04848\text{e}+01$
$B^+ / B^0 \rightarrow \bar{D}^{*(0/-)} \pi^+$	6	$3.18836\text{e}+02 \pm 5.57496\text{e}+01$
$B^+ \rightarrow \bar{D}^{*0} K^+$	7	$1.88041\text{e}+01 \pm 2.48315\text{e}+00$
$B^+ \rightarrow \bar{D}^0 \rho^+$	8	$2.34167\text{e}+02 \pm 9.04034\text{e}+01$
$B^+ / B^0 \rightarrow \bar{D}^0 [K\pi] X$	9	$3.74213\text{e}+01 \pm 3.24379\text{e}+00$
$B^+ \rightarrow \pi^+ \pi^- \pi^+$	10	$4.38797\text{e}+00 \pm 5.30545\text{e}-01$
$B^+ \rightarrow K^+ \pi^- \pi^+$	11	$1.17840\text{e}+01 \pm 1.73618\text{e}+00$
$B^+ \rightarrow K^+ K^- K^+$	12	$1.18474\text{e}+01 \pm 1.21177\text{e}+00$
$B^+ / B^0 \rightarrow \bar{D}^0 X (\text{remainder})$	15	$2.35550\text{e}+02 \pm 4.80861\text{e}+01$
fake- D background	16	$2.88795\text{e}+02 \pm 6.14074\text{e}+01$
real- D background	17	$1.49125\text{e}+02 \pm 3.73858\text{e}+01$

Table 6.6: Fit parameters returned in the $D^0[\pi^- \pi^+]X^-$ fits (negative and positive charges fit separately).

		Negative Charge Fit																										
		Correlation coefficients																										
Parameter	global	3	4	5	6	7	8	9	10	11	12	15	16	17	3	4	5	6	7	8	9	10	11	12	15	16	17	
3	0.79317	1.000	0.421	-0.140	-0.022	0.497	0.018	-0.019	0.516	0.421	0.637	0.016	-0.128	0.053	0.421	1.000	-0.103	-0.028	0.256	0.014	-0.009	0.267	0.213	0.329	0.004	-0.074	0.030	
4	0.44175	0.421	1.000	-0.103	-0.028	0.256	0.014	-0.009	0.267	0.213	0.329	0.004	-0.074	0.030	-0.140	0.421	1.000	-0.029	-0.068	0.049	-0.053	-0.078	-0.146	-0.091	0.661	-0.179	0.110	
5	0.29582	-0.140	-0.103	1.000	0.029	-0.029	-0.067	-0.007	-0.078	-0.146	-0.091	0.661	-0.179	0.110	0.029	0.029	1.000	1.000	0.024	-0.867	-0.001	-0.010	0.212	0.018	0.219	0.008	0.028	
6	0.88463	-0.022	-0.028	0.029	1.000	-0.024	1.000	0.010	0.259	0.212	0.018	0.219	0.008	0.028	-0.068	-0.024	-0.001	1.000	0.010	-0.001	1.000	-0.010	-0.010	0.333	0.004	-0.070	0.029	
7	0.50325	0.497	0.256	-0.068	-0.024	1.000	0.010	-0.024	0.259	0.212	0.018	0.219	0.008	0.028	0.212	0.010	0.010	0.010	1.000	-0.001	-0.001	-0.010	-0.010	0.333	0.004	-0.070	0.029	
8	0.93612	0.018	0.014	0.049	-0.867	0.010	1.000	-0.001	-0.001	-0.010	-0.010	-0.010	-0.010	-0.010	-0.001	-0.001	-0.001	-0.001	-0.001	1.000	-0.001	-0.001	-0.001	-0.001	-0.001	-0.001	-0.001	
9	0.10553	-0.019	-0.009	-0.053	-0.007	-0.024	-0.001	1.000	-0.010	-0.010	-0.010	-0.010	-0.010	-0.010	-0.010	-0.010	-0.010	-0.010	-0.010	-0.010	1.000	0.219	0.271	1.000	0.004	-0.092	0.041	
10	0.51897	0.516	0.267	0.213	-0.023	0.212	0.018	0.018	0.219	0.271	0.333	0.004	-0.092	0.041	0.219	0.271	0.333	0.004	0.009	0.009	0.009	0.009	0.009	0.009	0.009	0.009	0.009	0.009
11	0.43364	0.421	0.213	-0.146	-0.023	0.212	0.018	0.018	0.219	0.271	0.333	0.004	-0.092	0.041	0.219	0.271	0.333	0.004	0.009	0.009	0.009	0.009	0.009	0.009	0.009	0.009	0.009	0.009
12	0.64131	0.637	0.329	-0.091	-0.025	0.314	0.015	-0.016	0.333	0.271	1.000	0.005	-0.092	0.041	0.314	0.015	-0.016	0.333	0.271	1.000	0.005	-0.092	0.041	0.005	-0.092	0.041	0.005	-0.092
15	0.85702	0.016	0.004	0.033	0.661	-0.004	-0.776	-0.019	0.009	0.004	0.005	1.000	0.005	-0.315	0.016	0.004	0.033	0.661	-0.004	-0.776	-0.019	0.009	0.004	0.005	1.000	0.005	-0.315	
16	0.88700	-0.128	-0.074	-0.179	-0.095	-0.089	-0.025	-0.028	-0.070	-0.068	-0.092	-0.315	1.000	-0.835	-0.128	-0.074	-0.179	-0.095	-0.089	-0.025	-0.028	-0.070	-0.068	-0.092	-0.315	1.000	-0.835	
17	0.84627	0.053	0.030	0.110	0.060	0.045	0.007	0.018	0.029	0.028	0.041	0.005	-0.092	0.041	0.030	0.030	0.110	0.060	0.045	0.007	0.018	0.029	0.028	0.041	0.005	-0.092	0.041	0.030

		Positive Charge Fit																										
		Correlation coefficients																										
Parameter	global	3	4	5	6	7	8	9	10	11	12	15	16	17	3	4	5	6	7	8	9	10	11	12	15	16	17	
3	0.81832	1.000	0.453	-0.170	-0.019	0.515	0.021	-0.014	0.554	0.460	0.671	0.014	-0.146	0.061	0.453	1.000	-0.114	-0.025	0.277	0.016	-0.007	0.299	0.244	0.361	0.002	-0.146	0.061	
4	0.47035	0.453	1.000	-0.114	-0.025	0.277	0.016	-0.007	0.299	0.244	0.361	0.002	-0.146	0.061	-0.170	0.453	1.000	-0.032	-0.085	0.055	-0.054	-0.099	-0.154	-0.115	0.028	-0.208	0.123	
5	0.33326	-0.170	-0.114	1.000	0.032	-0.085	-0.055	-0.054	-0.099	-0.154	-0.115	0.028	-0.208	0.123	0.032	1.000	1.000	1.000	0.024	-0.871	-0.011	-0.011	-0.022	0.344	-0.096	-0.076	0.040	
6	0.88705	-0.019	-0.025	0.032	1.000	-0.024	1.000	0.016	0.288	0.221	0.344	-0.006	-0.076	0.040	-0.011	0.032	1.000	0.016	0.016	1.000	0.005	0.012	-0.006	0.375	-0.085	-0.085	0.032	
7	0.51989	0.515	0.277	-0.085	-0.024	1.000	0.016	-0.018	0.288	0.221	0.344	-0.006	-0.076	0.040	0.016	0.016	0.016	1.000	0.016	0.016	1.000	0.005	0.012	-0.006	0.375	-0.085	0.032	
8	0.93965	0.021	0.016	0.055	-0.871	0.005	1.000	0.005	0.012	-0.008	-0.012	-0.008	-0.012	-0.008	0.005	0.005	0.005	0.005	1.000	-0.008	-0.008	-0.008	-0.012	-0.008	-0.008	-0.008	-0.008	
9	0.10090	-0.014	-0.007	-0.054	-0.011	0.018	1.000	0.005	0.012	-0.008	-0.012	-0.008	-0.012	-0.008	-0.014	-0.007	-0.007	-0.007	1.000	-0.011	-0.011	-0.011	-0.012	-0.012	-0.012	-0.012	-0.012	
10	0.55667	0.554	0.299	-0.099	-0.011	0.288	0.012	-0.008	0.257	0.257	0.375	0.009	-0.085	0.032	0.299	0.299	0.299	0.299	0.299	1.000	0.005	0.012	-0.006	0.375	-0.085	-0.085	0.032	
11	0.46991	0.460	0.244	-0.154	-0.021	0.240	0.019	-0.006	0.257	0.257	0.375	0.009	-0.085	0.032	0.244	0.244	0.244	0.244	0.244	0.244	1.000	0.004	0.004	0.004	0.004	0.004	0.004	
12	0.67405	0.671	0.361	-0.115	-0.022	0.344	0.018	-0.012	0.375	0.312	1.000	0.004	-0.106	0.046	0.361	0.361	0.361	0.361	0.361	0.361	1.000	0.004	0.004	0.004	0.004	0.004	0.004	
15	0.86392	0.014	0.002	0.028	0.685	-0.006	-0.802	-0.020	0.009	0.003	0.004	1.000	0.004	-0.175	0.014	0.002	0.028	0.685	-0.006	-0.802	-0.020	0.009	0.003	0.004	1.000	0.004	-0.175	
16	0.86641	-0.146	-0.085	-0.208	-0.076	-0.096	-0.046	-0.029	-0.085	-0.080	-0.106	0.004	1.000	-0.804	-0.146	-0.085	-0.208	-0.076	-0.096	-0.046	-0.029	-0.085	-0.080	-0.106	0.004	1.000	-0.804	
17	0.81657	0.061	0.035	0.123	0.040	0.046	0.019	0.018	0.036	0.032	0.046	0.005	-0.092	0.041	0.061	0.035	0.123	0.040	0.046	0.019	0.018	0.036	0.032	0.046	0.005	-0.092	0.041	0.061

Table 6.7: Correlation coefficients for the $D^0[\pi^- \pi^+]X^-$ fit components (negative and positive charges fit separately).

Fit component	Mass PDF	Z PDF	normalization
$D^0[K^-K^+]X^-$ fits			
$B^- \rightarrow D^0\pi^-$	MC	prompt $D^* \rightarrow \pi, s : p$ reweight, shifted	floating
$B^- \rightarrow D^0\pi^-(n\gamma)$	MC	prompt $D^* \rightarrow \pi, s : p$ reweight, shifted	floating
$B^- \rightarrow D^0K^-$	MC	prompt $D^* \rightarrow K, s : p$ reweight	floating
$B^-/\bar{B}^0 \rightarrow D^{*(0/+)}\pi^-$	MC	prompt $D^* \rightarrow \pi, s : p$ reweight, shifted	floating
$B^- \rightarrow D^{*0}K^-$	MC	prompt $D^* \rightarrow K, s : p$ reweight	floating
$B^- \rightarrow D^0\rho^-$	MC	prompt $D^* \rightarrow \pi, s : p$ reweight, shifted	floating
$B^-/\bar{B}^0 \rightarrow D^0[K\pi]X$	MC	see Section 6.3.1 for explanation	constrained
$B^- \rightarrow \pi^-\pi^+\pi^-$	MC	see Section 6.3.1 for explanation	constrained
$B^- \rightarrow K^-\pi^+\pi^-$	MC	see Section 6.3.1 for explanation	constrained
$B^- \rightarrow K^-K^+K^-$	MC	see Section 6.3.1 for explanation	constrained
$B^-/\bar{B}^0 \rightarrow D^0X$ (remainder)	MC	see Section 6.2.1 for explanation	floating
fake- D background	D^0 SB	D^0 SB, reflection-subtracted	floating; shape fixed
real- D background	D^+X^+ WS SBS	D^+X^+ WS (D signal region)	floating; shape fixed

Table 6.8: Fit components of the $D^0[K^-K^+]X^-$ fits. See text for an explanation of the “Mass PDF” and “Z PDF” columns. “SB” denotes the D sidebands; “SBS” indicates sideband subtraction in the D mass.

fit component	par no	fit result
$B^- \rightarrow D^0 \pi^-$	3	$9.84588\text{e}+02 \pm 3.67479\text{e}+01$
$B^- \rightarrow D^0 \pi^- (n\gamma)$	4	$5.14315\text{e}+01 \pm 6.97615\text{e}+00$
$B^- \rightarrow D^0 K^-$	5	$1.05735\text{e}+02 \pm 2.08317\text{e}+01$
$B^- / \bar{B}^0 \rightarrow D^{*(0/+)} \pi^-$	6	$1.34926\text{e}+03 \pm 1.22326\text{e}+02$
$B^- \rightarrow D^{*0} K^-$	7	$6.86363\text{e}+01 \pm 8.25196\text{e}+00$
$B^- \rightarrow D^0 \rho^-$	8	$9.39637\text{e}+02 \pm 2.07506\text{e}+02$
$B^- / \bar{B}^0 \rightarrow D^0 [K\pi] X$	9	$1.13942\text{e}+02 \pm 5.75443\text{e}+00$
$B^- \rightarrow \pi^- \pi^+ \pi^-$	10	$5.52854\text{e}+00 \pm 5.98054\text{e}-01$
$B^- \rightarrow K^- \pi^+ \pi^-$	11	$4.05869\text{e}+01 \pm 5.67565\text{e}+00$
$B^- \rightarrow K^- K^+ K^-$	12	$1.39600\text{e}+01 \pm 1.18580\text{e}+00$
$B^- / \bar{B}^0 \rightarrow D^0 X (\text{remainder})$	15	$9.97438\text{e}+02 \pm 1.05099\text{e}+02$
fake- D background	16	$2.20435\text{e}+03 \pm 1.69643\text{e}+02$
real- D background	17	$3.75704\text{e}+02 \pm 4.92732\text{e}+01$
$B^+ \rightarrow \bar{D}^0 \pi^+$	3	$1.00853\text{e}+03 \pm 3.68506\text{e}+01$
$B^+ \rightarrow \bar{D}^0 \pi^+ (n\gamma)$	4	$5.21808\text{e}+01 \pm 7.11644\text{e}+00$
$B^+ \rightarrow \bar{D}^0 K^+$	5	$8.39370\text{e}+01 \pm 2.01090\text{e}+01$
$B^+ / B^0 \rightarrow \bar{D}^{*(0/-)} \pi^+$	6	$1.27091\text{e}+03 \pm 1.23962\text{e}+02$
$B^+ \rightarrow \bar{D}^{*0} K^+$	7	$7.27628\text{e}+01 \pm 8.47457\text{e}+00$
$B^+ \rightarrow \bar{D}^0 \rho^+$	8	$9.90939\text{e}+02 \pm 2.07552\text{e}+02$
$B^+ / B^0 \rightarrow \bar{D}^0 [K\pi] X$	9	$1.14096\text{e}+02 \pm 5.75681\text{e}+00$
$B^+ \rightarrow \pi^+ \pi^- \pi^+$	10	$5.60917\text{e}+00 \pm 6.09354\text{e}-01$
$B^+ \rightarrow K^+ \pi^- \pi^+$	11	$4.40637\text{e}+01 \pm 5.77912\text{e}+00$
$B^+ \rightarrow K^+ K^- K^+$	12	$1.42903\text{e}+01 \pm 1.20883\text{e}+00$
$B^+ / B^0 \rightarrow \bar{D}^0 X (\text{remainder})$	15	$8.75158\text{e}+02 \pm 1.06665\text{e}+02$
fake- D background	16	$2.47280\text{e}+03 \pm 1.62181\text{e}+02$
real- D background	17	$2.73976\text{e}+02 \pm 4.39580\text{e}+01$

Table 6.9: Fit parameters returned in the $D^0[K^-K^+]X^-$ fits (negative and positive charges fit separately).

		Negative Charge Fit																										
		Correlation coefficients																										
Parameter	global	3	4	5	6	7	8	9	10	11	12	15	16	17	3	4	5	6	7	8	9	10	11	12	15	16	17	
3	0.63674	1.000	0.276	-0.041	0.009	0.322	0.074	0.002	0.342	0.290	0.435	0.089	-0.281	0.092	0.276	1.000	-0.046	0.004	0.308	0.089	0.002	0.354	0.272	0.443	0.092	-0.291	0.108	
4	0.33544	0.276	1.000	0.046	-0.015	0.147	0.046	0.004	0.152	0.136	0.194	0.045	-0.163	0.062	0.287	0.276	1.000	-0.022	0.142	0.054	0.004	0.160	0.129	0.200	0.046	-0.169	0.071	
5	0.37773	-0.046	0.046	1.000	0.022	0.002	0.123	-0.010	-0.014	0.032	-0.066	0.088	-0.327	0.159	-0.049	-0.046	1.000	1.000	-0.035	-0.035	-0.012	-0.017	0.028	-0.324	0.080	-0.291	0.108	
6	0.88928	0.004	-0.015	0.009	1.000	-0.021	-0.836	0.000	0.002	0.012	0.000	0.664	-0.073	0.029	0.004	0.002	0.000	1.000	0.000	0.000	0.001	0.001	0.007	-0.000	0.046	0.089	0.000	
7	0.32734	0.308	0.142	-0.003	-0.021	1.000	0.038	-0.004	0.113	0.091	0.141	0.016	-0.134	0.058	0.054	0.021	0.000	0.000	1.000	0.038	-0.004	0.113	0.091	0.141	0.016	-0.134	0.058	
8	0.94336	0.089	0.054	0.140	-0.021	0.038	1.000	0.012	0.034	0.056	0.042	-0.641	-0.299	0.175	0.089	0.054	0.140	1.000	0.012	0.034	0.056	-0.004	0.001	0.161	0.025	-0.337	0.190	
9	0.08391	0.002	0.004	-0.012	-0.000	-0.004	0.012	1.000	0.001	0.009	0.001	0.000	-0.049	0.009	0.004	0.004	0.000	0.000	1.000	0.001	0.001	0.009	0.001	0.125	0.043	-0.337	0.190	
10	0.35952	0.354	0.160	-0.017	0.001	0.113	0.034	-0.004	0.099	1.000	0.125	0.062	-0.111	0.029	0.129	0.160	-0.017	0.001	0.001	1.000	0.001	0.001	0.099	0.125	0.062	-0.111	0.029	
11	0.31509	0.272	0.129	0.028	-0.000	0.091	0.056	-0.004	0.161	0.000	0.125	0.062	-0.111	0.029	0.443	0.129	0.028	-0.000	0.001	0.000	0.001	0.001	0.001	0.001	0.001	0.001	0.001	0.001
12	0.45222	0.443	0.200	-0.067	-0.000	0.141	0.042	0.001	0.161	0.000	0.125	0.062	-0.111	0.029	0.080	0.200	-0.067	-0.000	0.000	0.000	0.000	0.000	0.000	0.000	0.000	0.000	0.000	0.000
15	0.85728	0.092	0.046	0.080	0.648	0.016	-0.641	0.000	0.035	0.062	0.043	1.000	0.337	0.190	0.092	0.046	0.080	0.648	0.016	-0.641	0.000	0.035	0.062	0.043	1.000	0.337	0.190	
16	0.89044	-0.291	-0.169	-0.324	-0.046	-0.134	-0.299	-0.049	-0.111	-0.177	-0.137	-0.337	1.000	0.639	-0.291	-0.169	-0.324	-0.046	-0.134	-0.299	-0.049	-0.111	-0.177	-0.137	-0.337	1.000	0.639	
17	0.66320	0.108	0.071	0.168	0.014	0.058	0.175	0.009	0.029	0.006	0.052	0.190	0.639	1.000	0.108	0.071	0.168	0.014	0.058	0.175	0.009	0.029	0.006	0.052	0.190	0.639	1.000	

		Positive Charge Fit																										
		Correlation coefficients																										
Parameter	global	3	4	5	6	7	8	9	10	11	12	15	16	17	3	4	5	6	7	8	9	10	11	12	15	16	17	
3	0.63165	1.000	0.276	-0.041	0.009	0.322	0.074	0.002	0.342	0.290	0.435	0.089	-0.281	0.092	0.276	1.000	-0.046	0.009	0.308	0.089	0.002	0.354	0.272	0.443	0.092	-0.291	0.108	
4	0.32698	0.276	1.000	0.046	-0.015	0.147	0.046	0.004	0.152	0.136	0.194	0.045	-0.163	0.062	0.287	0.276	1.000	-0.022	0.142	0.054	0.004	0.160	0.129	0.200	0.046	-0.169	0.071	
5	0.37567	-0.041	0.046	1.000	0.022	0.002	0.123	-0.010	-0.014	0.032	-0.066	0.088	-0.327	0.159	-0.049	-0.046	1.000	1.000	-0.035	-0.035	-0.012	-0.017	0.028	-0.324	0.080	-0.291	0.108	
6	0.89309	0.009	-0.015	0.009	1.000	-0.021	-0.836	0.000	0.002	0.012	0.000	0.664	-0.073	0.029	0.004	0.002	0.000	1.000	0.000	0.000	0.001	0.001	0.007	-0.000	0.046	0.089	0.000	
7	0.34365	0.322	0.147	-0.002	-0.021	1.000	0.038	-0.004	0.114	0.091	0.141	0.016	-0.134	0.058	0.054	0.021	0.000	0.000	1.000	0.038	-0.004	0.114	0.091	0.141	0.016	-0.134	0.058	
8	0.94341	0.074	0.046	0.123	-0.021	0.041	1.000	0.012	0.028	0.051	0.035	-0.664	-0.251	0.136	0.089	0.046	0.123	1.000	0.012	0.028	0.051	-0.004	0.001	0.161	0.025	-0.337	0.190	
9	0.08543	0.002	0.004	-0.010	-0.000	0.012	0.001	1.000	0.001	0.009	0.001	0.000	-0.049	0.009	0.004	0.004	0.000	0.000	1.000	0.001	0.001	0.009	0.001	0.125	0.043	-0.337	0.190	
10	0.34731	0.342	0.152	-0.014	0.002	0.114	0.028	-0.004	0.161	0.000	0.125	0.062	-0.111	0.029	0.129	0.160	-0.017	0.001	0.001	1.000	0.001	0.001	0.099	0.125	0.062	-0.111	0.029	
11	0.33495	0.290	0.136	0.032	-0.003	0.104	0.051	-0.003	0.131	0.000	0.131	0.068	-0.191	0.006	0.443	0.136	0.032	-0.003	0.001	0.000	0.001	0.001	0.001	0.001	0.001	0.001	0.001	0.001
12	0.44478	0.435	0.194	-0.066	0.002	0.145	0.035	0.001	0.153	0.131	1.000	0.041	-0.131	0.044	0.092	0.194	-0.066	0.002	0.000	0.000	0.000	0.000	0.000	0.000	0.000	0.000	0.000	0.000
15	0.86272	0.089	0.045	0.088	0.664	0.016	-0.664	0.002	0.033	0.068	0.041	1.000	0.352	0.186	0.089	0.045	0.088	0.664	0.016	-0.664	0.002	0.033	0.068	0.041	1.000	0.352	0.186	
16	0.87924	-0.281	-0.163	-0.327	-0.046	-0.146	-0.251	-0.053	-0.104	-0.191	-0.131	-0.352	1.000	0.600	-0.281	-0.163	-0.327	-0.046	-0.146	-0.251	-0.053	-0.104	-0.191	-0.131	-0.352	1.000	0.600	
17	0.62510	0.092	0.062	0.159	0.029	0.060	0.136	0.011	0.024	0.006	0.044	0.186	0.600	1.000	0.092	0.062	0.159	0.029	0.060	0.136	0.011	0.024	0.006	0.044	0.186	0.600	1.000	

Table 6.10: Correlation coefficients for the $D^0[K^-K^+]X^-$ fit components (negative and positive charges fit separately).

	$q < 0$	$q > 0$
$D^0[K^-\pi^+]X$	0.0784 ± 0.0046	0.0741 ± 0.0043
$D^0[\pi^-\pi^+]X$	0.0862 ± 0.0345	0.0805 ± 0.0405
$D^0[K^-K^+]X$	0.1008 ± 0.0214	0.0781 ± 0.0197

Table 6.11: Central values and statistical errors of the relative branching ratios $BR(B^- \rightarrow D^0 K^-)/BR(B^- \rightarrow D^0 \pi^-)$ before XFT corrections.

	combined	$D^0[\pi^-\pi^+]$	$D^0[K^-K^+]$
R	0.0761 ± 0.0032	—	—
$R_{\text{CP}+}$	1.149 ± 0.173	1.101 ± 0.348	1.163 ± 0.197
$A_{\text{CP}+}$	0.103 ± 0.145	0.034 ± 0.321	0.127 ± 0.162

Table 6.12: Summary of statistical uncertainties on R , $R_{\text{CP}+}$, and $A_{\text{CP}+}$ for all three D^0 modes. Statistical uncertainties and central values also listed for reference. *N.B.:* Values quoted for R do not include the XFT correction factor of 1.050 ± 0.028 .

				$D^0[K^-\pi^+]X$	$q < 0$	$q > 0$	$D^0[\pi^-\pi^+]X$	$q < 0$	$q > 0$	$D^0[K^-K^+]X$	$q < 0$	$q > 0$
mass	scale	+1 σ	0.02	0.01	0.07	0.03	0.05	0.04				
		-1 σ	-0.03	-0.02	-0.03	-0.05	-0.04	-0.04				
		+1 σ	-0.04	0.00	0.02	0.16	-0.03	-0.02				
	resolution	-1 σ	-0.02	0.01	0.02	-0.11	-0.03	0.04				
		+1 σ	-0.11	-0.10	-0.08	-0.09	-0.14	-0.13				
		-1 σ	0.14	0.14	0.08	0.06	0.08	0.07				
Z	π shift stat.	+1 σ	-0.11	-0.10	-0.08	-0.09	-0.14	-0.13				
		-1 σ	0.14	0.14	0.08	0.06	0.08	0.07				
	K shift	-0.39	-0.19	-0.37	-0.19	-0.47	-0.20					
		-0.03	-0.03	-0.02	-0.03	-0.04	-0.03					
	sample dependence	-0.03	-0.03	-0.02	-0.03	-0.04	-0.03					
		0.01	0.01	-0.02	0.01	0.13	0.11					
real- D shape	+1 σ	-0.00	0.00	0.11	0.11	—						
	-1 σ	0.00	0.00	-0.07	-0.12	—						
bkgd mass shape	exp. slope	+1 σ	-0.00	0.00	0.11	0.11	—					
		-1 σ	0.00	0.00	-0.07	-0.12	—					

Table 6.13: Systematic uncertainties on the relative branching ratio $BR(B^- \rightarrow D^0 K^-)/BR(B^- \rightarrow D^0 \pi^-)$ for all three D^0 decay modes. *N.B.*: All values quoted are percentages. See text for details.

	R	$R_{\text{CP}+}$	$A_{\text{CP}+}$	corr. type
mass scale	0.0002	0.004	0.000	(ii)
mass resolution	0.0002	0.003	0.002	(ii)
pion Z shift	0.0010	0.016	0.010	(iii)
kaon Z shift	0.0028	0.001	0.010	(ii)
pion Z sample dependence	0.0002	0.004	0.002	(i)
real- D background shape	0.0001	0.009	0.008	(i)
fake- D background shape	0.0000	0.002	0.002	(i)
fitter bias	0.0001	0.008	0.007	(i)
total systematic error	0.0030	0.021	0.018	—
statistical error	0.0032	0.173	0.145	—
central value	0.0761	1.149	0.103	—

Table 6.14: Systematic uncertainties on R , $R_{\text{CP}+}$, and $A_{\text{CP}+}$. Statistical uncertainties and central values also listed for reference. *N.B.*: Values quoted for R do not include the XFT correction factor of 1.050 ± 0.028 .

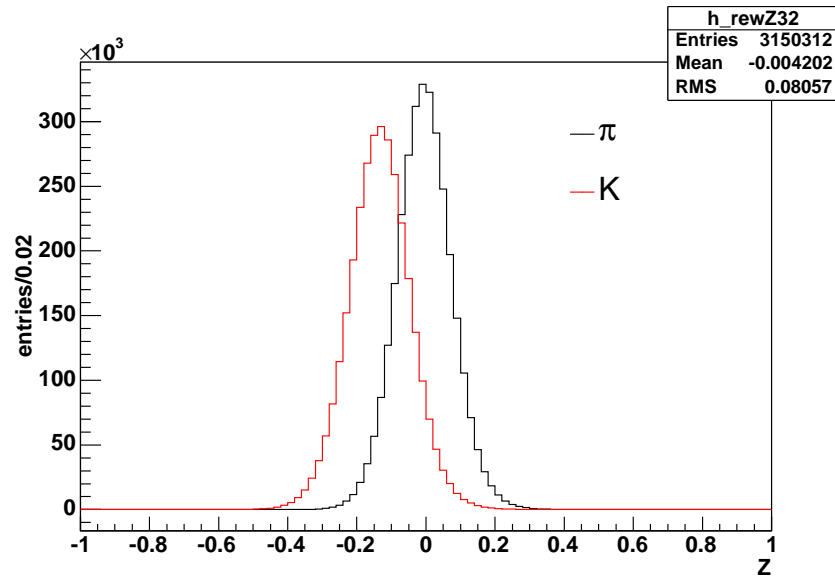


Figure 6.1: Pion and kaon Z template histograms for the $D^0[K^-\pi^+]X^-$ fit (both charges). These are obtained from the prompt D^* sample and reweighted simultaneously in $secance$ and p to the $D^0[K^-\pi^+]X^-$ distributions. Templates are shown before any ad hoc shift.

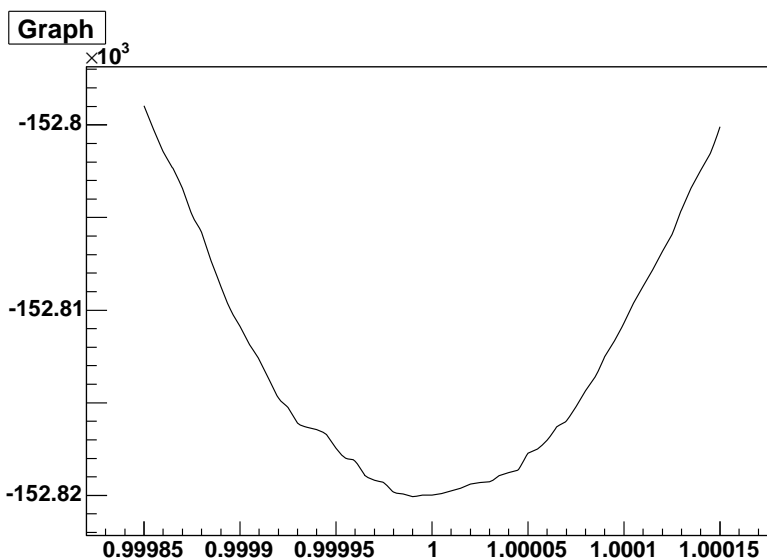


Figure 6.2: The negative log-likelihood of the fit on the $D^0[K^-\pi^+]X^-$ sample (both charges combined) as a function of the Monte Carlo mass-scale correction. The x -axis is the mass scale relative to the value 1.000233. To obtain the absolute mass scale, divide the x -axis value *into* 1.000233.

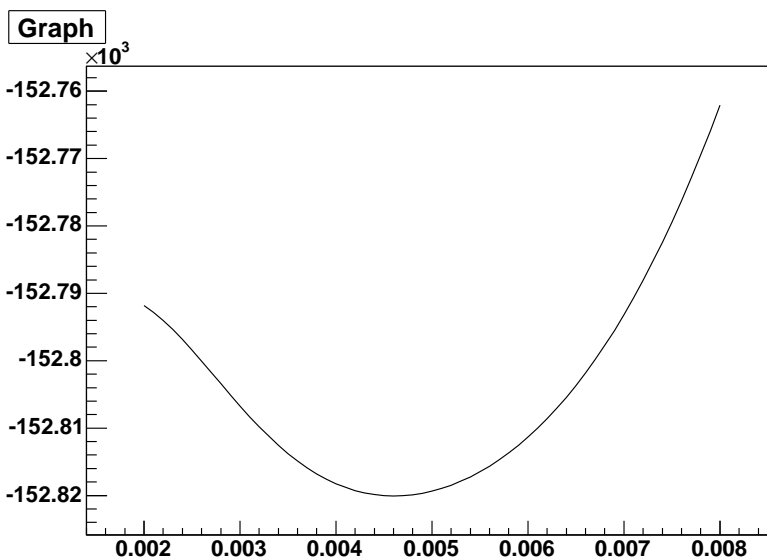


Figure 6.3: The negative log-likelihood of the $D^0[K^-\pi^+]X^-$ sample fit (both charges combined) as a function of the Monte Carlo smearing width.

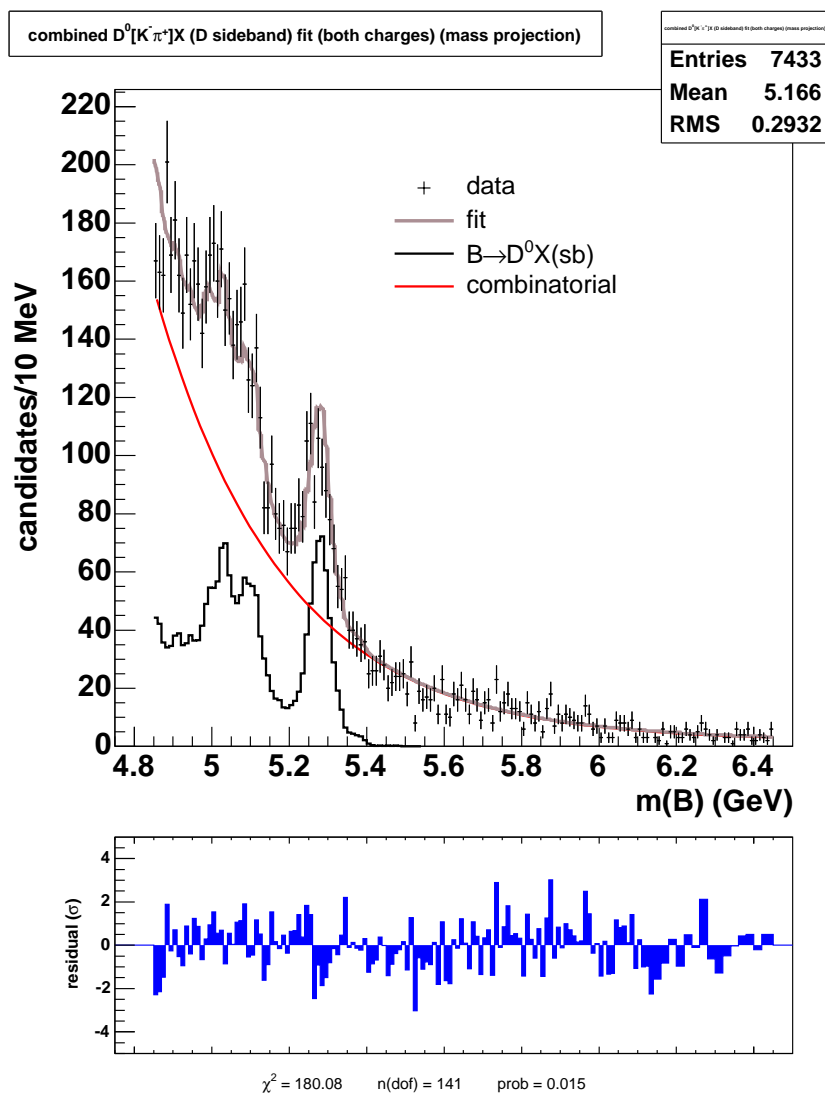


Figure 6.4: Auxiliary D^0 -sideband fit for the $D^0[K^-\pi^+]X^-$ sample (both charges).

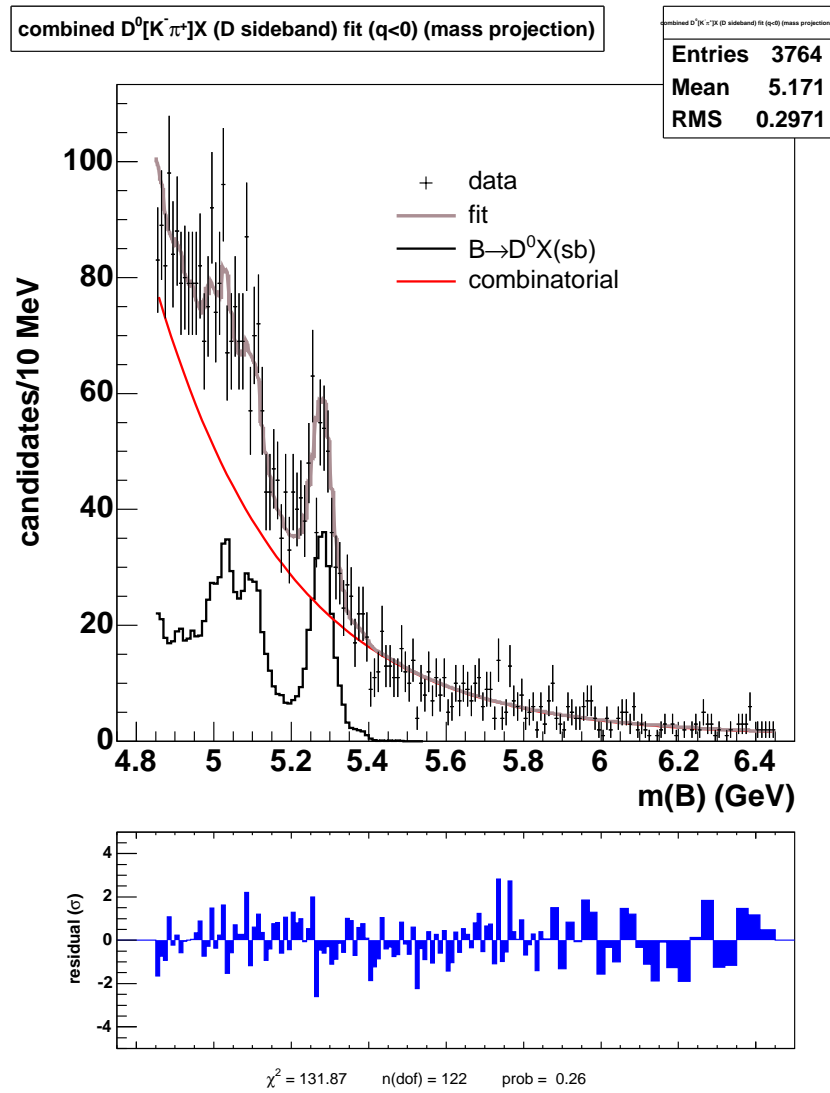


Figure 6.5: Auxiliary D^0 -sideband fit for the $D^0[K^-\pi^+]X^-$ sample (X^- only).

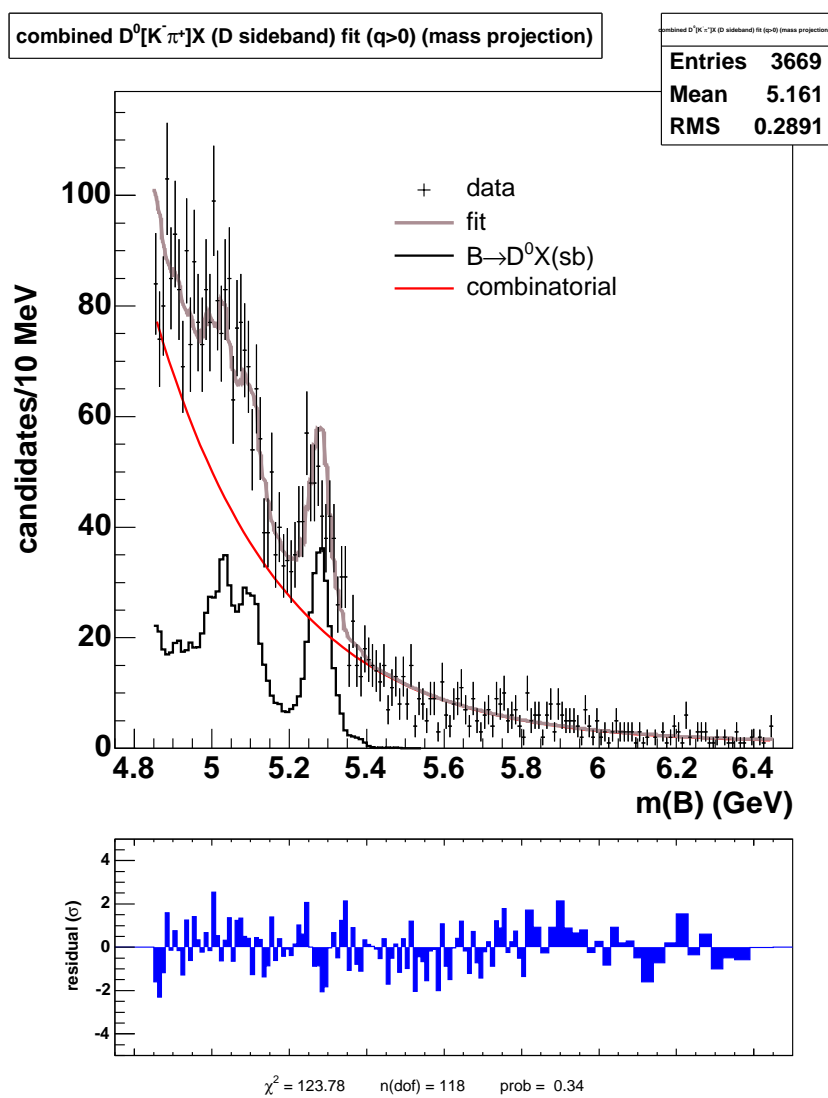


Figure 6.6: Auxiliary D^0 -sideband fit for the $\bar{D}^0[K^+\pi^-]X^+$ sample (X^+ only).

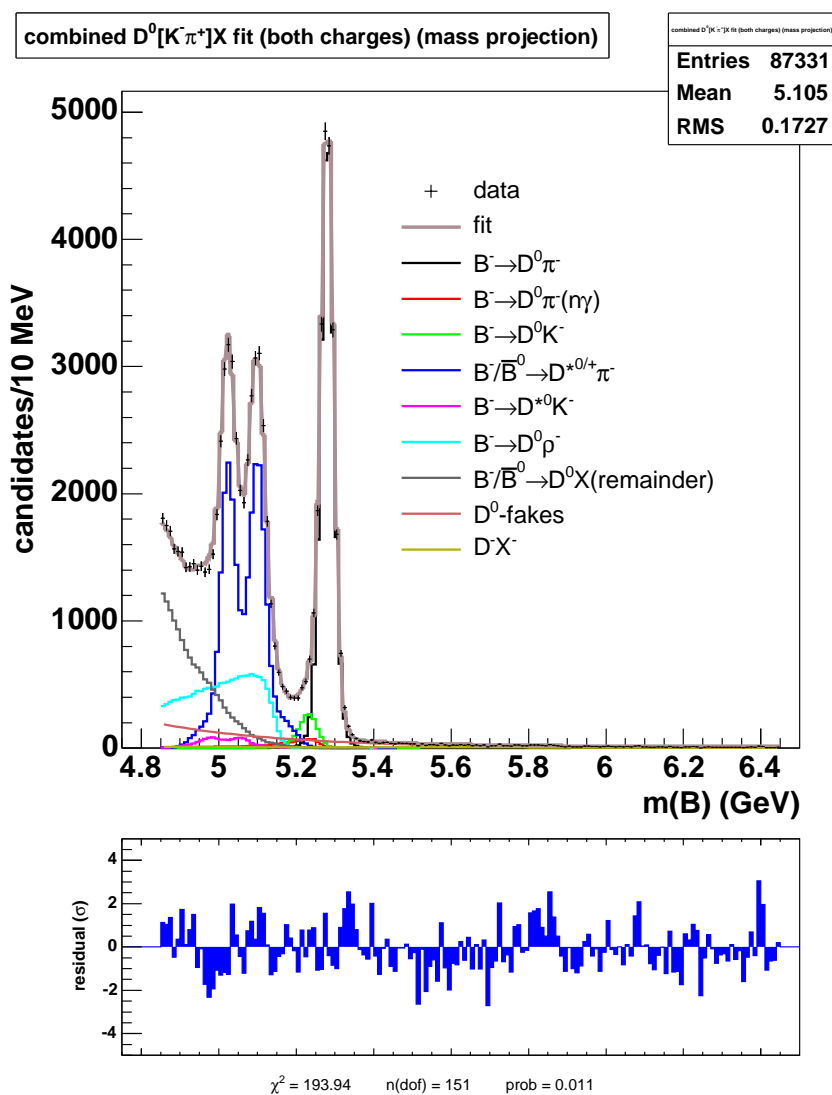


Figure 6.7: Mass projection of the fit on the $D^0[K^-\pi^+]X^-$ sample (both charges). (Fit not used in measuring R_c .)

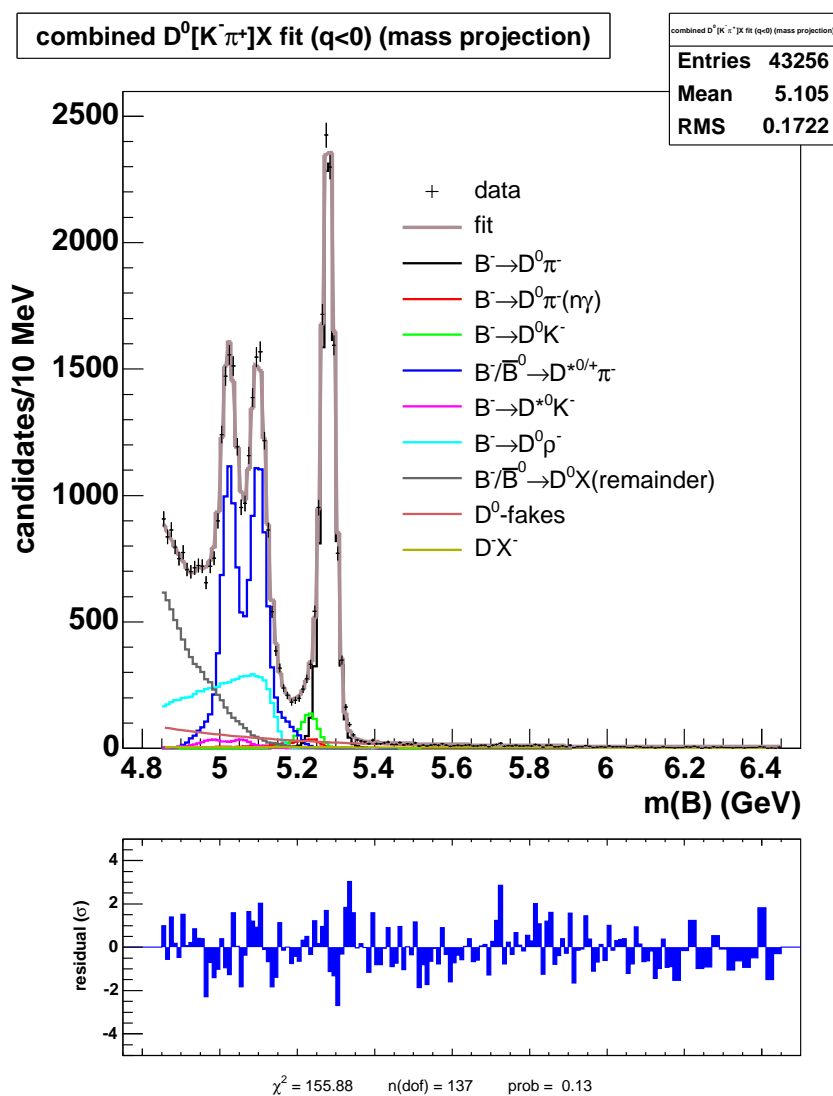


Figure 6.8: Mass projection of the fit on the $D^0[K^-\pi^+]X^-$ sample (X^- only).

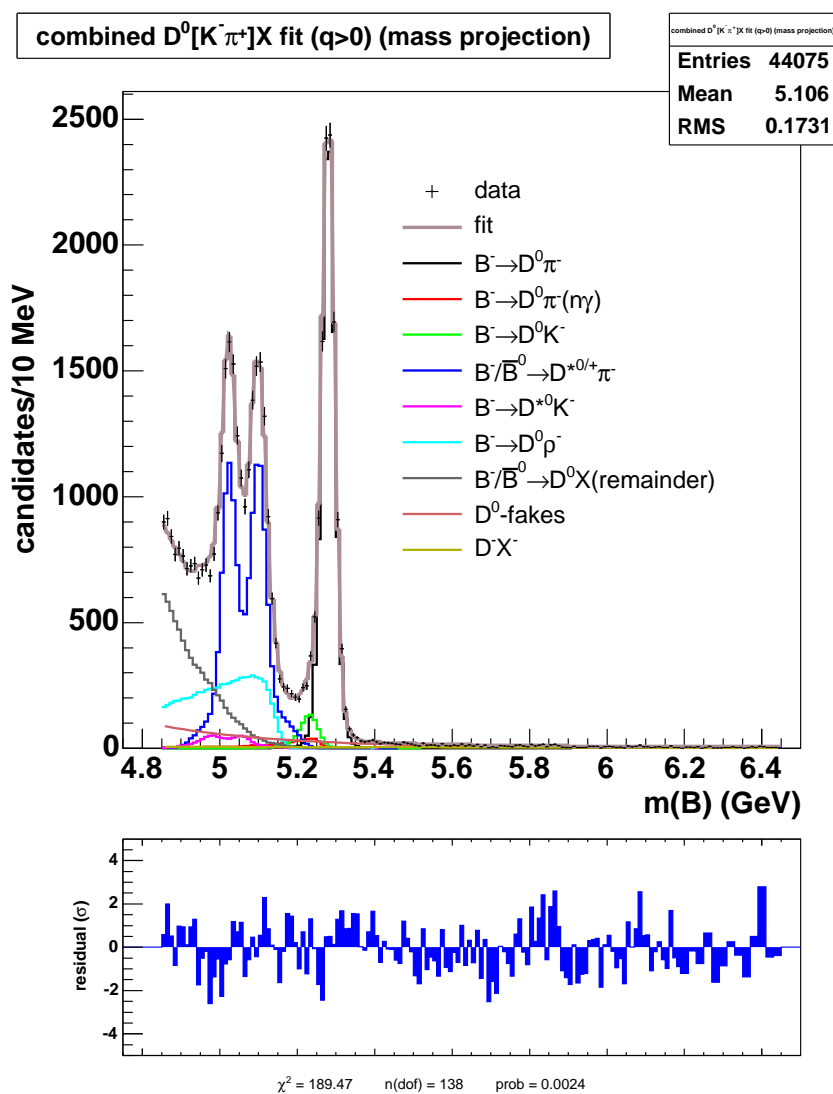


Figure 6.9: Mass projection of the fit on the $\bar{D}^0[K^+\pi^-]X^+$ sample (X^+ only).

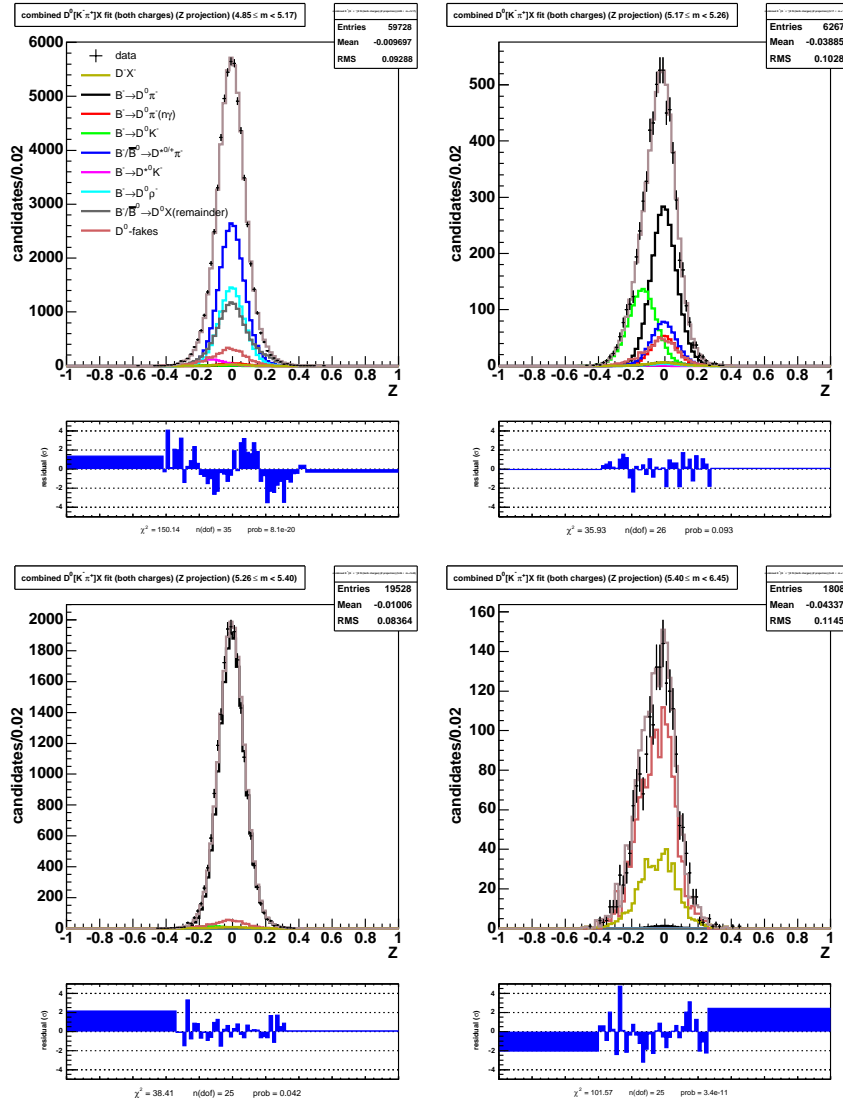


Figure 6.10: Z projections of the fit on the $D^0[K^-\pi^+]X^-$ sample (both charges). The Z projections are shown in four B mass regions:

upper-left	$[4.85, 5.17]$ GeV	upper-right	$[5.17, 5.26]$ GeV
lower-left	$[5.26, 5.40]$ GeV	lower-right	$[5.40, 6.45]$ GeV

The pion-dominated region is shown in the lower-left plot. This fit is not used for measuring R .

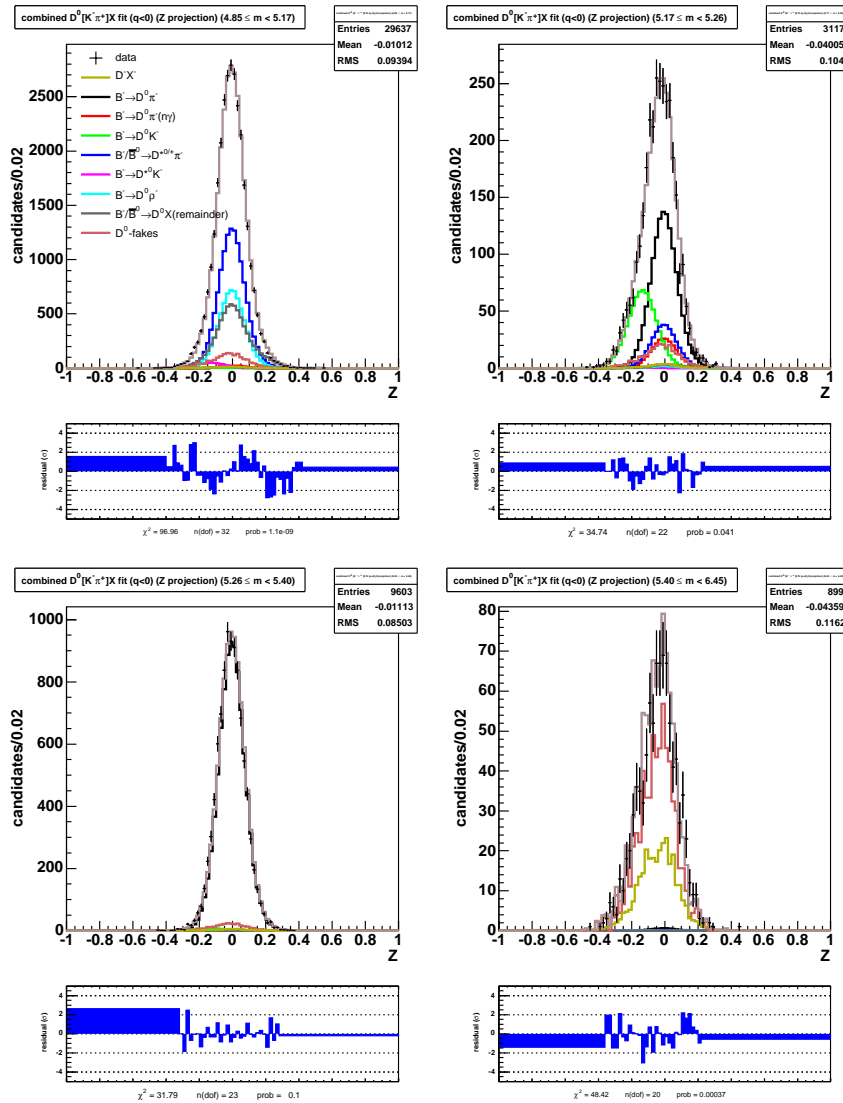


Figure 6.11: Z projections of the fit on the $D^0[K^-\pi^+]X^-$ sample (X^- only). The Z projections are shown in four B mass regions:

upper-left	[4.85, 5.17] GeV	upper-right	[5.17, 5.26] GeV
lower-left	[5.26, 5.40] GeV	lower-right	[5.40, 6.45] GeV

The pion-dominated region is shown in the lower-left plot.

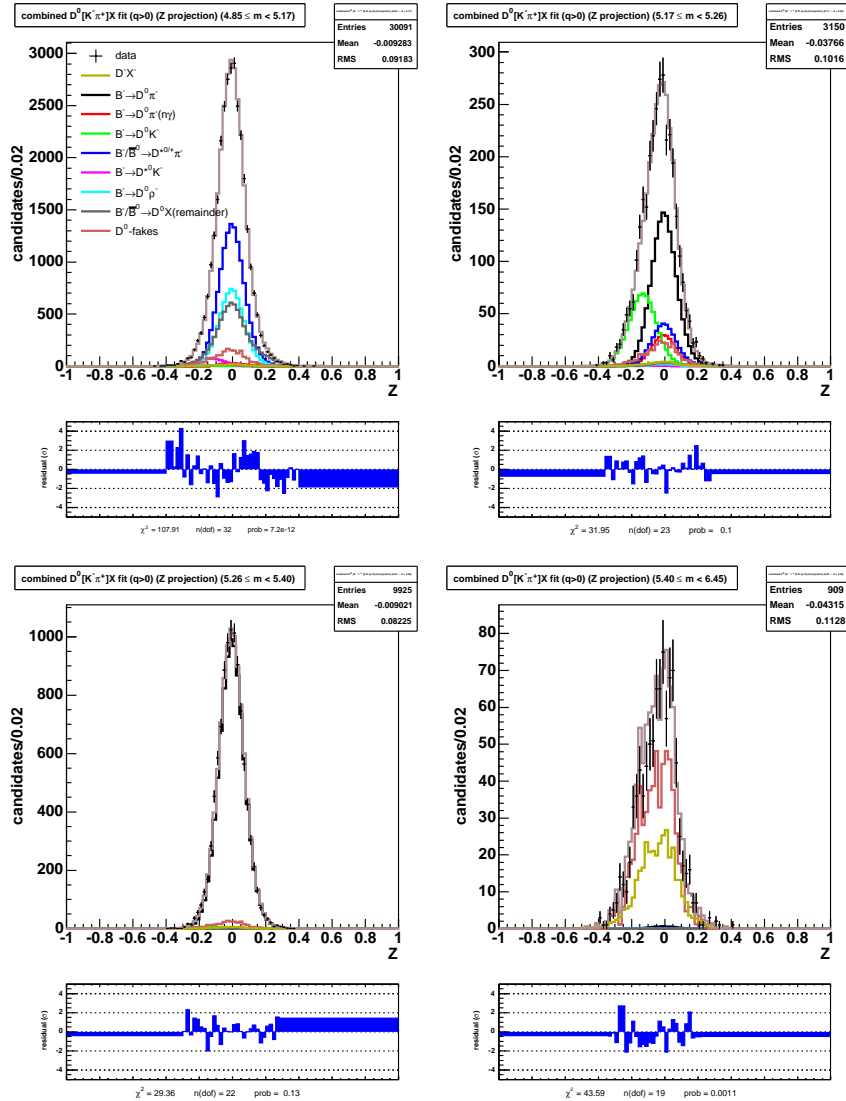


Figure 6.12: Z projections of the fit on the $\bar{D}^0[K^+\pi^-]X^+$ sample (X^+ only). The Z projections are shown in four B mass regions:

upper-left	$[4.85, 5.17]$ GeV	upper-right	$[5.17, 5.26]$ GeV
lower-left	$[5.26, 5.40]$ GeV	lower-right	$[5.40, 6.45]$ GeV

The pion-dominated region is shown in the lower-left plot.

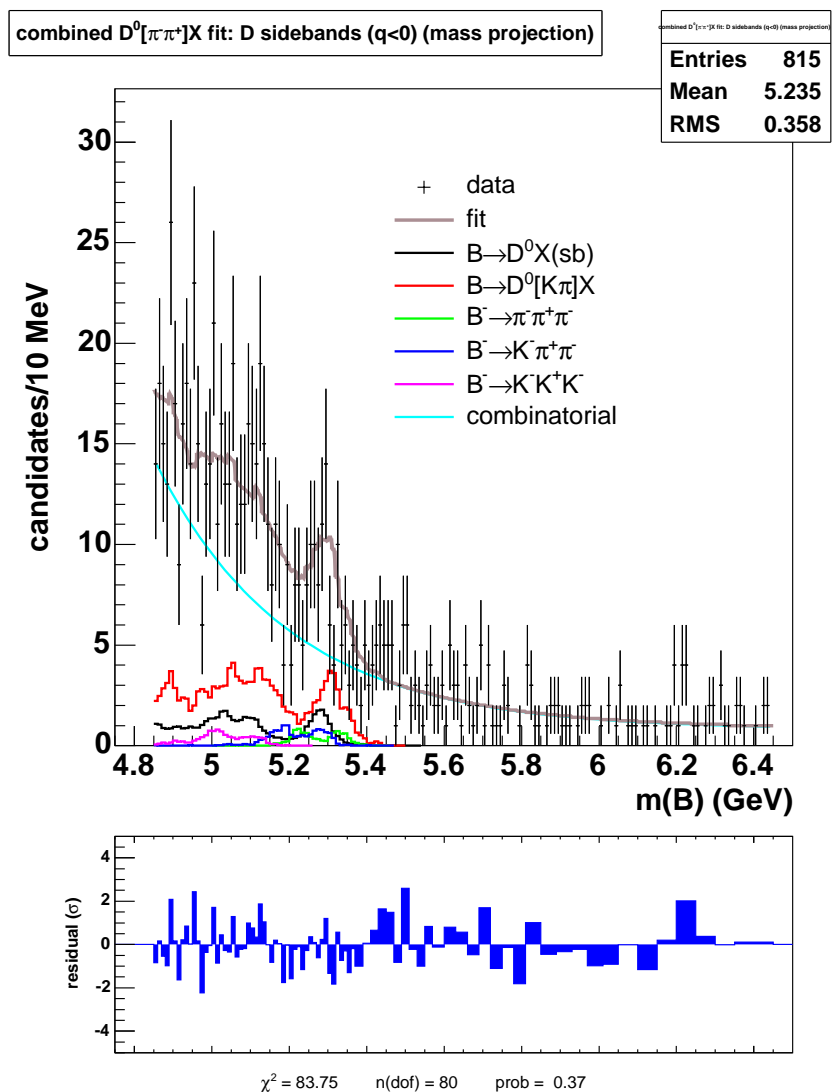


Figure 6.13: Auxiliary D^0 -sideband fit for the $D^0[\pi^-\pi^+]X^-$ sample (X^- only).

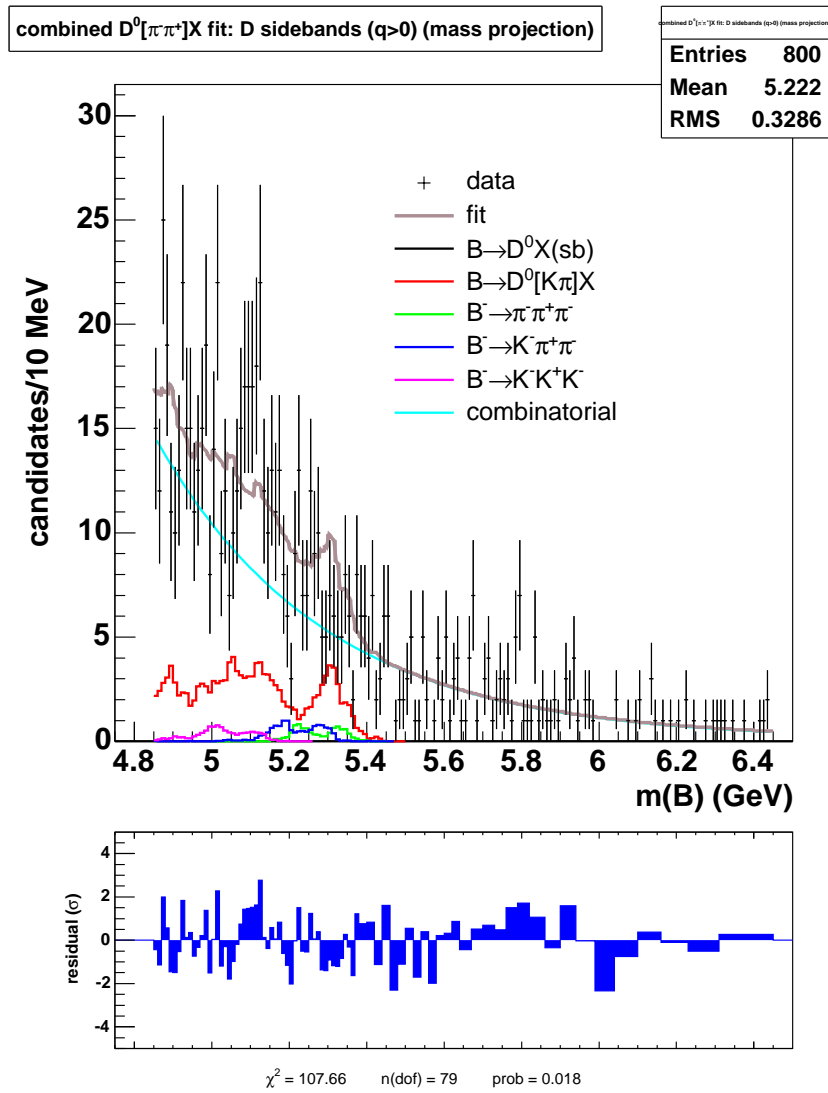


Figure 6.14: Auxiliary D^0 -sideband fit for the $\overline{D}^0[\pi^+\pi^-]X^+$ sample (X^+ only).

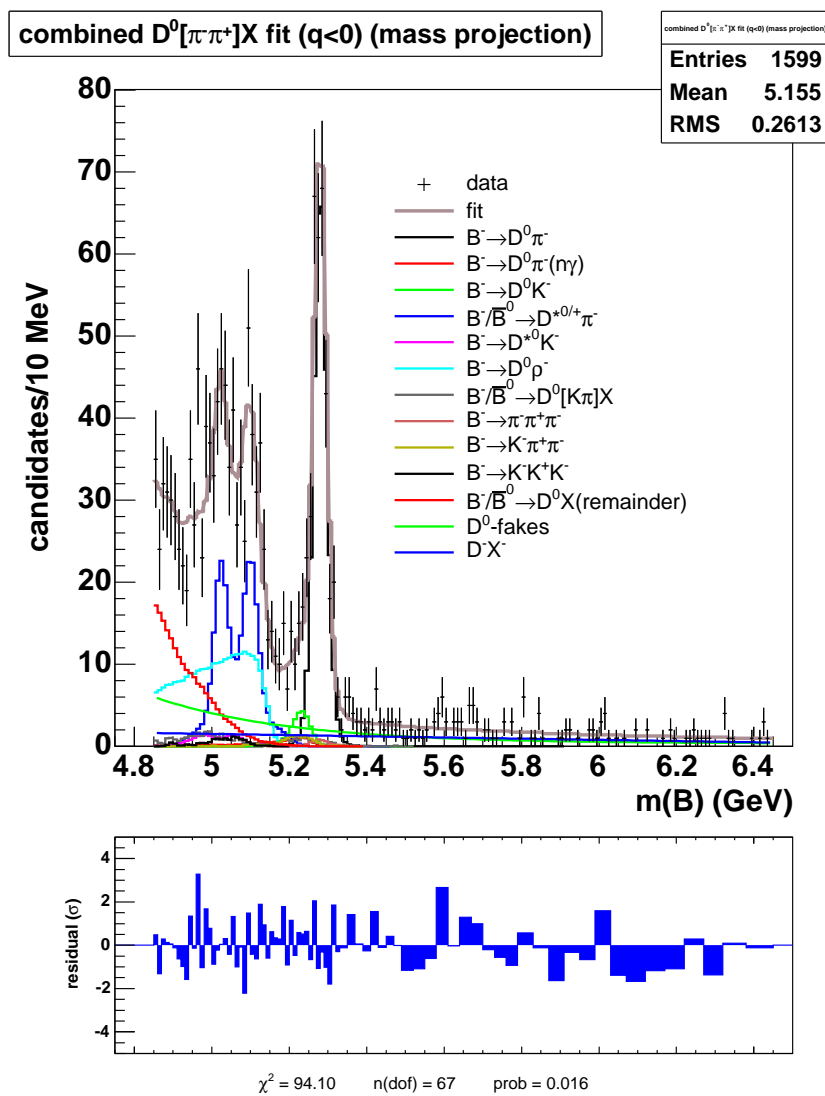


Figure 6.15: Mass projection of the fit on the $D^0[\pi^-\pi^+]X^-$ sample (X^- only).

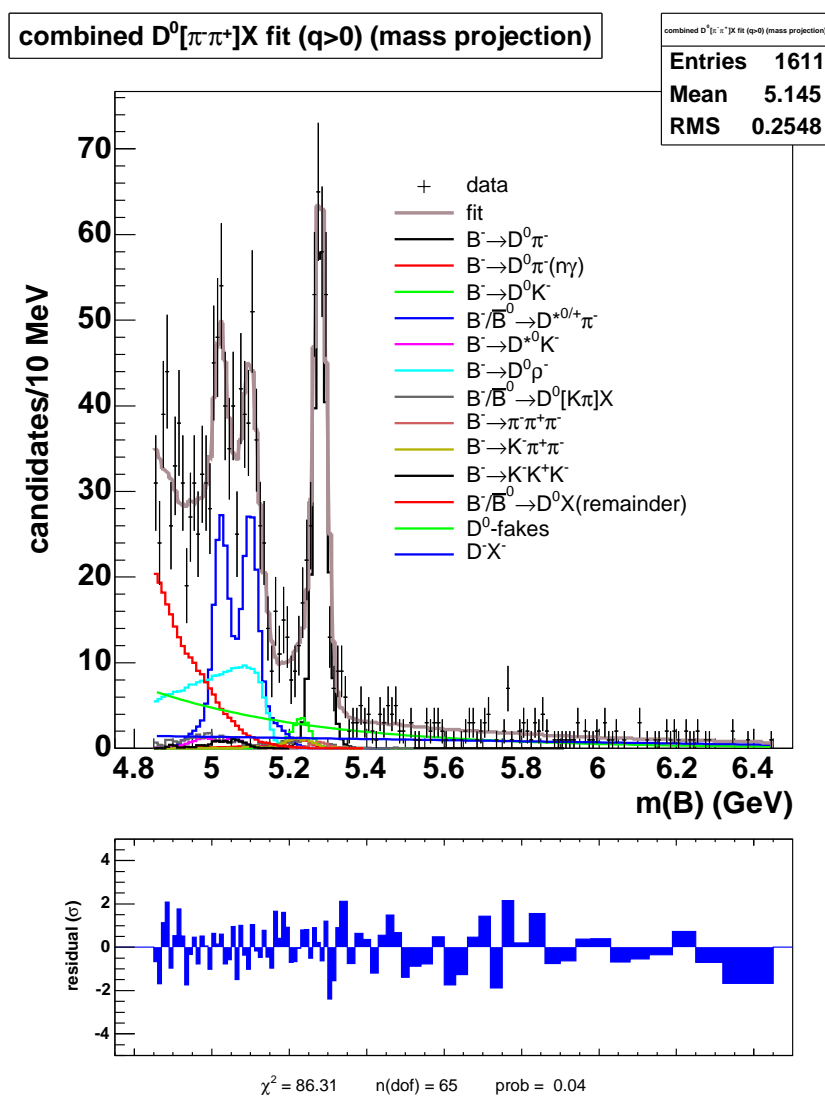


Figure 6.16: Mass projection of the fit on the $\bar{D}^0[\pi^+\pi^-]X^+$ sample (X^+ only).

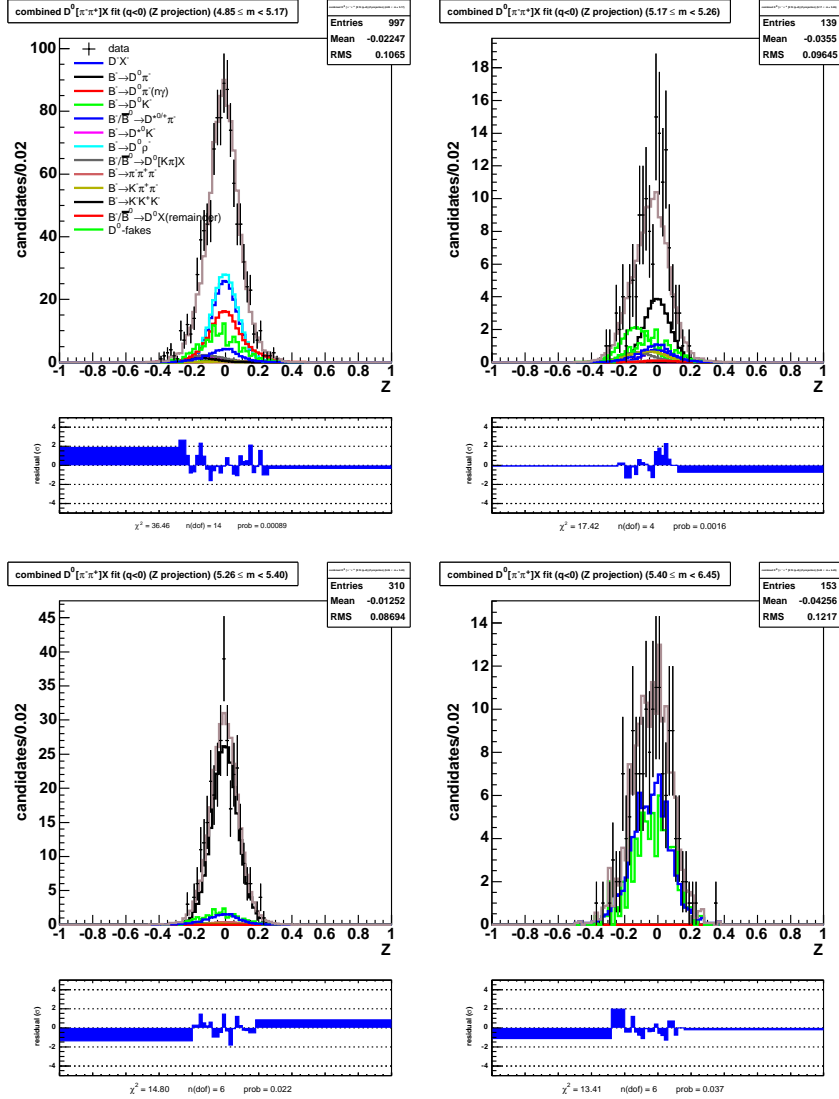


Figure 6.17: Z projections of the fit on the $D^0[\pi^-\pi^+]X^-$ sample (X^- only). The Z projections are shown in four B mass regions:

upper-left [4.85, 5.17] GeV upper-right [5.17, 5.26] GeV
lower-left [5.26, 5.40] GeV lower-right [5.40, 6.45] GeV

The pion-dominated region is shown in the lower-left plot.

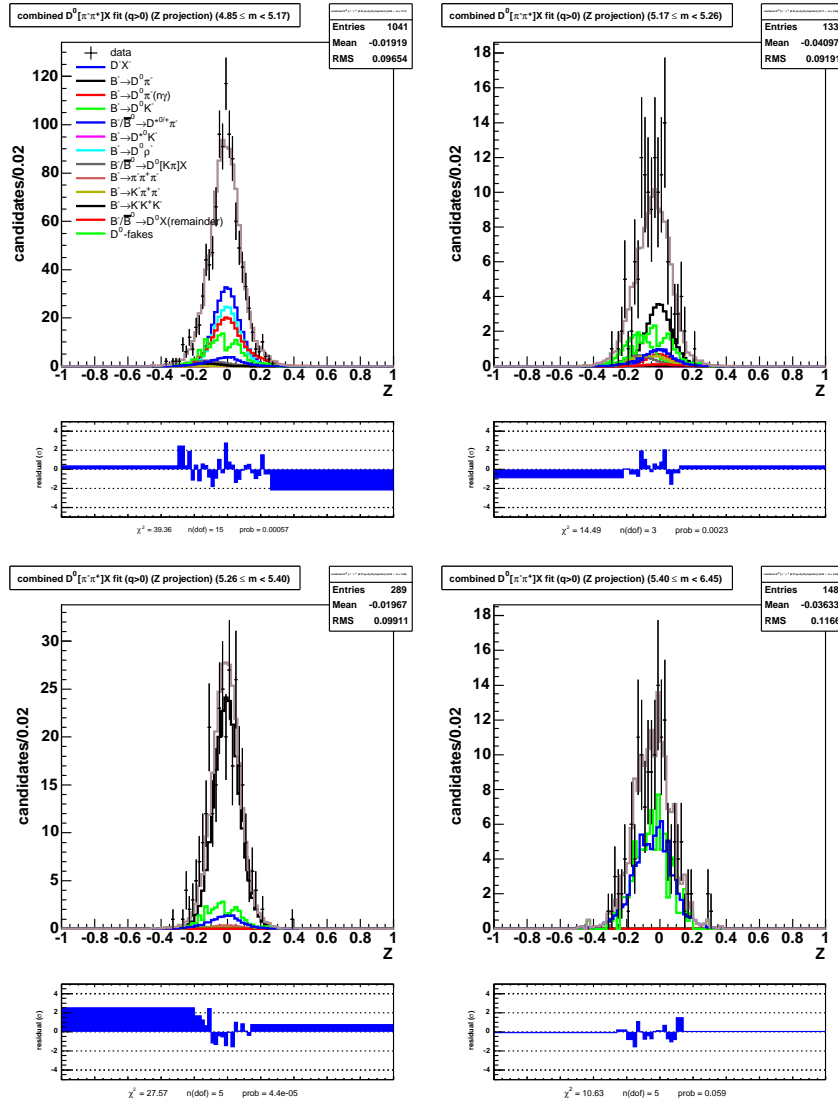


Figure 6.18: Z projections of the fit on the $\overline{D}^0[\pi^+\pi^-]X^+$ sample (X^+ only). The Z projections are shown in four B mass regions:

upper-left [4.85, 5.17] GeV upper-right [5.17, 5.26] GeV
lower-left [5.26, 5.40] GeV lower-right [5.40, 6.45] GeV

The pion-dominated region is shown in the lower-left plot.

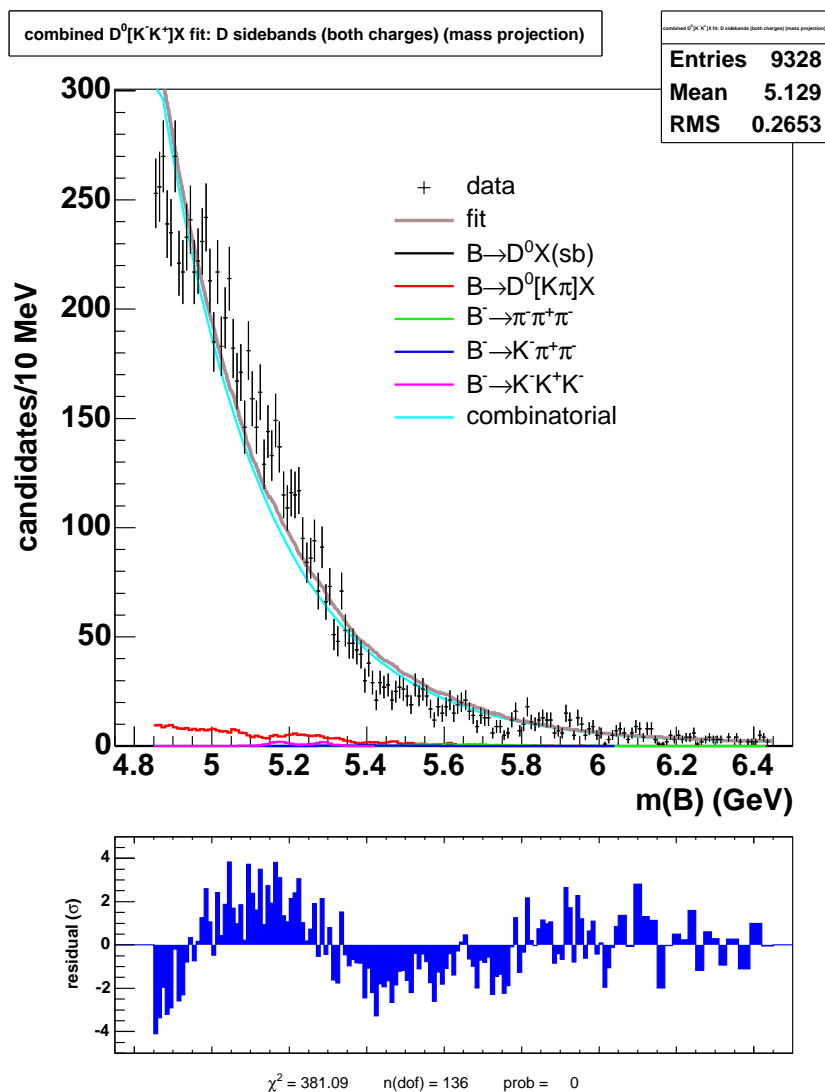


Figure 6.19: Auxiliary D^0 -sideband fit for the $D^0[K^-K^+]X^-$ sample (both charges). *N.B.:* We do not use this fit! The smooth curve labeled “combinatorial” does not adequately describe the shape of the remaining data. Instead, we use the data histogram with the three-body modes and the flavor mode reflection subtracted out as our fake- D template. The B^- and B^+ samples are treated separately. See Sec. 6.3.1 for details.

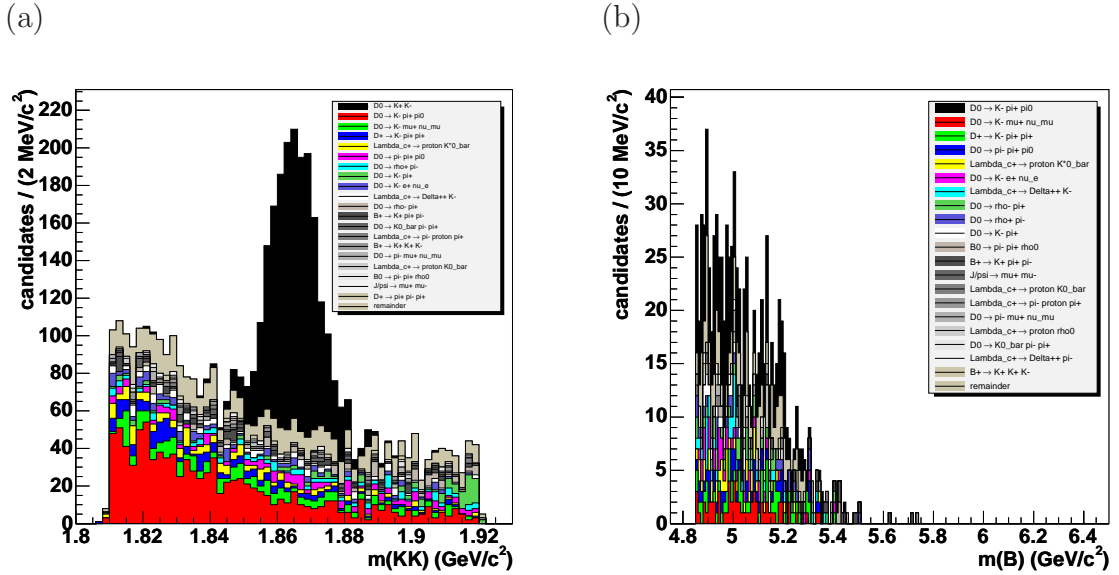


Figure 6.20: Stack histograms of K^-K^+ backgrounds from generic B Monte Carlo. The backgrounds are sorted by charm meson decay mode; if the B decay is charmless, the full B decay mode is displayed instead. (a) Stack histogram in K^-K^+ mass. The mass peak atop the other modes is the $D_{\text{CP}+}^0 \rightarrow K^-K^+$ signal. (b) Stack histogram in B ($K^-K^+\pi$) mass for the $D_{\text{CP}+}^0 \rightarrow K^-K^+$ sidebands. The top histogram in black is again the $D_{\text{CP}+}^0 \rightarrow K^-K^+$ signal. The wedge shape of the background tapers off at approximately the B mass. This explains why we cannot use the smooth curve Eqn. 4.13 to describe the fake- D background in this mode. Note: the histogram colors for a given mode are not necessarily the same in (a) and (b).

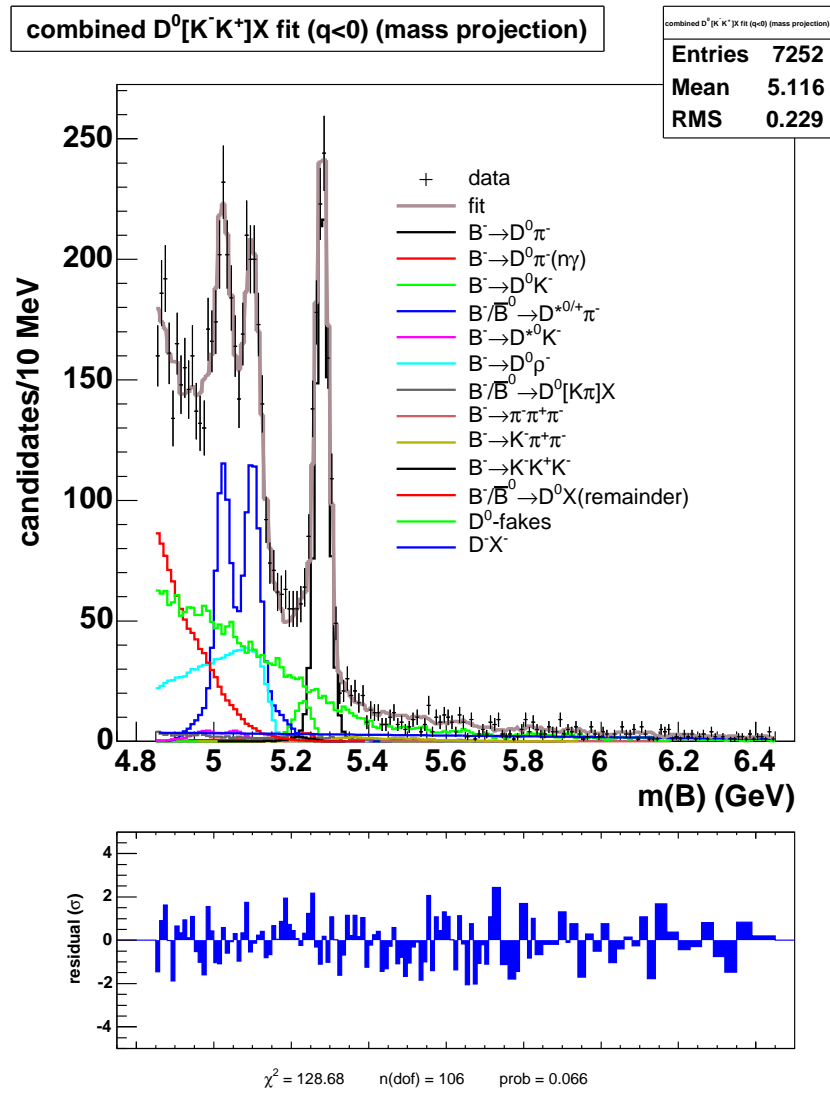


Figure 6.21: Mass projection of the fit on the $D^0[K^-K^+]X^-$ sample (X^- only).

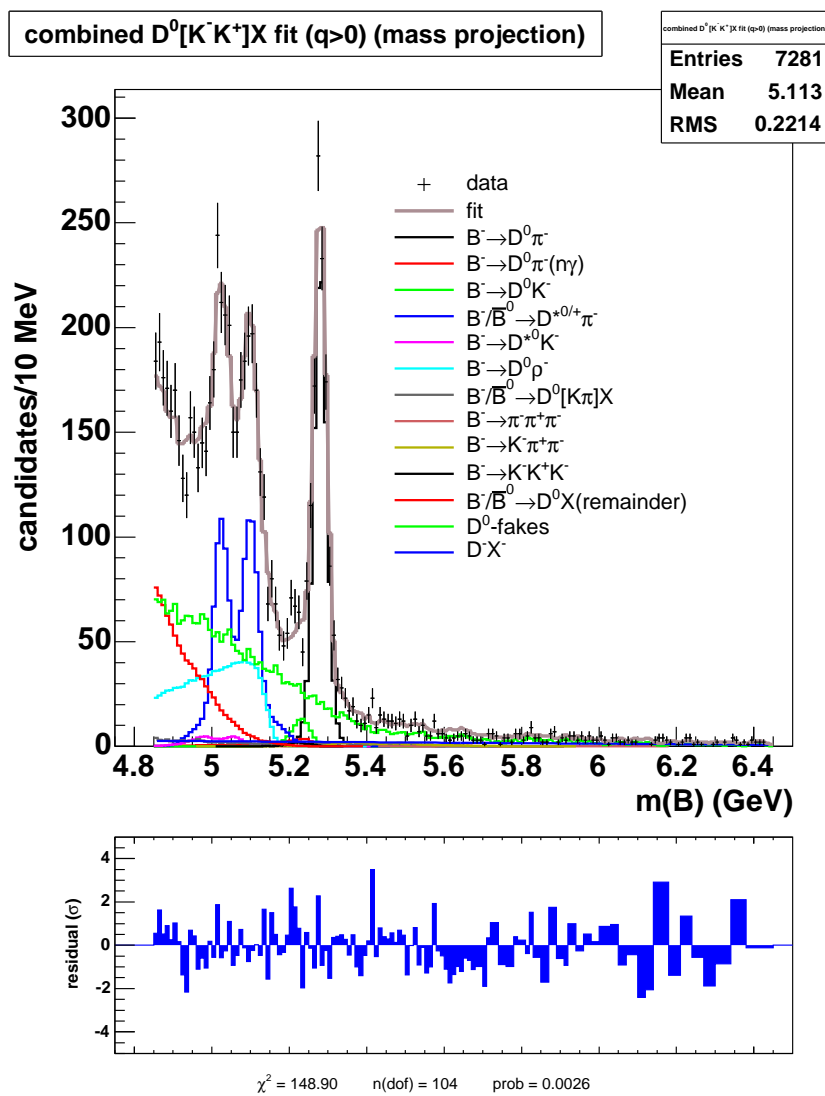


Figure 6.22: Mass projection of the fit on the $\bar{D}^0[K^+K^-]X^+$ sample (X^+ only).

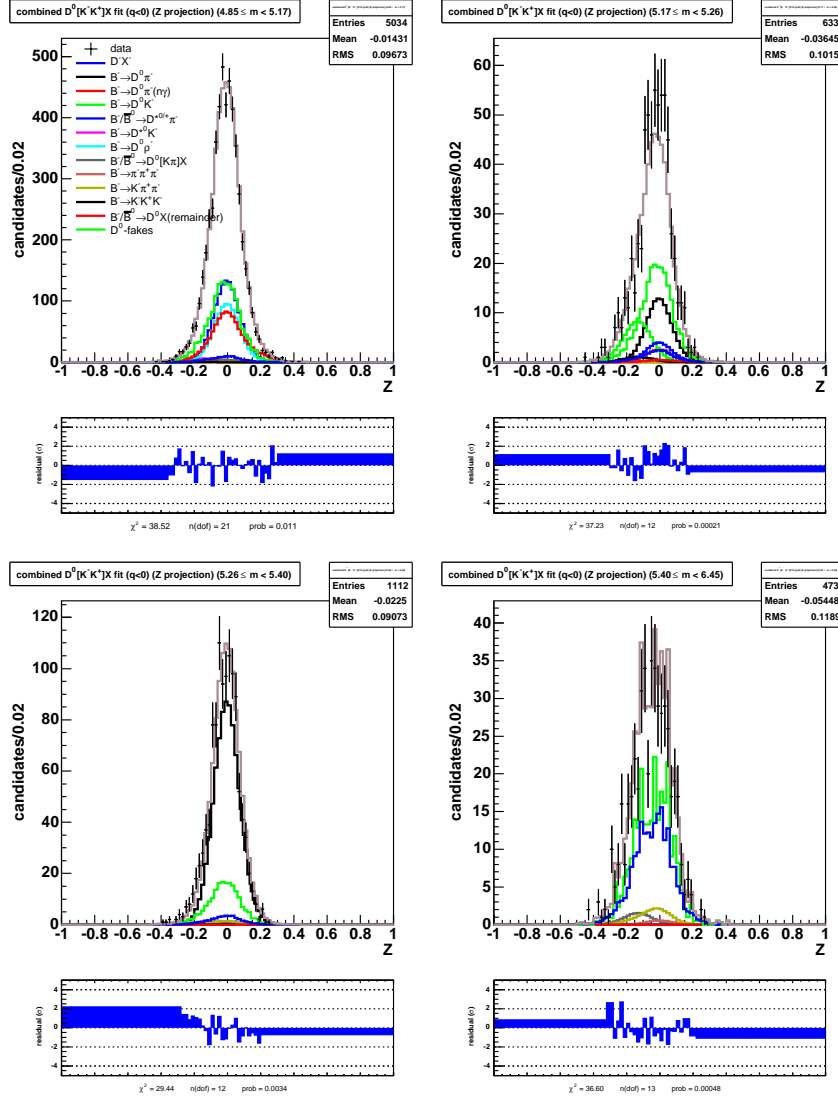


Figure 6.23: Z projections of the fit on the $D^0[K^-K^+]X^-$ sample (X^- only). The Z projections are shown in four B mass regions:

upper-left [4.85, 5.17] GeV upper-right [5.17, 5.26] GeV
lower-left [5.26, 5.40] GeV lower-right [5.40, 6.45] GeV

The pion-dominated region is shown in the lower-left plot.

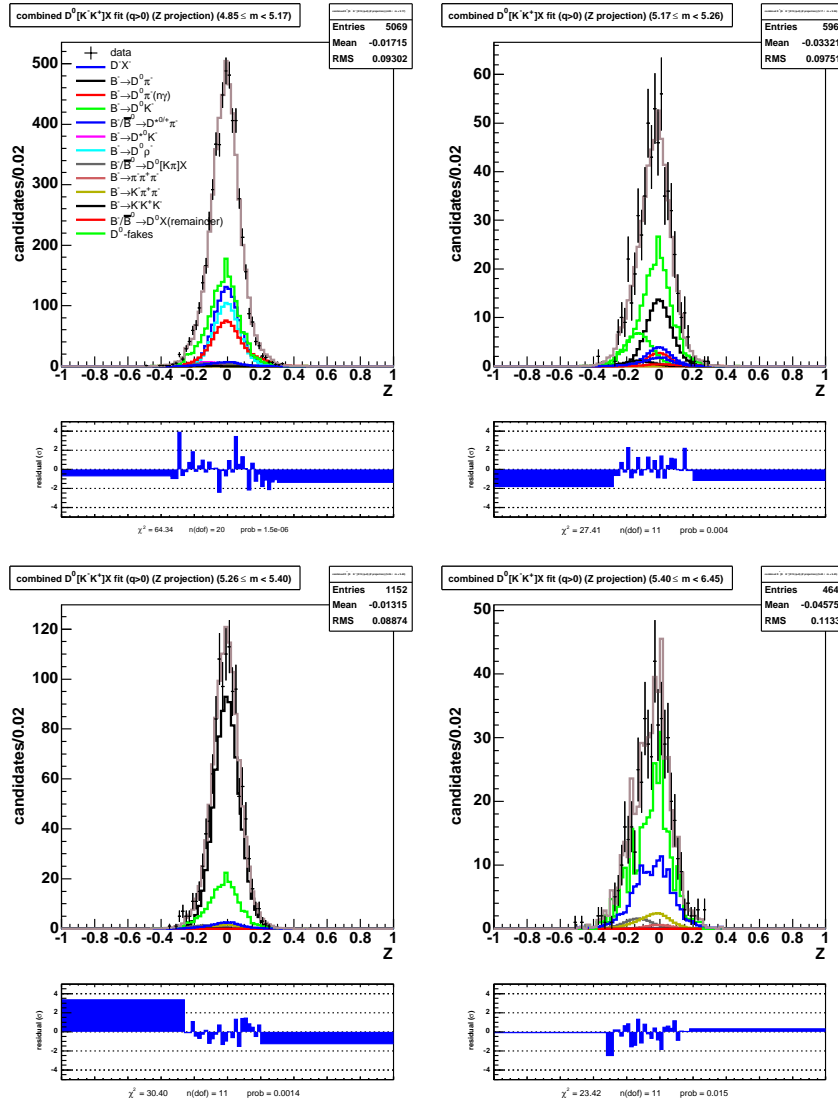


Figure 6.24: Z projections of the fit on the $\bar{D}^0[K^+K^-]X^+$ sample (X^+ only). The Z projections are shown in four B mass regions:

upper-left [4.85, 5.17] GeV upper-right [5.17, 5.26] GeV
lower-left [5.26, 5.40] GeV lower-right [5.40, 6.45] GeV

The pion-dominated region is shown in the lower-left plot.

Chapter 7

Results and Conclusions

We have performed two-dimensional maximum likelihood fits in dE/dx and mass on $\sim 1.3 \text{ fb}^{-1}$ of CDF two-track trigger data acquired during Run II of the Tevatron to measure the relative branching ratio $BR(B^- \rightarrow D^0 K^-)/BR(B^- \rightarrow D^0 \pi^-)$ and its charge conjugate in the D^0 flavor decay mode $D_f^0 \rightarrow K^- \pi^+$ and the CP-even decay modes $D^0 \rightarrow K^- K^+$ and $D^0 \rightarrow \pi^- \pi^+$. See Table 6.11 for a summary.

From these measurements, we derive the following quantities:

$$\begin{aligned}
 R &= \frac{BR(B^- \rightarrow D_f^0 K^-) + BR(B^+ \rightarrow \overline{D}_f^0 K^+)}{BR(B^- \rightarrow D_f^0 \pi^-) + BR(B^+ \rightarrow \overline{D}_f^0 \pi^+)} \\
 &= (7.99 \pm 0.33 \text{ (stat.)} \pm 0.32 \text{ (sys.)} \pm 0.21 \text{ (XFT)})\% \\
 R_{\text{CP}^+} &= \frac{BR(B^- \rightarrow D_{\text{CP}^+}^0 K^-) + BR(B^+ \rightarrow D_{\text{CP}^+}^0 K^+)}{[BR(B^- \rightarrow D_f^0 K^-) + BR(B^+ \rightarrow \overline{D}_f^0 K^+)]/2} \\
 &= 1.15 \pm 0.17 \text{ (stat.)} \pm 0.02 \text{ (sys.)} \\
 A_{\text{CP}^+} &= \frac{BR(B^- \rightarrow D_{\text{CP}^+}^0 K^-) - BR(B^+ \rightarrow D_{\text{CP}^+}^0 K^+)}{BR(B^- \rightarrow D_{\text{CP}^+}^0 K^-) + BR(B^+ \rightarrow D_{\text{CP}^+}^0 K^+)} \\
 &= 0.10 \pm 0.15 \text{ (stat.)} \pm 0.02 \text{ (sys.)}
 \end{aligned}$$

A summary of the systematic uncertainties can be found in Table 6.13.

As described in Section 2.3, measuring γ using the GLW method in $B \rightarrow DK$ decays presents many challenges to the experimentalist. So far it has been difficult for any individual measurement, on its own, to provide strong constraints on γ .¹ For us, we are further hindered by the fact that we cannot measure A_{CP^-} and R_{CP^-} in our

¹For instance, Ref. [34] quotes three disjoint intervals for γ at 68% confidence level and $7.0^\circ < \gamma < 173.0^\circ$ at 95% confidence level.

	R_{CP+}	A_{CP+}
This analysis	$1.15 \pm 0.17 \pm 0.02$	$0.10 \pm 0.15 \pm 0.02$
BaBar (2010) [34]	$1.18 \pm 0.09 \pm 0.05$	$0.25 \pm 0.06 \pm 0.02$
Belle (2006) [35]	$1.13 \pm 0.16 \pm 0.08$	$0.06 \pm 0.14 \pm 0.05$
CDF (2010) [36]	$1.30 \pm 0.24 \pm 0.12$	$0.39 \pm 0.17 \pm 0.04$
Belle (2011 preliminary) [21]	$1.03 \pm 0.07 \pm 0.03$	$0.29 \pm 0.06 \pm 0.02$
LHCb (2011 preliminary) [21]	$1.48 \pm 0.31 \pm 0.12$	$0.07 \pm 0.18 \pm 0.07$

Table 7.1: Comparison of our measured values for R_{CP+} and A_{CP+} with those from other analyses. The first uncertainty quoted is statistical; the second is systematic.

experimental environment. However, with the increase in measurement precision at multiple experiments, we expect global combinations of GLW observables to produce useful constraints on γ in the near future.

As shown in Table 7.1, our measured values of R_{CP+} and A_{CP+} are consistent with those from other measurements, both published and preliminary. Our measurements are also compatible with Standard Model constraints. Our statistical uncertainties are smaller than those of the other hadron collider results; our systematic uncertainties are comparable to those of the B factory measurements.

Bibliography

- [1] M. E. Peskin and D. V. Schroeder, *An Introduction to Quantum Field Theory* (Addison-Wesley, Reading, Massachusetts, USA, 1995).
- [2] H. Georgi, Draft update to *Weak Interactions*,
<http://www.people.fas.harvard.edu/~hgeorgi/weak.pdf>,
February 10, 2009.
- [3] G. C. Branco, L. Lavoura and J. P. Silva, *CP Violation* (Oxford University Press, Oxford, United Kingdom, 1999).
- [4] I. I. Bigi and A. I. Sanda, *CP Violation* (Cambridge University Press, Cambridge, United Kingdom, 2000).
- [5] C. Amsler *et al.*, Phys. Lett. **B667**, 1 (2008).
- [6] *The CKM Quark-Mixing Matrix*, a review in Ref. [5].
- [7] *CP Violation in Meson Decays*, a review in Ref. [5].
- [8] D. H. Perkins, *Introduction to High Energy Physics*, Fourth ed. (Cambridge University Press, Cambridge, United Kingdom, 2000).
- [9] L. H. Ryder, *Quantum Field Theory*, Second ed. (Cambridge University Press, Cambridge, United Kingdom, 1996).
- [10] E. D. Commins and P. H. Bucksbaum, *Weak Interactions of Leptons and Quarks* (Cambridge University Press, Cambridge, United Kingdom, 1983).
- [11] *Quantum Chromodynamics and Its Coupling*, a review in Ref. [5].
- [12] *Electroweak Model and Constraints on New Physics*, a review in Ref. [5].
- [13] *Neutrino Mass, Mixing, and Flavor Change*, a review in Ref. [5].
- [14] S. P. Martin, *A Supersymmetry Primer*, 1997, hep-ph/9709356v5.
- [15] M. Kobayashi and T. Maskawa, Prog. Theor. Phys. **49**, 652 (1973).

- [16] L. Wolfenstein, Phys. Rev. Lett. **51**, 1945 (1983).
- [17] N. Cabibbo, Phys. Rev. Lett. **10**, 531 (1963).
- [18] The CKMfitter Group, <http://ckmfitter.in2p3.fr/>.
- [19] The UTfit Collaboration, <http://www.utfit.org/>.
- [20] The Particle Data Group, <http://pdg.lbl.gov/>.
- [21] The Heavy Flavor Averaging Group,
<http://www.slac.stanford.edu/xorg/hfag/>.
- [22] A. B. Carter and A. Sanda, Phys. Rev. Lett. **45**, 952 (1980).
- [23] A. B. Carter and A. Sanda, Phys. Rev. **D23**, 1567 (1981).
- [24] I. I. Bigi and A. Sanda, Phys. Lett. **B211**, 213 (1988).
- [25] $D^0-\bar{D}^0$ *Mixing*, a review in Ref. [5].
- [26] M. Gronau and D. London, Phys. Lett. **B253**, 483 (1991).
- [27] M. Gronau and D. Wyler, Phys. Lett. **B265**, 172 (1991).
- [28] D. Atwood, I. Dunietz and A. Soni, Phys. Rev. Lett. **78**, 3257 (1997), hep-ph/9612433.
- [29] D. Atwood, I. Dunietz and A. Soni, Phys. Rev. **D63**, 036005 (2001), hep-ph/0008090.
- [30] A. Giri, Y. Grossman, A. Soffer and J. Zupan, Phys. Rev. **D68**, 054018 (2003), hep-ph/0303187.
- [31] A. Poluektov *et al.*, Phys. Rev. **D70**, 072003 (2004), hep-ex/0406067.
- [32] M. Gronau, Phys. Rev. **D58**, 037301 (1998), hep-ph/9802315.
- [33] M. Gronau, Phys. Lett. **B557**, 198 (2003), hep-ph/0211282.
- [34] P. del Amo Sanchez *et al.*, Phys. Rev. **D82**, 072004 (2010), 1007.0504.
- [35] K. Abe *et al.*, Phys. Rev. **D73**, 051106 (2006), hep-ex/0601032.
- [36] T. Aaltonen *et al.*, Phys. Rev. **D81**, 031105 (2010), 0911.0425.
- [37] *Accelerator Concepts*, version 3.5, Accelerator Division, Fermi National Accelerator Laboratory, April 22, 2009.

- [38] *Booster Rookie Book*, version 4.1, Accelerator Division, Fermi National Accelerator Laboratory, April 8, 2009.
- [39] *Antiproton Source Rookie Book*, version 2.0, Accelerator Division, Fermi National Accelerator Laboratory, February 17, 2009.
- [40] *Main Injector Rookie Book*, version 1.0, Accelerator Division, Fermi National Accelerator Laboratory, June, 2003.
- [41] *Recycler Rookie Book*, version 1.2, Accelerator Division, Fermi National Accelerator Laboratory, May 30, 2008.
- [42] *Tevatron Rookie Book*, version 2.3, Accelerator Division, Fermi National Accelerator Laboratory, July 15, 2009.
- [43] *High-energy Collider Parameters*, a review in Ref. [5].
- [44] *The CDF II Detector Technical Design Report*, The CDF II Collaboration, FERMILAB-Pub-96/390-E, October, 1996.
- [45] D. Acosta *et al.*, Phys. Rev. **D71**, 032001 (2005), hep-ex/0412071.
- [46] D. Acosta *et al.*, Phys. Rev. **D71**, 052003 (2005), hep-ex/0410041.
- [47] A. Abulencia *et al.*, J. Phys. **G34**, 2457 (2007), hep-ex/0508029.
- [48] A. Sill, Nucl. Instrum. Meth. **A447**, 1 (2000).
- [49] C. S. Hill, Nucl. Instrum. Meth. **A530**, 1 (2004).
- [50] T. Nelson, Int. J. Mod. Phys. **A16S1C**, 1091 (2001).
- [51] A. A. Affolder *et al.*, Nucl. Instrum. Meth. **A453**, 84 (2000).
- [52] A. A. Affolder *et al.*, Nucl. Instrum. Meth. **A526**, 249 (2004).
- [53] B. Ashmanskas *et al.*, Nucl. Instrum. Meth. **A518**, 532 (2004), physics/0306169.
- [54] J. A. Adelman *et al.*, Nucl. Instrum. Meth. **A572**, 361 (2007).
- [55] K. Nakamura *et al.*, J. Phys. **G37**, 075021 (2010).
- [56] E. J. Thomson *et al.*, IEEE Trans. Nucl. Sci. **49**, 1063 (2002).
- [57] Alessandro Cerri, private communication.
- [58] A. Cerri, A. Deisher, H.-C. Fang, J. Mülmenstädt, M. D. Shapiro, D. Lucchesi, S. Pagan Griso, and G. Salamanna, Measurement of B^0 Branching Fractions Using Combined Mass and dE/dx Fits, CDF note 8705.

- [59] A. Cerri, A. Deisher, H.-C. Fang, J. Mülmenstädt, M. D. Shapiro, D. Lucchesi, S. Pagan Griso, and G. Salamanna, Measurement of B^- Relative Branching Fractions with a Combined Mass and dE/dx fit, CDF note 8777.
- [60] A. Cerri, A. Deisher, H.-C. Fang, J. Mülmenstädt, and M. D. Shapiro, dE/dx Templates for the Measurement of the Relative Branching Ratios $BR(B \rightarrow DK) / BR(B \rightarrow D\pi)$, CDF note 8716.
- [61] J. Marriner, Secondary Vertex Fit with Mass and Pointing Constraints (CTVMFT), CDF note 1996.
- [62] P. Sphicas, A $b\bar{b}$ Monte Carlo Generator, CDF note 2655.
- [63] K. Anikeev, Ch. Paus, P. Murat, Description of Bgenerator II, CDF note 5092.
- [64] D. J. Lange, Nucl. Instrum. Meth. **A462**, 152 (2001).
- [65] E. Barberio and Z. Was, Comput. Phys. Commun. **79**, 291 (1994).
- [66] Zoltan Ligeti, private communication.
- [67] A. Abulencia *et al.*, Phys. Rev. Lett. **97**, 062003 (2006), hep-ex/0606027.
- [68] A. Abulencia *et al.*, Phys. Rev. Lett. **97**, 242003 (2006), hep-ex/0609040.
- [69] G. Cowan, *Statistical Data Analysis* (Oxford University Press, Oxford, United Kingdom, 1998).
- [70] F. James and M. Roos, Comput. Phys. Commun. **10**, 343 (1975).
- [71] R. Brun and F. Rademakers, Nucl. Instrum. Meth. **A389**, 81 (1997).
- [72] S.-S. Yu, J. Heinrich, N. Lockyer, D. Ambrose and P. Wittich, COT dE/dx Measurement and Corrections, CDF note 6361.
- [73] S. D'Auria *et al.*, Track-based calibration of the COT specific ionization, CDF note 6932.
- [74] Aseet Mukherjee, private communication.
- [75] S. Giagu *et al.*, BR ratios and direct CP violation in Cabibbo suppressed decays of D^0 , CDF note 6391.
- [76] K. Abe *et al.*, Phys. Rev. **D69**, 112002 (2004), hep-ex/0307021.
- [77] K. Abe *et al.*, Phys. Rev. Lett. **87**, 111801 (2001), hep-ex/0104051.
- [78] B. Aubert *et al.*, Phys. Rev. Lett. **96**, 011803 (2006), hep-ex/0509036.

- [79] W. M. Yao *et al.*, J. Phys. **G33**, 1 (2006), and 2007 partial update for the 2008 edition.

Appendix A

dE/dx templates

A.1 Introduction

In this appendix we describe the procedure for obtaining the dE/dx templates of kaons and pions for use in the maximum likelihood fits described in Chapters 4 to 6.

The likelihood functions, used to extract relative branching fractions of the form $BR(B \rightarrow DK)/BR(B \rightarrow D\pi)$, are described in Section 4.5. To summarize, the likelihoods are expressed in two variables: (1) $m_{D\pi}$, the invariant mass of the track– D combination under the assumption that the track is a pion, and (2) the track Z , a variable related to the dE/dx (see below).

All of our dE/dx -related quantities presuppose the hit-level corrections of CDF note 6361 [72] and the track-based corrections of CDF note 6932 [73]. The dE/dx reconstruction, part of the standard CDF reconstruction, contains the hit-level corrections; the track-based corrections are applied with the help of a macro provided by the CDF B group and documented in Ref. [73] cited above. It should be noted that these corrections already give quite accurate results; here we only attempt to account for residual effects that may arise from the particular properties of our signal samples.

A.2 The Z variable

The value of Z , as calculated using the macro mentioned above, depends on the predicted dE/dx , which is obtained in the macro from a universal curve parameterized as a function of $\beta\gamma$. For a track with a given momentum p , its $\beta\gamma = p/m$ is determined solely by the mass m of the track. Since we do not know *a priori* the mass/species of the track, we are forced to choose a tentative mass assumption. Unless otherwise noted, **we will always assume that Z is calculated in the pion hypothesis, *i. e.*,**

$$Z \equiv \ln(dE/dx)[\text{measured}] - \ln(dE/dx)[\text{predicted for pions}], \quad (4.7)$$

regardless of the actual species of the particle in question.

The Z distribution for a given particle species tends to be very close to Gaussian. For pions, since we are in the correct mass hypothesis, the distribution should be centered around $Z = 0$.

A.3 Data samples and candidate selection

As usual, the decay products of the D^0 in the decay chain $D^{*+} \rightarrow D^0[K^-\pi^+]\pi^+$ provide the cleanest samples of kaons and pions at CDF. We use two such samples in this study:

The “prompt” D^* sample. A very high statistics sample ($\sim 1.3 \times 10^7$ candidates, $\sim 2.8 \times 10^6$ tracks/species after sideband subtraction) of $D^{*\pm}$ candidates reconstructed without a minimum L_{xy} requirement. This is the ultimate source of our Z templates.

The $B \rightarrow D^*X$ sample. A substantially smaller sample ($\sim 1\text{--}2\%$ of the above) of $D^{*\pm}$ candidates, mostly from the decays of B mesons. This sample is used for cross-checking sample-dependent effects.

Both samples are drawn from the two-track trigger datasets and selected with standard B group software tools. A standard good run list is used to filter out unsuitable runs. The run range coincides with that of our samples as described in Section 4.2.

There are two levels of selection cuts for either of the samples. The pre-analysis sample selection cuts differ for the two samples and are tabulated in the top half of Table A.1. The analysis-level cuts, however, are identical for the two samples; these are tabulated in the bottom half of Table A.1.

A.4 Sideband subtraction

To ensure the purity of our D^* sample, we perform sideband subtraction in the variable $\Delta m = m(D^*) - m(D^0)$. The background in Δm is fit to a curve of the form

$$a_0 \left(1 - \exp \left(\frac{-(\Delta m - 0.140 \text{ GeV})}{a_1} \right) \right) \quad (\text{A.1})$$

in the Δm range $[0.140, 0.170]$ GeV. The D^* signal is modeled as a sum of two Gaussians. The signal region is defined to be $[0.144, 0.147]$ GeV, the sideband region $[0.155, 0.165]$ GeV.

	$B \rightarrow D^{*+}[D^0\pi^+]X$ $D^0 \rightarrow K^-\pi^+$	“prompt” $D^{*+} \rightarrow D^0\pi^+$ $D^0 \rightarrow K^-\pi^+$
Pre-analysis selection cuts		
$m(D^0)$	$\in [1.81, 1.92]$ GeV	$\in [1.70, 2.00]$ GeV
$\Delta\phi(D^0)$	< 1.5	—
$\Delta R(D^0)$	< 2	—
$\Delta z(D^0)$	< 5 cm	< 5 cm
$p_T(K_D) + p_T(\pi_D)$	> 2.4 GeV	> 5.5 GeV
$p_T(D^0)$	> 2.4 GeV	> 4.5 GeV
$L_{xy}(D^0)$	> 0.02 cm	> 0.02 cm
$\chi_{xy}^2(D^0)$	< 30	—
$m(B)$	$\in [4.65, 6.50]$ GeV	—
$\Delta\phi(B)$	< 3	—
$\Delta R(B)$	< 2	—
$\Delta z(B)$	< 5 cm	—
$p_T(D^0) + p_T(\pi_D) + p_T(\pi_*)$	> 5.5 GeV	—
$p_T(B)$	> 5 GeV	—
$\Delta z(D^*)$	—	< 5 cm
$p_T(D^0) + p_T(\pi_*)$	—	> 5.5 GeV
$p_T(D^*)$	—	> 5 GeV
$L_{xy}(B)$	> 0.03 cm	—
$ d_0(B) $	< 0.01 cm	—
$\chi_{xy}^2(B)$	< 30	—
$\Delta m \equiv m(D^*) - m(D^0)$	$\in [0, 0.2]$ GeV	$\in [0, 0.2]$ GeV
Analysis level D^0 cuts		
$m(D^0)$	$\in [1.8446, 1.8846]$ GeV	
$p_T(K_D)$ or $p_T(\pi_D)$	> 2 GeV	
Analysis level template track cuts		
p_T (offline)	> 2 GeV	
track-SVT match distance	< 25	
χ^2 of matching SVT track	< 15	
p_T of matching SVT track	> 2 GeV	
valid Z measurement	yes	
good run	yes	

Table A.1: B and $D^{(*)}$ selection cuts and Z template track cuts.

A.5 Z dependences and reweighting

In this section, we describe sample-dependent effects we have observed, the likely cause of such effects, and the measures we have taken to minimize this dependence.

Ideally, the kaon and pion templates generated from either of our D^* samples would have very similar mean Z values, at least when statistical uncertainties are taken into account. This was initially not the case. (See the rows labeled “before” in either of Tables A.2 and A.3 for examples of this.)

As a general rule, $\langle Z \rangle_\pi$, the mean Z for pions, is approximately 0, whereas $\langle Z \rangle_K$, the mean Z for kaons, is roughly -130×10^{-3} . It is often useful to compare the sizes of the various $\langle Z \rangle$ dependences described below to this π - K separation of $\sim 130 \times 10^{-3}$ in Z .

A.6 Run-dependent corrections

At the time of analysis, the track-based dE/dx corrections from Ref. [73] only existed for runs up to early November in 2005. By default, the corrections for runs taken from early June to early November of 2005, the last section for which there were dedicated corrections, are extended to those runs beyond November 2005. The η - and ϕ -dependent corrections, thus extended, are expected to be adequate. We cannot, however, rule out a run-dependent offset due to changes in the COT gain. In fact, applying the default corrections, one observes offsets of the pion $\langle Z \rangle$ of up to $\sim 20 \times 10^{-3}$ in this later data. These offsets are shown for all run ranges in Fig. A.1.

In principle, we need not correct for this offset, as long as our template samples have the same luminosity profile as our signal samples, since no bias would have been introduced. Such an offset, however, has the effect of smearing the templates and reducing our ability to separate kaons from pions. Therefore, we perform a run-dependent additive correction to Z in the following manner:

- Group runs into bins of 1000 runs each
- Progressively merge bins so that each bin has at least 10000 events after side-band subtraction
- Require that the additive correction gives $\langle Z \rangle = 0$ for each bin

For consistency, this run-dependent correction is performed for the entire sample, not just for runs after November 2005.

A.7 Z profiles

In order to understand the origin of the sample dependence of our templates, we have produced profile histograms of $\langle Z \rangle$, the mean Z , against a number of variables,

for both pions and kaons. (As usual, Z is calculated in the pion hypothesis.) From here on, we assume that the run-dependent corrections of Section A.6 have been applied.

We have produced Z profiles for each of the subsets of the two-track trigger dataset, the datasets labeled `xbhd0d`, `xbhd0h`, and `xbhd0i`. For the purpose of illustration, we include here the Z profiles made for the `xbhd0i` subset. To avoid repetition, those for the other subsets are omitted. Figure A.2 shows the Z profiles for pions in the `xbhd0i` subset of the prompt D^* sample. Figure A.3 shows the same for kaons. Figures A.4 and A.5 show the Z profiles for pions and kaons, respectively, in the `xbhd0i` $B \rightarrow D^*X$ sample. Here we describe the variables against which $\langle Z \rangle$ is plotted:

- p , the track momentum;
- p_T , the transverse momentum of the track;
- η , the pseudorapidity of the track;
- ϕ_0 of the track;
- N_{hits} , the number of hits used in calculating the dE/dx truncated mean;
- the run number;
- $\min(\Delta R)$, the ΔR of the closest track as measured in the variable $\Delta R \equiv \sqrt{(\Delta\phi)^2 + (\Delta\eta)^2}$;
- $\min(\Delta\eta)$, the $\Delta\eta$ of the closest track in η ;
- $\min(\Delta\phi)$, the $\Delta\phi$ of the closest track in ϕ_0 ;
- `iso(0.3)`, `iso(0.5)`, and `iso(0.7)`, the track isolation calculated for the specified cone size, where `iso(ΔR_{max})` for a given track i is defined as

$$\text{iso}(\Delta R_{max}) \equiv \frac{p_T^i}{p_T^i + \sum_{j \neq i} p_T^j} \quad (\Delta R(i, j) < \Delta R_{max}); \quad (\text{A.2})$$

- $N_{\text{trks}}(\Delta R < 0.3)$, $N_{\text{trks}}(\Delta R < 0.5)$, $N_{\text{trks}}(\Delta R < 0.7)$, the number of other tracks within a ΔR cone of the specified size ;
- N_{trks} , the total number of default tracks in the event;
- “secance”, defined as the number of r - ϕ intersections (of the track in question with other tracks) that occur within the nominal COT radii of $40 < r < 137$ cm.

For the pion $\langle Z \rangle$ profile, Figure A.2, we note that the variables on which $\langle Z \rangle$ has the greatest dependence are $N_{\text{trks}}(\Delta R < 0.5)$, $N_{\text{trks}}(\Delta R < 0.7)$, N_{trks} , and secance. $\langle Z \rangle$ varies over a range of $\gtrsim 60 \times 10^{-3}$, roughly 1/2 of the mean $K-\pi$ separation, for these four variables.

For the kaon profile, Figure A.3, we may add to these four a fifth variable, namely the track momentum, p (or largely interchangeably, the transverse momentum, p_T). In the pion case, the universal curve prediction removes almost all of the p dependence; for the kaons, the incorrect mass hypothesis distorts the prediction and a large $\langle Z \rangle$ dependence results.

A.8 Hit merging and proxies

It is likely that the large $\langle Z \rangle$ dependence on the four variables is a result of hit merging in the COT. There are at least two sources of merging: [74]

1. Charge from different tracks may be deposited close enough in time on a single wire to merge into a single, wider hit. This should occur more frequently as the hit density increases.
2. A portion of the charge deposited by a single track may take long enough to arrive on a sense wire to form a separate hit. The dE/dx reconstruction code accounts for this by merging hits with a gap of < 15 ns between them. In high-density environments, hits from different tracks may be merged.

In both cases, the merging (a) would tend to inflate the (truncated) mean width of the hits associated with a track, and therefore the measured dE/dx and Z values, and (b) should be positively correlated with the hit density of the track's environment. Thus the dependence of $\langle Z \rangle$ on the four variables mentioned in the previous section is qualitatively explained—all four reflect, to varying degrees, the density of hits around the track in question. [74]

A.9 Reweighting in two dimensions

We have described two categories of Z dependences: (1) the momentum dependence of $\langle Z \rangle_K$, the mean Z of the kaons, as a result of our pion mass hypothesis, and (2) those dependences that ultimately arise from hit merging in the COT and the dE/dx reconstruction.

To correct for (1), we may simply reweight our templates so that the momentum distribution of our reweighted template sample agrees with that of our target (signal) samples.

To account for (2), we have more options. One might choose to model the hit merging in the detector and offline in detail and thereby derive an additional hit-level correction. A slightly less involved solution would be to use a suitably defined measure of hit density as a proxy for the strength of hit merging. Both of these options would entail going back to the hit level quantities. As a third possibility, one may simply find a track-level variable that would be a good proxy to the hit density, and by extension, a reasonable proxy to the hit merging strength, and reweight in such a variable. Since our aim here is not to improve K - π separation, but simply to minimize our template bias, we choose this last option of reweighting.

In other words, we have chosen to perform a simultaneous (two-dimensional) reweighting in the track momentum p and a variable that is correlated with the hit density. It remains to be decided which variable to choose. In fact, we have four candidates, $N_{\text{trks}}(\Delta R < 0.5)$, $N_{\text{trks}}(\Delta R < 0.7)$, N_{trks} , and *secance*, as we have seen before. We will exclude *a priori* the first two on the grounds that the 0-bin for both of these variables are populated in the target samples but nearly unpopulated in our template samples (see Figs. A.6(c) and (d))—this would cause difficulties in the reweighting.

We are then left with the two variables N_{trks} and *secance*. The *secance* has the advantage of being a far more local variable than N_{trks} . The higher mean value of N_{trks} (~ 50 versus ~ 10), however, speaks in its favor—as a proxy to the local hit density, the correlation is less likely to be washed out by statistical fluctuations.

The final choice of reweighting variable is decided by comparing the degree to which N_{trks} and *secance* reduce the differences between the prompt D^* and $B \rightarrow D^* X$ templates. We start by applying two separate two-dimensional reweighting schemes in (a) $N_{\text{trks}}-p$ and (b) *secance*- p on both D^* samples. (See Figure A.7 for an example of the two schemes as applied on the `xbhd0i` prompt D^* sample.) We then compare the two schemes by noting in which case the difference in $\langle Z \rangle$ between the prompt D^* and the $B \rightarrow D^* X$ templates is smaller. From Tables A.2 and A.3, it can be seen that scheme (b) almost always (in 16 out of 18 cases) reduces the sample dependence of the template means to a greater degree. We therefore choose scheme (b) to be the default. Scheme (a) is used to assess systematic uncertainties.

A.10 Summary of procedure

1. Start with the “prompt” D^* sample. The hit-level corrections of [72] have already been applied during dE/dx reconstruction.
2. Apply the candidate selection cuts of Table A.1 to the prompt D^* sample.
3. Apply the track-based Z corrections of [73].
4. Apply the run-dependent Z corrections of Section A.6.

5. Apply the analysis level cuts of Table A.1 to the D^0 candidate tracks.
6. For each π or K daughter of the D^0 , record the triplet of values (Z , p , secance). Vectors of these triplets are classified according to whether the events they contain (a) are kaons or pions, and (b) fall in the signal or sideband region of the $D^* \Delta m$ histogram. Additionally, the `xbhd0d/0h/0i` datasets are treated separately.
7. For each target (signal) sample, find the prompt D^* template sample with the appropriate run range (`0d`, `0h` or `0i`). Create the 2-D secance: p histograms for the target sample and the corresponding template sample. Take the ratio of these two histograms to obtain the secance: p histogram of weights for reweighting. Separate histograms of weights are made for pions and kaons.
8. Perform 2-D reweighting by taking the four template sample vectors in step 6 (either K or π , signal or sideband) and filling four Z template histograms with the appropriate event-by-event weights as determined by a lookup in the ratio histograms found in step 7. The template histograms contain 100 Z bins in the range $[-1, 1]$.
9. Separately for the kaons and pions, sideband subtract the Z templates in the variable Δm .

Reweighting in secance- p

	$\langle Z \rangle_\pi$			$\langle Z \rangle_K$			$\langle Z \rangle_\pi - \langle Z \rangle_K$		
	$B \rightarrow D^*X$	prompt	diff.	$B \rightarrow D^*X$	prompt	diff.	$B \rightarrow D^*X$	prompt	diff.
Od before	+2.02	+0.00	+2.02	-130.44	-137.24	+6.80	132.47	137.24	-4.78
Od after	-2.16	-3.01	+0.85	-135.80	-135.54	-0.26	133.64	132.52	+1.11
Oh before	+2.30	+0.03	+2.27	-125.88	-132.66	+6.77	128.18	132.69	-4.51
Oh after	-4.48	-3.87	-0.62	-131.45	-131.53	+0.08	126.97	127.67	-0.70
Oi before	+1.57	-0.07	+1.64	-125.26	-131.99	+6.73	126.83	131.92	-5.09
Oi after	-4.93	-4.72	-0.21	-130.82	-131.29	+0.47	125.89	126.57	-0.68

Reweighting in $N_{\text{trks-}p}$

	$\langle Z \rangle_\pi$			$\langle Z \rangle_K$			$\langle Z \rangle_\pi - \langle Z \rangle_K$		
	$B \rightarrow D^*X$	prompt	diff.	$B \rightarrow D^*X$	prompt	diff.	$B \rightarrow D^*X$	prompt	diff.
Od before	+2.02	+0.00	+2.02	-130.44	-137.24	+6.80	132.47	137.24	-4.78
Od after	-4.00	-1.73	-2.27	-135.50	-132.99	-2.51	131.50	131.26	+0.24
Oh before	+2.30	+0.03	+2.27	-125.88	-132.66	+6.77	128.18	132.69	-4.51
Oh after	-3.69	-2.59	-1.10	-131.60	-129.27	-2.33	127.91	126.68	+1.22
Oi before	+1.57	-0.07	+1.64	-125.26	-131.99	+6.73	126.83	131.92	-5.09
Oi after	-5.28	-3.40	-1.88	-130.31	-129.49	-0.82	125.03	126.09	-1.06

Table A.2: Comparison table showing values of $\langle Z \rangle$ for pions, kaons, and kaon-pion separation, before and after reweighting in secance- p (top half) and $N_{\text{trks-}p}$ (bottom half) to the *target* $D^{*+}X^-$ sample. Separate entries are shown for the prompt D^* and $B \rightarrow D^*X$ template source samples. The difference in $\langle Z \rangle$ for the two source samples is also shown.

Reweighting in secance- p

	$\langle Z \rangle_\pi$			$\langle Z \rangle_K$			$\langle Z \rangle_\pi - \langle Z \rangle_K$		
	$B \rightarrow D^*X$	prompt	diff.	$B \rightarrow D^*X$	prompt	diff.	$B \rightarrow D^*X$	prompt	diff.
Od before	+2.02	+0.00	+2.02	-130.44	-137.24	+6.80	132.47	137.24	-4.78
Od after	-2.98	-3.16	+0.18	-136.09	-135.47	-0.62	133.11	132.31	+0.80
Oh before	+2.30	+0.03	+2.27	-125.88	-132.66	+6.77	128.18	132.69	-4.51
Oh after	-4.15	-3.72	-0.43	-130.73	-131.31	+0.58	126.59	127.59	-1.00
Oi before	+1.57	-0.07	+1.64	-125.26	-131.99	+6.73	126.83	131.92	-5.09
Oi after	-5.29	-4.65	-0.63	-130.87	-130.76	-0.11	125.58	126.11	-0.53

Reweighting in $N_{\text{trks-}p}$

	$\langle Z \rangle_\pi$			$\langle Z \rangle_K$			$\langle Z \rangle_\pi - \langle Z \rangle_K$		
	$B \rightarrow D^*X$	prompt	diff.	$B \rightarrow D^*X$	prompt	diff.	$B \rightarrow D^*X$	prompt	diff.
Od before	+2.02	+0.00	+2.02	-130.44	-137.24	+6.80	132.47	137.24	-4.78
Od after	-3.51	-1.45	-2.06	-135.67	-132.75	-2.92	132.16	131.30	+0.86
Oh before	+2.30	+0.03	+2.27	-125.88	-132.66	+6.77	128.18	132.69	-4.51
Oh after	-3.87	-2.30	-1.57	-132.15	-129.18	-2.97	128.28	126.88	+1.40
Oi before	+1.57	-0.07	+1.64	-125.26	-131.99	+6.73	126.83	131.92	-5.09
Oi after	-4.97	-3.27	-1.70	-130.47	-128.60	-1.86	125.49	125.33	+0.16

Table A.3: Comparison table showing values of $\langle Z \rangle$ for pions, kaons, and kaon-pion separation, before and after reweighting in secance- p (top half) and $N_{\text{trks-}p}$ (bottom half) to the *target* D^+X^- sample. Separate entries are shown for the prompt D^* and $B \rightarrow D^*X$ template source samples. The difference in $\langle Z \rangle$ for the two source samples is also shown.

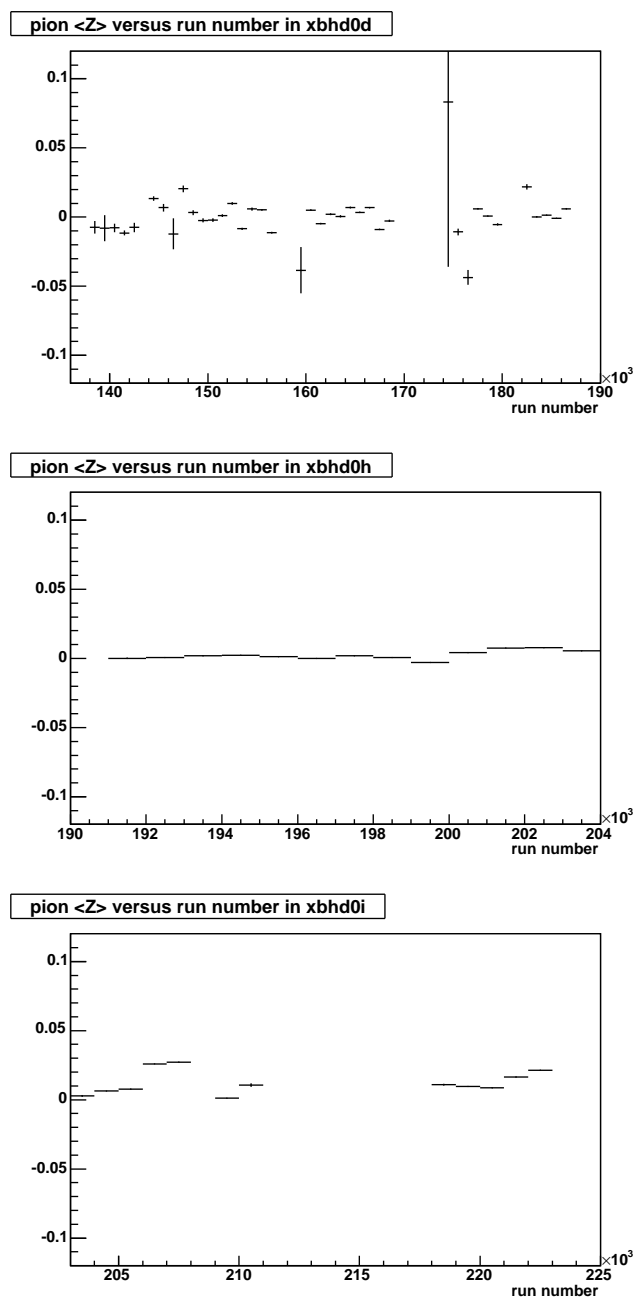


Figure A.1: $\langle Z \rangle$ versus run number in the prompt D^* sample for the three datasets `xbhd0d`, `xbhd0h`, and `xbhd0i`. There is one bin overlap between the `xbhd0h` and `xbhd0i` samples. Due to the merging of low statistics bins, the actual run-dependent corrections, as explained in Section A.6, differ somewhat from the bin values shown here, especially in the `xbhd0d` run range.

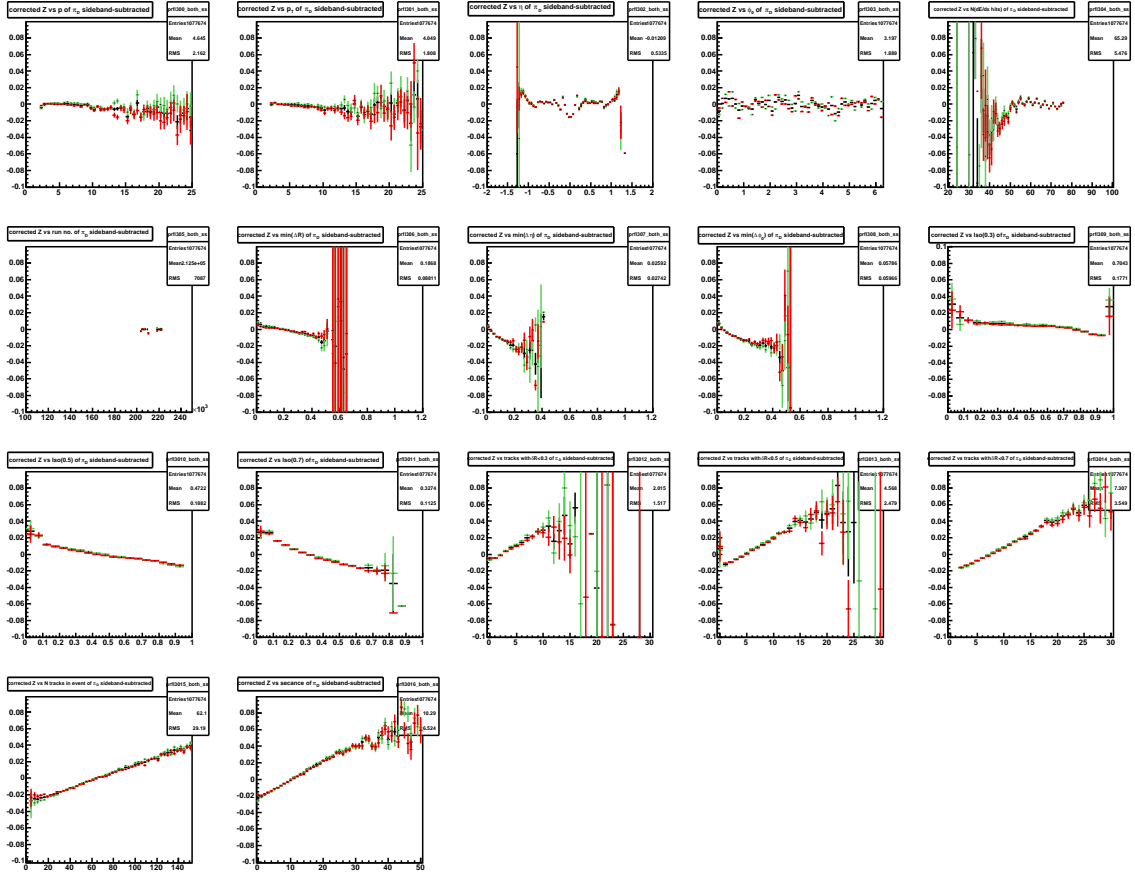


Figure A.2: Pion Z profiles for the `xbhd0i` prompt- D^* sample after sideband subtraction in Δm .

- Top row (L-R): p , p_T , η , ϕ_0 , N_{hits} .
- Second row (L-R): run number, $\min(\Delta R)$, $\min(\Delta\eta)$, $\min(\Delta\phi)$, $\text{iso}(0.3)$.
- Third row (L-R): $\text{iso}(0.5)$, $\text{iso}(0.7)$, $N_{\text{trks}}(0.3)$, $N_{\text{trks}}(0.5)$, $N_{\text{trks}}(0.7)$.
- Bottom row (L-R): N_{trks} , secance .

See Section A.7 for definitions of variables. Profiles are after run-dependent corrections of Section A.6. Red data points are for positive tracks, green for negative ones, and black for both charges combined. The full y -axis range is 200×10^{-3} in $\langle Z \rangle$, roughly 1.5 times the typical K - π separation.

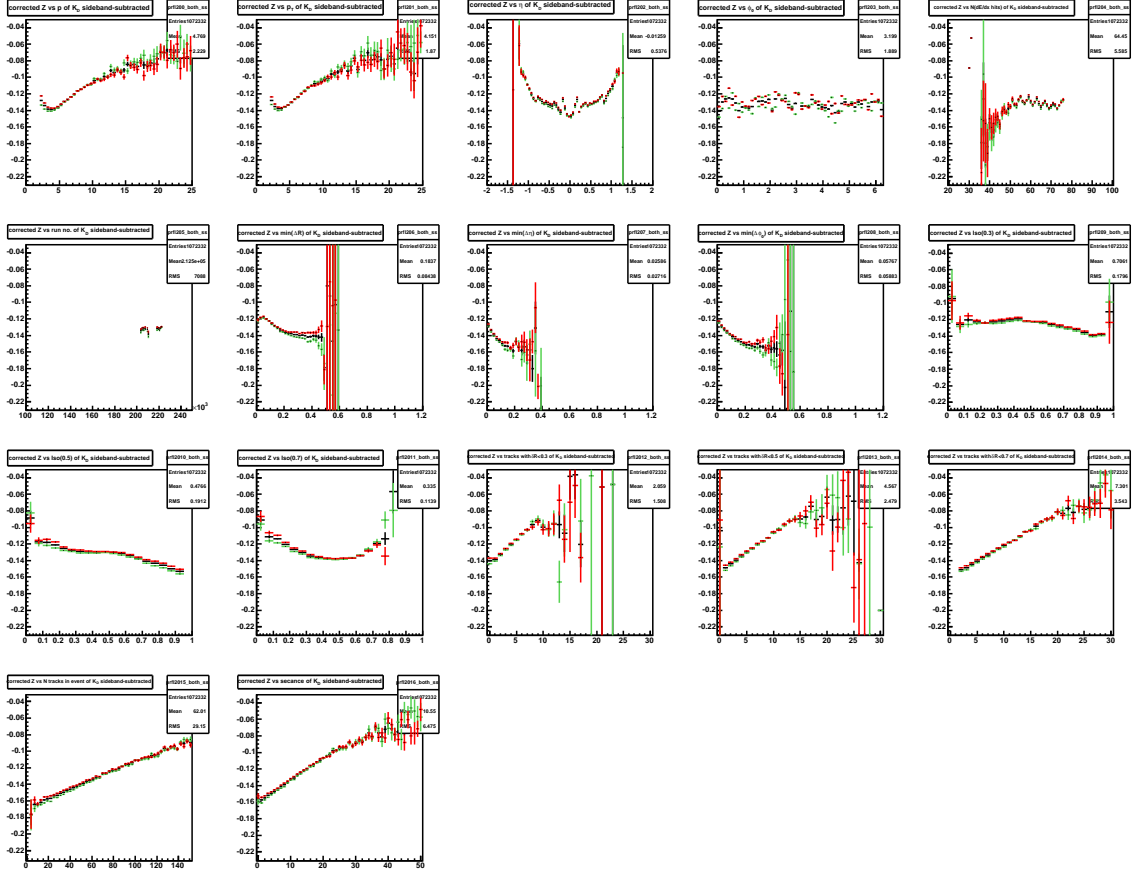


Figure A.3: Kaon Z profiles for the $xbhd0i$ prompt- D^* sample after sideband subtraction in Δm .

- | | |
|------------|---|
| Top row | (L-R): p , p_T , η , ϕ_0 , N_{hits} . |
| Second row | (L-R): run number, $\min(\Delta R)$, $\min(\Delta\eta)$, $\min(\Delta\phi)$, $\text{iso}(0.3)$. |
| Third row | (L-R): $\text{iso}(0.5)$, $\text{iso}(0.7)$, $N_{\text{trks}}(0.3)$, $N_{\text{trks}}(0.5)$, $N_{\text{trks}}(0.7)$. |
| Bottom row | (L-R): N_{trks} , secance . |

See Section A.7 for definitions of variables. Profiles are after run-dependent corrections of Section A.6. Red data points are for positive tracks, green for negative ones, and black for both charges combined. The full y -axis range is 200×10^{-3} in $\langle Z \rangle$, roughly 1.5 times the typical $K-\pi$ separation.

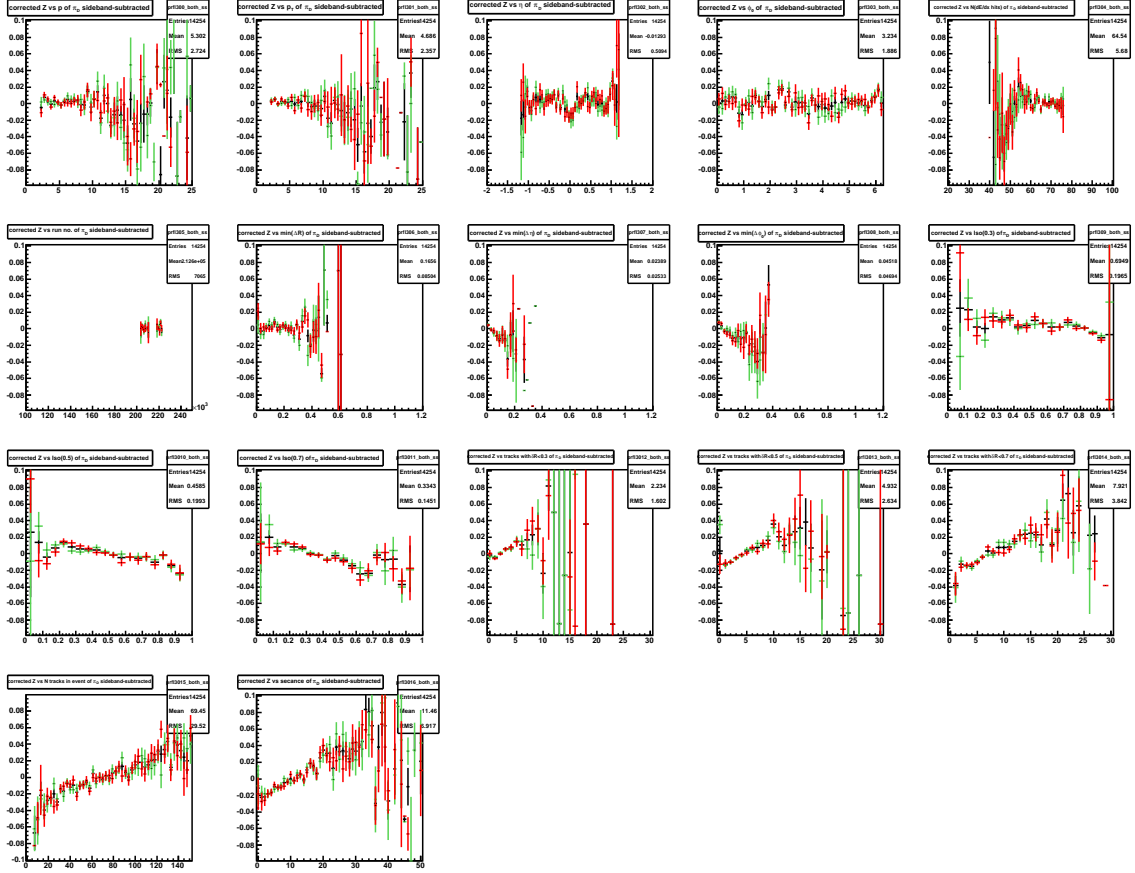


Figure A.4: Pion Z profiles for the $\text{xbhd0i } B \rightarrow D^* X$ sample after sideband subtraction in Δm .

- Top row (L-R): p , p_T , η , ϕ_0 , N_{hits} .
- Second row (L-R): run number, $\min(\Delta R)$, $\min(\Delta \eta)$, $\min(\Delta \phi)$, $\text{iso}(0.3)$.
- Third row (L-R): $\text{iso}(0.5)$, $\text{iso}(0.7)$, $N_{\text{trks}}(0.3)$, $N_{\text{trks}}(0.5)$, $N_{\text{trks}}(0.7)$.
- Bottom row (L-R): N_{trks} , secance .

See Section A.7 for definitions of variables. Profiles are after run-dependent corrections of Section A.6. Red data points are for positive tracks, green for negative ones, and black for both charges combined. The full y -axis range is 200×10^{-3} in $\langle Z \rangle$, roughly 1.5 times the typical $K-\pi$ separation.

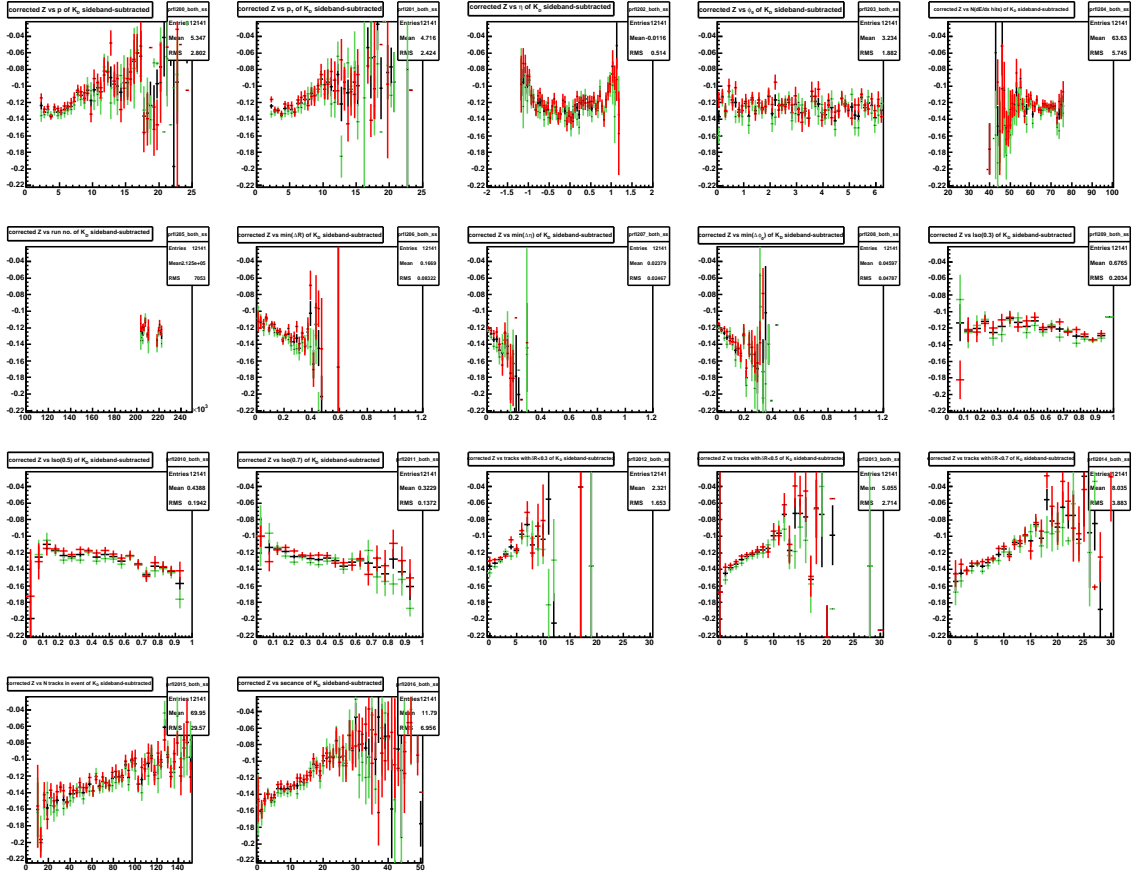


Figure A.5: Kaon Z profiles for the $xbhd0i$ $B \rightarrow D^*X$ sample after sideband subtraction in Δm .

- Top row (L-R): p , p_T , η , ϕ_0 , N_{hits} .
- Second row (L-R): run number, $\min(\Delta R)$, $\min(\Delta\eta)$, $\min(\Delta\phi)$, $\text{iso}(0.3)$.
- Third row (L-R): $\text{iso}(0.5)$, $\text{iso}(0.7)$, $N_{\text{trks}}(0.3)$, $N_{\text{trks}}(0.5)$, $N_{\text{trks}}(0.7)$.
- Bottom row (L-R): N_{trks} , secance .

See Section A.7 for definitions of variables. Profiles are after run-dependent corrections of Section A.6. Red data points are for positive tracks, green for negative ones, and black for both charges combined. The full y -axis range is 200×10^{-3} in $\langle Z \rangle$, roughly 1.5 times the typical $K-\pi$ separation.

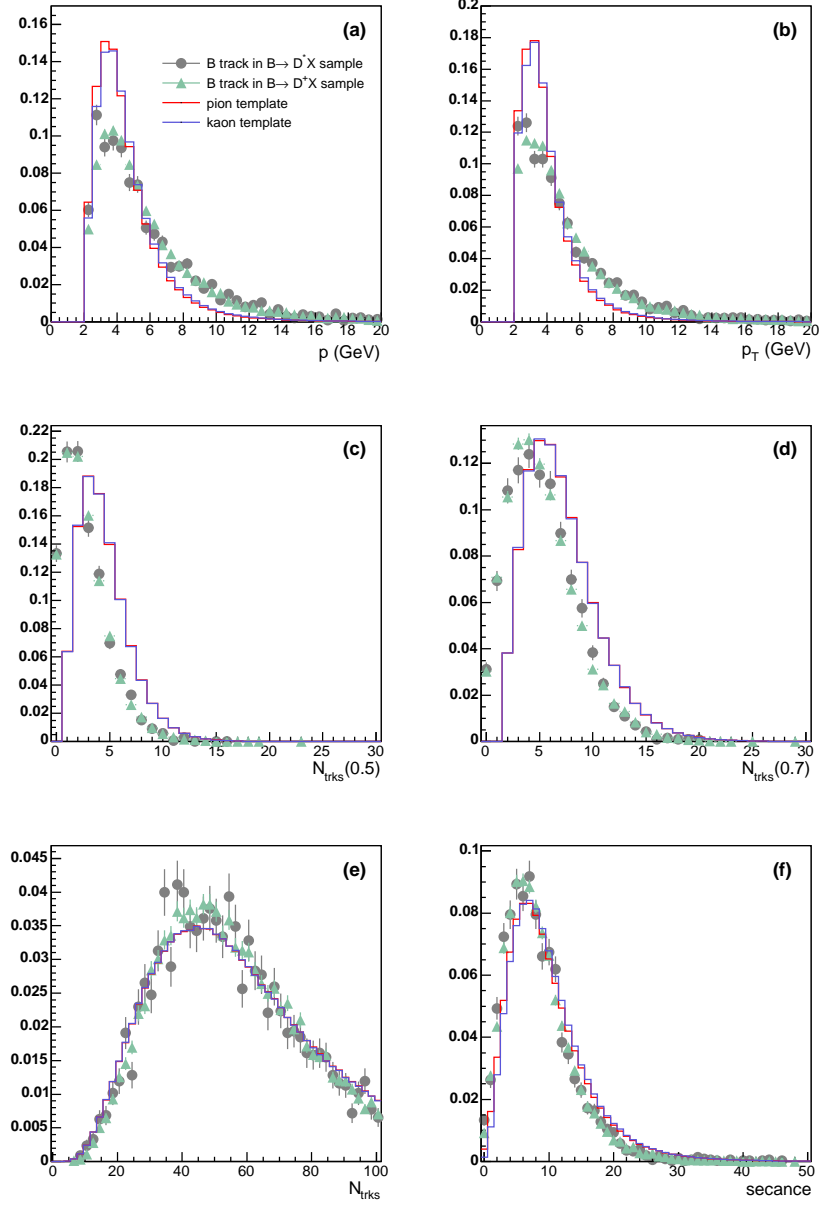


Figure A.6: Kinematic variable distributions of tracks from four different populations. The run range is that of the `xbhd0h` dataset. The six plots correspond to the six kinematic variables (a) p , (b) p_T , (c) $N_{\text{trks}}(0.5)$, (d) $N_{\text{trks}}(0.7)$, (e) N_{trks} , and (f) `secance`. See Section A.7 for definition of variables. Gray circles are for the lone B track from the $B \rightarrow D^*X$ target sample; pale green triangles are for the lone B track from the $B \rightarrow D^+X$ target sample; red and blue histograms show the distributions for the pions and kaons respectively in the “prompt” D^* sample.

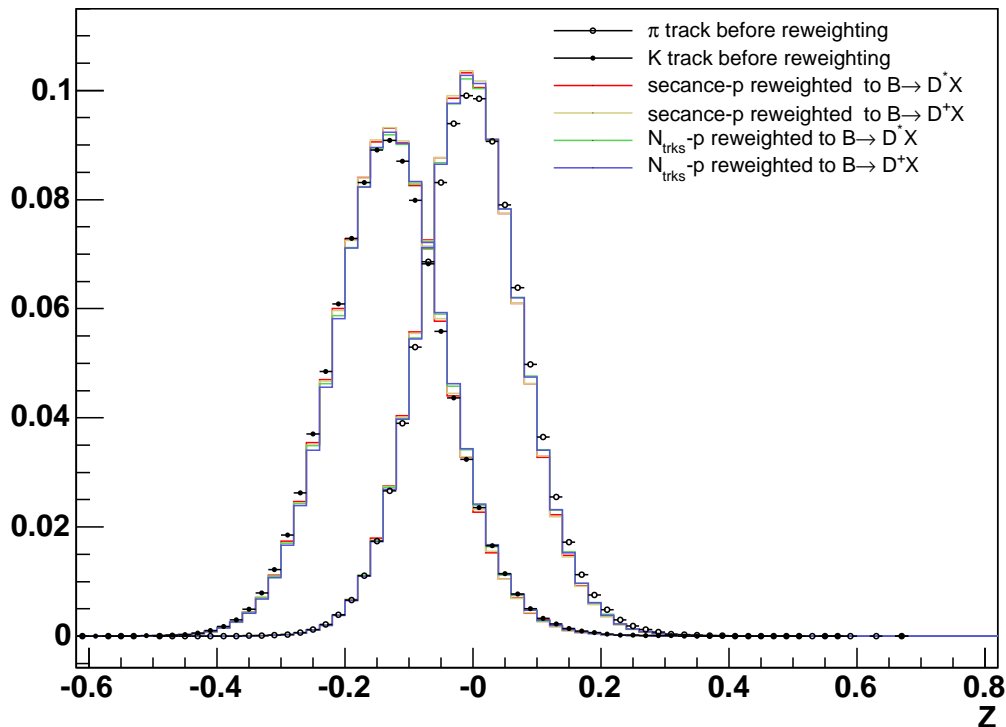


Figure A.7: Z templates in `xbhd0i`, before and after various reweighting schemes. The empty and filled circles represent the pions and kaons, respectively, before reweighting. Histograms are shown in pairs of the same color; in each pair, the left and right histograms are the kaon and pion templates, respectively, after a given reweighting scheme. The reweighting schemes are designated with the following colors:

- Red: secance- p reweighted to target $B \rightarrow D^*X$ sample
- Gold: secance- p reweighted to target $B \rightarrow D^+X$ sample
- Green: $N_{\text{trks}}-p$ reweighted to target $B \rightarrow D^*X$ sample
- Blue $N_{\text{trks}}-p$ reweighted to target $B \rightarrow D^+X$ sample

All templates are after run-dependent corrections of Section A.6. As described in Section A.9, the default reweighting scheme is secance- p reweighting.